Spin and Flavour dependent Interactions within a Quark Model for Baryons

Dissertation

zur

Erlangung des Doktorgrades (Dr. rer. nat.)

der

Mathematisch-Naturwissenschaftlichen Fakultät

der

Rheinischen Friedrich-Wilhelms-Universität Bonn

vorgelegt von

Michael Ronniger

aus

Düsseldorf

Bonn 2013

Angefertigt mit der Genehmigung der Mathmatisch-Naturwissenschaftlichen Fakultät der Rheinischen Friedrich-Wilhelms-Universität Bonn

Diese Dissertation ist auf dem Hochschulschriftenserver der ULB Bonn
`http://hss.ulb.uni-bonn.de/diss_online` elektronisch publiziert.

Referent:	PD. Dr. Bernard Ch. Metsch
Koreferent:	Prof. Dr. Carsten Urbach
Tag der Promotion:	10. Juni 2013
Erscheinungsjahr:	2013

To My Family.

Diese Welt ist unergründlich. Wir sind es auch, genau wie alle Wesen, die es auf dieser Welt gibt.

Menschen sind wahrnehmende Wesen, aber die Welt, die sie wahrnehmen, ist eine Illusion: eine Illusion geschaffen durch die Beschreibung, die ihnen seit ihrer Geburt erzählt wurde.
Im Grunde ist jene Welt, die sie mit ihrer Vernuft aufrechterhalten möchten, eine Welt, geschaffen durch eine Beschreibung und deren dogmatische und unumstößliche Regeln, die ihre Vernuft zu akzeptieren und zu verteidigen gelernt hat.

Don Juan Matus

Carlos Casterneda, *Das Rad der Zeit*
Fisher Taschenbuch Verlag, 1. Auflage (2007)

Zusammenfassung

Im Rahmen eines relativistisch kovarianten Quarkmodells, werden die Auswirkungen von zwei neuen Quarkwechselwirkungen auf die Massenspektren der leichten Baryonen sowie einer Vielzahl von Obsevablen, wie elektroschwache Formfaktoren, Helizitätsamplituden, Zerfallsamplituden, magnetische Momente und Ladungsradien, untersucht. Das hierbei benutzte Quarkmodell basiert auf der sogenannten Bethe-Salpeter Gleichung, mit der sich gebundene Zustände in der Quantenfeldtheorie beschreiben lassen.

Nach einer kurzen Zusammenfassung der theoretischen Grundlagen des verwendeten Quarkmodells werden die bisher veröffentlichten Ergebnisse diskutiert. Danach werden zwei verschiedene Ansätze für alternative Wechselwirkungen eingeführt. Dies entspricht dem Hauptteil dieser Arbeit: Zusätzlich zu dem sogenannten Confinement-Potential und der instanton-induzierten 't Hooft Wechselwirkung wird eine neue Spin-Flavour-abhängige Wechselwirkung eingeführt, die durch pseudoskalaren Meson-Austausch motiviert ist. Hierbei nehmen wir an, dass pseudoskalare Oktett- und Singlett-Mesonen mit den Quarks über pseudoskalare Kopplung wechselwirken. Hierfür nehmen wir ein kurzreichweitiges Gauss-Potential an. Dies bedingt drei zusätzliche Modellparameter: Die Oktett- und Singlett-Kopplungen sowie die Reichweite dieses Potentials. Es zeigt sich, dass diese zusätzliche Spin-Flavour-abhängige Wechselwirkung, verglichen mit den bisherigen Ergebnissen, eine bessere Beschreibung der baryonischen Massenspektren erlaubt. Es verbessert ebenso die Beschreibung der elektromagnetischen Formfaktoren und Helizitätsamplituden sowie der anderen oben genannten Observablen. Eine weitere Wechselwirkung ergibt sich aus einer Modifikation der Spin-Abhängigkeit des Confinement-Potentials, das durch weitere Spin-Spin- und Tensor-Terme ergänzt wird. Dieses modifizierte Confinement-Potential wird in Kombination mit der instanton-induzierten 't Hooft-Wechselwirkung wie auch mit der neuen Spin-Flavour abhängigen Wechselwirkung verwendet. Obwohl den Ergebnissen der obigen neuen Spin-Flavour abhängigen Wechselwirkung nicht überlegen, zeigte sich auch für Modelle mit modifiziertem Confinement-Potential, verglichen mit den bisherigen Modellvarianten, eine Verbesserung in der Beschreibung der Massenspektren und elektroschwachen Observablen.

Der Inhalt dieser Dissertation ist großteils in den folgenden Publikationen veröffentlicht worden:

- M. Ronniger und B. C. Metsch, *Effects of a spin-flavour dependent interaction on the baryon mass spectrum*, Eur. Phys. J. A **47**, 162 (2011), [arXiv:hep-ph/1111.3835].

- M. Ronniger und B. C. Metsch, *Effects of a spin-flavour dependent interaction on light-flavoured baryon helicity amplitudes*, Eur. Phys. J. A **49**, 8 (2013), [arXiv:hep-ph/1207.2640].

Abstract

Within the framework of a relativistic covariant quark model the effects of two novel quark interactions on the light-flavoured baryon mass spectra as well as on a multitude of observables, such as electroweak form factors, helicity amplitudes, decay amplitudes, magnetic moments and charge radii, are studied. This quark model is based on the so-called Bethe-Salpeter equation, which describes bound-state systems in quantum field theory.

After a brief summary of the basic ingredients of the quark model, we discuss the results published so far. Then we introduce two different forms for alternative interactions. This is the major subject of this thesis: In addition to the so-called confinement potential and an instanton-induced 't Hooft interaction a novel spin-flavour dependent interaction motivated by pseudoscalar meson-exchange is introduced. Thereby we assume, that pseudoscalar octet and singlet mesons interact with quarks via pseudoscalar coupling. Assuming a short-range Gaussian potential in coordinate space, we introduce only three additional model parameters: The octet and singlet-coupling strength as well as the range of this interaction. It is found, that this additional spin-flavour dependent interaction leads to a better description of the light-flavoured baryon mass spectra than has been obtained so far. It also improves the description of the electroweak form factors and helicity amplitudes as well as of the other observables mentioned above. A second interaction is studied, which corresponds to a modification of the spin dependence of the confinement potential by introducing specific spin-spin and tensor contributions. This modified confinement potential was used in combination with the instanton-induced 't Hooft interaction and with the novel spin-flavour dependent interaction as well. Although not superior to the results found with the new spin-flavour dependent interaction as mentioned above, also for models with a modified confinement potential a, compared to the previous results, improved description of both the spectra and electroweak observables was found.

The major part of this thesis can also be found in the following publications:

- M. Ronniger and B. C. Metsch, *Effects of a spin-flavour dependent interaction on the baryon mass spectrum*, Eur. Phys. J. A **47**, 162 (2011) [arXiv:hep-ph/1111.3835].
- M. Ronniger and B. C. Metsch, *Effects of a spin-flavour dependent interaction on light-flavoured baryon helicity amplitudes*, Eur. Phys. J. A **49**, 8 (2013) [arXiv:hep-ph/1207.2640].

Contents

1 Introduction **1**

2 The Bethe-Salpeter model for three fermions **5**
2.1 Introduction . . . 5
2.2 The six-point Green's function . . . 5
2.3 The Bethe-Salpeter equation and its normalisation condition . . . 8
2.4 Reduction to the instantaneous Salpeter equation . . . 12
2.4.1 The free quark propagator approximation . . . 12
2.4.2 The instantaneous approximation . . . 12
2.4.3 The Salpeter equation . . . 13
2.4.4 The projective structure of the Salpeter equation . . . 15
2.4.5 The Hamiltonian formulation of the Salpeter equation . . . 15
2.4.6 The normalisation condition of the Salpeter amplitudes . . . 17
2.5 Current-matrix elements . . . 18
2.6 Electroweak form factors and charge radii of non-strange baryons . . . 22
2.7 Helicity amplitudes and $\Delta \leftrightarrow N$ transition form factors . . . 24
2.8 Summary . . . 25

3 Results of previous calculations **27**
3.1 Introduction . . . 27
3.2 The confinement potential . . . 27
3.3 The instanton-induced interaction . . . 28
3.4 The one-gluon exchange . . . 28
3.5 Baryon spectra . . . 29
3.5.1 Scale dependence . . . 29
3.5.2 Model parameters . . . 29
3.5.3 Δ- and Ω-spectra . . . 30
3.5.4 N-spectrum . . . 33
3.5.5 Hyperon-spectra . . . 33
3.6 Electroweak observables . . . 37
3.7 Summary . . . 37

4 Alternative interaction kernels **39**
4.1 Introduction . . . 39
4.2 The spin-flavour dependent interaction . . . 39
4.2.1 Model parameters . . . 41
4.2.2 Δ- and Ω-spectrum . . . 42
4.2.3 N-spectrum . . . 43
4.2.4 Hyperon-spectra . . . 50
4.2.5 Electroweak form factors of the nucleon . . . 50
4.2.6 Helicity amplitudes . . . 54

4.2.7 Photon couplings . . . 68
4.2.8 $\Delta(1232) \leftrightarrow N$ transition form factors . . . 70
4.3 A modified confinement potential . . . 71
4.3.1 Model parameters . . . 71
4.3.2 Δ- and Ω-spectrum . . . 72
4.3.3 N-spectrum . . . 72
4.3.4 Hyperon-spectra . . . 73
4.3.5 Electroweak form factors of the nucleon . . . 80
4.3.6 Some helicity amplitudes . . . 82
4.3.7 Photon couplings . . . 89
4.3.8 $\Delta(1232) \leftrightarrow N$ transition form factors . . . 91
4.4 Summary . . . 91

5 Summary and Outlook **95**

A One-meson-exchange **101**
A.1 The instantaneous approximation . . . 102
A.2 Flavour-matrix elements . . . 102

Danksagung **111**

Chapter 1

Introduction

The description of the hadronic excitation spectrum remains a major challenge in strong interaction theory. In particular, the physics of baryons in the low- and intermediate energy regime of **Q**uantum **C**hromo **D**ynamics is not well understood due to the non-perturbative nature of QCD. Additionally, new data for baryon resonances have been published in the last years. Besides new baryon resonances, new data for electromagnetic nucleon form factors and helicity amplitudes are now available, which have been measured at the CB-ELSA experiment in Bonn for instance and other experimental facilities like the CEBAF at Jefferson Lab. From the theoretical point of view two approaches exist to approximate QCD in the low energy regime: **Ch**iral **P**erturbation **T**heory and lattice QCD. Here, ChPT describes QCD in the framework of an effective **Q**uantum **F**ield **T**heory, which preserves all symmetries, in particular the chiral symmetry of the original QCD-Lagrangian, but uses hadrons as the relevant degrees of freedom instead of quarks and gluons and a systematic expansion in terms of small masses and the momenta. This has been discussed by Leutwyler [1] for instance. By construction, it is not applicable to the physics of excited baryons. The second approach in principle is an *ab initio* calculation: it numerically simulates QCD on a discrete space-time lattice. This leads to a enormous numerical effort, because all appearing correlation functions and path-integrals have to be evaluated numerically in order to extract hadronic properties. However, with increasing computing power, lattice QCD will be able to reproduce all hadronic spectra in future, but presently, in spite of recent progress in unquenched lattice QCD, access to excited states is still very limited [2, 3]. Therefore, alternative approaches manageable with less numerical effort are presently still relevant. In the past, the **C**onstituent **Q**uark **M**odel has been widely used to describe properties of excited baryons. Such models should offer an efficient description of masses (resonance positions), static properties such as magnetic moments, charge radii, electroweak amplitudes (form factors and helicity amplitudes) with only a few model parameters. Furthermore, they can serve as a framework to judge, which resonances can be considered exotic as well as a guideline in the search of new excited baryon states. Therefore, it presently still seems worthwhile to improve upon constituent quark model descriptions, which in view of the light quark masses (even taken as effective constituent masses) have to be formulated in terms of relativistically covariant equations of motion. About a decade ago such a quark model for baryons has been formulated, see [4–7], on the basis of an instantaneous formulation of the Bethe-Salpeter equation. In this model the quark interactions reflect a string-like description of quark confinement through a confinement potential rising linearly with interquark distances as well as a spin-flavour dependent interaction based on instanton effects: The latter explains the major spin-dependent splittings in the baryon spectrum. Löring *et al.* [5–7] discussed two different models, which differ by their confinement Dirac-structure (*i.g.* the spin dependence) and are simply called model $\mathcal{A}$ and $\mathcal{B}$, respectively. A satisfactory description of the major features in the light-flavoured baryonic mass spectrum could indeed be obtained. This also applies to the description of the electroweak nucleon form factors and helicity amplitudes in case of the model version called $\mathcal{A}$. The prominent features, that can be accounted for include

- the linear Regge trajectories with an universal slope for all flavours including states up to total angular momenta of $J = \frac{15}{2}$ and excitation energies up to 3 GeV, see [5, 6];
- the low position of the so-called Roper-resonance in model $\mathcal{A}$ and three other positive parity excited nu-

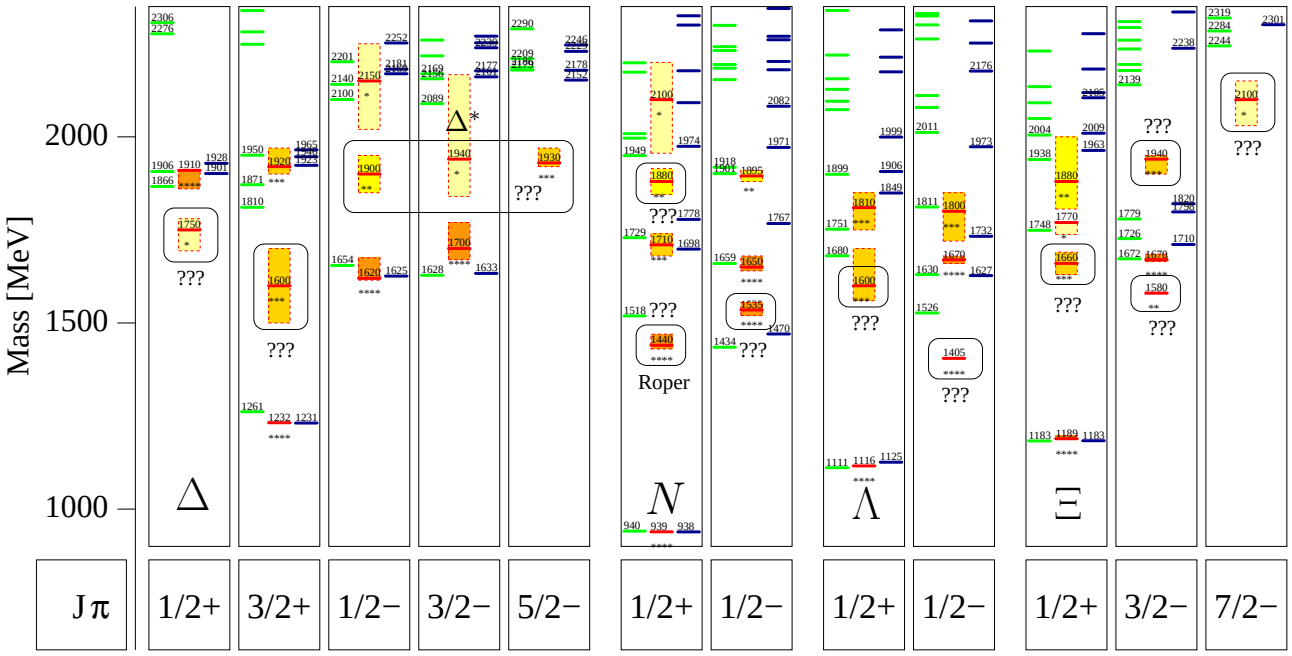

Fig. 1.1: Discrepancies in the baryonic mass spectra: The left and right side of each column represents the results obtained from model $\mathcal{A}$ and $\mathcal{B}$, respectively, of [5] in comparison with experimental data from the Particle Data Group [8] (middle of each column), where lines indicates the resonance position (mass) with its mass uncertainty represented by a shaded box. The rating of each resonance is indicated by stars according to [8]. J and π denotes the total angular momentum and parity, respectively. Deficiencies are indicates with a box and question marks.

cleon states ($N_{1/2^+}(1710)$, $N_{3/2^+}(1720)$, $N_{5/2^+}(1680)$) well below all other states of this kind. These can be largely accounted for by the instanton-induced force, the strength of which was chosen to reproduce the groundstate $\Delta - N$ splitting [5, 6];

- a plethora of electroweak properties, which can be explained within the framework of model $\mathcal{A}$ without introducing any additional parameters, see [9–14];
- a satisfactory description of the transverse $S_{11}(1535)$-, $D_{13}(1520)$-, $S_{31}(1620)$- and $D_{33}(1700)$-helicity amplitudes for model $\mathcal{A}$.

Nevertheless, some specific discrepancies remain; most prominent are:

- the newly discovered $N_{1/2^+}(1880)$-resonance (see [8, 15–17]) cannot be accurately accounted for by both models as well as the negative parity state $N_{1/2^-}(1535)$, which is predicted too low, see Fig. 1.1;
- the conspicuously low position as well as the decay properties of the negative parity $\Lambda_{1/2^-}(1405)$-resonance. The calculated mass of this state exceeds the experimental value by more than 100 MeV in model $\mathcal{A}$ and by more than 200 MeV in model $\mathcal{B}$;
- there is experimental evidence [8] for excited negative parity Δ^*-resonances well below 2 GeV ($\Delta_{1/2^-}(1900)$, $\Delta_{3/2^-}(1940)$ and $\Delta_{5/2^-}(1930)$), which cannot be accounted for by the quark model mentioned above, see Fig. 1.1, nor by any other constituent quark model we are aware of;
- the mass of the positive parity Roper-like $\Delta_{3/2^+}(1600)$-resonance, see also Fig. 1.1, the low value of which with respect to other excited states of this kind cannot be traced back to instanton-induced effects, since these are absent for flavour symmetric states;
- the Roper-like resonances $\Lambda_{1/2^+}(1600)$ and $\Sigma_{1/2^+}(1660)$ are not satisfactorily reproduced by both models, see Fig. 1.1;

- the position of the $\Sigma_{3/2^-}(1580)$-resonance as well as the $J^\pi = \frac{7}{2}^-$-state $\Sigma_{7/2^-}(2100)$, which cannot be accounted for by both models, see Fig. 1.1;

- the description of the transverse $P_{11}(1440)$-helicity amplitude within the framework of model $\mathcal{A}$, see [9], does not account for the node found experimentally in novel data from Aznauryan *et al.* [18–20] from the CLAS-collaboration at CEBAF. Furthermore, the $S_{11}(1535)$-amplitude does not describe the minimum in the data from Burkert *et al.* [21]. See also Figs. 4.14 and 4.19 for further information.

Furthermore, there are more resonances than can be found in Merten *et al.* [9, 10] for which helicity amplitudes can be calculated. Also novel data on helicity amplitudes from Aznauryan *et al.* [18–20], can be used to compare to theoretical calculations. In particular, there now exists data for the longitudinal amplitudes of some resonances, which have been measured in these experiments and can serve as a further test of the model.

Therefore, we want to explore whether the deficiencies mentioned above are inherent to the constituent quark model itself or can be overcome by the introduction of an additional quark interaction, which improves upon the issues mentioned above without deteriorating the excellent description of the majority of the other states. In view of the fact, that the discrepancies mainly affect the Δ-spectrum, this additional interaction is likely to be flavour dependent. An obvious candidate in this respect would be a single pseudoscalar meson-exchange potential as has been used as a basis of an effective spin-flavour dependent quark interaction very successfully by the Graz-group [22–30]. This model uses a so-called Goldstone-Boson exchange within a relativised constituent quark model. Furthermore, the model describes baryon states with $J \leq \frac{5}{2}$ and electroweak form factors quite well. In particular the electric neutron form factor can be accurately accounted for.

In the present thesis we shall investigate two different implementations of alternative interactions, which are able to rectify at least partially the deficiencies mentioned above. The thesis is organised as follows: After a detailed recapitulation of the ingredients and basic equations of our Bethe-Salpeter model in chapter 2 as presented by Löring, Merten, Kretzschmar and Haupt [4, 7, 9, 10, 12–14], we summarise in chapter 3 the numerical results obtained so far on the light-flavoured baryon spectra for model $\mathcal{A}$ and $\mathcal{B}$, respectively. Subsequently we introduce the new alternative interactions in chapter 4. Thereby, section 4.2 contains the results and discussion of the baryon mass spectra, electroweak form factors and helicity amplitudes including a new spin-flavour dependent interaction (see Ronniger *et al.* [31, 32]) in comparison to the older results obtained from Löring *et al.* [5, 6]. In the subsequent section 4.3 we present the results of a modified confinement potential including spin-spin and tensor interactions, before concluding with a summary in chapter 5.

A part of this work has been published in [31, 32] (section 4.2). A synopsis of the major chapters is given as follows:

Chapter 2: After a brief introduction, chapter 2 starts with the introduction of the six-point Green's function defined as the vacuum expectation value of the time-order product of three-fermion Heisenberg field operators and their adjoint operators and its major contribution from the incoming and outgoing baryon-state in section 2.2. Following the work of Löring *et al.* [4, 7], the Bethe-Salpeter equation and its normalisation condition are derived from the six-point Green's function in section 2.3. Here, we show the underlying method how to extract the Bethe-Salpeter equation from the Green's function by defining the corresponding Bethe-Salpeter amplitudes using a Laurent- and Taylor-expansion around a pole in the energy. Subsequent to this section, in section 2.4, a reduction method of the Bethe-Salpeter equation to the instantaneous Salpeter equation is discussed. In particular, the free quark-propagator approximation enters within this reduction method together with the instantaneous approximation itself. Here, also the Salpeter amplitudes are defined. Due to the projective structure of the Salpeter equation it is possible to rewrite the Salpeter equation in terms of an Hamiltonian as shown in subsection 2.4.5. Consequently, the Salpeter equation corresponds to an eigenvalue problem in which the Salpeter amplitudes enter as eigenvectors, while the eigenvalues correspond to the baryon masses. In the next section 2.5, the calculation of current-matrix elements is discussed in order to calculate electroweak nucleon form factors and helicity amplitudes. The calculation of current-matrix elements starts from a seven-point Green's function in the same manner as the Bethe-Salpeter equation has been derived from the six-point Green's function. The underlying concept has been worked out by Merten and Kretzschmar *et al.* [9, 10, 12]

and allows the calculation of electroweak form factors and helicity amplitudes. It is summarised in section 2.6 and 2.7.

Chapter 3: Chapter 3 summarises the results for model $\mathcal{A}$ and $\mathcal{B}$, respectively. We start in section 3.2 with a brief introduction to the different approaches for the confinement potential for these models before discussing the major points for the implementation of the instanton-induced 't Hooft interaction in section 3.3. Since the one-gluon exchange offers an alternative to the instanton-induced 't Hooft interaction, we have summarised the basics of the one-gluon exchange in this section for the sake of completeness and without discussing the results, which can be found in the thesis from U. Löring [7]. Subsequently, we begin the discussion of the light-flavoured baryon spectra in section 3.5 with the determination of the optimal length scale for each resonance and of the other parameters of the model. The chapter concludes with a brief overview on electroweak form factors and helicity amplitudes from Merten and Kretzschmar *et al.* [9, 10, 12] in section 3.6, which will be discussed in detail in the next chapter in comparison with the new spin-flavour dependent interaction.

Chapter 4: After a short introduction, we present the novel spin-flavour dependent interaction in section 4.2. We start with the introduction of two interaction Lagrangians, which couple pseudoscalar mesons to quarks via pseudoscalar- or pseudovector coupling. Here, we prefer the pseudoscalar quark-meson coupling, since it has found to lead to the most favourable results. For the pseudoscalar coupled interaction, we substitute the radial dependence of the corresponding Yukawa-potential in coordinate space by a short-range Gaussian potential. Based on this new interaction a new model, called model $\mathcal{C}$, will be introduced. The effects of the new interaction on the light-flavoured baryon spectra, electroweak form factors, helicity amplitudes, photon couplings and $\Delta(1232) \leftrightarrow N$ transition form factors will be discussed in the subsequent subsections in detail. Thereby, we compare additionally with the older predictions of model $\mathcal{A}$, which however were recalculated with higher numerical accuracy. The discussion of the results starts with the determination of the optimal length scale for each resonance and the parameters of model $\mathcal{C}$ in subsection 4.2.1. In the next three subsequent subsections we discuss the Δ-, N- and hyperon-spectra. Here, we discuss also the nature of some new N-resonances as presently available in the compilation by the PDG [8]. Subsequently, we show the results for the electroweak form factors in subsection 4.2.5. These include the electric- and magnetic proton and neutron form factors as well as the axial form factor. For completeness, we also present results for the ratio of the electric- and magnetic proton form factor as well as for magnetic moments and charge radii. Thereby, the magnetic moments and charge radii of the octet and decuplet hyperons were calculated with the method from Haupt *et al.* [13, 14]. In the next subsection 4.2.6 we discuss in some detail the results for a multitude of helicity amplitudes for model $\mathcal{A}$ and $\mathcal{C}$. Here, we extend the treatment of Merten *et al.* [9, 10] to more baryon resonances and notably also to the longitudinal helicity amplitudes. Finally, the discussion of the effects of the new spin-flavour dependent interaction closes with a listing of all calculated photon decay amplitudes and the discussion of the $\Delta(1232) \leftrightarrow N$ transition form factors in subsections 4.2.7 and 4.2.8, respectively.

In section 4.3 we propose an alternative form of a linear confinement potential, which includes spin-spin and tensor interactions. The corresponding constituent quark models with this form of the confinement potential are called model $\mathcal{D}$ and $\mathcal{E}$. Thereby, model $\mathcal{D}$ uses the new confinement potential in combination with the instanton-induced 't Hooft interaction, whereas model $\mathcal{E}$ uses additionally the new spin-flavour dependent interaction of model $\mathcal{C}$. In the following subsections we calculate again the baryon spectra, electroweak form factors, helicity amplitudes, photon couplings and $\Delta(1232) \leftrightarrow N$ transition form factors for model $\mathcal{D}$ and $\mathcal{E}$, respectively. All results are compared to the results of model $\mathcal{A}$ and $\mathcal{C}$. In subsection 4.3.1 we discuss again the scale dependencies of the baryon resonances and list all model parameters. Subsequently, we show all light-flavoured baryon spectra before presenting the results of the electroweak form factors in subsection 4.3.5. For a selection of baryon resonances, we display helicity amplitudes in subsection 4.3.6 for model $\mathcal{D}$ and $\mathcal{E}$. Again, we close the discussion for the new models $\mathcal{D}$ and $\mathcal{E}$ with a listing of all calculated photon decay amplitudes and the $\Delta(1232) \leftrightarrow N$ transition form factors. The chapter ends with a short summary.

Chapter 5: Chapter 5 contains a summary and outlook.

Chapter 2

The Bethe-Salpeter model for three fermions

2.1 Introduction

In the following chapter the fundamental ideas and concepts of the relativistic Bethe-Baryon quark model based on the Bethe-Salpeter equation, which had been already used in order to describe baryonic bound-states, will be discussed and summarised. The model was mainly developed and implemented by U. Löring *et al.* in 2001 and results were published in [4, 5] and [6] (see also the PhD thesis of U. Löring for more information [7]). The calculation of form factors, helicity amplitudes and other strong-decay properties has been developed by K. Kretzschmar, D. Merten *et al.* [9] and S. Migura *et al.* [33] (see also the PhD of K. Kretzschmar, D. Merten and S. Migura, [12], [10] and [34]). In order to describe bound-state systems within the framework of quantum field theory, the so-called *Bethe-Salpeter equation* is basic for the construction of a baryonic model, which has the potential to describe excited spectra and electroweak properties of baryons in a unified manner. We will start with introducing the six-point Green's function, which describes baryonic bound-states in the framework of QFT and then derive the Bethe-Salpeter equation and its normalisation condition subsequently. Here, the *Bethe-Salpeter amplitudes* for three fermions will be introduced. This procedure can be generalised in principle to more than three particles. The Bethe-Salpeter equations are relativistically covariant integral equations. Assuming, that all interactions are completely instantaneous, which means that retardation effects can be neglected, it is possible to reduce the Bethe-Salpeter equation to the (instantaneous) *Salpeter equation*. In doing so, the Bethe-Salpeter amplitudes are substituted by the so-called *Salpeter amplitudes*. Also the Salpeter equation is relativistically covariant. In the non-relativistic limit the Salpeter equation gets equivalent to the Pauli equation and the Salpeter amplitude then corresponds to the usual non-relativistic wave-function. Finally, the Salpeter equation is reformulated as an eigenvalue equation, which then can be solved numerically.

2.2 The six-point Green's function

The six-point Green's function is the fundamental quantity for the description of systems consisting of three interacting particles in the framework of QFT. Thereby, the six-point Green's function is defined as the vacuum expectation value of the time-ordered product of three-fermion Heisenberg field operators ψ^i and their adjoint operators $\bar{\psi}^i := \psi^{i\dagger}\gamma_0$ as

$$\begin{aligned} &G_{a_1,a_2,a_3;a_1',a_2',a_3'}(x_1,x_2,x_3;x_1',x_2',x_3') \\ &\qquad := -\langle 0|T\,\psi^1_{a_1}(x_1)\psi^2_{a_2}(x_2)\psi^3_{a_3}(x_3)\bar{\psi}^1_{a_1'}(x_1')\bar{\psi}^2_{a_2'}(x_2')\bar{\psi}^3_{a_3'}(x_3')|0\rangle\,, \end{aligned} \tag{2.1}$$

where $a_i = (\alpha_i,\, f_i,\, c_i)$ denotes a multi-index, which collects the Dirac-, Flavour- and Colour-quantum numbers $\alpha_i,\, f_i,\, c_i$. The vacuum is denoted by $|0\rangle$ and T defines the usual time-ordering operator as defined in many textbooks. Following any standard textbook about quantum field theory (*e.g.* [35]) the Green's function can be

expanded in perturbation theory as

$$G(x_1,x_2,x_3;x_1',x_2',x_3') = \frac{-1}{\langle 0|T\,\exp\left(-\mathrm{i}\int_{-\infty}^{+\infty}\mathrm{d}t\,\hat{H}_I(t)\right)|0\rangle}\sum_{k=1}^{\infty}\frac{(-\mathrm{i})^k}{k!}\int \mathrm{d}^4y_1\ldots\mathrm{d}^4y_k$$
$$\times\,\langle 0|T\psi^1(x_1)\psi^2(x_2)\psi^3(x_3)\bar{\psi}^1(x_1')\bar{\psi}^2(x_2')\bar{\psi}^3(x_3')\hat{\mathcal{H}}_I(y_1)\ldots\hat{\mathcal{H}}_I(y_k)|0\rangle\,. \tag{2.2}$$

Thereby, $\hat{H}_I$ denotes the interaction Hamilton and $\hat{\mathcal{H}}_I$ the corresponding density, while the field operators are given in the interaction picture. The sum within Eq. (2.2) generates a power series, which corresponds in every order to a finite number of Feynman diagrams according to Wick's theorem. In opposite to high energy scattering processes, where in every interaction perturbation theory can be applied, this is not applicable to low energy states. Here, poles within the total energy can occur. Such poles never arise from a finite set of Feynman diagrams. Thus, the problem is to find a method which takes into account an infinite set of diagrams.

The problem can be solved by finding an integral equation with an iterative structure, which circumvents the explicit summation within the Green's function and effectively sums up an infinite set of Feynman diagrams. This leads to the so-called Bethe-Salpeter equation. We consider two possibilities for interactions in systems of three fermions, while distinguishing three- and two-body interactions. The first one is denoted as $K^{(3)}_{a_1,a_2,a_3;a_1',a_2',a_3'}(x_1,x_2,x_3;x_1',x_2',x_3')$ and the second one as $K^{(2)}_{a_1,a_2;a_1',a_2'}(x_1,x_2;x_1',x_2')$. The interactions are generated by *irreducible* diagrams only, where irreducible means, that they cannot be decomposed into two smaller diagrams by cutting three or two fermion lines at once. With the definition of the full fermion-propagator

$$S^i_{F\,a_i;a_i'}(x_i,x_i') := \langle 0|T\,\psi^i_{a_i}(x_i)\bar{\psi}^i_{a_i'}(x_i')|0\rangle\,, \tag{2.3}$$

Eq. (2.2) can be rewritten with three- and two-body interactions as a Dyson-Schwinger equation

$$\begin{aligned}
G_{a_1,a_2,a_3;a_1',a_2',a_3'}(x_1,x_2,x_3;x_1',x_2',x_3') &= S^1_{F\,a_1;a_1'}(x_1,x_1')\,S^2_{F\,a_2;a_2'}(x_2,x_2')\,S^3_{F\,a_3;a_3'}(x_3,x_3')\\
&-\mathrm{i}\int \mathrm{d}^4y_1\,\mathrm{d}^4y_2\,\mathrm{d}^4y_3\,S^1_{F\,a_1;b_1}(x_1,y_1)\,S^2_{F\,a_2;b_2}(x_2,y_2)\,S^3_{F\,a_3;b_3}(x_3,y_3)\\
&\times\int \mathrm{d}^4y_1'\,\mathrm{d}^4y_2'\,\mathrm{d}^4y_3'\,K^{(3)}_{b_1,b_2,b_3;b_1',b_2',b_3'}(y_1,y_2,y_3;y_1',y_2',y_3')\,G_{b_1',b_2',b_3';a_1',a_2',a_3'}(y_1',y_2',y_3';x_1',x_2',x_3')\\
&-\mathrm{i}\sum_{\substack{\text{cycl. perm.}\\(123)}}\int \mathrm{d}^4y_1\,\mathrm{d}^4y_2\,S^1_{F\,a_1;b_1}(x_1,y_1)\,S^2_{F\,a_2;b_2}(x_2,y_2)\\
&\times\int \mathrm{d}^4y_1'\mathrm{d}^4y_2'\,K^{(2)}_{b_1,b_2;b_1',b_2'}(y_1,y_2;y_1',y_2')\,G_{b_1',b_2',a_3;a_1',a_2',a_3'}(y_1',y_2',x_3;x_1',x_2',x_3')\,.
\end{aligned} \tag{2.4}$$

Introducing the inverse fermion-propagator S_F^{-1} as

$$\int \mathrm{d}^4y_i\,S^i_{F\,a_i;b_i}(x_i,y_i)\,{S^i_F}^{-1}_{b_i;a_i'}(y_i,x_i') = \delta_{a_i\,a_i'}\delta^{(4)}(x_i-x_i') \tag{2.5}$$

allows the redefinition of the sum of two-body kernels in order to rewrite them as a three-body kernel

$$\bar{K}^{(2)}_{a_1,a_2,a_3;a_1',a_2',a_3'}(x_1,x_2,x_3;x_1',x_2',x_3') := \sum_{\text{cycl. perm. ((12)3)}} K^{(2)}_{a_1,a_2;a_1',a_2'}(x_1,x_2;x_1',x_2')\,{S^3_F}^{-1}_{a_3;a_3'}(x_3,x_3')\,. \tag{2.6}$$

With that definition a total interaction kernel K can be defined as

$$K := K^{(3)} + \bar{K}^{(2)}\,, \tag{2.7}$$

which includes the three- and two-body kernels as displayed in Fig. 2.1. In order to simplify the notation the product of the three (free) fermion propagators will be substituted by the *free Green's function* G_0, which is defined by

$$G_{0\,a_1,a_2,a_3;a_1',a_2',a_3'}(x_1,x_2,x_3;x_1',x_2',x_3') := S^1_{F\,a_1;a_1'}(x_1,x_1')\,S^2_{F\,a_2;a_2'}(x_2,x_2')\,S^3_{F\,a_3;a_3'}(x_3,x_3')\,. \tag{2.8}$$

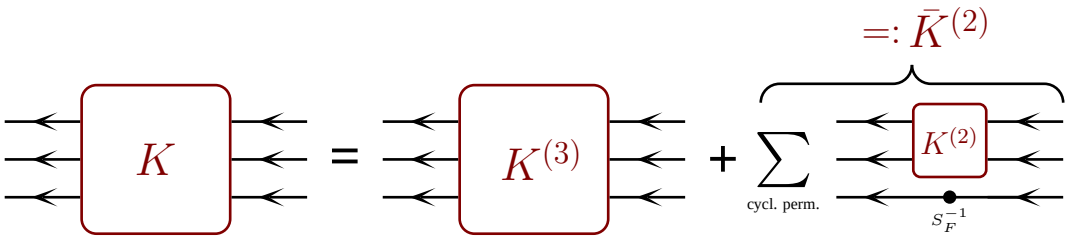

Fig. 2.1: Schematic representation of the total kernel K composed by three- and two-body kernels. The interaction kernels are displayed by the red rectangles. Free quarks are displayed as black arrows, which denotes the quark-propagation.

Furthermore, it is useful to introduce a compact notation, since many integrals and summations occur within the equations. Therefore, we define the symbolical compact notation for the integrals

$$[AB]_{a_1,a_2,a_3;a_1',a_2',a_3'}(x_1,x_2,x_3;x_1',x_2',x_3') := \int \mathrm{d}y_1\,\mathrm{d}y_2\,\mathrm{d}y_3\, A_{a_1,a_2,a_3;b_1,b_2,b_3}(x_1,x_2,x_3;y_1,y_2,y_3) \times B_{b_1,b_2,b_3;a_1',a_2',a_3'}(y_1,y_2,y_3;x_1',x_2',x_3')\,, \tag{2.9}$$

Thus, Eq. (2.4) can be rewritten compactly as

$$G = G_0 - \mathrm{i}\, G_0\, K\, G\,, \tag{2.10a}$$
$$G = G_0 - \mathrm{i}\, G\, K\, G_0\,, \tag{2.10b}$$

where additionally all indices and spatial dependencies are suppressed. Eq. (2.10b) corresponds to the adjoint form of Eq. (2.4). It can be proven, that G is invariant under space-time translations, see thesis of Löring [7]. Exploiting this symmetry it allows to use the centre-of-mass frame, where the so-called Jacobi-coordinates X, ξ and η can be introduced. A schematic representation of the Jacobi-coordinates has been displayed in Fig. 2.2 .

$$\left.\begin{aligned} X &:= \tfrac{1}{3}\,(x_1+x_2+x_3)\,,\\ \xi &:= x_1 - x_2\,,\\ \eta &:= \tfrac{1}{2}\,(x_1+x_2-2x_3)\,, \end{aligned}\right\} \Leftrightarrow \left\{\begin{aligned} x_1 &= X + \tfrac{1}{2}\xi + \tfrac{1}{3}\eta\,,\\ x_2 &= X - \tfrac{1}{2}\xi + \tfrac{1}{3}\eta\,,\\ x_3 &= X - \tfrac{2}{3}\eta\,. \end{aligned}\right. \tag{2.11}$$

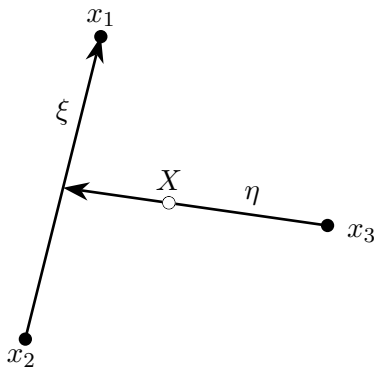

Fig. 2.2: The Jacobi coordinates for three particles.

Since the manipulations of the Bethe-Salpeter equation are simpler in momentum space it is useful to introduce Jacobi-coordinates in momentum space P , p_ξ and p_η as well

$$\left.\begin{aligned} P &:= p_1+p_2+p_3\,,\\ p_\xi &:= \tfrac{1}{2}\,(p_1-p_2)\,,\\ p_\eta &:= \tfrac{1}{3}\,(p_1+p_2-2p_3)\,, \end{aligned}\right\} \Leftrightarrow \left\{\begin{aligned} p_1 &= \tfrac{1}{3}P + p_\xi + \tfrac{1}{2}p_\eta\,,\\ p_2 &= \tfrac{1}{3}P - p_\xi + \tfrac{1}{2}p_\eta\,,\\ p_3 &= \tfrac{1}{3}P - p_\eta\,. \end{aligned}\right. \tag{2.12}$$

From the translation symmetry mentioned above it follows, that the total momentum P is conserved. After performing a Fourier transformation, integrals of type

$$\begin{aligned}[\mathcal{F}A](p_1,p_2,p_3;p_1',p_2',p_3') &= \int \mathrm{d}^4x_1\,\mathrm{d}^4x_2\,\mathrm{d}^4x_3\,\mathrm{e}^{\mathrm{i}\,(\langle p_1,x_1\rangle+\langle p_2,x_2\rangle+\langle p_3,x_3\rangle)}\\ &\quad\times\int \mathrm{d}^4x_1'\,\mathrm{d}^4x_2'\,\mathrm{d}^4x_3'\,\mathrm{e}^{-\mathrm{i}\left(\langle p_1',x_1'\rangle+\langle p_2',x_2'\rangle+\langle p_3',x_3'\rangle\right)}\,A(x_1,x_2,x_3;x_1',x_2',x_3')\\ &:= (2\pi)^4\delta^{(4)}(P-P')\,A(p_\xi,p_\eta;p_\xi',p_\eta'), \end{aligned} \tag{2.13}$$

occur, where $\langle\cdot,\cdot\rangle$ denotes the Minkowski scalar product. All Fourier integrals, which occur in Eq. (2.10a) or (2.10b) are of this type. Since P is conserved, all quantities will be labelled with an extra subscript P and the Green's function from Eq. (2.4) now reads in momentum space

$$\begin{aligned}
G_P(p_\xi,p_\eta;p'_\xi,p'_\eta) =& G_{0\,P}(p_\xi,p_\eta;p'_\xi,p'_\eta) - \mathrm{i}\int \mathrm{d}^4p'''_\xi\,\mathrm{d}^4p'''_\eta\,\mathrm{d}^4p''_\xi\,\mathrm{d}^4p''_\eta \\
&\times G_{0\,P}(p_\xi,p_\eta;p'''_\xi,p'''_\eta)\,K_P(p'''_\xi,p'''_\eta;p''_\xi,p''_\eta)\,G_P(p''_\xi,p''_\eta;p'_\xi,p'_\eta) \\
=& S_F^1(\tfrac{1}{3}P+p_\xi+\tfrac{1}{2}p_\eta)\,S_F^2(\tfrac{1}{3}P-p_\xi+\tfrac{1}{2}p_\eta)\,S_F^3(\tfrac{1}{3}P-p_\eta) \\
&\times (2\pi)^4\delta^{(4)}(p_\xi-p'_\xi)\,(2\pi)^4\delta^{(4)}(p_\eta-p'_\eta) \\
&+ S_F^1(\tfrac{1}{3}P+p_\xi+\tfrac{1}{2}p_\eta)\,S_F^2(\tfrac{1}{3}P-p_\xi+\tfrac{1}{2}p_\eta)\,S_F^3(\tfrac{1}{3}P-p_\eta) \\
&\times(-\mathrm{i})\int \mathrm{d}^4p''_\xi\,\mathrm{d}^4p''_\eta\,K_P(p_\xi,p_\eta;p''_\xi,p''_\eta)G_P(p''_\xi,p''_\eta;p'_\xi,p'_\eta)\,,
\end{aligned} \tag{2.14}$$

with the definition of the free Green's function $G_{0\,P}$ in momentum space

$$\begin{aligned}
G_{0\,P}(p_\xi,p_\eta;p'_\xi,p'_\eta) :=& S_F^1(\tfrac{1}{3}P+p_\xi+\tfrac{1}{2}p_\eta)\,S_F^2(\tfrac{1}{3}P-p_\xi+\tfrac{1}{2}p_\eta)\,S_F^3(\tfrac{1}{3}P-p_\eta) \\
&\times(2\pi)^4\delta^{(4)}(p_\xi-p'_\xi)\,(2\pi)^4\delta^{(4)}(p_\eta-p'_\eta)\,.
\end{aligned} \tag{2.15}$$

In doing so, the two-body part of the interaction kernel K_P is given by

$$\begin{aligned}
\bar{K}^{(2)}_{P,a_1,a_2,a_3;a'_1,a'_2,a'_3}(p_\xi,p_\eta;p'_\xi,p'_\eta) =& \sum_{\substack{(ijk)=(123),\\(231),(312)}} K^{(2)}_{\frac{2}{3}P+p_{\eta_k},a_i,a_j;a'_i,a'_j}(p_{\xi_k},p'_{\xi_k}) \\
&\times S_{F\,a_k;a'_k}^{k\,-1}(\tfrac{1}{3}P-p_{\eta_k})\,(2\pi)^4\delta^{(4)}(p_{\eta_k}-p'_{\eta_k})\,,
\end{aligned} \tag{2.16}$$

where the additional numbering in the kernel subscripts labels different sets of Jacobi coordinates, transformed via Talmi-Moshinski transformations

$$\begin{pmatrix} p_\xi \\ p_\eta \end{pmatrix} := \begin{pmatrix} p_{\xi_3} \\ p_{\eta_3} \end{pmatrix} = \begin{pmatrix} -\frac{1}{2} & -\frac{3}{4} \\ 1 & -\frac{1}{2} \end{pmatrix} \begin{pmatrix} p_{\xi_1} \\ p_{\eta_1} \end{pmatrix} = \begin{pmatrix} -\frac{1}{2} & \frac{3}{4} \\ 1 & -\frac{1}{2} \end{pmatrix} \begin{pmatrix} p_{\xi_2} \\ p_{\eta_2} \end{pmatrix}. \tag{2.17}$$

Analogous to the definition made within Eq. (2.9), a shorter notation in momentum space can be introduced, which suppresses all integrals and summations. Thus, Eq. (2.14) is written symbolically as

$$G_P = G_{0\,P} - \mathrm{i}\,G_{0\,P}\,K_P\,G_P\,, \tag{2.18a}$$

$$G_P = G_{0\,P} - \mathrm{i}\,G_P\,K_P\,G_{0\,P}\,, \tag{2.18b}$$

where the second equation again corresponds to the adjoint equation.

2.3 The Bethe-Salpeter equation and its normalisation condition

So far, we did not choose a particular time-ordering for the Green's function and it describes scattering processes as well as bound-states. Here, we are interested in three-fermion bound-states, that propagate forward in time. In particular, we assume the existence of a bound-state with the (positive) total mass M defined as the invariant mass $\bar{P}^2 = M^2$ with $\bar{P} = (\omega_P, \mathbf{P})$ and $\omega_{\mathbf{P}} = \sqrt{\mathbf{P}^2+M^2}$, which is an eigenstate of the total momentum operator $\hat{\bar{P}}$:

$$\hat{P}|\bar{P}\rangle = \bar{P}|\bar{P}\rangle \tag{2.19}$$

normalised as

$$\langle\bar{P}|\bar{P}'\rangle = (2\pi)^3\,2\omega_{\mathbf{P}}\delta^{(3)}(\mathbf{P}-\mathbf{P}')\,. \tag{2.20}$$

We thus consider the particular time-ordering $\min(x_1^0, x_2^0, x_3^0) > \max(x_1'^0, x_2'^0, x_3'^0)$, which separates the initial- and final three-fermions states and can be written in terms of the Heaviyside-function θ

$$\theta(\min(x_1^0, x_2^0, x_3^0) - \max(x_1'^0, x_2'^0, x_3'^0)) = \begin{cases} 1 & \text{for } \min(x_1^0, x_2^0, x_3^0) > \max(x_1'^0, x_2'^0, x_3'^0) \\ 0 & \text{otherwise} \end{cases} . \tag{2.21}$$

The crucial idea, in order to obtain the Bethe-Salpeter equation and its normalisation condition from the Green's function formalism, is an expansion of Eq. (2.18a) in the vicinity of $\bar{P}$, while isolating the given time-ordering from above. Then, the Green's function can be written as

$$\begin{aligned} &G_{\bar{P}\, a_1,a_2,a_3;a_1',a_2',a_3'}(x_1,x_2,x_3;x_1',x_2',x_3') \\ &\quad := -\langle 0|T\{\psi^1_{a_1}(x_1)\psi^2_{a_2}(x_2)\psi^3_{a_3}(x_3)\}T\{\bar{\psi}^1_{a_1'}(x_1')\bar{\psi}^2_{a_2'}(x_2')\bar{\psi}^3_{a_3'}(x_3')\}|0\rangle \\ &\qquad\quad \times \theta(\min(x_1^0, x_2^0, x_3^0) - \max(x_1'^0, x_2'^0, x_3'^0)) \\ &\qquad\quad + \text{other terms arising from different time-orderings} \\ &\quad := -\int \frac{\mathrm{d}^3P}{(2\pi)^3 2\omega_{\mathbf{P}}} \langle 0|T\{\psi^1_{a_1}(x_1)\psi^2_{a_2}(x_2)\psi^3_{a_3}(x_3)\}|\bar{P}\rangle\langle\bar{P}|T\{\bar{\psi}^1_{a_1'}(x_1')\bar{\psi}^2_{a_2'}(x_2')\bar{\psi}^3_{a_3'}(x_3')\}|0\rangle \\ &\qquad\quad \times \theta(\min(x_1^0, x_2^0, x_3^0) - \max(x_1'^0, x_2'^0, x_3'^0)) \\ &\qquad\quad + \text{other terms from diff. time-orderings and other intermediate states.} \end{aligned} \tag{2.22}$$

The amplitudes, containing the time-ordered product of three fermion states and the state with total momentum $\bar{P}$ then are the *Bethe-Salpeter amplitude* and its adjoint, defined by

$$\chi_{\bar{P}\, a_1a_2a_3}(x_1,x_2,x_3) := \langle 0|T\{\psi^1_{a_1}(x_1)\psi^2_{a_2}(x_2)\psi^3_{a_3}(x_3)\}|\bar{P}\rangle, \tag{2.23a}$$

$$\bar{\chi}_{\bar{P}\, a_1'a_2'a_3'}(x_1',x_2',x_3') := \langle \bar{P}|T\{\bar{\psi}^1_{a_1'}(x_1')\bar{\psi}^2_{a_2'}(x_2')\bar{\psi}^3_{a_3'}(x_3')\}|0\rangle , \tag{2.23b}$$

respectively. In Jacobi-coordinates, the centre-of-mass variable X separates and the Bethe-Salpeter amplitudes as introduced in Eq. (2.23a) and (2.23b) can be written in the form

$$\begin{aligned} \chi_{\bar{P}}(x_1,x_2,x_3) &= \mathrm{e}^{-\mathrm{i}\,\langle \bar{P},X\rangle}\chi_{\bar{P}}(\xi,\eta) \\ &=: \mathrm{e}^{-\mathrm{i}\,\langle \bar{P},X\rangle}\int \frac{\mathrm{d}^4p_\xi}{(2\pi)^4}\frac{\mathrm{d}^4p_\eta}{(2\pi)^4}\mathrm{e}^{-\mathrm{i}\,\langle p_\xi,\xi\rangle}\mathrm{e}^{-\mathrm{i}\,\langle p_\eta,\eta\rangle}\chi_{\bar{P}}(p_\xi,p_\eta)\,, \end{aligned} \tag{2.24a}$$

$$\begin{aligned} \bar{\chi}_{\bar{P}}(x_1',x_2',x_3') &= \mathrm{e}^{\mathrm{i}\,\langle \bar{P},X'\rangle}\bar{\chi}_{\bar{P}}(\xi',\eta') \\ &=: \mathrm{e}^{\mathrm{i}\,\langle \bar{P},X'\rangle}\int \frac{\mathrm{d}^4p'_\xi}{(2\pi)^4}\frac{\mathrm{d}^4p'_\eta}{(2\pi)^4}\mathrm{e}^{\mathrm{i}\,\langle p'_\xi,\xi'\rangle}\mathrm{e}^{\mathrm{i}\,\langle p'_\eta,\eta'\rangle}\bar{\chi}_{\bar{P}}(p'_\xi,p'_\eta)\,. \end{aligned} \tag{2.24b}$$

The equations for the Bethe-Salpeter amplitude indeed reflect translational invariance and depend only on internal coordinates ξ and η or p_ξ and p_η in momentum space. For the Heaviyside-function θ in Eq. (2.22) we now write

$$\theta(X_0) = \mathrm{i}\int \frac{\mathrm{d}P^0}{2\pi}\frac{\mathrm{e}^{-\mathrm{i}\,P^0X_0}}{P^0+\mathrm{i}\,\epsilon} \tag{2.25}$$

and insert Eq. (2.24a) and (2.24b) in Eq. (2.22). Then, after a Laurent-expansion around the pole $P^0 = \omega_{\mathbf{P}}$, we obtain in lowest order for the Green's function

$$G_P(p_\xi,p_\eta;p'_\xi,p'_\eta) = \frac{-\mathrm{i}}{2\omega_{\mathbf{P}}}\frac{\chi_{\bar{P}}(p_\xi,p_\eta)\bar{\chi}_{\bar{P}}(p'_\xi,p'_\eta)}{P^0-\omega_{\mathbf{P}}+\mathrm{i}\,\epsilon} + \text{ regular terms for } P^0\to\omega_{\mathbf{P}}\,. \tag{2.26}$$

Eq. (2.26) can also be reformulated in its covariant form

$$G_P(p_\xi,p_\eta;p'_\xi,p'_\eta) = -\,\mathrm{i}\,\frac{\chi_{\bar{P}}(p_\xi,p_\eta)\bar{\chi}_{\bar{P}}(p'_\xi,p'_\eta)}{P^2-M^2+\mathrm{i}\,\epsilon} + \text{ regular terms for } P^2\to M^2\,, \tag{2.27}$$

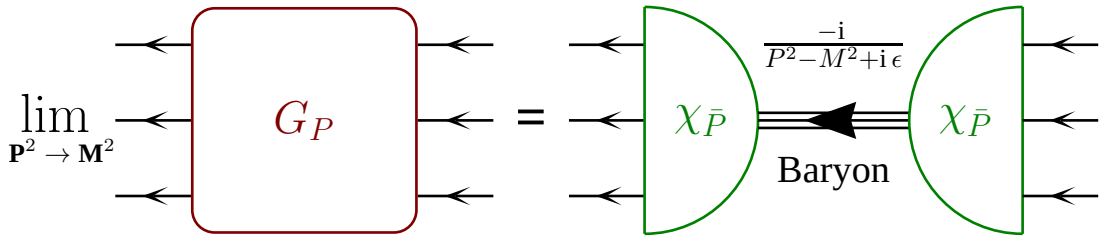

Fig. 2.3: The Green's function in the vicinity of a three-fermion pole in lowest order of the Laurent-expansion. The Bethe-Salpeter amplitudes are displayed by the green semidisks and the Green's function by the red rectangles. Quarks are presented by black arrows, which denotes the quark-propagation.

which has been displayed also schematically in Fig. 2.3 . Furthermore, Eqs. (2.18a) and (2.18b) can be rewritten as

$$G_P = G_{0\,P} - \mathrm{i}\, G_{0\,P}\, K_P\, G_P, \qquad \Leftrightarrow \qquad (G_{0\,P}^{-1} + \mathrm{i}\, K_P) G_P = \mathbb{1}\,, \tag{2.28a}$$

$$G_P = G_{0\,P} - \mathrm{i}\, G_P\, K_P\, G_{0\,P}, \qquad \Leftrightarrow \qquad G_P (G_{0\,P}^{-1} + \mathrm{i}\, K_P) = \mathbb{1}\,, \tag{2.28b}$$

where the identity and the inverse-operators are defined by

$$\mathbb{1}_{a_1,a_2,a_3;a_1',a_2',a_3'}(p_\xi, p_\eta; p_\xi', p_\eta') := \delta_{a_1;a_1'}\delta_{a_2;a_2'}\delta_{a_2;a_2'}\,(2\pi)^4\delta^{(4)}(p_\xi - p_\xi')\,(2\pi)^4\delta^{(4)}(p_\eta - p_\eta')\,, \tag{2.29a}$$

$$G_{0\,P}\, G_{0\,P}^{-1} := \mathbb{1}\,, \tag{2.29b}$$

still using the compact notation of Eq. (2.9). From the right hand side form of Eqs. (2.28a) and (2.28b) the definition of a pseudo-Hamiltonian $H_P := G_{0\,P}^{-1} + \mathrm{i}\, K_P$ is possible with the Green's function G_P as the corresponding resolvent

$$H_P\, G_P = G_P\, H_P = \mathbb{1}. \tag{2.30}$$

In the vicinity of the bound-state $|\bar{P}\rangle$, the Bethe-Salpeter equation and its normalisation condition can be evaluated from a Laurent- and Taylor-expansion of the Green's function G_P and the pseudo-Hamiltonian H_P , respectively. Thereby, only terms in lowest order will be taken into account and Eq. (2.26) can be written in form

$$G_P(p_\xi, p_\eta; p_\xi', p_\eta') = \frac{-\mathrm{i}}{2\omega_{\mathbf{P}}} \frac{\chi_{\bar{P}}(p_\xi, p_\eta)\bar{\chi}_{\bar{P}}(p_\xi', p_\eta')}{P^0 - \omega_{\mathbf{P}} + \mathrm{i}\epsilon} + \frac{\partial}{\partial P^0}\left(P^0 - \omega_{\mathbf{P}}\right) G_P\Big|_{P^0=\omega_{\mathbf{P}}} + \mathcal{O}\left(P^0 - \omega_{\mathbf{P}}\right)\,, \tag{2.31}$$

while for the pseudo Hamiltonian simply

$$H_P = H_{\bar{P}} + \frac{\partial}{\partial P^0} H_P\Big|_{P^0=\omega_{\mathbf{P}}} \left(P^0 - \omega_{\mathbf{P}}\right) + \mathcal{O}\left((P^0 - \omega_{\mathbf{P}})^2\right) \tag{2.32}$$

follows. Multiplying G_P and H_P with each other and using Eq. (2.30), the coefficients of the resulting expansion can be compared order by order. From this, the Bethe-Salpeter equation and its normalisation condition appear

$$H_{\bar{P}}\, \chi_{\bar{P}} \bar{\chi}_{\bar{P}} = 0\,, \tag{2.33a}$$

$$H_{\bar{P}} \left[\frac{\partial}{\partial P^0}\left(P^0 - \omega_{\mathbf{P}}\right) G_P\right]_{P^0=\omega_{\mathbf{P}}} - \frac{\mathrm{i}}{2\omega_{\mathbf{P}}} \left[\frac{\partial}{\partial P^0} H_{\bar{P}}\right]_{P^0=\omega_{\mathbf{P}}} \chi_{\bar{P}} \bar{\chi}_{\bar{P}} = \mathbb{1}\,. \tag{2.33b}$$

From Eq. (2.33a) the Bethe-Salpeter equation and its adjoint

$$H_{\bar{P}}\, \chi_{\bar{P}} = 0\,, \tag{2.34a}$$

$$\bar{\chi}_{\bar{P}}\, H_{\bar{P}} = 0\,, \tag{2.34b}$$

follow. According to the definitions of the pseudo Hamiltonian (2.28a) and (2.28b), Eqs. (2.34a) and (2.34b) can also be written as

$$\chi_{\bar{P}} = -\,\mathrm{i}\, G_{0\,\bar{P}}\, K_{\bar{P}}\, \chi_{\bar{P}}\,, \tag{2.35a}$$
$$\bar{\chi}_{\bar{P}} = -\,\mathrm{i}\, \bar{\chi}_{\bar{P}}\, K_{\bar{P}}\, G_{0\,\bar{P}}\,, \tag{2.35b}$$

which are the so-called *Bethe-Salpeter equations*. The Bethe-Salpeter equation in the full notation then have the form of a relativistically covariant, homogeneous and eight-dimensional integral equation. The Bethe-Salpeter equation is explicitly given by

$$\begin{aligned}
\chi_{\bar{P}\,a_1,a_2,a_3}(p_\xi,p_\eta) &= S^1_{F\,a_1;a_1'}(\tfrac{1}{3}P+p_\xi+\tfrac{1}{2}p_\eta)\, S^2_{F\,a_2;a_2'}(\tfrac{1}{3}P-p_\xi+\tfrac{1}{2}p_\eta)\, S^3_{F\,a_3;a_3'}(\tfrac{1}{3}P-p_\eta)\\
&\times(-\mathrm{i})\int\frac{\mathrm{d}^4p'_\xi}{(2\pi)^4}\frac{\mathrm{d}^4p'_\eta}{(2\pi)^4}\,K^{(3)}_{\bar{P}\,a_1',a_2',a_3';a_1'',a_2'',a_3''}(p_\xi,p_\eta;p'_\xi,p'_\eta)\chi_{\bar{P}\,a_1'',a_2'',a_3''}(p'_\xi,p'_\eta)\\
&\quad+S^1_{F\,a_1a_1'}(\tfrac{1}{3}P+p_\xi+\tfrac{1}{2}p_\eta)\, S^2_{F\,a_2a_2'}(\tfrac{1}{3}P-p_\xi+\tfrac{1}{2}p_\eta)\\
&\times(-\mathrm{i})\int\frac{\mathrm{d}^4p'_{\xi_3}}{(2\pi)^4}\,K^{(2)}_{\left(\frac{2}{3}\bar{P}+p_{\eta_3}\right)\,a_1',a_2';a_1'',a_2''}(p_{\xi_3};p'_{\xi_3})\chi_{\bar{P}\,a_1'',a_2'',a_3}(p'_{\xi_3},p_{\eta_3})\\
&\quad+S^1_{F\,a_1a_1'}(\tfrac{1}{3}P+p_\xi+\tfrac{1}{2}p_\eta)\, S^3_{F\,a_3a_3'}(\tfrac{1}{3}P-p_\eta)\\
&\times(-\mathrm{i})\int\frac{\mathrm{d}^4p'_{\xi_2}}{(2\pi)^4}\,K^{(2)}_{\left(\frac{2}{3}\bar{P}+p_{\eta_2}\right)\,a_1',a_2';a_1'',a_2''}(p_{\xi_2};p'_{\xi_2})\chi_{\bar{P}\,a_1'',a_2'',a_3}(-\tfrac{1}{2}p'_{\xi_2}+\tfrac{3}{4}p_{\eta_2},-p'_{\xi_2}-\tfrac{1}{2}p_{\eta_2})\\
&\quad+S^2_{F\,a_2a_2'}(\tfrac{1}{3}P-p_\xi+\tfrac{1}{2}p_\eta)\, S^3_{F\,a_3a_3'}(\tfrac{1}{3}P-p_\eta)\\
&\times(-\mathrm{i})\int\frac{\mathrm{d}^4p'_{\xi_1}}{(2\pi)^4}\,K^{(2)}_{\left(\frac{2}{3}\bar{P}+p_{\eta_1}\right)\,a_1',a_2';a_1'',a_2''}(p_{\xi_1};p'_{\xi_1})\chi_{\bar{P}\,a_1'',a_2'',a_3}(-\tfrac{1}{2}p'_{\xi_1}-\tfrac{3}{4}p_{\eta_1},p'_{\xi_1}-\tfrac{1}{2}p_{\eta_1})\,.
\end{aligned} \tag{2.36}$$

We refer to Fig. 2.4 for a schematic representation of the Bethe-Salpeter equation.

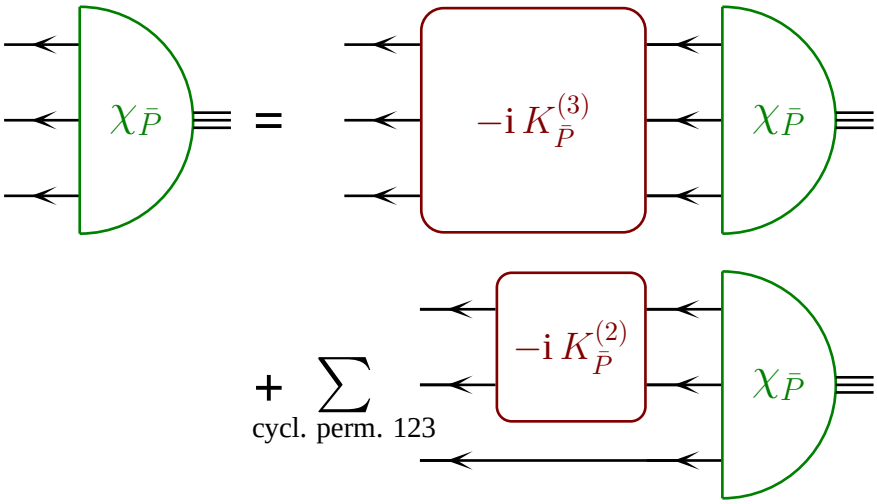

Fig. 2.4: A schematic representation of the Bethe-Salpeter equation. The Bethe-Salpeter amplitudes are displayed by the green semidisks and the interaction kernels by the red rectangles. Quarks are presented by black arrows.

Concerning the normalisation condition Eq. (2.33b) a multiplication with $\bar{\chi}_{\bar{P}}$ from the left with Eq. (2.34b) leads to

$$-\mathrm{i}\bar{\chi}_{\bar{P}}\left[\frac{\partial}{\partial P^0}H_{\bar{P}}\right]_{P^0=\omega_{\mathbf{P}}}\chi_{\bar{P}} = 2\omega_{\mathbf{P}}\,, \tag{2.37}$$

which can also be written in its full integral form as

$$
\begin{aligned}
&-\mathrm{i}\int\frac{\mathrm{d}^4p'_\xi}{(2\pi)^4}\frac{\mathrm{d}^4p'_\eta}{(2\pi)^4}\int\frac{\mathrm{d}^4p_\xi}{(2\pi)^4}\frac{\mathrm{d}^4p_\eta}{(2\pi)^4}\\
&\bar{\chi}_{\bar{P}}(p'_\xi,p'_\eta)\left[\frac{\partial}{\partial P^0}\left(G_{0\,\bar{P}}^{-1}(p'_\xi,p'_\eta;p_\xi,p_\eta)+\mathrm{i}\,K_{\bar{P}}(p'_\xi,p'_\eta;p_\xi,p_\eta)\right)\right]_{P^0=\omega_{\mathbf{P}}}\chi_{\bar{P}}(p_\xi,p_\eta)=2\omega_{\mathbf{P}}\,,
\end{aligned}
\tag{2.38}
$$

while the covariant form of the normalisation condition is given by

$$
-\mathrm{i}\,\bar{\chi}_{\bar{P}}\left[P_\mu\frac{\partial}{\partial P_\mu}H_P\right]_{P=\bar{P}}\chi_{\bar{P}}=2M^2\,,
\tag{2.39}
$$

which is displayed schematically in Fig. 2.5. Based on the Bethe-Salpeter equation the so-called Salpeter

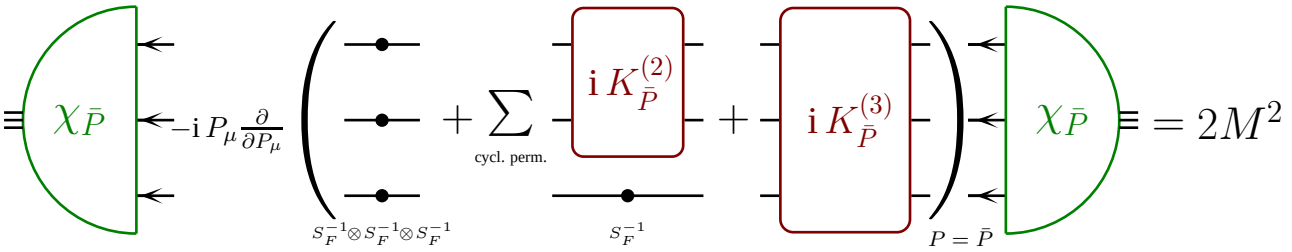

Fig. 2.5: A schematic representation of the normalisation condition of the Bethe-Salpeter equation. The Bethe-Salpeter amplitudes are displayed by the green semidisks and the interaction kernels by the red rectangles. Quarks are represented by black arrows, which denotes the quark-propagation.

equation can be derived by assuming instantaneous interactions. This is the topic of the subsequent section.

2.4 Reduction to the instantaneous Salpeter equation

In order to make the Bethe-Salpeter equation more tractable for further studies we make some approximations, which reduce the analytical (and numerical) effort. These approximations are itemised in the next subsections and leads finally to the Salpeter equation as it has been worked out by Löring *et al.* [4, 7] for baryons and by Münz and Resag *et al.* [36–45] for mesons. These approximations are partially motivated by the success of non-relativistic constituent quark models.

2.4.1 The free quark propagator approximation

The first model assumption is, that the full quark propagators S_F^i can be replaced by free-form quark propagators:

$$
S_F^i(p_i)\stackrel{!}{=}\frac{\mathrm{i}}{\not{p}_i-m_i+\mathrm{i}\,\epsilon}\,.
\tag{2.40}
$$

In doing so, we tacitly assume that some part of the quark self-energy can be subsumed in effective constituent quark masses m_i, which thus enters as free parameters in the model. This makes the Salpeter approach more phenomenological, but it reduces the numerical and analytical effort drastically.

2.4.2 The instantaneous approximation

The second model assumption is, that all interaction kernels are assumed to be represented by instantaneous potentials V, which thus excludes retardation effects in general. The instantaneous approximation can be

formulated in the centre-of-mass frame $P = \bar{P} = (M, 0)$ as

$$K_P^{(3)}\left(p_\xi, p_\eta; {p_\xi}', {p_\eta}'\right)\Big|_{P=\bar{P}=(M,0)} \stackrel{!}{=} V^{(3)}\left(\mathbf{p}_\xi, \mathbf{p}_\eta; {\mathbf{p}_\xi}', {\mathbf{p}_\eta}'\right), \tag{2.41a}$$

$$K^{(2)}_{\frac{2}{3}P+p_{\eta_k}}\left(p_{\xi_k}; {p_{\xi_k}}'\right)\Big|_{P=\bar{P}=(M,0)} \stackrel{!}{=} V^{(2)}\left(\mathbf{p}_{\xi_k}; {\mathbf{p}_{\xi_k}}'\right), \tag{2.41b}$$

where the sub-index k labels different sets of Jacobi coordinates in case of the two-body interaction kernel $K^{(2)}$. Thereby, the instantaneous approximation preserves the covariance of the Bethe-Salpeter equation as shown by Wallace and Mandelzweig [46]. In order to elucidate that, we follow the idea of Wallace and Mandelzweig by decomposing the relative momenta p within the interactions into space- and time-like components along and perpendicular to the arbitrary space-time vector P. Let p be one of the relative momenta, then it decomposes into orthogonal and parallel components $p_\perp$ and $p_\parallel$ with respect to the direction of P. The decomposition is given by

$$p_\parallel = \frac{\langle p, P\rangle}{P^2} P\,, \tag{2.42a}$$

$$p_\perp = p - \frac{\langle p, P\rangle}{P^2} P\,, \tag{2.42b}$$

The crucial point is, that $p_\perp$ is definitely three-dimensional and the instantaneous approximation, which is formulated in the centre-of-mass frame, can be reformulated in any other reference frame as

$$K_P^{(3)}\left(p_\xi, p_\eta; {p_\xi}', {p_\eta}'\right)\Big|_{P=\bar{P}} \stackrel{!}{=} V^{(3)}\left(p_{\xi\perp}, p_{\eta\perp}; {p_\xi}'_\perp, {p_\eta}'_\perp\right), \tag{2.43a}$$

$$K^{(2)}_{\frac{2}{3}P+p_{\eta_k}}\left(p_{\xi_k}; {p_{\xi_k}}'\right)\Big|_{P=\bar{P}} \stackrel{!}{=} V^{(2)}\left(p_{\xi_k\perp}; p'_{\xi_k\perp}\right). \tag{2.43b}$$

Indeed, setting $P = \bar{P} = (M, \mathbf{0})$ returns the instantaneous potentials Eqs. (2.41a) and (2.41b) in the centre-of-mass frame. This thus preserves the formal covariance of the Bethe-Salpeter equation.

2.4.3 The Salpeter equation

In this subsection, the Salpeter equation will be derived from the Bethe-Salpeter equation by taking into account the previously introduced approximations. To outline the procedure we concentrate on the case without two-body interactions. Starting point are the Bethe-Salpeter equations

$$\chi_{\bar{P}} = -\,\mathrm{i}\, G_{0\,\bar{P}}\, K_{\bar{P}}^{(3)}\, \chi_{\bar{P}}\,, \tag{2.44a}$$

$$\bar{\chi}_{\bar{P}} = -\,\mathrm{i}\, \bar{\chi}_{\bar{P}}\, K_{\bar{P}}^{(3)}\, G_{0\,\bar{P}}\,. \tag{2.44b}$$

Inserting the unretarded kernel of Eq. (2.41a) and integrating out all parallel components $p_\parallel$ of the relative momenta in the centre-of-mass frame, *i.e.* all energy dependencies (p_ξ^0 and p_η^0), of the complete Bethe-Salpeter equation, we obtain the Salpeter equation. To this end we define the *Salpeter amplitude* and its adjoint

$$\phi_M(\mathbf{p}_\xi, \mathbf{p}_\eta) := \int \frac{\mathrm{d}p_\xi^0}{2\pi}\frac{\mathrm{d}p_\eta^0}{2\pi}\, \chi_{\bar{P}}((p_\xi^0, \mathbf{p}_\xi), (p_\eta^0, \mathbf{p}_\eta))\Big|_{\bar{P}=(M,\mathbf{0})}\,, \tag{2.45a}$$

$$\bar{\phi}_M(\mathbf{p}_\xi, \mathbf{p}_\eta) := \int \frac{\mathrm{d}p_\xi^0}{2\pi}\frac{\mathrm{d}p_\eta^0}{2\pi}\, \bar{\chi}_{\bar{P}}((p_\xi^0, \mathbf{p}_\xi), (p_\eta^0, \mathbf{p}_\eta))\Big|_{\bar{P}=(M,\mathbf{0})}\,. \tag{2.45b}$$

This leads to a reformulation of the Bethe-Salpeter equation, which can hence be rewritten as

$$\chi_M = -\,\mathrm{i}\, G_{0\,M}\, V^{(3)}\, \phi_M\,, \tag{2.46a}$$

$$\bar{\chi}_M = -\,\mathrm{i}\, \bar{\phi}_M\, V^{(3)}\, G_{0\,M}\,. \tag{2.46b}$$

Note, that these equations allows the reconstruction of the original Bethe-Salpeter amplitudes if the Salpeter amplitudes are known and the interaction kernels includes no retardation effects. Furthermore, a common definition of the so-called *vertex function* is useful, in the rest frame $\bar{P} = (M, \mathbf{0})$

$$\Gamma_M(p_\xi, p_\eta) := \left[G_{0\,M}^{-1}\,\chi_{\bar{P}}\right](p_\xi, p_\eta) = -\mathrm{i}\,\left[V^{(3)}\,\phi_M\right](\mathbf{p}_\xi, \mathbf{p}_\eta) \equiv \Gamma_M(\mathbf{p}_\xi, \mathbf{p}_\eta)\,, \tag{2.47a}$$

$$\bar{\Gamma}_M(p_\xi, p_\eta) := \Gamma_M^\dagger(p_\xi, p_\eta)\,\gamma_0 \otimes \gamma_0 \otimes \gamma_0 \equiv \bar{\Gamma}_M(\mathbf{p}_\xi, \mathbf{p}_\eta)\,, \tag{2.47b}$$

which does not depend on the relative energies. The adjoint vertex function is likewise defined. In order to reduce the Bethe-Salpeter equation by integrating out all remaining energies p_ξ^0 and p_η^0 it is also useful to define a energy-integrated short-notation

$$\langle A\rangle(\mathbf{p}_\xi, \mathbf{p}_\eta; \mathbf{p}'_\xi, \mathbf{p}'_\eta) := \int \frac{\mathrm{d}p_\xi^0}{2\pi}\frac{\mathrm{d}p_\eta^0}{2\pi}\int \frac{\mathrm{d}{p'_\xi}^0}{2\pi}\frac{\mathrm{d}{p'_\eta}^0}{2\pi}\,A(p_\xi, p_\eta; p'_\xi, p'_\eta)\,. \tag{2.48}$$

From the Bethe-Salpeter equation without two-body interactions according to Eq. (2.36) the Salpeter equation can be written in the short-notation of Eq. (2.48) as

$$\begin{aligned}
\phi_M(\mathbf{p}_\xi, \mathbf{p}_\eta) \quad &= \quad \int \frac{\mathrm{d}p_\xi^0}{2\pi}\frac{\mathrm{d}p_\eta^0}{2\pi}\,\chi_{\bar{P}}((p_\xi^0, \mathbf{p}_\xi), (p_\eta^0, \mathbf{p}_\eta))\Big|_{\bar{P}=(M,\mathbf{0})} \\
&= \quad -\mathrm{i}\int \frac{\mathrm{d}p_\xi^0}{2\pi}\frac{\mathrm{d}p_\eta^0}{2\pi}\int \frac{\mathrm{d}^4p'_\xi}{(2\pi)^4}\frac{\mathrm{d}^4p'_\eta}{(2\pi)^4}\,G_{0\,M}(p_\xi, p_\eta; p'_\xi, p'_\eta)\left[V^{(3)}\phi_M\right](\mathbf{p}'_\xi, \mathbf{p}'_\eta) \\
&\overset{\text{Eq. (2.48)}}{=} \quad -\mathrm{i}\int \frac{\mathrm{d}^3p'_\xi}{(2\pi)^3}\frac{\mathrm{d}^3p'_\eta}{(2\pi)^3}\,\langle G_{0\,M}\rangle(\mathbf{p}_\xi, \mathbf{p}_\eta; \mathbf{p}'_\xi, \mathbf{p}'_\eta)\left[V^{(3)}\phi_M\right](\mathbf{p}'_\xi, \mathbf{p}'_\eta) \\
&\overset{\text{Eq. (2.9)}}{=} \quad -\mathrm{i}\left[\langle G_{0\,M}\rangle V^{(3)}\phi_M\right](\mathbf{p}_\xi, \mathbf{p}_\eta)\,.
\end{aligned} \tag{2.49}$$

For the evaluation of $\langle G_{0\,M}\rangle = \langle S_F^1 \otimes S_F^2 \otimes S_F^3\rangle$ the residue theorem will be used, where the Feynman propagators involved are decomposed into positive- and negative energy parts. We thus define projectors $\Lambda^\pm$, which projects on pure positive- or negative energies

$$\Lambda_i^\pm(\mathbf{p}_i) := \frac{\omega_i(\mathbf{p}_i)\mathbb{1} \pm H_i(\mathbf{p}_i)}{2\omega_i(\mathbf{p}_i)}\,, \tag{2.50}$$

where $\omega_i(\mathbf{p}_i) := \sqrt{|\mathbf{p}_i|^2 + m_i^2}$ and $H_i(\mathbf{p}_i) = \gamma_0(\boldsymbol{\gamma}\cdot\mathbf{p}_i + m_i)$ denotes the free Dirac-Hamiltonian. With these projectors it is possible to decompose the fermion propagators $S_F^i(p_i)$ for each particle into positive- and negative energy parts

$$S_F^i(p_i) = \frac{\mathrm{i}}{\not{p}_i - m_i + \mathrm{i}\,\epsilon} = \mathrm{i}\left(\frac{\Lambda_i^+(\mathbf{p}_i)}{p_i^0 - \omega_i(\mathbf{p}_i) + \mathrm{i}\,\epsilon} + \frac{\Lambda_i^-(\mathbf{p}_i)}{p_i^0 + \omega_i(\mathbf{p}_i) - \mathrm{i}\,\epsilon}\right)\gamma_0\,. \tag{2.51}$$

This procedure has the advantage, that the pole position of $\langle G_{0\,M}\rangle$ can be isolated in the energy variables p_i^0, which will subsequently be integrated out with the residue theorem. Integrating out all energies within $G_{0\,M}$ yields

$$\begin{aligned}
&\langle G_{0\,M}\rangle(\mathbf{p}_\xi, \mathbf{p}_\eta; \mathbf{p}'_\xi, \mathbf{p}'_\eta) = \\
&\quad \mathrm{i}\left[\frac{\Lambda_1^+(\mathbf{p}_1)\otimes\Lambda_2^+(\mathbf{p}_2)\otimes\Lambda_3^+(\mathbf{p}_3)}{M - \Omega(\mathbf{p}_1,\mathbf{p}_2,\mathbf{p}_3) + \mathrm{i}\,\epsilon} + \frac{\Lambda_1^-(\mathbf{p}_1)\otimes\Lambda_2^-(\mathbf{p}_2)\otimes\Lambda_3^-(\mathbf{p}_3)}{M + \Omega(\mathbf{p}_1,\mathbf{p}_2,\mathbf{p}_3) - \mathrm{i}\,\epsilon}\right] \\
&\quad \times \gamma_0\otimes\gamma_0\otimes\gamma_0\,(2\pi)^3\delta^{(3)}(\mathbf{p}_\xi - \mathbf{p}'_\xi)\,(2\pi)^3\delta^{(3)}(\mathbf{p}_\eta - \mathbf{p}'_\eta)\,,
\end{aligned} \tag{2.52}$$

with the definition $\Omega(\mathbf{p}_1, \mathbf{p}_2, \mathbf{p}_3) := \omega_1(\mathbf{p}_1) + \omega_2(\mathbf{p}_2) + \omega_3(\mathbf{p}_3)$. It is remarkable, that only projections on pure positive- or pure negative energies appears, which will not be the case if we include two-body interactions.

This property follows directly from the usage of the residue theorem and the structure of $G_{0\,M}$. Based on this, the Salpeter equation (2.49) for three-fermions can be formulated as

$$\begin{aligned}\phi_M(\mathbf{p}_\xi,\mathbf{p}_\eta) = &\left[\frac{\Lambda_1^+(\mathbf{p}_1)\otimes\Lambda_2^+(\mathbf{p}_2)\otimes\Lambda_3^+(\mathbf{p}_3)}{M-\Omega(\mathbf{p}_1,\mathbf{p}_2,\mathbf{p}_3)+\mathrm{i}\,\epsilon}+\frac{\Lambda_1^-(\mathbf{p}_1)\otimes\Lambda_2^-(\mathbf{p}_2)\otimes\Lambda_3^-(\mathbf{p}_3)}{M+\Omega(\mathbf{p}_1,\mathbf{p}_2,\mathbf{p}_3)-\mathrm{i}\,\epsilon}\right]\\ &\times\gamma_0\otimes\gamma_0\otimes\gamma_0\int\frac{\mathrm{d}^3p'_\xi}{(2\pi)^3}\frac{\mathrm{d}^3p'_\eta}{(2\pi)^3}\,V^{(3)}(\mathbf{p}_\xi,\mathbf{p}_\eta;\mathbf{p}'_\xi,\mathbf{p}'_\eta)\,\phi_M(\mathbf{p}'_\xi,\mathbf{p}'_\eta)\,.\end{aligned}\tag{2.53}$$

In order to solve the integral equation, it is useful to reformulate the equation in the form of an eigenvalue problem, which allows a direct extraction of the mass M as an eigenvalue. However, before performing such a reformulation some properties, regarding the projective structure of the Salpeter equation, will be discussed first.

2.4.4 The projective structure of the Salpeter equation

Since the action of a positive- or negative projector on the Salpeter equation (2.53) will be absorbed within the projector structure in front of the integral, the Salpeter amplitudes are indeed eigenfunctions of the projectors

$$\Lambda_\pm := \Lambda^{+++}\pm\Lambda^{---}\,,\qquad \Lambda := \Lambda_+\,,\tag{2.54a}$$

$$\Lambda^{\pm\pm\pm} := \Lambda_1^\pm\otimes\Lambda_2^\pm\otimes\Lambda_3^\pm\,.\tag{2.54b}$$

This defines the so-called *projected Salpeter amplitudes*

$$\phi_M = \Lambda\phi_M \equiv \phi_M^\Lambda = \Lambda^{+++}\phi_M+\Lambda^{---}\phi_M := \phi_M^{+++}+\phi_M^{---}\tag{2.55a}$$

$$\bar\phi_M = \bar\phi_M\bar\Lambda \equiv \bar\phi_M^\Lambda = \bar\phi_M\bar\Lambda^{+++}+\bar\phi_M\bar\Lambda^{---} := \bar\phi_M^{+++}+\bar\phi_M^{---}\,,\tag{2.55b}$$

with the definition of the adjoint projected Salpeter amplitude $\bar\phi_M := \gamma_0\otimes\gamma_0\otimes\gamma_0\,\phi_M\,\gamma_0\otimes\gamma_0\otimes\gamma_0$. The important point is, that all amplitudes with mixed positive- and negative energy components such as, *e.g.* ϕ^{++-}, do not occur in the dynamical equations in case of pure three-body interactions as already argued in the previous subsection. Furthermore, it is important to note, that only the projected part of the potential defined by

$$V_\Lambda^{(3)} := \bar\Lambda V^{(3)}\Lambda\,,\tag{2.56}$$

is relevant in the Salpeter equation, where the adjoint projector is defined as $\bar\Lambda := \gamma_0\otimes\gamma_0\otimes\gamma_0\Lambda\gamma_0\otimes\gamma_0\otimes\gamma_0$. This leads to the definition of the so-called *residual part*

$$\bar V_R^{(3)} := V^{(3)}-V_\Lambda^{(3)}\,,\tag{2.57}$$

containing all mixed energy parts, which here have no effect when considering only three-body interactions. With the inclusion of two-body interactions a more complicated residual part occurs. This will be addressed briefly in the next subsection.

2.4.5 The Hamiltonian formulation of the Salpeter equation

As already mentioned it is useful to reformulate the Salpeter equation as an eigenvalue problem in terms of a Hamiltonian $\mathcal{H}$ with eigenvalue M, which than can be solved numerically

$$\mathcal{H}\phi_M = M\phi_M\qquad\text{with}\qquad\Lambda\phi_M=\phi_M\,.\tag{2.58}$$

Again with pure three-body interactions, the Salpeter Hamiltonian can be defined as

$$\begin{aligned}[\mathcal{H}\phi_M](\mathbf{p}_\xi,\mathbf{p}_\eta) =&[\mathcal{H}_0\phi_M](\mathbf{p}_\xi,\mathbf{p}_\eta)\\ &+\Lambda(\mathbf{p}_\xi,\mathbf{p}_\eta)\,\gamma_0\otimes\gamma_0\otimes\gamma_0\int\frac{\mathrm{d}^3p'_\xi}{(2\pi)^3}\frac{\mathrm{d}^3p'_\eta}{(2\pi)^3}\,V^{(3)}(\mathbf{p}_\xi,\mathbf{p}_\eta;\mathbf{p}'_\xi,\mathbf{p}'_\eta)\,\phi_M(\mathbf{p}'_\xi,\mathbf{p}'_\eta)\,,\end{aligned}\tag{2.59}$$

while $\mathcal{H}_0$ is defined as the free Hamiltonian in terms of single particle Dirac-operators

$$\mathcal{H}_0(\mathbf{p}_\xi, \mathbf{p}_\eta) := H_1(\mathbf{p}_1) \otimes \mathbb{1} \otimes \mathbb{1} \; + \; \mathbb{1} \otimes H_2(\mathbf{p}_2) \otimes \mathbb{1} \; + \; \mathbb{1} \otimes \mathbb{1} \otimes H_3(\mathbf{p}_3)\,. \tag{2.60}$$

Eq. (2.59) can be easily obtained from the Salpeter equation (2.53) by projecting the complete equation with Λ_i^+ and/or Λ_i^-, $i = 1, 2, 3$. This leads to

$$\begin{aligned} (M \mp \Omega)\Lambda_i^\pm \phi_M(\mathbf{p}_\xi, \mathbf{p}_\eta) &= \Lambda^{\pm\pm\pm}\gamma_0 \otimes \gamma_0 \otimes \gamma_0 \, [V^{(3)}\phi_M](\mathbf{p}_\xi, \mathbf{p}_\eta)\,, \\ \overset{\text{Eq. (2.50)}}{\Rightarrow} (\omega_i M - \Omega H_i)\phi_M(\mathbf{p}_\xi, \mathbf{p}_\eta) &= \omega_i \Lambda\gamma_0 \otimes \gamma_0 \otimes \gamma_0 \, [V^{(3)}\,\phi_M](\mathbf{p}_\xi, \mathbf{p}_\eta) \qquad \forall\, i = 1, 2, 3\,. \end{aligned} \tag{2.61}$$

Furthermore, adding up the contributions for each i returns the Hamiltonian formulation of the Salpeter equation as given by Eq. (2.59).

Considering two-particle interactions leads to mixed energy projectors within the Salpeter equation as shown by Löring *et al.* [4, 7] and thus the residual part of the interaction does not vanish. Projecting the complete Salpeter equation on pure positive and negative energy components with $\Lambda^{\pm\pm\pm}$ all mixed energy projectors vanishes and the problem becomes solvable. Therefore, it is necessary to introduce the projected Salpeter amplitude

$$\phi_M^\Lambda := \Lambda\phi_M \tag{2.62}$$

before extracting Eq. (2.59) to include the two-body interactions

$$\begin{aligned} [\mathcal{H}\phi_M^\Lambda](\mathbf{p}_\xi, \mathbf{p}_\eta) =& [\mathcal{H}_0\phi_M^\Lambda](\mathbf{p}_\xi, \mathbf{p}_\eta) \\ &+ \Lambda^+(\mathbf{p}_\xi, \mathbf{p}_\eta)\,\gamma_0 \otimes \gamma_0 \otimes \gamma_0 \int \frac{\mathrm{d}^3 p'_\xi}{(2\pi)^3} \frac{\mathrm{d}^3 p'_\eta}{(2\pi)^3}\, V^{(3)}(\mathbf{p}_\xi, \mathbf{p}_\eta; \mathbf{p}'_\xi, \mathbf{p}'_\eta)\, \phi_M^\Lambda(\mathbf{p}'_\xi, \mathbf{p}'_\eta) \\ &+ \Lambda^-(\mathbf{p}_\xi, \mathbf{p}_\eta)\,\gamma_0 \otimes \gamma_0 \otimes \mathbb{1} \int \frac{\mathrm{d}^3 p'_\xi}{(2\pi)^3}\, V^{(2)}(\mathbf{p}_\xi; \mathbf{p}'_\xi) \otimes \mathbb{1}\, \phi_M^\Lambda(\mathbf{p}'_\xi, \mathbf{p}_\eta) \\ &+ \text{corresponding quark interactions (23) and (31)}\,. \end{aligned} \tag{2.63}$$

The derivation of Eq. (2.63) can be found in the PhD thesis from U. Löring [7], which takes at least a longer discussion and will be only briefly summarised here.

In course of the discussion it is useful to substitute G_M by $\mathcal{G}_M$, which is defined as the resolvent of the pseudo Hamiltonian $H_M^R := G_{0\,M}^{-1} + \mathrm{i}\, V_R^{(3)} + \mathrm{i}\, \bar{K}_M^{(2)}$ as defined before in Eq. (2.30) by only including residual interactions. We start from the full Bethe-Salpeter equation according to Eqs. (2.35a) and (2.35b)

$$\chi_M = -\,\mathrm{i}\, G_{0\,M} \left[V_\Lambda^{(3)} + V_R^{(3)} + \bar{K}^{(2)}\right] \chi_M\,, \tag{2.64a}$$

$$\bar{\chi}_M = -\,\mathrm{i}\, \bar{\chi}_M \left[V_\Lambda^{(3)} + V_R^{(3)} + \bar{K}^{(2)}\right] G_{0\,M}\,, \tag{2.64b}$$

and introduce a pseudo Hamiltonian, which fulfils

$$\mathcal{G}_M H_M^R = H_M^R \mathcal{G}_M = \mathbb{1}\,, \tag{2.65a}$$

$$\Rightarrow \mathcal{G}_M = G_{0\,M} - \mathrm{i}\, G_{0\,M} \left[V_R^{(3)} + \mathrm{i}\, \bar{K}_M^{(2)}\right] \mathcal{G}_M\,. \tag{2.65b}$$

Using these definitions, the Bethe-Salpeter equation can be written as

$$\chi_M = -\,\mathrm{i}\, \mathcal{G}_M\, V_\Lambda^{(3)}\, \chi_M = -i\mathcal{G}_M\, V_\Lambda^{(3)}\, \phi_M^\Lambda\,. \tag{2.66}$$

In the last step, the energies p_ξ^0 and p_η^0 have been integrated out and the projected Salpeter equation can be written as

$$\phi_M^\Lambda = -\,\mathrm{i}\, \langle \mathcal{G}_M \rangle_\Lambda\, V_\Lambda^{(3)}\, \phi_M^\Lambda\,, \tag{2.67}$$

while the Green's function is given by

$$\langle \mathcal{G}_M \rangle_\Lambda(\mathbf{p}_\xi, \mathbf{p}_\eta; \mathbf{p}'_\xi, \mathbf{p}'_\eta) = \Lambda(\mathbf{p}_\xi, \mathbf{p}_\eta) \int \frac{\mathrm{d}p^0_\xi}{2\pi} \frac{\mathrm{d}p^0_\eta}{2\pi} \int \frac{\mathrm{d}{p'_\xi}^0}{2\pi} \frac{\mathrm{d}{p'_\eta}^0}{2\pi} \mathcal{G}_M(p_\xi, p_\eta; p'_\xi, p'_\eta) \bar{\Lambda}(\mathbf{p}'_\xi, \mathbf{p}'_\eta) \,. \tag{2.68}$$

Due to Eq. (2.65b), $\langle \mathcal{G}_M \rangle_\Lambda$ can be written as a Neumann series in powers of $(V_R^{(3)} + \bar{K}_M^{(2)})$

$$\langle \mathcal{G}_M \rangle_\Lambda = \langle G_{0\,M} \rangle + \Lambda \langle G_{0\,M} (-\mathrm{i}\,) \left[V_R^{(3)} + \bar{K}_M^{(2)} \right] G_{0\,M} \rangle \bar{\Lambda} + \dots \,. \tag{2.69}$$

The expansion allows to classify reducible- and irreducible diagrams with respect to the free Salpeter propagator $\langle G_{0\,M} \rangle$, which corresponds to the introduction of an effective potential V_M^{eff} by rewriting $\langle \mathcal{G}_M \rangle_\Lambda$ as

$$\langle \mathcal{G}_M \rangle_\Lambda \stackrel{!}{=} \langle G_{0\,M} \rangle - \mathrm{i}\,\Lambda \langle G_{0\,M} \rangle V_M^{\text{eff}} \langle \mathcal{G}_M \rangle_\Lambda \,, \tag{2.70}$$

where only the projected part of V_M^{eff} appears, which thus acts only on pure positive- and negative energy components. With the conditions

$$V_M^{\text{eff}} = \bar{\Lambda} V_M^{\text{eff}} = V_M^{\text{eff}} \Lambda, \qquad \langle G_{0\,M} \rangle = \Lambda \langle G_{0\,M} \rangle \bar{\Lambda} \,, \tag{2.71}$$

the projected Salpeter equation can be regained as

$$\phi_M^\Lambda = -\mathrm{i}\,\langle G_{0\,M} \rangle \left[V^{(3)} + V_M^{\text{eff}} \right] \phi_M^\Lambda \,, \tag{2.72}$$

and the effective potential V_M^{eff} can be expanded into a power series in the argument $V_R^{(3)} + \bar{K}_M^{(2)}$ given by

$$V_M^{\text{eff}} = \sum_{i=1}^{\infty} {V_M^{\text{eff}}}^{(i)} \,. \tag{2.73}$$

Cutting the series at order k, the k-th order Salpeter equation is given by

$${\phi_M^\Lambda}^{(k)} = -\mathrm{i}\,\langle G_{0\,M} \rangle \left[V^{(3)} + {V_M^{\text{eff}}}^{(k)} \right] {\phi_M^\Lambda}^{(k)} \,. \tag{2.74}$$

Only the Born-approximation ($k = 1$) has been taken into account in order to derive Eq. (2.63).

2.4.6 The normalisation condition of the Salpeter amplitudes

Based on the normalisation condition of the Bethe-Salpeter amplitudes from subsection 2.3 given in Eq. (2.37)

$$-\mathrm{i}\,\bar{\chi}_M \left[\tfrac{\partial}{\partial M} H_M \right] \chi_M = 2M \,, \tag{2.75}$$

which includes the pseudo Hamiltonian $H_M := G_{0\,M}^{-1} + \mathrm{i}\,V^{(3)} + \mathrm{i}\,\bar{K}_M^{(2)} = H_M^R + \mathrm{i}\,V_\Lambda^{(3)}$, the condition can be rewritten as

$$\mathrm{i}\,\bar{\phi}_M^\Lambda V^{(3)} \Lambda \mathcal{G}_M \left[\tfrac{\partial}{\partial M} H_M^R \right] \mathcal{G}_M \bar{\Lambda} V^{(3)} \phi_M^\Lambda = 2M \,, \tag{2.76}$$

where the Salpeter amplitudes satisfy Eq. (2.66). Note, that $V_\Lambda^{(3)}$ in Eq. (2.76) does not depend on M.

With the definition of the resolvent according to Eq. (2.65a) it can be shown, that the derivative of the pseudo Hamiltonian fulfils

$$\mathcal{G}_M \left[\tfrac{\partial}{\partial M} H_M^R \right] \mathcal{G}_M = -\tfrac{\partial}{\partial M} \mathcal{G}_M \tag{2.77}$$

and the normalisation condition then reads

$$-\mathrm{i}\,\bar{\phi}_M^\Lambda V^{(3)}\Lambda\left[\tfrac{\partial}{\partial M}\mathcal{G}_M\right]\bar{\Lambda}V^{(3)}\phi_M^\Lambda = 2M\,, \tag{2.78}$$

where the integration over the Salpeter amplitudes now is six-dimensional in contrast to the eight-dimensional integration of the original normalisation condition for the Bethe-Salpeter amplitudes. Consequently, all remaining energies can be integrated out and Eq. (2.78) can be written as

$$-\mathrm{i}\,\bar{\phi}_M^\Lambda V^{(3)}\Lambda\left\langle\tfrac{\partial}{\partial M}\mathcal{G}_M\right\rangle\bar{\Lambda}V^{(3)}\phi_M^\Lambda = 2M\,. \tag{2.79}$$

The derivative can be transformed further via the relation

$$\Lambda\left\langle\tfrac{\partial}{\partial M}\mathcal{G}_M\right\rangle\bar{\Lambda} = \tfrac{\partial}{\partial M}\left[\Lambda\left\langle\mathcal{G}_M\right\rangle\bar{\Lambda}\right] = \tfrac{\partial}{\partial M}\left\langle\mathcal{G}_M\right\rangle_\Lambda = -\left\langle\mathcal{G}_M\right\rangle_\Lambda\tfrac{\partial}{\partial M}\left[h_{0\,M}+\mathrm{i}V_M^{\mathrm{eff}}\right]\left\langle\mathcal{G}_M\right\rangle_\Lambda\,, \tag{2.80}$$

where $h_{0\,M}$ is defined by the condition $\langle\mathcal{G}_M\rangle h_{0\,M} = h_{0\,M}\langle\mathcal{G}_M\rangle = \Lambda$ and can explicitly be written as

$$h_{0\,M}(\mathbf{p}_\xi,\mathbf{p}_\eta;\mathbf{p}'_\xi,\mathbf{p}'_\eta) := -\,\mathrm{i}\gamma_0\otimes\gamma_0\otimes\gamma_0[\mathbb{1}M-\mathcal{H}_0]\,(2\pi)^3\delta^{(3)}(\mathbf{p}_\xi-\mathbf{p}'_\xi)(2\pi)^3\delta^{(3)}(\mathbf{p}_\eta-\mathbf{p}'_\eta)\,. \tag{2.81}$$

Inserting Eq. (2.80) in Eq. (2.79) then leads to

$$\begin{aligned}\mathrm{i}\,\bar{\phi}_M^\Lambda V^{(3)}\left\langle\mathcal{G}_M\right\rangle_\Lambda\tfrac{\partial}{\partial M}\left[h_{0\,M}+\mathrm{i}V_M^{\mathrm{eff}}\right]\left\langle\mathcal{G}_M\right\rangle_\Lambda\bar{\Lambda}V^{(3)}\phi_M^\Lambda &= 2M\\ \Leftrightarrow\qquad -\mathrm{i}\,\bar{\phi}_M^\Lambda\tfrac{\partial}{\partial M}\left[h_{0\,M}+\mathrm{i}V_M^{\mathrm{eff}}\right]\phi_M^\Lambda &= 2M\,,\end{aligned} \tag{2.82}$$

where in the last step the Salpeter equation (2.67) has been used in order to simplify the equation. The action of the derivative reduces $h_{0\,M}$ in Eq. (2.82) to the δ-functions given in Eq. (2.81), which can be integrated out and the normalisation condition finally results in

$$\langle\phi_M^\Lambda|\phi_M^\Lambda\rangle - \langle\phi_M^\Lambda|\gamma_0\otimes\gamma_0\otimes\gamma_0\left[\tfrac{\partial}{\partial M}V_M^{\mathrm{eff}}\right]|\phi_M^\Lambda\rangle = 2M\,. \tag{2.83}$$

Consequently, there occurs an additional contribution to the normalisation condition compared to the case with pure three-body interactions, which however vanishes in case of the Born approximation $V_M^{\mathrm{eff}} \simeq V_M^{\mathrm{eff}\,(1)}$. For further details on this extensive calculation we refer to the PhD thesis from Löring [7]. Thus, finally we find

$$\langle\phi_M^\Lambda|\phi_M^\Lambda\rangle \simeq 2M\,. \tag{2.84}$$

Due to this simple relation, every Salpeter amplitude can normalised to unity by a factor $\frac{1}{\sqrt{2M}}$, where M is the mass of the corresponding baryon resonance.

2.5 Current-matrix elements

The study of electromagnetic form factors and helicity amplitudes for (excited states of) baryons is an ongoing important challenge in hadron physics. Within the framework of the Bethe-Baryon model, discussed in the previous sections, it is possible to calculate current-matrix elements given by the expression $\langle\bar{P}|j^\mu_{\mathcal{O}}(0)|\bar{P}'\rangle$, which allow the extraction of electromagnetic properties. The basic ideas on the relation between current-matrix elements and the Bethe-Salpeter formalism can be found in Merten and Kretzschmar *et al.* [9, 10, 12]. Starting with the definition of the current

$$j^\mu_{\mathcal{O}}(x) := :\bar{\psi}(x)\mathcal{O}^\mu\psi(x):\,, \tag{2.85}$$

for an arbitrary current-operator $\mathcal{O}$ it is possible to find a relation to the current-matrix elements. Below a brief summary with the crucial steps in the derivation of current-matrix elements will be given according to the derivation performed by Merten and Kretzschmar *et al.* [9, 10, 12]. The derivation runs similar to that of the

Bethe-Salpeter equation, as outlined in section 2.3. In this case, we start from a seven-point Green's function, defined by

$$\begin{aligned} &G^{\mu}_{a_1,a_2,a_3;a_1',a_2',a_3'}(x_1,x_2,x_3;x;x_1',x_2',x_3') \\ &\quad := -\langle 0|T\big\{\psi^1_{a_1}(x_1)\psi^2_{a_2}(x_2)\psi^3_{a_3}(x_3)j^{\mu}_{\mathcal{O}}(x)\bar{\psi}^1_{a_1'}(x_1')\bar{\psi}^2_{a_2'}(x_2')\bar{\psi}^3_{a_3'}(x_3')\big\}|0\rangle\,. \end{aligned} \tag{2.86}$$

Here, we choose the time-ordering $\min(x_1^0,x_2^0,x_3^0) > x^0 > \max({x_1'}^0,{x_2'}^0,{x_3'}^0)$ and concentrate on pole contributions as in Eq. (2.25). Introducing again a basis $|\bar{P}\rangle$ in momentum space the current-matrix element can be written as

$$\begin{aligned} \langle \bar{P}|j^{\mu}_{\mathcal{O}}(0)|\bar{P}'\rangle &:= -\,\bar{\chi}_{\bar{P}}\,K^{\mu}_{\bar{P},\bar{P}'}\chi_{\bar{P}'} \\ &= -\int \frac{\mathrm{d}^4p_\xi}{(2\pi)^4}\frac{\mathrm{d}^4p_\eta}{(2\pi)^4}\frac{\mathrm{d}^4p'_\xi}{(2\pi)^4}\frac{\mathrm{d}^4p'_\eta}{(2\pi)^4}\,\bar{\chi}_{\bar{P}}(p_\xi,p_\eta)\,K^{\mu}_{\bar{P},\bar{P}'}(p_\xi,p_\eta;p'_\xi,p'_\eta)\chi_{\bar{P}'}(p'_\xi,p'_\eta)\,, \end{aligned} \tag{2.87}$$

by defining the so-called current-kernel including contributions up to first order contributions[1] as given by

$$K^{\mu}_{\bar{P},\bar{P}'} = K^{\mu(0)}_{\bar{P},\bar{P}'} + K^{\mu(1)}_{\bar{P},\bar{P}'}\,. \tag{2.88}$$

The contributions itself are defined as

$$\begin{aligned} K^{\mu(0)}_{\bar{P},\bar{P}'} =& {S_F^1}^{-1}\Big(\tfrac{1}{3}\bar{P}+p_\xi+\tfrac{1}{2}p_\eta\Big)\otimes {S_F^2}^{-1}\Big(\tfrac{1}{3}\bar{P}-p_\xi+\tfrac{1}{2}p_\eta\Big)\otimes\mathcal{O}^{\mu} \\ &\times(2\pi)^4\delta^{(4)}(p_\xi-p'_\xi)(2\pi)^4\delta^{(4)}\Big(\tfrac{2}{3}(\bar{P}-\bar{P}')+p_\eta-p'_\eta\Big) \\ &+\text{cycl. perm. (23) and (31)}\,, \end{aligned} \tag{2.89}$$

and

$$\begin{aligned} K^{\mu(1)}_{\bar{P},\bar{P}'} =& \mathrm{i}\,K^{(2)}_{\frac{2}{3}\bar{P}+p_\eta}(p_\xi,p'_\xi)\otimes\mathcal{O}^{\mu}\,(2\pi)^4\delta^{(4)}\Big(\tfrac{2}{3}\Big(\bar{P}-\bar{P}'\Big)+p_\eta-p'_\eta\Big) \\ &+\text{cycl. perm. (23) and (31)}\,. \end{aligned} \tag{2.90}$$

In Fig. 2.6 the equation for the current-matrix element of Eqs. (2.87), (2.89) and (2.90) is shown schematically. In order to calculate current-matrix elements according to Eq. (2.87), it is necessary to reconstruct the Bethe-Salpeter amplitude from the Salpeter amplitude. Without two-body interactions the relation is given by the Bethe-Salpeter equation itself (see Eq. (2.46a))

$$\chi_M = -\,\mathrm{i}\,G_{0\,M}\,V^{(3)}\,\phi_M\,. \tag{2.91}$$

However, including two-body interaction the situation is more complicated. Knowing the effective potential V_{eff} and the projected Salpeter amplitude ϕ^{Λ}_M due to Eqs. (2.73) and (2.74), the Bethe-Salpeter amplitude can also be reconstructed exactly according to Eq. (2.66)

$$\chi_M = -\,\mathrm{i}\mathcal{G}_M\,V^{(3)}_{\Lambda}\,\phi^{\Lambda}_M\,. \tag{2.92}$$

A general problem appears at this point, since the projected Salpeter amplitude is computed up to k-th order $\phi^{\Lambda,\,(k)}_M$ and the Bethe-Salpeter amplitude, which is reconstructed by the approximated Salpeter amplitude, is no longer an exact solution of the Bethe-Salpeter equation. Thus, in order to stay consistent order by order, there is need for an approximation within the reconstruction formula, what is consistent with the above introduced effective potential defined by Eq. (2.73). Therefore, we assume that the effective potential can be truncated at the k-th order and can be written as

$$\mathcal{V}^{\text{eff}\,(k)}_M := \sum_{i=1}^{k} V^{\text{eff}\,(i)}_M\,. \tag{2.93}$$

[1]The orders of the current-kernel are labelled by their parenthesised numbers, which are not the bracketed numbers of the interaction kernel itself labelling three- and two-body interactions.

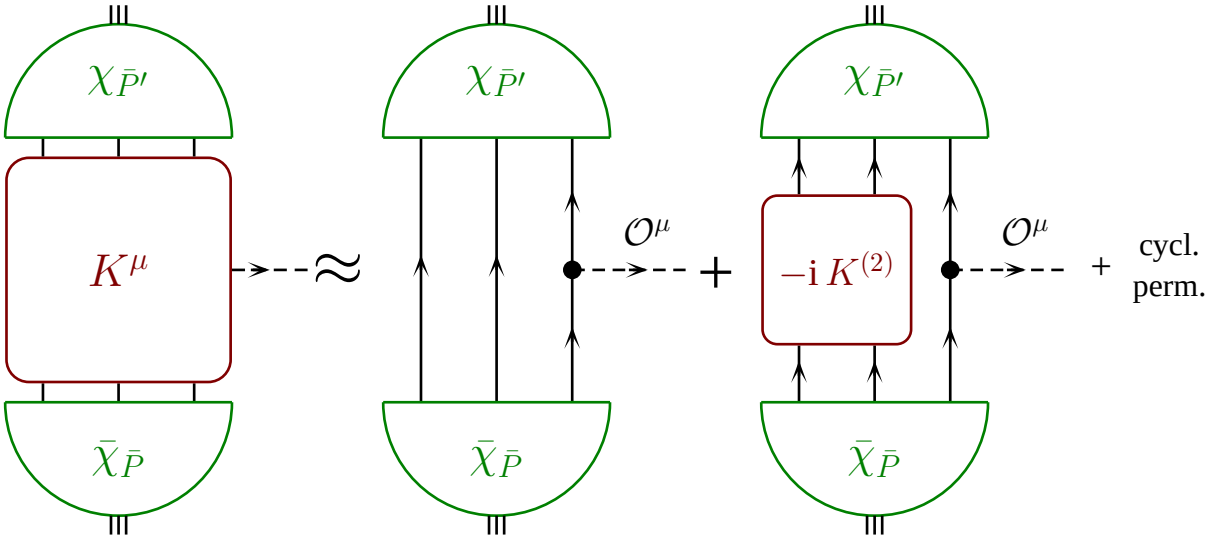

Fig. 2.6: The schematic current-kernel in lowest order of the ladder-approximation. The Bethe-Salpeter amplitudes are displayed by the green semidisks and the interaction kernels by the red rectangles. Free quarks are displayed as black arrows, which denotes the quark-propagation, where the photon propagation is denoted by the dashed lines.

Starting with the exact Bethe-Salpeter equation Eq. (2.91) and writing the potential adapted to the problem by decomposing the kernel into the projected- and residual part we write

$$\chi_M = -\,\mathrm{i}\,G_{0\,M}\left[\left(V_\Lambda^{(3)} + \sum_{i=1}^{k} V_M^{\mathrm{eff}\,(i)}\right) + \left(\bar{K}_M^{(2)} + V_R^{(3)} - \sum_{i=1}^{k} V_M^{\mathrm{eff}\,(i)}\right)\right]\phi_M\,. \tag{2.94}$$

Then, following the PhD thesis of Merten [10], it is possible to rewrite Eq. (2.94) as

$$\chi_M = -\,\mathrm{i}\,\mathcal{G}_M^{R,k}\left(V_\Lambda^{(3)} + \sum_{i=1}^{k} V_M^{\mathrm{eff}\,(i)}\right)\phi_M\,, \tag{2.95}$$

where the residual propagator $\mathcal{G}_M^{R,k}$ truncated at k-th order has been defined by

$$\mathcal{G}_M^{R,k} := G_{0\,M} - iG_{0\,M}\left(\bar{K}_M^{(2)} + V_R^{(3)} - \sum_{i=1}^{k} V_M^{\mathrm{eff}\,(i)}\right)\mathcal{G}_M^{R,k}\,. \tag{2.96}$$

After integrating out all energy components p_ξ^0 and p_η^0, the Salpeter equation can be reformulated as

$$\phi_M^\Lambda = -\,\mathrm{i}\,\langle\mathcal{G}_M^{R,k}\rangle_\Lambda\left(V_\Lambda^{(3)} + \sum_{i=1}^{k} V_M^{\mathrm{eff}\,(i)}\right)\phi_M^\Lambda, \tag{2.97}$$

while the reduced and projected k-th order Green's function can be written as

$$\langle\mathcal{G}_M^{R,k}\rangle_\Lambda = \langle G_{0\,M}\rangle - \mathrm{i}\,\langle G_{0\,M}\rangle\sum_{i=k+1}^{\infty} V_M^{\mathrm{eff}\,(i)}\langle\mathcal{G}_M^{R,k}\rangle_\Lambda\,. \tag{2.98}$$

After the first term $\langle G_{0\,M}\rangle$, the corresponding Neumann series thus starts at $(k+1)$-th order of the residual part $\bar{K}_M^{(2)} + V_R^{(3)}$. Writing the propagator $\mathcal{G}_M^{R,k}$ similar to the effective kernel V_M^{eff} in powers of k and with the definition

$$\mathcal{G}_M^{R,k} := \sum_{i=1}^{\infty}\mathcal{G}_M^{R,k\,(i)} \tag{2.99}$$

it is obvious, that

$$\left\langle \sum_{i=1}^{k} \mathcal{G}_M^{R,k\,(i)} \right\rangle_{\Lambda} = \Lambda \left\langle \sum_{i=1}^{k} \mathcal{G}_M^{R,k\,(i)} \right\rangle \bar{\Lambda} = \langle G_{0\,M} \rangle \tag{2.100}$$

is fulfilled. Replacing the exact residual propagator $\mathcal{G}_M^{R,k}$ in the exact Bethe-Salpeter equation by the up to k-th order approximated one, it is possible to obtain an approximation, which remains consistent with the Salpeter equation (2.72) . Thus, the k-th order approximation of the Bethe-Salpeter amplitude is given by

$$\chi_M^{(k)} = -\,\mathrm{i} \sum_{i=1}^{k} \mathcal{G}_M^{R,k\,(i)} \left(V_\Lambda^{(3)} + \sum_{j=1}^{k} V_M^{\mathrm{eff}\,(j)} \right) \phi_M^{(k)} \,. \tag{2.101}$$

In the further discussion it is also convenient to introduce the k-th order truncated vertex function

$$\Gamma_M^{(k)} := -\,\mathrm{i} \left(V_\Lambda^{(3)} + \sum_{j=1}^{k} V_M^{\mathrm{eff}\,(j)} \right) \phi_M^{(k)} \,. \tag{2.102}$$

Then, the reconstruction formulae for the Bethe-Salpeter amplitude and its adjoint reduce to

$$\chi_M^{(k)} = \sum_{i=1}^{k} \mathcal{G}_M^{R,k\,(i)} \Gamma_M^{(k)} \,, \tag{2.103a}$$

$$\bar{\chi}_M^{(k)} = \bar{\Gamma}_M^{(k)} \sum_{i=1}^{k} \mathcal{G}_M^{R,k\,(i)} \,, \tag{2.103b}$$

where the adjoint vertex function of k-th order is analogously defined as in Eq. (2.47b)

$$\bar{\Gamma}_M^{(k)} := {\Gamma_M^{(k)}}^{\dagger} \, \gamma_0 \otimes \gamma_0 \otimes \gamma_0 \,. \tag{2.104}$$

With Eqs. (2.87), (2.103a) and (2.103b) it is also convenient to introduce the effective current-kernel $\mathcal{K}^{\mu}_{\bar{P},\bar{P}'}$ by

$$\langle \bar{P} | j^{\mu}_{\mathcal{O}}(0) | \bar{P}' \rangle = -\,\bar{\chi}^{(k)}_{\bar{P}} \, K^{\mu}_{\bar{P},\bar{P}'} \chi^{(k)}_{\bar{P}'} = -\bar{\Gamma}^{(k)}_{\bar{P}} \, \mathcal{K}^{\mu}_{\bar{P},\bar{P}'} \Gamma^{(k)}_{\bar{P}'} \tag{2.105}$$

with the definition

$$\mathcal{K}^{\mu}_{\bar{P},\bar{P}'} := \left(\sum_{i=1}^{k} \mathcal{G}_M^{R,k\,(i)} \right) K^{\mu}_{\bar{P},\bar{P}'} \left(\sum_{j=1}^{k} \mathcal{G}_M^{R,k\,(j)} \right) \,. \tag{2.106}$$

The effective current-kernel can also be expanded in powers of the residual-kernel

$$\mathcal{K}^{\mu}_{\bar{P},\bar{P}'} := \sum_{i=1}^{k} \mathcal{K}^{\mu\,(i)}_{\bar{P},\bar{P}'} \tag{2.107}$$

before truncating at k-th order. This leads to the approximated current-matrix element

$$\langle \bar{P} | j^{\mu}_{\mathcal{O}}(0) | \bar{P}' \rangle = -\bar{\Gamma}^{(k)}_{\bar{P}} \left(\sum_{i=1}^{k} \mathcal{K}^{\mu\,(i)}_{\bar{P},\bar{P}'} \right) \Gamma^{(k)}_{\bar{P}'} \,. \tag{2.108}$$

Since the implementation of first order effects in the approximated current-matrix element (2.108) is very complicated only lowest order contributions are taken into account. Note, that the first order contributions vanish in the static limit $\bar{P} = \bar{P}' = (M, \mathbf{0})$ due to the normalisation condition of the charge

$$\bar{\Gamma}_{\bar{P}} \mathcal{K}^{0\,(1)}_{\bar{P},\bar{P}'} \Gamma_{\bar{P}} = 0 \,, \tag{2.109}$$

since the charge normalisation is completely absorbed within the normalisation condition of the Salpeter amplitudes in lowest order for the time-component of the electromagnetic current.

Neglecting first and higher order contributions in the effective current-kernel, this yields to the current-matrix element approximated by only lowest order contributions. If the incoming baryon is calculated in its rest-frame $\bar{P}' = (M', \mathbf{0}) \equiv M'$, the outgoing baryon is boosted by $q := \bar{P} - \bar{P}'$ and the current-matrix element is given by

$$\begin{aligned}\langle \bar{P}|j^{\mu}_{\mathcal{O}}(0)|\bar{P}'\rangle \simeq & -\bar{\Gamma}_{\bar{P}}\,\mathcal{K}^{\mu\,(0)}_{\bar{P},\bar{P}'}\,\Gamma_{\bar{P}'} \\ = & -3\int \frac{\mathrm{d}^4p_\xi}{(2\pi)^4}\frac{\mathrm{d}^4p_\eta}{(2\pi)^4}\bar{\Gamma}_{\bar{P}}\Big(p_\xi, p_\eta - \tfrac{2}{3}q\Big)S_F^1\Big(\tfrac{1}{3}\bar{P} + p_\xi + \tfrac{1}{2}p_\eta\Big)\otimes S_F^2\Big(\tfrac{1}{3}\bar{P} - p_\xi + \tfrac{1}{2}p_\eta\Big) \\ & \otimes S_F^3\Big(\tfrac{1}{3}\bar{P} - p_\eta\Big)\mathcal{O}^\mu S_F^3\Big(\tfrac{1}{3}\bar{P}' - p'_\eta\Big)\Gamma_{\bar{P}'}\left(\mathbf{p}_\xi, \mathbf{p}_\eta\right)\,, \end{aligned} \tag{2.110}$$

where q denotes the momentum transfer. Thereby, the lowest order contribution of the effective current-kernel

$$\begin{aligned}\mathcal{K}^{\mu\,(0)}_{\bar{P},\bar{P}'}(p_\xi, p_\eta; p'_\xi, p'_\eta) = & S_F^1\Big(\tfrac{1}{3}\bar{P} + p_\xi + \tfrac{1}{2}p_\eta\Big)\otimes S_F^2\Big(\tfrac{1}{3}\bar{P} - p_\xi + \tfrac{1}{2}p_\eta\Big)\otimes S_F^3\Big(\tfrac{1}{3}\bar{P} - p_\eta\Big)\mathcal{O}^\mu S_F^3\Big(\tfrac{1}{3}\bar{P}' - p'_\eta\Big) \\ & \times (2\pi)^4\delta^{(4)}(p_\xi - p'_\xi)(2\pi)^4\delta^{(4)}\big(\tfrac{2}{3}(\bar{P} - \bar{P}') + p_\eta - p'_\eta\big) \\ & + \text{cycl. perm. (23) and (31)}\,, \end{aligned} \tag{2.111}$$

has been used. Furthermore, Eq. (2.110) involves an additional factor 3 as a result of the corresponding three cyclic permutations of quark pairs as indicated in Eq. (2.111).

2.6 Electroweak form factors and charge radii of non-strange baryons

This section discusses the computation of electromagnetic form factors and helicity amplitudes using the current-matrix elements discussed in the previous section. Restricting to a final nucleon state $|N, \bar{P}_f, \lambda_f\rangle$ with total momentum $\bar{P}_f$ and helicity λ_f, the current-matrix element can be written as

$$\langle N, \bar{P}_f, \lambda_f|j^{E,A}_{\mu\,(a)}(0)|B, \bar{P}_i, \lambda_i\rangle\,, \tag{2.112}$$

while B denotes an arbitrary initial baryon state with total momentum $\bar{P}_i$ and helicity λ_i. j^E_μ and $j^A_{\mu\,a}$ denote the electromagnetic- and axial current-operators, respectively. These operators are defined by

$$j^E_\mu(x) =: \bar{\psi}(x)\hat{q}\gamma_\mu\psi(x): \qquad \text{and} \qquad j^A_{\mu\,a}(x) =: \bar{\psi}(x)\gamma_\mu\gamma_5\tfrac{\tau_a}{2}\psi(x):, \tag{2.113}$$

where $\hat{q}$ denotes the charge operator and τ_a the isospin Pauli matrices. The current-matrix element is related to the form factors for $B = N$ via

$$\begin{aligned}&\langle N, \bar{P}_f, \lambda_f|j^{E,A}_{\mu\,(a)}(0)|N, \bar{P}_i, \lambda_i\rangle := \\ &\qquad e\,\bar{u}_{\lambda'}(\bar{P}')\left[\gamma_\mu\left(F_1^N(Q^2) + F_2^N(Q^2)\right) - \frac{\bar{P}_{i,\mu} + \bar{P}_{f,\mu}}{2M}F_2^N(Q^2)\right]u_\lambda(\bar{P})\,, \end{aligned} \tag{2.114}$$

with the so-called Dirac and Pauli form factors $F_1^N(Q^2)$ and $F_2^N(Q^2)$, which are scalar functions of $Q^2 := -q^2$. Thereby, q defines the momentum transfer $q = \bar{P}_f - \bar{P}_i$ and the Dirac-spinor $u_\lambda(\bar{P})$ is normalised to $\bar{u}_{\lambda'}(\bar{P})u_\lambda(\bar{P}) = 2\omega_{\bar{P}}\,\delta_{\lambda\lambda'}$ with $\omega_{\bar{P}} := \sqrt{M^2 + \mathbf{P}^2}$. The so-called electric and magnetic Sachs form factors G_E^N and G_M^N are related to the above defined Dirac form factors via the linear combinations

$$G_E^N(Q^2) := F_1^N(Q^2) - \frac{Q^2}{4M^2}F_2^N(Q^2)\,, \tag{2.115a}$$

$$G_M^N(Q^2) := F_1^N(Q^2) + F_2^N(Q^2)\,. \tag{2.115b}$$

Furthermore, the electric and magnetic Sachs form factors are related to the static nucleon properties and the charge in the static limit ($Q^2 = 0$) by

$$G_E^p(0) = 1, \qquad G_E^n(0) = 0\,, \tag{2.116a}$$

$$G_M^N(0) = \mu_p, \qquad G_M^n(0) = \mu_n\,, \tag{2.116b}$$

where μ_p and μ_n are the magnetic moments of the proton and neutron. Below, we compute the current-matrix element in the rest frame of the excited initial baryon-state $|B\rangle$ with the mass $M_i = M_B$ and

$$\bar{P}_i \equiv M_i = M_B = \begin{pmatrix} M_B \\ 0 \\ 0 \\ 0 \end{pmatrix}, \bar{P}_f = \bar{P}_N = \begin{pmatrix} \omega_{\bar{P}_N} \\ 0 \\ 0 \\ |\mathbf{k}| \end{pmatrix} \quad \text{and} \quad q = \begin{pmatrix} \omega_{\bar{P}_N} - M_B \\ 0 \\ 0 \\ |\mathbf{k}| \end{pmatrix}, \tag{2.117}$$

where $M_f = M_N$ denotes the nucleon mass and $\omega_f := \sqrt{M_f^2 + |\mathbf{k}|^2}$ for the final state $|N\rangle$ and $\mathbf{k} := \mathbf{P}_N$. Then, from kinematics we find for the momentum of the finial baryon state, which is defined as the nucleon

$$\mathbf{k}^2 = Q^2 + \frac{(M_i^2 - M_f^2 - Q^2)^2}{4M_i^2}\,. \tag{2.118}$$

For $B = N$ the elastic electromagnetic form factors are then given by

$$G_E^N(Q^2) := \frac{\langle N, \bar{P}_N, \frac{1}{2}|j_0^E(0)|N, M_N, \frac{1}{2}\rangle}{\sqrt{4M^2 + Q^2}}\,, \tag{2.119a}$$

$$G_M^N(Q^2) := \frac{\langle N, \bar{P}_N, \frac{1}{2}|j_+^E(0)|N, M_N, -\frac{1}{2}\rangle}{2\sqrt{Q^2}}\,. \tag{2.119b}$$

Here

$$j_\pm^E(0) = j_1^E(0) \pm \mathrm{i}\, j_2^E(0)\,, \tag{2.120}$$

denotes the transverse electromagnetic current-operators in their spherical representation[2]. Likewise, the axial form factor is defined by

$$G_A(Q^2) = \frac{\langle p, \bar{P}_f, \frac{1}{2}|j_{1+}^A(0) + \mathrm{i}\, j_{2+}^A(0)|n, M_i, -\frac{1}{2}\rangle}{\sqrt{4M^2 + Q^2}}\,, \tag{2.121}$$

where the axial current-operator is defined by $j_{\mu\pm}^A(0) := j_{\mu 1}^A(0) \pm \mathrm{i} j_{\mu 2}^A(0)$. Here, the axial coupling is given by

$$g_A := G_A(0)\,. \tag{2.122}$$

Finally, the mean-square radii for the nucleon are given by

$$\langle r^2\rangle := -6\frac{1}{G(0)}\frac{\mathrm{d}G(Q^2)}{\mathrm{d}Q^2}\bigg|_{Q^2=0}\,. \tag{2.123}$$

Since the neutron form factor vanishes at $G_E^n(0) \approx 0$, the squared electric neutron charge radius is slightly differently defined by

$$\langle r^2\rangle_E^n := -6\frac{\mathrm{d}G_E^n(Q^2)}{\mathrm{d}Q^2}\bigg|_{Q^2=0}\,. \tag{2.124}$$

[2]Note, that in literature a pre-factor $-\frac{1}{\sqrt{2}}$ is introduced in Eq. (2.120), see *e.g.* Tiator *et al.* [47].

2.7 Helicity amplitudes and $\Delta \leftrightarrow N$ transition form factors

Apart from the electromagnetic properties of the groundstate nucleon such as μ_p, μ_n, $\langle r_p^2\rangle$, $\langle r_n^2\rangle$, g_a it is very interesting to study helicity amplitudes and transition form factors, in order to obtain further information about the internal structure of nucleon and other (excited) baryon states. Following Warns, Tiator, Aznauryan and Burkert *et al.* [47–49] the transverse and longitudinal helicity amplitudes $A^N_{1/2}$, $A^N_{3/2}$ and $S^N_{1/2}$ are related to current-matrix elements according to

$$A^N_{\frac{1}{2}}(Q^2) = \frac{\zeta}{\sqrt{2}} K \left\langle B, M_B, \tfrac{1}{2} \middle| j^E_+(0) \middle| N, \bar{P}_N, -\tfrac{1}{2} \right\rangle, \tag{2.125a}$$

$$A^N_{\frac{3}{2}}(Q^2) = \frac{\zeta}{\sqrt{2}} K \left\langle B, M_B, \tfrac{3}{2} \middle| j^E_+(0) \middle| N, \bar{P}_N, \tfrac{1}{2} \right\rangle, \tag{2.125b}$$

$$S^N_{\frac{1}{2}}(Q^2) = \zeta K \left\langle B, M_B, \tfrac{1}{2} \middle| j^E_0(0) \middle| N, \bar{P}_N, \tfrac{1}{2} \right\rangle, \tag{2.125c}$$

where $K := \sqrt{(\pi\,\alpha)/(M_N(M_B^2 - M_N^2))}$ and α is the fine structure constant. Moreover, N denotes the ground-state nucleon with four-momentum $\bar{P}_N$ (see Eq. (2.117)) and is related to the momentum transfer Q^2 by $\mathbf{k}^2$ (see Eq. (2.118)), where ξ denotes a phase of the decay amplitude. Note, that the pre-factor K includes already the normalisation factor of the Salpeter amplitudes according to Eq. (2.84). The amplitudes at $Q^2 = 0$ correspond to the photon couplings also-called the photon decay amplitudes. In the literature many publications use other definitions of the longitudinal amplitude, *e.g.* related to the third component of the current, which are then denoted by $L^N_{1/2}$ or $C^N_{1/2}$. These redefined versions of the longitudinal amplitude are related via current-conservation to the definition given in Eq. (2.125c): Due to $k^\mu j^E_\mu = \omega_f j^E_0 - |\mathbf{k}| j^E_3 = 0$, the following relation holds

$$S^N_{\frac{1}{2}}(Q^2) := \frac{|\mathbf{k}|}{\omega_f} C^N_{\frac{1}{2}}(Q^2)\,, \tag{2.126}$$

where $\omega_f := \frac{(M_i^2 - M_f^2 - Q^2)}{2M_i}$ and $\mathbf{k}^2 = \omega_f^2 + Q^2$ defines the virtual-photon momentum as known from Eq. (2.118). The notation has been adopted from Tiator *et al.* [47] and is consistent with the notation of Warns *et al.* [48], Aznauryan *et al.* [49] and the previous section. Note, that the pre-factor in Eqs. (2.125a) and (2.125b) involves a factor $-\frac{1}{\sqrt{2}}$, which normally is absorbed in the definition of the spherical current-operator $j^E_\pm$ in Eq. (2.120). In this thesis we will use $S^N_{1/2}$ of Eq. (2.125c) in all further calculations. In most cases we shall fix the common phase ζ such as to reproduce the sign of the proton decay amplitude reported in [8]. Furthermore, note that $\langle p,\ \bar{P}_N, \tfrac{1}{2}|j^E_0(0)|p,\ M_N, \tfrac{1}{2}\rangle$ is normalised to +1 at $Q^2 = 0$.

According to Tiator *et al.* [47], the transition form factors for $\Delta_{3/2^+}(1232)$ electro-production, called G^*_M and G^*_E are defined as

$$G^*_M(Q^2) = F(Q^2)\left(\sqrt{3} A^N_{\frac{3}{2}}(Q^2) + A^N_{\frac{1}{2}}(Q^2)\right)\,, \tag{2.127a}$$

$$G^*_E(Q^2) = F(Q^2)\left(\frac{1}{\sqrt{3}} A^N_{\frac{3}{2}}(Q^2) - A^N_{\frac{1}{2}}(Q^2)\right)\,, \tag{2.127b}$$

where $F(Q^2)$ is a kinematical pre-factor defined as

$$F(Q^2) = -\sqrt{\frac{M_N}{4\pi\alpha}\frac{M_\Delta^2 - M_N^2}{2M_\Delta^2}}\frac{M_N}{|\mathbf{k}|}\,, \tag{2.128}$$

in the notation of Ash *et al.* [50], which reduces at the photon point to

$$F(Q^2 = 0) = -\sqrt{\frac{2M_N^3}{4\pi\alpha}\frac{1}{M_\Delta^2 - M_N^2}}\,. \tag{2.129}$$

Furthermore, for the sake of completeness the Coulomb-transition form factor is given by

$$G_C^*(Q^2) = -2\frac{M_\Delta}{|\mathbf{k}|}F(Q^2)\sqrt{2}\,S_{\frac{1}{2}}^N(Q^2)\,, \tag{2.130}$$

which is proportional to the longitudinal helicity amplitude for the $P_{33}(1232)$-state.

2.8 Summary

In this chapter we discussed the fundamentals of the Bethe-Baryon model, which is based on the fully relativistic Bethe-Salpeter equation describing bound-state systems in the framework of quantum field theory. In section 2.2, we have followed the major steps of the calculations of Löring *et al.* [4, 7] by starting with the derivation of the Bethe-Salpeter equation from the six-point Green's function. The latter is given in terms of the propagation of three free quarks and a three- and two-body interaction kernel. We focused on the three-body interactions for simplicity. A specific time-ordering for the field operators allows the introduction of the three-fermion Bethe-Salpeter amplitudes associated with a pole of the Green's function in the total energy of the three quark system. The Bethe-Salpeter equation and its normalisation condition then follows from a Laurent- and Taylor-expansion of the Green's function in the vicinity of the pole in the energy.

It is possible to reduce the Bethe-Salpeter equation to the Salpeter equation if the propagators, which are involved in the free Green's function, are of free form and if the interaction kernels are assumed to be instantaneous. Accordingly, constituent effective quark masses enter as free parameters in the model. By integration of the energies, it is then possible to derive the Salpeter equation from the Bethe-Salpeter equation. The Salpeter amplitude can be interpreted as an analogon of the usual wave function in non-relativistic quantum-mechanics.

We also discussed the calculation of electroweak observables, starting with the electroweak form factors and the helicity amplitudes. All these observables are based on current-matrix elements. The details of this method, published already by Merten and Kretzschmar *et al.* [9, 10, 12], were briefly recapitulated in section 2.5. The derivation of the current-matrix elements starts from the definition of a seven-point Green's function for a photon coupled to a three-quark system and runs analogously to the derivation of the Bethe-Salpeter equation. The relations of the current-matrix elements to electroweak form factors, magnetic moments and charge radii as well as to the helicity amplitudes and $\Delta \leftrightarrow N$ transition form factors are given in section 2.6 and 2.7.

Chapter 3

Results of previous calculations

3.1 Introduction

This chapter recapitulates the major results of the work of Löring *et al.* [5–7] as well as of Merten and Kretzschmar *et al.* [9,10,12]. Furthermore, the interaction potentials $V^{(3)}$ and $V^{(2)}$, see Eq. (2.63), will be specified more precisely. These phenomenologically introduced potentials are the so-called *confinement potential* and the *instanton-induced 't Hooft interaction*. For the confinement potential there exists many possibilities to implement its Dirac-structure. Two Dirac-structures have been found, which reproduce the spectra quite well: These were called model $\mathcal{A}$ and $\mathcal{B}$. Since the confinement potential itself is flavour independent, a further potential based on an instanton-induced interaction had been introduced to account for the major spin-dependent splittings of baryons. The instanton-induced force is flavour dependent and has a definite Dirac-structure. An other candidate for a spin-dependent interaction, the so-called one-gluon exchange, has been discussed in the PhD thesis from Löring [7] and will be briefly commented here.

3.2 The confinement potential

The confinement potential will be introduced phenomenologically by a linear rising potential, which leads to a satisfactory description of the baryon spectra and the so-called Regge-trajectories $M^2 \propto J$, where J denotes the total angular momentum of the baryon state. The interpretation of this empirical picture motivates a string-like connection between quarks (flux-tubes) generated by gluonic interactions. There exists several types of confinement potentials (see also Löring *et al.* [5, 7] or Carlson *et al.* [51, 52] for more information), which increase linearly with the inter-quark distance, whereas confinement is thus implemented by subjecting quarks to a potential, supplemented by an appropriate three particle Dirac-structure Γ. Then, the potential contains two parameters: the offset a and the slope b and is assumed to be of the following form in coordinate space

$$\begin{aligned}\mathcal{V}^{(3)}(x_1,x_2,x_3;x_1',x_2',x_3') =& V^{(3)}_{\text{conf}}(\mathbf{x}_1,\mathbf{x}_2,\mathbf{x}_3)\,\delta(x_1^0-x_2^0)\delta(x_2^0-x_3^0)\\ &\times\delta^{(4)}(x_1-x_1')\delta^{(4)}(x_2-x_2')\delta^{(4)}(x_3-x_3')\,,\end{aligned} \tag{3.1}$$

with

$$V^{(3)}_{\text{conf}}(\mathbf{x}_1,\mathbf{x}_2,\mathbf{x}_3) = 3\,a\,\Gamma_o + b\sum_{i<j}|\mathbf{x}_i-\mathbf{x}_j|\;\Gamma_s\,, \tag{3.2}$$

where Γ_o and Γ_s are suitably chosen Dirac-structures. According to [5–7], two different Dirac-structures have been found, which reproduce the light-quark baryon spectra quite well. As mentioned in the introduction, the different Dirac-structures label the corresponding models, called model $\mathcal{A}$ and $\mathcal{B}$. Tab. 3.1 summarises the Dirac-structures used in these models. The prediction of the spectra is very sensitive to the choice of the Dirac-structure. This choice depends additionally on other involved potentials, such as the instanton-induced 't Hooft interaction within model $\mathcal{A}$ and $\mathcal{B}$. For the one-gluon exchange alternative Dirac-structures are more favourable and can be found in the PhD thesis of Löring [7].

Table 3.1: The confinement Dirac-structures as used in [5–7] for the so-called models $\mathcal{A}$ and $\mathcal{B}$, which contains the instanton-induced 't Hooft force.

Model	Γ_o (offset)	Γ_s (slope)
$\mathcal{A}$	$\frac{1}{4}\,(\mathbb{1}\otimes\mathbb{1}\otimes\mathbb{1} + \mathbb{1}\otimes\gamma_0\otimes\gamma_0 + \text{cycl. perm.})$	$\frac{1}{2}\,(-\mathbb{1}\otimes\mathbb{1}\otimes\mathbb{1} + \mathbb{1}\otimes\gamma_0\otimes\gamma_0 + \text{cycl. perm.})$
$\mathcal{B}$	$\frac{1}{4}\,(\mathbb{1}\otimes\mathbb{1}\otimes\mathbb{1} + \mathbb{1}\otimes\gamma_0\otimes\gamma_0 + \text{cycl. perm.})$	$\frac{1}{4}\,(\mathbb{1}\otimes\mathbb{1}\otimes\mathbb{1} + \mathbb{1}\otimes\gamma_0\otimes\gamma_0 + \text{cycl. perm.})$

3.3 The instanton-induced interaction

The effect of instantons on quark-quark interactions have been firstly pointed out by 't Hooft [53] for the $SU(2)$-group. Accordingly, the instanton-induced interaction will be called 't Hooft force in the following text. The extension to the $SU_F(3)$-group has been performed subsequently to 't Hooft by Shifman *et al.* [54] in which an effective Lagrangian for single instanton- and anti-instanton configurations was derived. Instantons are solutions of the euclidean Yang-Mills equations with a given topological quantum number Q_T, which is also-called the topological charge. Thereby it turns out, that Q_T can only take integer numbers. This important condition characterises different vacua and thus instantons can be interpreted as tunnelling events between these different vacua. Hence QCD sustains a complex vacuum structure within an enumerable infinite number of topological inequivalent vacua. Each of these vacua can also be characterised by another topological number, the so-called *winding number* or "Chern-Simons" number N_{CS}. Instanton- and anti-instantons are the simplest building blocks with non-trivial structure, which communicates between such vacua with a topological charge $Q_T = 1$ and $Q_T = -1$. However, by fulfilling $Q_T = N_{\text{CS}} - N'_{\text{CS}}$, see [7].

The details of the implementation of the instanton-induced 't Hooft force are given in [5, 7] and will be recapitulated here very briefly. Instanton effects leads to an effective quark-quark interaction, which acts only on quark pairs antisymmetric in flavour and can be written in coordinate space as

$$\mathcal{V}^{(2)}_{\text{Inst}}(x_1, x_2; x'_1, x'_2) = V^{(2)}_{\text{Inst}}(\mathbf{x}_1 - \mathbf{x}_2)\,\delta(x_1^0 - x_2^0)\,\delta^{(4)}(x_1 - x'_1)\,\delta^{(4)}(x_2 - x'_2) \tag{3.3}$$

with

$$V^{(2)}_{\text{Inst}}(\mathbf{x}) \;\; = \;\; -4v(\mathbf{x})\left(\mathbb{1}\otimes\mathbb{1} + \gamma^5\otimes\gamma^5\right)\,\mathcal{P}^{\mathcal{D}}_{S_{12}=0}\left(g_{nn}\,\mathcal{P}^{\mathcal{F}}_{\mathcal{A}}(nn) + g_{ns}\,\mathcal{P}^{\mathcal{F}}_{\mathcal{A}}(ns)\right)\,, \tag{3.4}$$

where $\mathcal{P}^{\mathcal{D}}_{S_{12}=0}$ is a projector on spin-singlet states and $\mathcal{P}^{\mathcal{F}}_{\mathcal{A}}(f_1 f_2)$ projects on flavour-antisymmetric quark pairs with quark flavours f_1 and f_2. The two couplings g_{nn} and g_{ns} are in principle determined by integrals over instanton densities, which can be calculated *e.g.* in an instanton gas approximation. Nevertheless, they are treated as free parameters in the model. Furthermore, as it stands, the 't Hooft force is a contact interaction and $v(\mathbf{x})$ is given as a delta-function in Eq. (3.4). In order to implement the interaction within the framework of the Bethe-Baryon model it is necessary to regularise $v(\mathbf{x})$, *e.g.* as a Gaussian potential with a specific effective range in coordinate space

$$v_\lambda(\mathbf{x}) = \frac{1}{\lambda^3\,\pi^{\frac{3}{2}}}\,\exp\left(-\tfrac{|\mathbf{x}|^2}{\lambda^2}\right)\,. \tag{3.5}$$

The effective range parameter λ is assumed to be equal for each quark-flavour and enters as an additional parameter in the model.

3.4 The one-gluon exchange

Apart from the instanton-induced 't Hooft force there exists another possibility in order to split nucleon- and Δ-states by the so-called **O**ne-**G**luon **E**xchange. The corresponding one-gluon propagator is given by

$$D_{\mu\nu}(k^2) := \frac{-\mathrm{i}g_{\mu\nu}}{k^2 + \mathrm{i}\epsilon}\,. \tag{3.6}$$

Based on the OGE-propagator and the gluon-fermion vertex structure, the second-order matrix element of the OGE can be extracted according to [7, 55]

$$\gamma^\mu D_{\mu\nu}(k^2)\gamma^\nu = 4\pi \left(\frac{\gamma_0 \otimes \gamma_0}{|\mathbf{k}|^2} + \frac{(\boldsymbol{\gamma}\cdot\otimes\boldsymbol{\gamma}) - (\boldsymbol{\gamma}\cdot\hat{\mathbf{k}})\otimes(\boldsymbol{\gamma}\cdot\hat{\mathbf{k}})}{k^2 + \mathrm{i}\epsilon} \right), \tag{3.7}$$

in Coulomb gauge with $\hat{\mathbf{k}} := \frac{\mathbf{k}}{|\mathbf{k}|}$. The corresponding potential can be written in coordinate space as

$$V^{(2)}_{\mathrm{OGE}}(\mathbf{x}) = -\frac{2}{3}\frac{\alpha_S}{r}\left(\gamma_0\otimes\gamma_0 + \tfrac{1}{2}(\boldsymbol{\gamma}\cdot\otimes\boldsymbol{\gamma}) - \tfrac{1}{2}(\boldsymbol{\gamma}\cdot\hat{\mathbf{x}})\otimes(\boldsymbol{\gamma}\cdot\hat{\mathbf{x}})\right) \tag{3.8}$$

which defines the OGE-potential. The direction of the position vector is denoted by $\hat{\mathbf{x}} := \frac{\mathbf{x}}{r}$, $r := |\mathbf{x}|$, while α_S is the strong running coupling constant, which is at $|\mathbf{k}|^2 = 0$ in momentum space usually given as a finite value.

The OGE generates the $\Delta - N$ mass-splitting via its spin-dependent Dirac-structures, which are reflected in Eq. (3.8) by the factors involving the Dirac-matrices $\boldsymbol{\gamma}$. Hence, the mass-splitting mechanism differs from the instanton-induced interaction as it is obvious in the previous section. The OGE has been investigated in [7] in order to give a moderately satisfactory description of the full nucleon- and Δ-spectrum. But in particular, especially excited resonances cannot be reproduced, *e.g.* the mass of the $N_{1/2^-}(1535)$-state, which is predicted much to low, as shown in [7].

3.5 Baryon spectra

Introducing the confinement potential and the instanton-induced 't Hooft interactions within the Salpeter equation (2.62) leads to the prediction of mass spectra for model $\mathcal{A}$ and $\mathcal{B}$, which will be briefly discussed in this section. We start with a discussion on the scale dependence of the mass spectra. The scale characterises the finite basis in which the Salpeter equation is solved.

3.5.1 Scale dependence

Solving the Salpeter equation according to Eqs. (2.62) and (2.63) yields to an eigenvalue problem, which can be solved numerically. For this purpose, the Salpeter amplitudes will be expanded within a large, but finite basis of harmonic oscillator states with oscillator quantum numbers $N \leq N_{\max}$. The harmonic oscillator basis is characterised by a specific oscillator length scale β, which has to be chosen such, that for the baryon mass M: $\frac{\partial M_\beta}{\partial \beta} \simeq 0$ holds. With an increasing number of oscillator shells the curvature of M_β in the vicinity of $\bar{\beta}$ with $\frac{\partial M_\beta}{\partial \beta}\big|_{\beta=\bar{\beta}} = 0$ becomes smaller and the range of values for the scale parameter with the property $\frac{\partial M_\beta}{\partial \beta} \approx 0$ increases. This is demonstrated in Fig. 3.1 for $N_{\max} = 8$ and 18 oscillator shells for model $\mathcal{A}$. For the total angular momentum J a common value for β is chosen. This guarantees the orthogonality of the amplitudes. Tab. 3.1 summarises all (minimal) scale parameters β, which are chosen for all light-flavoured baryon states as the average of the ground- and first excited state. This selection has been done by hand.

Table 3.2: Optimal values of the length scale β for various baryons in model $\mathcal{A}$.

baryon	$2J+1$	β [fm]
Δ	≥ 2	0.60
N	2	0.45
	≥ 4	0.50
$\Lambda\,\Sigma$, Ξ, Ω	≥ 2	0.60

3.5.2 Model parameters

Still following the work of Löring *et al.* [5–7], the complete light-flavoured baryon mass spectra including the Δ-, N-, Λ-, Σ-, Ξ- and Ω-spectra, can be calculated by taking into account the confinement and instanton-induced interactions from the previous sections 3.2 and 3.3, respectively. For the calculation of the mass spectra it becomes necessary to determine the free parameters of the confinement and of the instanton-induced 't Hooft forces as well as of the non-strange and strange quark masses, m_n and m_s. A compilation of the parameters is

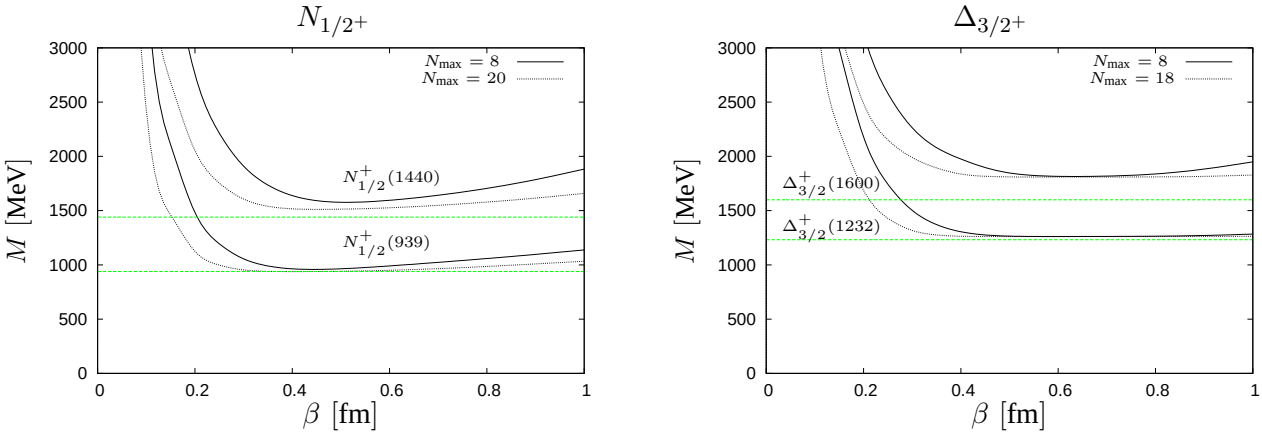

Fig. 3.1: Scale dependence for the $N_{1/2}(939, 1440)$-states (right side) and for the $\Delta_{3/2}(1232, 1600)$-states (left side) for model $\mathcal{A}$. Different model spaces are used within $N_{\max} = 8$ and $N_{\max} = 18$ ($N_{\max} = 20$) oscillator shells, respectively. It is obvious, that the minima of the ground- and first excited states are not located exactly at the same β. Nevertheless, suitable values for β are at $\beta = 0.45\,\text{fm}$ for the $N_{1/2}(939, 1440)$-states and at $\beta = 0.6\,\text{fm}$ for the $\Delta_{3/2}(1232, 1600)$-states. Furthermore, the curvature reduces with increasing number of oscillator shells.

Table 3.3: Model parameters for the current model $\mathcal{A}$ in comparison to those of model $\mathcal{B}$, cited from [5–7].

		parameter	model $\mathcal{A}$	model $\mathcal{B}$
masses	non-strange	m_n [MeV]	330.0	300.0
	strange	m_s [MeV]	670.0	620.0
confinement	offset	a [MeV]	-744.0	-1086.0
	slope	b [MeV/fm]	440.0	1193.0
instanton induced interaction	nn-coupling	g_{nn} [MeV fm^3]	136.0	89.6
	ns-coupling	g_{ns} [MeV fm^3]	96.0	61.7
	eff. range	λ [fm]	0.4	0.4

Table 3.4: List of baryon resonances of which the masses were used to determine the model parameters in a least-squares fit, where every resonance was attributed a weight reciprocal to its uncertainty in its position as given in [8]. Nominal masses are given in MeV.

Δ	N	Λ
$P_{33}(1232)$	$P_{11}(939)$	$P_{01}(1116)$
$F_{37}(1950)$		
$H_{3\,11}(2420)$		
$K_{3\,15}(2950)$		

given in Tab. 3.3 as used by Löring *et al.* [5, 6]. The parameters in Tab. 3.3 have been determined by fitting the confinement parameters on the Regge trajectory $\Delta_{3/2^+}(1232)$, $\Delta_{7/2^+}(1950)$, $\Delta_{11/2^+}(1232)$ and $\Delta_{16/2^+}(2950)$ and the instanton-induced couplings at the $N_{1/2^+}(939)$- and $\Lambda_{1/2^+}(1116)$-resonances. The resonances, used in the fit, are again summarised in Tab. 3.4. The resulting spectra are displayed in Figs. 3.2-3.6. Each column corresponds to a spectrum characterised by the total angular momentum J and parity π. The predicted and measured resonances are displayed by horizontal lines located at the value of the mass, while the uncertainties of the experimental masses are represented as shaded boxes in the central part of each column. Furthermore, the PDG-rating [56] is indicated by stars, where the left and right part of each column displays the results of model $\mathcal{A}$ and $\mathcal{B}$ from Löring *et al.* [5]. The middle of each column shows the experimental data from the PDG [56] of 2010 for comparison. Resonances, that cannot be accounted for, are indicated by round boxes and labelled with question marks.

3.5.3 Δ- and Ω-spectra

We start with the discussion of the Δ-spectrum, displayed in Fig. 3.2, from which it is evident, that most of the groundstate masses are reproduced quite well with the exception of the $J = \frac{1}{2}^+$- and $J = \frac{5}{2}^-$-groundstate's for

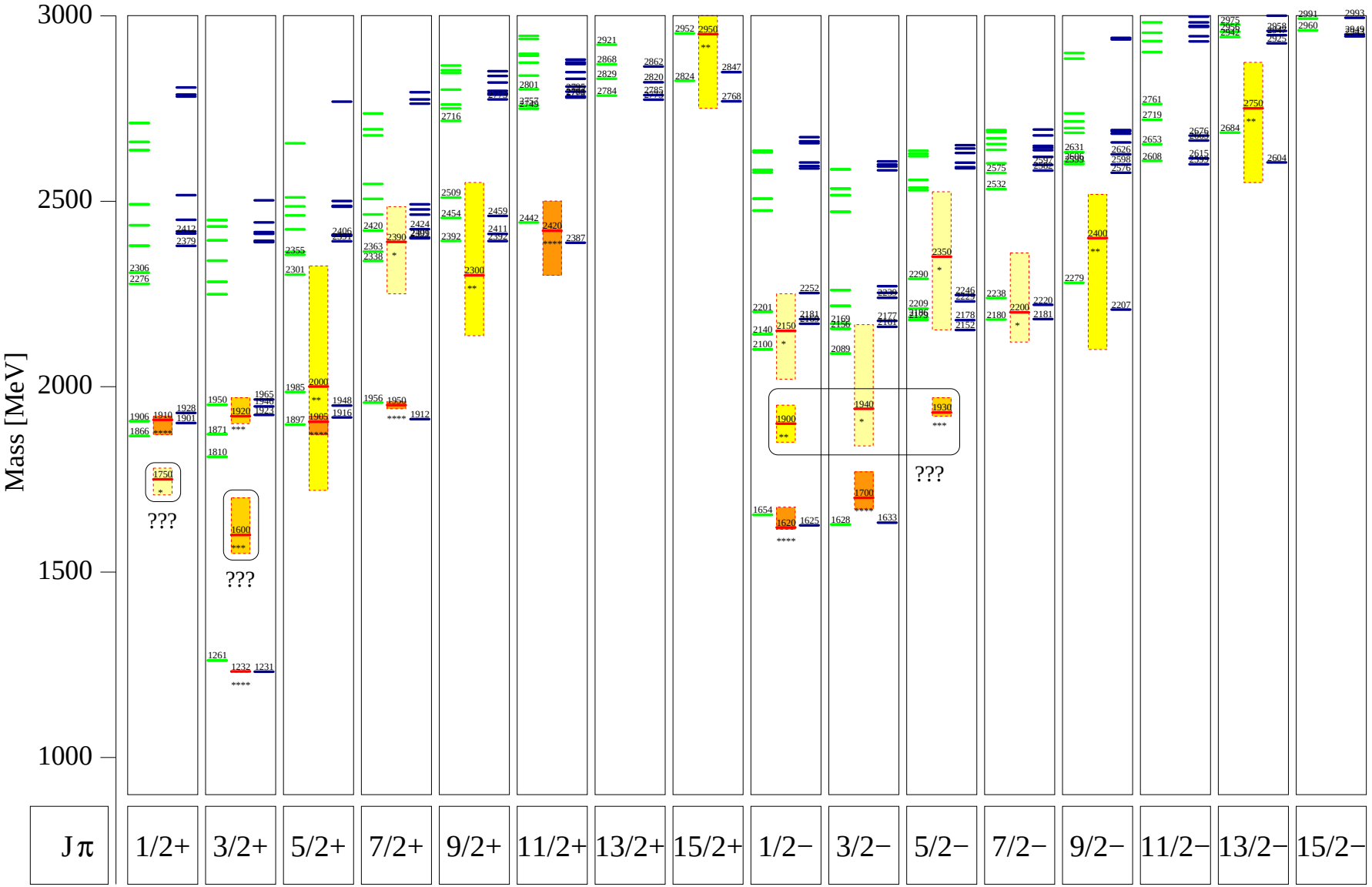

Fig. 3.2: Comparison of the Δ-spectrum calculated within model $\mathcal{A}$ and $\mathcal{B}$ [5] (left and right side of each column) with the experimental data from the Particle Data Group [56] (central in each column); Lines indicate the resonance position (mass) with the mass uncertainty represented by a shaded box and the rating of the PDG [56] indicated by stars. The small numbers give the mass in MeV. J and π denote total angular momentum and parity, respectively. Occurring problems are indicated by question-marks. All calculations are performed with a basis with up to $N_{\max} = 12$ or 14 oscillator shells.

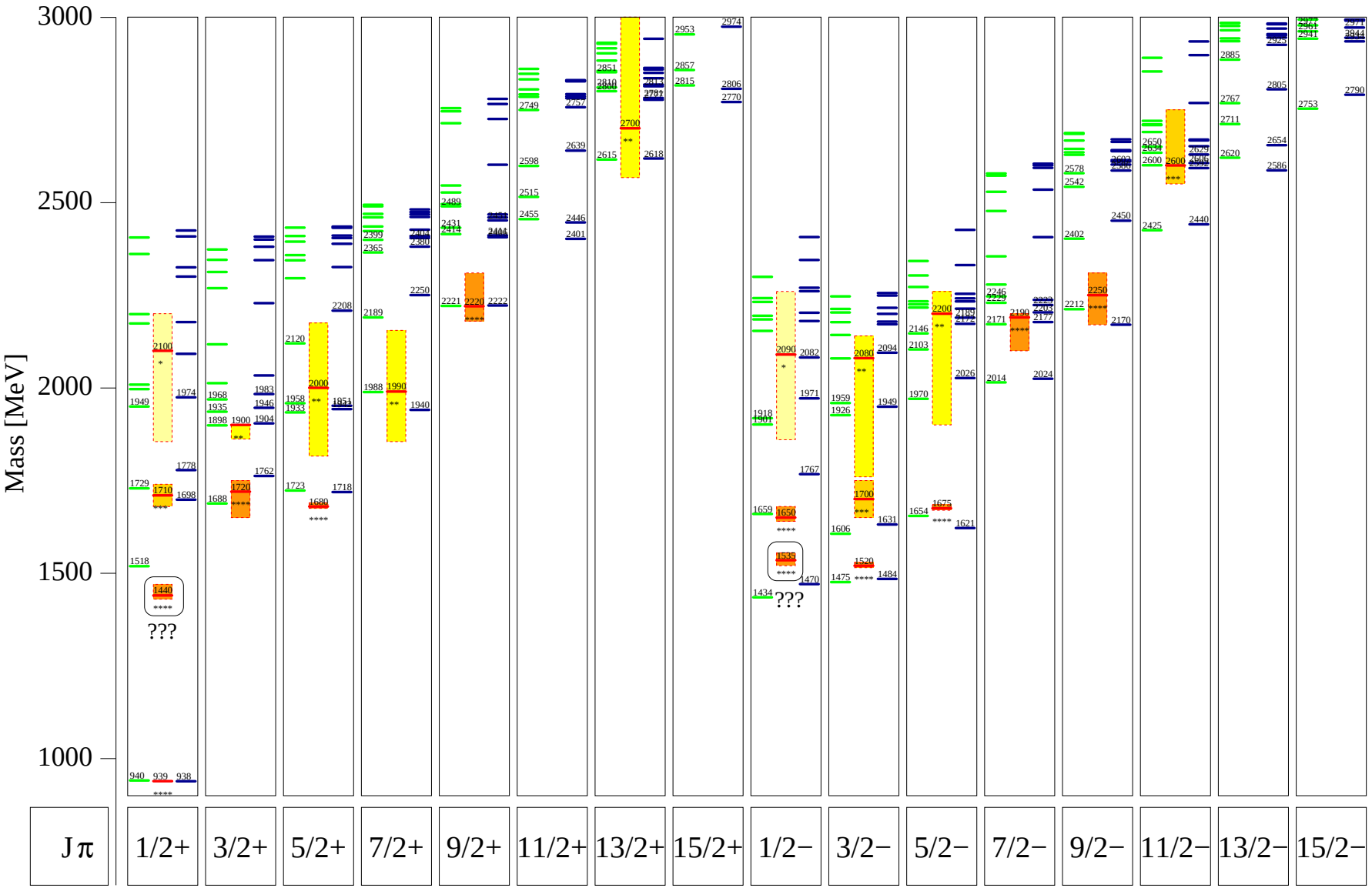

Fig. 3.3: Comparison of the N-spectrum calculated within the model $\mathcal{A}$ and $\mathcal{B}$ [5] (left and right side of each column) with experimental data from the Particle Data Group [56] (central in each column). See also caption to Fig. 3.2.

both models. The Δ-spectrum is determined by the non-strange mass and the confinement potential parameters only. For excited resonances, as already mentioned in the introduction, some discrepancies in both models exists. Especially excited resonances with negative parity, *e.g.* the $\Delta_{1/2^-}(1910)$-, $\Delta_{3/2^-}(1940)$- and $\Delta_{5/2^-}(1930)$-resonance as well as the positive parity Roper-like $\Delta^+_{3/2}(1600)$-resonance are not reproduced. These resonances are indicated by boxes and question marks in Fig. 3.2 and are the major motivation for the introduction of a new interaction, which allows a satisfactory description in the framework of the Bethe-Baryon model. Such a new interaction will be discussed in the next chapter. As it is obvious from Fig. 3.2, model $\mathcal{A}$ generates a slightly better description of the mass-splittings of the Δ-spectrum than model $\mathcal{B}$.

The experimental Ω-spectrum consists only of the $\Omega_{3/2^+}(1672)$-resonance and depends only on the strange-quark mass and the confinement potential. In fact the strange-quark mass was adjusted to this state after fixing the confinement parameters via the Regge trajectory. A part of the Ω-spectrum with $J \leq \frac{7}{2}$ is displayed on the right side of Fig. 3.6. It turns out, that all excited resonances are predicted in the mass region above $\gtrsim 2000\,\mathrm{MeV}$, supported by measurements of Ω-baryons listed in the PDG [8].

Thus in model $\mathcal{A}$ and $\mathcal{B}$, which differ from each other only by their confinement Dirac-structures, most of the resonances in the Δ- and Ω-spectra are reproduced quite well.

3.5.4 N-spectrum

The nucleon-spectrum depends additionally on the parameters of the instanton-induced 't Hooft force. Note, that the confinement parameters are already fixed by the Δ-Regge trajectory as mentioned in the previous subsection, this also holds for the non-strange and strange constituent quark mass. Fig. 3.3 displays the nucleon-spectrum for model $\mathcal{A}$ and $\mathcal{B}$, respectively. Comparing both models with each other, it is conspicuous that model $\mathcal{A}$ can account for most of the excited resonances, *e.g.* even approximately for the Roper-resonance $N_{1/2^+}(1440)$, which is labelled with the box, whereas model $\mathcal{B}$ does not. Furthermore, model $\mathcal{B}$ cannot reproduce the mass-splittings of the $J^\pi = \frac{1}{2}^-$-states as well: In particular the mass of the $N_{1/2^-}(1650)$-resonance is overestimated. A further discrepancy in both models is the mass of the $N_{1/2^-}(1535)$-resonance, which is predicted too low. The $N_{1/2^-}(1535)$-resonance offers a persistent problem in the Bethe-Baryon quark model as also shown in the subsequent chapter 4, where a new spin-flavour dependent interaction will be introduced. In general, model $\mathcal{A}$ reproduces the nucleon-spectrum better than model $\mathcal{B}$, as it was also found from the Δ-spectrum.

3.5.5 Hyperon-spectra

The hyperon-spectra are displayed in Figs. 3.4, 3.5 and in the left part of Fig. 3.6 . Starting with the discussion of the Λ-spectrum, model $\mathcal{A}$ reproduces the mass-splitting much better then model $\mathcal{B}$ just as for the nucleon and Δ-sector. Model $\mathcal{B}$ does not reproduce the Roper-like $\Lambda_{1/2^+}(1600)$- and the $\Lambda_{1/2^-}(1405)$-resonance as marked by boxes. Concerning the latter Jido, Meißner, Oset and Hyodo *et al.* [57–59] interpreted this resonance as a meson-baryon bound-state close to the $\bar{K}N$-threshold, which thus cannot be described satisfactorily as a q^3-bound-state in the Bethe-Baryon model.

Both models can account for most of the resonances in the Σ-spectrum as displayed in Fig. 3.5, where again some discrepancies occur in the description of excited states, which are indicated partially by boxes. Apart from the Roper-like $\Sigma_{1/2^+}(1660)$-resonance two negative parity resonances, $\Sigma_{3/2^-}(1580)$ and $\Sigma_{7/2^-}(2100)$, cannot be accounted for in the models also the two star rated $\Sigma_{3/2^-}(1580)$-resonance poses a persistent problem in the Bethe-Baryon model. Furthermore, model $\mathcal{B}$ cannot account for any of the excited $\Sigma_{1/2^+}$-resonances nor for the $\Sigma_{3/2^+}(1840)$- and $\Sigma_{1/2^-}(1620)$-resonances. All other observed Σ-resonances can be reproduced very well by model $\mathcal{B}$ and in particular by model $\mathcal{A}$.

Finally, for the Ξ-baryons there exist less data for a more detailed comparison with the experimental data. Both models reproduce nicely all of the known Ξ-resonances, but differ in their predictions for excited states as displayed on the left side of Fig. 3.6. Similar to the N-, Λ- and Σ-spectra, it can be concluded, that model $\mathcal{A}$ accounts for the internal structure better than model $\mathcal{B}$. Within the framework of model $\mathcal{A}$ a Roper-like $\Xi_{1/2^+}$-resonance is predicted around $\approx$1870 MeV, while the lower $J^\pi = \frac{1}{2}^-$-state should be located at around $\approx$1770 MeV.

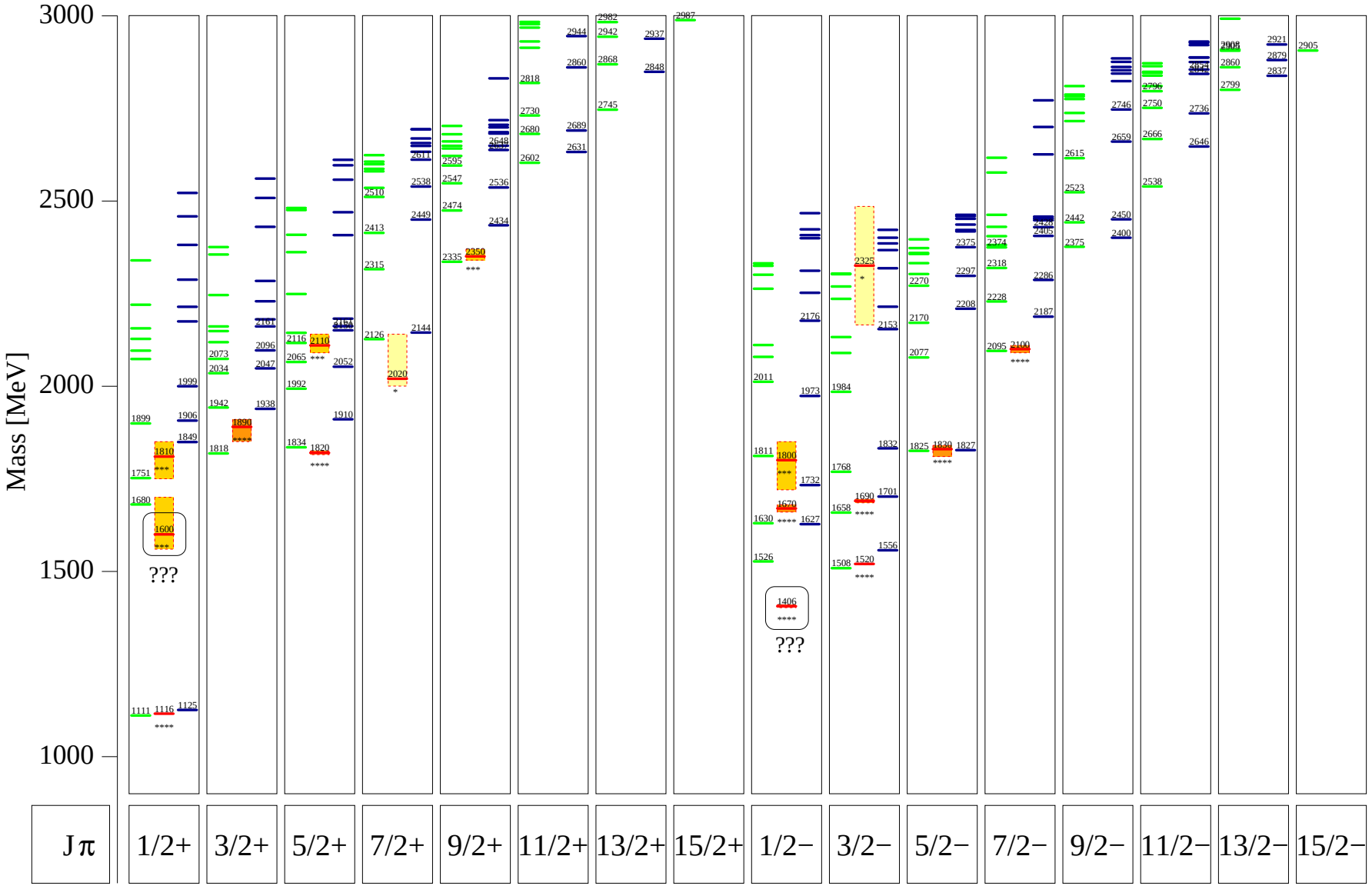

Fig. 3.4: Comparison of the Λ-spectrum calculated within the model $\mathcal{A}$ and $\mathcal{B}$ [5] (left and right side of each column) with experimental data from the Particle Data Group [56] (central in each column). See also caption to Fig. 3.2.

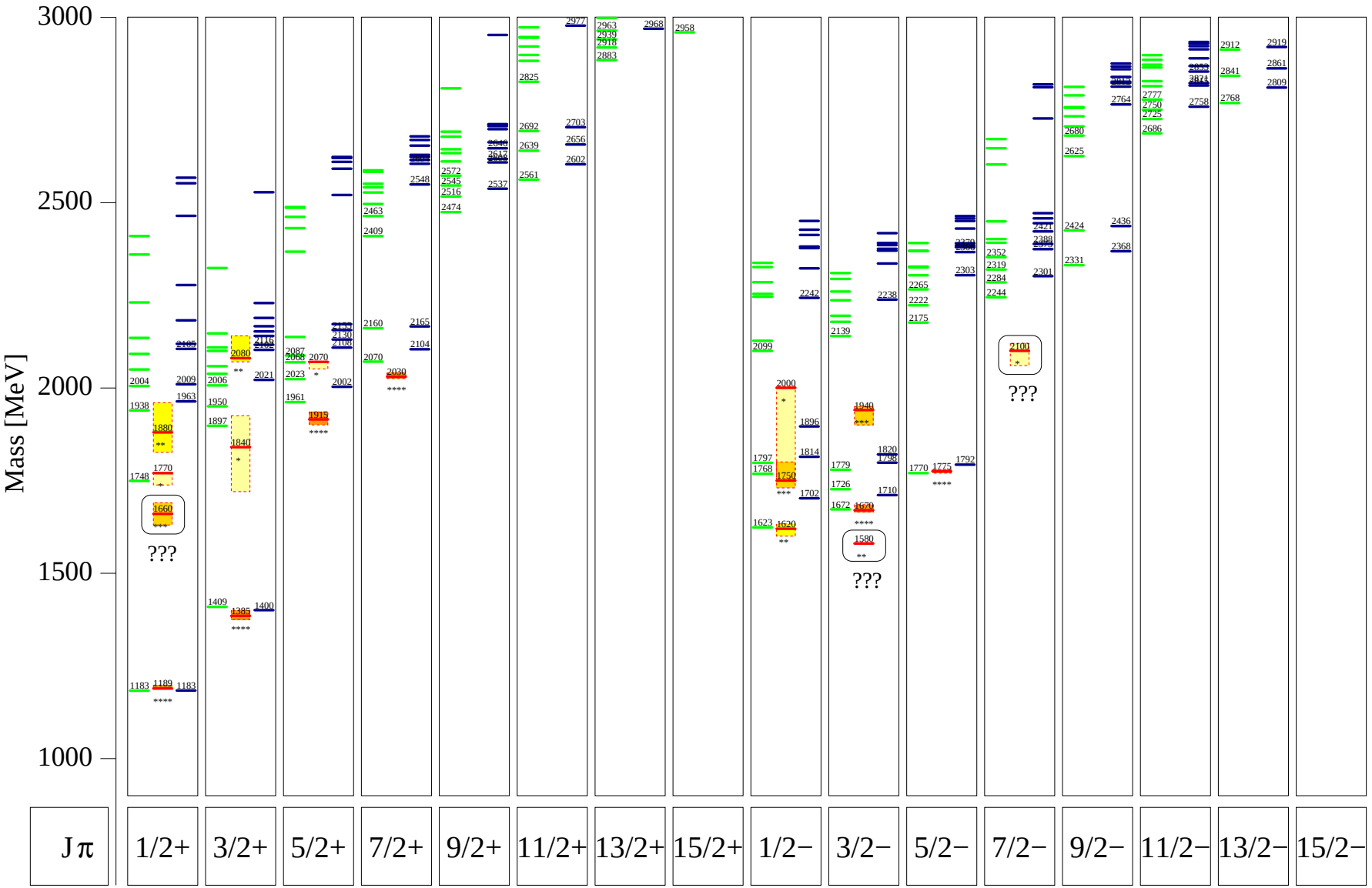

Fig. 3.5: The Σ-spectrum calculated within the model $\mathcal{A}$ and $\mathcal{B}$ [5] (left and right side of each column) with experimental data from the Particle Data Group [56] (central in each column). See also caption to Fig. 3.2.

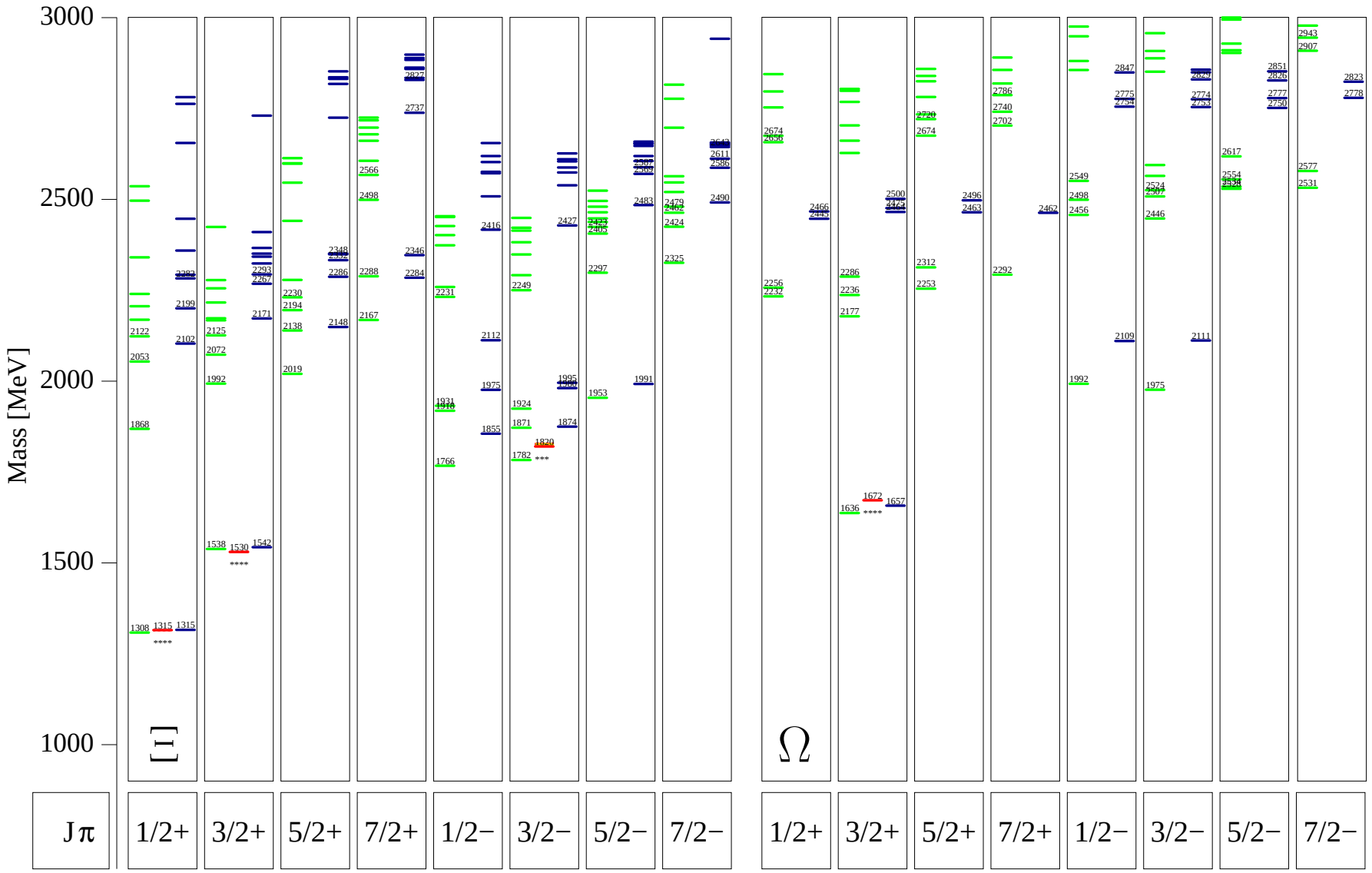

Fig. 3.6: Comparison of the Ξ- and Ω-spectrum calculated within the model $\mathcal{A}$ and $\mathcal{B}$ [5] (left and right side of each column) with experimental data from the Particle Data Group [8] (central in each column). The Ξ-spectrum has been displayed on the left side and the Ω-spectrum on the right side restricting on resonances with $J \leq \frac{7}{2}$. See also caption to Fig. 3.2.

Thus model $\mathcal{A}$ was favoured, since it reproduces most of the resonances better than model $\mathcal{B}$. In particular model $\mathcal{A}$ accounts for most of the Roper-like resonances in the Λ- and Σ-baryon sector with acceptable accuracy ($\Lambda_{1/2^+}(1600)$ and $\Sigma_{1/2^+}(1660)$), whereas model $\mathcal{B}$ does not reproduce any of the Roper-like resonances. In the Σ-baryon sector for instance, the Roper-like resonance is predicted at 1869 MeV by model $\mathcal{A}$ and at 2102 MeV by model $\mathcal{B}$. Here, we favour the prediction of model $\mathcal{A}$. In the next chapter 4, a further extension of the Bethe-Baryon model will be introduced and compared with a recalculated version of model $\mathcal{A}$ by increasing its numerical accuracy in order to reduce numerical uncertainties. This leads to a secondary and not directly intended effect, since the increased numerical accuracy induces a readjustment of some of the parameters, which shifts the resonance positions slightly, see sections 4.2.2, 4.2.3 and 4.2.4 in the next chapter for more information.

3.6 Electroweak form factors, helicity amplitudes, photon decay amplitudes and other static observables

The work of Merten and Kretzschmar *et al.* [9, 10, 12] studies electromagnetic form factors and helicity amplitudes as well as photon decay amplitudes in the framework of the Bethe-Baryon model. These studies were exclusively made for model $\mathcal{A}$, since, as discussed above, it describes the nucleon- and Δ-spectra better then model $\mathcal{B}$. Furthermore, static observables, such as the magnetic moment and the charge radius have been extracted by Merten *et al.* [9, 10] from extrapolations of the electromagnetic form factors to the photon point at vanishing momentum transfer. An alternative method for the calculation of static observables has been developed from Haupt *et al.* [13, 14], which calculates the magnetic moments and charge radii directly without extrapolating the form factors to the photon point. In the next chapter, all studies of Merten *et al.* [9, 10] will be recalculated with a higher numerical accuracy and can be found in the figures to sections 4.2.5 and 4.2.6, where also the results of a new approach, called model $\mathcal{C}$, will be discussed. The next chapter 4 shows calculations of model $\mathcal{A}$ for the baryon spectra, electroweak form factors, helicity amplitudes, photon decay amplitudes, magnetic moments and charge radii. Such calculations can also be found in Merten *et al.* [9, 10] and Haupt *et al.* [13, 14], but with less numerical accuracy.

3.7 Summary

This chapter summarises and assesses the results of the Bethe-Baryon model on the light-flavoured baryon spectra of Löring *et al.* [5–7]. It starts with the introduction of the two quark interactions used: The confinement potential, which has been introduced phenomenologically as a linear rising potential with an offset- and a slope parameter in order to confine quarks within a baryon (see section 3.2). For the Dirac-structure of the confinement potential, Löring *et al.* [5] studied two different forms, which lead to reasonable results: model $\mathcal{A}$ and $\mathcal{B}$. The second interaction is based on instanton effects between quarks in QCD and is called the instanton-induced 't Hooft interaction. This force is derived as a two-body contact interaction and has been regularised by a Gaussian potential in coordinate space. The interaction acts only on spin-singlet states and flavour-antisymmetric quark pairs and thus is responsible *e.g.* for the $\Delta - N$ mass-splitting in the baryon spectra. In section 3.5 we discussed the light-flavoured baryon spectra. After a brief discussion on the scale dependencies, we recapitulate the results for the baryon spectra for model $\mathcal{A}$ and $\mathcal{B}$: The light-flavoured-spectra are in general reproduced quite well by both models. However, there are some discrepancies in these spectra, which cannot be described by either of the models $\mathcal{A}$ and $\mathcal{B}$. Most prominent are here the three positions of the Δ^*-resonances around 1900 MeV ($\Delta_{1/2^-}(1900)$, $\Delta_{3/2^-}(1940)$ and $\Delta_{5/2^-}(1930)$) and the Roper-like $\Delta_{3/2^+}(1600)$-resonance in the Δ-spectrum as well as that of the Roper $N_{1/2^+}(1440)$-resonance and of the $N_{1/2^-}(1535)$-resonance in the nucleon-spectrum. Overall, model $\mathcal{A}$ accounts better for the light-flavoured baryon spectra than model $\mathcal{B}$ as already concluded by Löring *et al.* [5–7]. Accordingly, Merten, Kretzschmar and Haupt *et al.* [9, 10, 12–14] used model $\mathcal{A}$ for the calculation of electroweak form factors, helicity amplitudes, photon decay amplitudes, magnetic moments and charge radii as discussed in subsection 3.6. For these the results, obtained with an increased numerical accuracy, are discussed in the next chapter 4.

Chapter 4

Alternative interaction kernels in the Bethe-Salpeter model

4.1 Introduction

As mentioned in the previous chapter, the Bethe-Baryon model does not account for all resonances within the light-flavoured baryon spectra. There are still missing some resonances within the Δ-baryon sector, which cannot be reproduced by using a linear confinement potential. Furthermore, the well known Roper-like resonances are not predicted very accurately by using an instanton-induced 't Hooft force for the $\Delta - N$ mass-splitting. This suggests the issue if an additional interaction can solve these problems. There exists many options to introduce new interactions between quarks inside a baryon in the framework of the Bethe-Salpeter model. In this chapter two possibilities will be discussed. The first one is based on the introduction of a new spin-flavour dependent interaction motivated by pseudoscalar meson exchange, which indeed will be found to rectify some of the problems in the baryon spectra mentioned before in section 3.5 in the previous chapter. The second candidate will be a phenomenological modified version of the confinement potential, which includes spin-spin and tensor interactions. This leads to additional spin-spin and tensor contributions in the Dirac-structure of the confinement potential. Finally, both interactions will be combined, which leads to an additional model. The discussion will start with the novel spin-flavour dependent interaction, which can be found in Ronniger *et al.* [31, 32].

4.2 The spin-flavour dependent interaction

Assuming, that a part of the effective interaction between quarks in a baryon is mediated by exchange of pseudoscalar mesons, *Ansatzes* for the two different types of couplings for the fermion-meson vertex can be studied: the pseudoscalar- or pseudovector coupling. Here, we shall analyse both possibilities. The coupling of spin-$\frac{1}{2}$ fermions to a pseudoscalar mesonic nonet in the interaction Lagrange density is, in case of pseudoscalar coupling, given by

$$\mathcal{L}_I^{(\mathrm{ps})} = -\mathrm{i}\sum_{a=0}^{8} g_a\,\bar{\psi}\,\gamma^5\,\lambda^a\,\psi\,\phi^a\,, \tag{4.1}$$

while with pseudovector coupling it is given by

$$\mathcal{L}_I^{(\mathrm{pv})} = -\sum_{a=0}^{8} \frac{g_a}{2m}\,\bar{\psi}\,\gamma^5\,\gamma^\mu\,\lambda^a\,\psi\,\partial_\mu\phi^a\,. \tag{4.2}$$

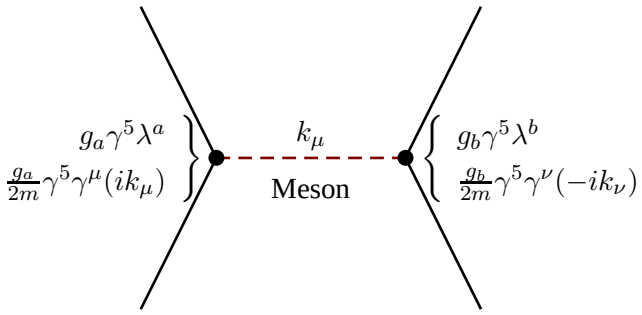

Fig. 4.1: One-meson-exchange between two quarks. The vertices are labelled with the corresponding couplings, where the upper line shows the pseudoscalar- and the lower line the pseudovector coupling.

Here, ψ represents a quark fields with mass m, ϕ^a the pseudoscalar meson fields with mass μ_a, while the flavour index runs over $a = \pi^{\pm,0}, \eta_8^0, \eta_1^0, K^{\pm}, K^0, \bar{K}^0$. The flavour dependence is represented by the usual Gell-Mann matrices $\lambda^a, a = 1, \ldots, 8$ and λ^0 is proportional to the identity operator in flavour space normalised to $\mathrm{Tr}(\lambda^0\lambda^0) = 2$. For details on the corresponding interaction Hamiltonians to Eqs. (4.1) and (4.2), we refer to appendix A and Caia *et al.* [60].

We extract the mesonic potential within second-order from the scattering-matrix element corresponding to the diagram of Fig. 4.1. As shown in appendix A the corresponding instantaneous potentials in momentum space are given for pseudoscalar coupling by

$$V^{(2)}_{(ps)}(\mathbf{k}) = \sum_a g_a^2 \left[\lambda^a \otimes \lambda^a\right] \frac{1}{|\mathbf{k}|^2 + \mu_a^2} \left[\gamma^5 \otimes \gamma^5\right] \tag{4.3}$$

and for pseudovector coupling as

$$\begin{aligned} V^{(2)}_{(pv)}(\mathbf{k}) &= \sum_a \frac{g_a^2}{4m^2} \left[\lambda^a \otimes \lambda^a\right] \left[\frac{-1}{|\mathbf{k}|^2 + \mu_a^2} \left[(\gamma^5 \boldsymbol{\gamma} \cdot \mathbf{k}) \otimes (\gamma^5 \boldsymbol{\gamma} \cdot \mathbf{k}) \right] - \frac{1}{2} \left[\gamma^5\gamma^0 \otimes \gamma^5\gamma^0\right] \right] \\ &= \sum_a \frac{g_a^2}{4m^2} \left[\lambda^a \otimes \lambda^a\right] \left[\frac{-|\mathbf{k}|^2}{|\mathbf{k}|^2 + \mu_a^2} \left[(\gamma^5 \boldsymbol{\gamma} \cdot \widehat{\mathbf{k}}) \otimes (\gamma^5 \boldsymbol{\gamma} \cdot \widehat{\mathbf{k}}) \right] - \frac{1}{2} \left[\gamma^5\gamma^0 \otimes \gamma^5\gamma^0\right] \right] \\ &= \sum_a \frac{g_a^2}{4m^2} \left[\lambda^a \otimes \lambda^a\right] \Bigg[-\frac{1}{3} \frac{|\mathbf{k}|^2}{|\mathbf{k}|^2 + \mu_a^2} \left[(\gamma^5 \boldsymbol{\gamma} \cdot \otimes \gamma^5 \boldsymbol{\gamma}) \right] - \frac{1}{2} \left[\gamma^5\gamma^0 \otimes \gamma^5\gamma^0\right] \\ &\quad + \frac{1}{3} \frac{|\mathbf{k}|^2}{|\mathbf{k}|^2 + \mu_a^2} \left[(\gamma^5 \boldsymbol{\gamma} \cdot \otimes \gamma^5 \boldsymbol{\gamma}) - 3 (\gamma^5 \boldsymbol{\gamma} \cdot \widehat{\mathbf{k}}) \otimes (\gamma^5 \boldsymbol{\gamma} \cdot \widehat{\mathbf{k}}) \right] \Bigg], \end{aligned} \tag{4.4}$$

respectively, where $\widehat{\mathbf{k}} := \frac{\mathbf{k}}{|\mathbf{k}|}$ is the direction of the momentum transfer $\mathbf{k}$ and the first term in the second line of Eq. (4.4) is the tensor interaction. The last step in Eq. (4.4) decomposes the tensor-like Dirac-structure of the pseudovector coupled potential into tensors of rank $r = 0$ and 2. Furthermore, there appear two contact terms (in coordinate space) in Eq. (4.4), coming from the constant part of the propagator

$$\frac{|\mathbf{k}|^2}{|\mathbf{k}|^2 + \mu_a^2} = 1 - \frac{\mu_a^2}{|\mathbf{k}|^2 + \mu_a^2} \tag{4.5}$$

and from the constant term with Dirac-structure $[\gamma^5\gamma^0 \otimes \gamma^5\gamma^0]$. Here, for further details we refer to Lêvy and Brueckner *et al.* [61, 62]

As it stands, the expression for the potential in the instantaneous approximation for pseudoscalar coupling leads, after Fourier transformation, to a local Yukawa potential in coordinate space with the usual range determined by the mass of the exchanged pseudoscalar meson. For pseudovector coupling the non-relativistic approximation to the Fourier transform leads to the usual spin-spin contact interaction together with the usual tensor force. In the simplest form adopted by the Graz group [22–24, 26–30] the latter was ignored, in addition the contact term was regularised by a Gaussian function and the Yukawa terms were regularised to avoid singularities at the origin. Also Eq. (4.3) can be rewritten in coordinate space

$$V^{(2)}_{(ps)}(\mathbf{x}) = \sum_a \frac{g_a^2}{4\pi} \left[\lambda^a \otimes \lambda^a\right] \frac{\exp(-\mu_a r)}{r} \left[\gamma^5 \otimes \gamma^5\right], \tag{4.6}$$

with $r := |\mathbf{x}|$, which describes a regular Yukawa potential. In view of these necessary approximations, we decided to parametrise the new spin-flavour dependent interaction purely phenomenologically as a local potential in coordinate space based on the pseudoscalar coupled meson-exchange as pointed out in the appendix A.1. In its simple form it is given by

$$V^{(2)}(\mathbf{x}) = \sum_a g_a^2 \left[\lambda^a \otimes \lambda^a\right] v_{\lambda_a}(\mathbf{x}) \left[\gamma^5 \otimes \gamma^5\right], \tag{4.7}$$

where $v_\lambda(\mathbf{x})$ is of the same Gaussian form as given in Eq. (3.5). Other Dirac-structures, such as $\left[\gamma^5 \boldsymbol{\gamma} \cdot \widehat{\mathbf{x}} \otimes \gamma^5 \boldsymbol{\gamma} \cdot \widehat{\mathbf{x}}\right]$ were tried, but were found to be less effective.

4.2.1 Model parameters

With the new spin-flavour dependent interaction a new determination of the length scale in the harmonic oscillator basis was used to fulfil the requirement $\frac{\partial M_\beta}{\partial \beta} = 0$. Fig. 4.2 shows the length scale dependence of the $N_{1/2^+}$- and $\Delta_{3/2^+}$-baryons for the ground- and first excited state. A summary of the resulting minimising β-values for each sector is given in Tab. 4.1. Comparing the plots of model $\mathcal{C}$ with those of model $\mathcal{A}$ (see Tab. 3.2 for

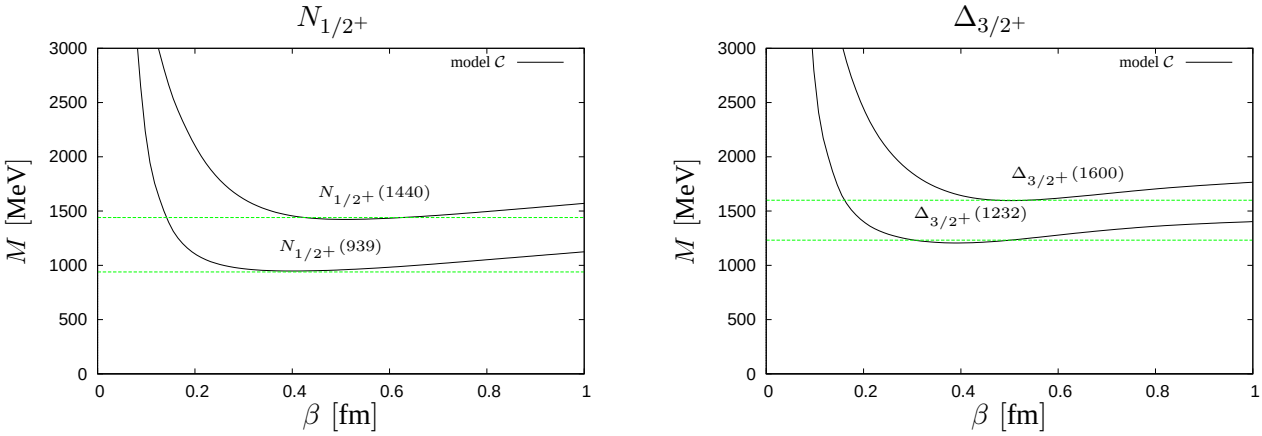

Fig. 4.2: Scale dependence of the ground- and first excited states in model $\mathcal{C}$. On the left side we have displayed the $N_{1/2}$-nucleon resonances and on the right side the $\Delta_{3/2}$-resonances. The optimal length scale β is chosen close to the average of the positions of the minima of the ground- and first-excited state. For $N_{1/2}$-states we choose $\beta = 0.45\,\text{fm}$ and for $\Delta_{3/2}$-states $\beta = 0.50\,\text{fm}$. All other baryon states have been investigated in the same way. Their resulting values for β are summarised in Tab. 4.1. The curves are calculated at $N_{\text{max}} = 20$ for the nucleon and $N_{\text{max}} = 18$ for the Δ-baryons.

comparison), it is obvious that the curves are different in particular for Δ-baryons. Thereby, the optimal β-value is chosen close to the average of the positions of the minima of the ground- and first excited state, which seems to be a good compromise, when insisting on the computation of the complete mass spectra for a given J with a single value of β.

Table 4.1: Optimal values of the length scale β for various baryons in model $\mathcal{C}$.

baryon	$2J+1$	β [fm]
Δ	2, 4	0.50
	6	0.55
	$\geq$8	0.60
N	2	0.45
	$\geq$4	0.50
Λ , Σ	$\geq$2	0.50
Ξ	$\geq$2	0.45
Ω	$\geq$2	0.40

The resulting baryon mass spectra were obtained by fitting the parameters of the model, *viz.* the offset a and slope b of the confinement potential, the constituent quark masses $m_n = m_u = m_d$ and m_s, the strengths of the instanton-induced force g_{nn} and g_{ns} as well as the strengths of the additional spin-flavour dependent interaction, given by $g_8 = g_a$, $a = 1, ..., 8$ and g_0 for flavour octet and flavour singlet exchange (thus assuming $SU_F(3)$ symmetry) to a selection of baryon resonances, see Tab. 4.2. The range λ given to the instanton-induced force was kept to the value used in [5, 6] and is roughly in accordance with typical instanton sizes. The optimal value for the range of the additional spin-flavour dependent interaction was found to be $\lambda_8 = \lambda_0 \approx 0.25\,\text{fm}$ and thus turned out to be of rather short range. A comparison of the parameters, obtained with the parameters of model $\mathcal{A}$ of [5,6], is given in Tab. 4.3 (see also Ronniger *et al.* [31,32] for calculations with higher numerical accuracy for model $\mathcal{A}$). In further studies, after the publication by Ronniger *et al.* [31], an improved description of the baryon spectra and their form factors was found, [32]. Here, in particular the scale parameters β were found be different from that one used in Ronniger *et al.* [31]: These new values are listed in Tab. 4.1. Accordingly, the parameters, as given in Tab. 4.3, are slightly different from the values from [31], which are listed in brackets. The parameters need some comments: In the original paper of Löring *et al.* [5, 6] the Dirac-structures (*i.e.* the spin dependence) of the confinement potential in model $\mathcal{A}$ were taken to be $\Gamma_0 = \frac{1}{4}(\mathbb{1}\otimes\mathbb{1}\otimes\mathbb{1} + \gamma^0\otimes\gamma^0\otimes\mathbb{1} + \text{cycl. perm.})$ and $\Gamma_s = \frac{1}{2}(-\mathbb{1}\otimes\mathbb{1}\otimes\mathbb{1} + \gamma^0\otimes\gamma^0\otimes\mathbb{1} + \text{cycl. perm.})$ for the

offset and slope, respectively, and were considered to be a three-body kernel. In the present model, including the additional octet and singlet flavour exchange potential, we obtained the best results with $\Gamma_0 = \mathbb{1} \otimes \mathbb{1} \otimes \mathbb{1}$ and $\Gamma_s = \gamma^0 \otimes \gamma^0$ and treating the interaction corresponding to the latter term as a two-body interaction. This

Table 4.2: List of baryon resonances of which the masses were used to determine the model parameters in a least-squares fit, where every resonance was attributed a weight reciprocal to its uncertainty in its position as given in [8]. Nominal masses are given in MeV.

Δ	N	Λ/Σ	Ξ	Ω
$S_{31}(1620)$	$S_{11}(1535)$	$S_{21}(1620)$	$S_{11}(1309)$	
$S_{31}(1900)$	$S_{11}(1650)$	$S_{21}(1750)$		
$P_{31}(1750)$	$P_{11}(939)$	$P_{01}(1116)$	$P_{13}(1530)$	$P_{01}(1672)$
$P_{31}(1910)$	$P_{11}(1440)$	$P_{21}(1289)$		
$P_{33}(1232)$		$P_{01}(1600)$		
$P_{33}(1600)$		$P_{21}(1660)$		
$P_{33}(1920)$				
$D_{33}(1700)$			$D_{13}(1820)$	
$D_{33}(1940)$				
$D_{35}(1930)$				
$F_{35}(1905)$				
$F_{35}(2000)$				
$F_{37}(1950)$				
$G_{37}(2200)$				
$G_{39}(2400)$				
$H_{39}(2300)$				
$H_{3\,11}(2420)$				
$K_{3\,15}(2950)$				

Table 4.3: Model parameters for the current model $\mathcal{C}$ [31,32] in comparison to those of model $\mathcal{A}$ of [5, 6]. Some of the parameters have been slightly changed with respect to the original values (listed in brackets) of [5, 6], since the calculation has been performed with higher numerical accuracy by taking more basis states in the diagonalisation of the Salpeter Hamiltonian into account, see also text. Note, that in comparison with Ronniger *et al.* [31] (values listed in brackets), a different set of parameters has been chosen, which improves the description of the baryon spectra and their form factors.

parameter		$\mathcal{C}$	$\mathcal{A}$
masses	m_n [MeV]	350.0 [325.0]	330.0
	m_s [MeV]	625.0 [600.0]	670.0
confinement	a [MeV]	-370.8 [-366.8]	-734.6 [-744.0]
	b [MeV/fm]	208.4 [212.8]	453.6 [440.0]
instanton-induced interaction	g_{nn} [MeVfm^3]	317.9 [341.5]	130.3 [136.0]
	g_{ns} [MeVfm^3]	260.0 [263.6]	81.8 [96.0]
	λ [fm]	0.4	0.4
octet exchange	$\frac{g_8^2}{4\pi}$ [MeVfm^3]	118.0 [100.9]	–
singlet exchange	$\frac{g_0^2}{4\pi}$ [MeVfm^3]	1715.5 [1897.4]	–
	$\lambda_8 = \lambda_0$ [fm]	0.25	–

of course impedes a direct comparison of the corresponding parameters. Furthermore, it was found that the strengths of the instanton-induced interaction are roughly tripled compared to the original values. Note, that the additional flavour exchange interaction has the same spin-flavour dependence as parts of the instanton interaction. The flavour singlet exchange could effectively also be considered as an other spin-dependent part of the confinement potential. Possibly this explains the extraordinary large coupling in this case. In summary, it thus must be conceded that the present treatment is phenomenological altogether and that here unfortunately the relation to more fundamental QCD parameters, such as instanton couplings and string tension is lost. Nevertheless, with only 10 parameters we consider the present treatment to be effective, especially in view of its merits in the improved description of some resonances to be discussed below.

4.2.2 Δ- and Ω-spectrum

In Fig. 4.3 we compare the results from the present calculation (model $\mathcal{C}$) (right side of each column) with experimental data from the Particle Data Group [8] (central in each column) and with the results from model

J^π	Mass	pos. $^4 10_J[56]$	$^2 10_J[70]$		J^π	Mass	pos. $^4 10_J[56]$	$^2 10_J[70]$	
		neg. $^4 10_J[56]$	$^2 10_J[70]$				neg. $^4 10_J[56]$	$^2 10_J[70]$	
$\frac{1}{2}^-$	1636	99.1	6.2	**92.8**	$\frac{3}{2}^-$	1959	98.7	**65.0**	33.8
		0.9	0.6	0.3			1.3	0.7	0.5
$\frac{1}{2}^-$	1956	98.6	17.8	**80.8**	$\frac{5}{2}^-$	2022	99.1	**90.1**	8.9
		1.4	0.9	0.5			0.9	0.5	0.4
$\frac{1}{2}^-$	2050	99.0	**79.3**	19.7	$\frac{5}{2}^-$	2132	99.3	14.5	**84.8**
		1.0	0.5	0.5			0.7	0.2	0.4
$\frac{3}{2}^-$	1600	98.5	9.1	**89.4**	$\frac{5}{2}^-$	2161	99.2	**88.8**	10.4
		1.5	0.7	0.7			0.8	0.3	0.5
$\frac{3}{2}^-$	1896	97.9	28.2	**69.7**					
		2.1	1.4	0.7					

Table 4.4: Multiplet decomposition of amplitudes of negative parity Δ-resonances. For each amplitude the contribution to the Salpeter norm, see [4] and Eq. (2.84) is given in $\%$, in each row the upper line and the lower line give the positive and negative energy contribution, respectively. States are labelled by the calculated mass and J^π denotes total angular momentum and parity, $^{2S+1}\mathcal{F}_J[D]$ label amplitudes with spin S, flavour representation with dimension $\mathcal{F}$, $SU(6)$ representation with dimension D. The dominant contribution is underlined.

$\mathcal{A}$ of [5] (left side in each column). The parameters used are listed in Tab. 4.3. The spectrum of the Δ- (see Fig. 4.3) and Ω- (see right panel of Fig. 4.7) resonances is determined by the confinement potential and the new spin-flavour exchange interaction only, since the instanton-induced 't Hooft interaction does not act on flavour symmetric states. Concerning the positive parity resonances we see that in the present calculation we can now indeed account for the low position of the $\Delta_{3/2^+}(1600)$-resonance. In addition the next excitations in this channel now lie closer to 2000 MeV in better agreement with experimental data, as is also the case for the splitting of the two $\Delta_{1/2^+}$-resonances. Note, however, that these states were included in the parameter fit. Additionally there is support for a parity doublet $\Delta_{3/2^+}(1920)$ and $\Delta_{3/2^-}(1940)$ as argued in [63].

Likewise, we can now account for the excited negative parity resonances: $\Delta_{1/2^-}(1900)$, $\Delta_{3/2^-}(1940)$ and $\Delta_{5/2^-}(1930)$ and even find two states in the $\Delta_{3/2^-}$-channel, which could correspond to the poorly established $\Delta_{3/2^-}(1940)$-state. In view of the near degeneracy of the $\Delta_{1/2^-}(1900)$, $\Delta_{3/2^-}(1940)$ and $\Delta_{5/2^-}(1930)$ states it is tempting to classify these in a non-relativistic scheme as a total spin $S = \frac{3}{2}$, total quark angular momentum $L = 1$ multiplet which, because of total isospin $I = \frac{3}{2}$ must then belong to a $(56, 1^-)$ multiplet, which is lowered with respect to the bulk of the other negative parity states that in an oscillator classification would be attributed to the $N = 3$ band. Obviously this is not supported by the calculations: As Tab. 4.4 shows, although the lowest $J^\pi = \frac{5}{2}^-$-resonance has a dominant component in this multiplet, the second excited $J^\pi = \frac{1}{2}^-, \frac{3}{2}^-$-resonances have dominant components in the $(70, 1^-)$ multiplet; indeed the third excited states in these channels can be attributed to the $(56, 1^-)$ multiplet. Otherwise the description and in particular the Δ-Regge-trajectory are of a similar quality as in the original model $\mathcal{A}$. In Tab. 4.5 we have summarised the calculation of Δ-resonances.

Concerning the Ω-spectrum, see Fig. 4.7 (right panel), apart from the appearance of an excited $\Omega_{3/2^+}$-state at 2014 MeV no spectacular changes in the predictions with respect to the original model $\mathcal{A}$ were found. Note, that the present model predicts, that this state is almost degenerated with the first negative parity states $\Omega_{1/2^-}$ at 2020 MeV and $\Omega_{3/2^-}$ at 1996 MeV.

4.2.3 N-spectrum

In Fig. 4.4 we present the results for the nucleon spectrum. As was the case for the Δ-spectrum, comparing to the results from the former model $\mathcal{A}$, we indeed obtain an improved description of the position of the first excited state with the same quantum numbers as the groundstate, the so-called Roper-resonance, while at the same time improving also on the position of the first excited negative parity resonances $J^\pi = \left(\frac{1}{2}^-\right)_1$, $\left(\frac{1}{2}^-\right)_2$, $\left(\frac{3}{2}^-\right)_1$, $\left(\frac{3}{2}^-\right)_2$ and $\left(\frac{5}{2}^-\right)_1$. With the exception of the $J^\pi = \frac{5}{2}^+$-state, which compared to model $\mathcal{A}$ is shifted

Table 4.5: Comparison of experimental [8] and calculated masses in MeV of Δ-resonances. The corresponding spectra are shown in Fig. 4.3 .

exp.	error	rating	model $\mathcal{C}$
$S_{31}(1620)$	1615-1675	****	1636
$S_{31}(1900)$	1850-1950	***	1956
$S_{31}(2150)$	2020-2250	*	2049/2121
$P_{31}(1750)$	1708-1780	*	1765
$P_{31}(1910)$	1870-1920	****	1892
$P_{33}(1232)$	1230-1234	****	1231
$P_{33}(1600)$	1550-1700	***	1596
$P_{33}(1920)$	1900-1970	***	1899/1932
$D_{33}(1700)$	1670-1770	****	1600
$D_{33}(1940)$	1840-2167	*	1895/1959
$D_{35}(1930)$	1920-1970	***	2022
$F_{35}(1905)$	1870-1920	****	1896
$F_{35}(2000)$	1720-2325	*	1955
$F_{37}(1950)$	1940-1960	****	1934
$F_{37}(2390)$	2250-2485	*	many res.
$G_{37}(2200)$	2120-2360	*	2123/2188
$G_{39}(2400)$	2100-2518	**	2220
$H_{39}(2300)$	2137-2550	**	2313
$H_{3,11}(2420)$	2300-2500	****	2363
$I_{3,13}(2750)$	2550-2874	**	2573
$K_{3,15}(2950)$	2750-3090	**	2712/2876

Table 4.6: Comparison of experimental [8] and calculated masses in MeV of N-resonances. The corresponding spectra are shown in Fig. 4.4.

exp.	error	rating	model $\mathcal{C}$
$S_{11}(1535)$	1520-1555	****	1475
$S_{11}(1650)$	1640-1680	****	1681
$S_{11}(1895)$	1880-1910	**	1839/1882
$P_{11}(939)$	939-939	****	950
$P_{11}(1440)$	1430-1470	****	1430
$P_{11}(1710)$	1680-1740	***	1712
$P_{11}(1880)$	1915-1845	**	1872
$P_{11}(2100)$	1855-2200	*	many res.
$P_{13}(1720)$	1650-1750	****	1690
$P_{13}(1900)$	1862-1900	**	1840
$P_{13}(2040)$	2031-2065	*	2029/2045
$D_{13}(1520)$	1515-1530	****	1520
$D_{13}(1700)$	1650-1750	***	1686
$D_{13}(1875)$	1855-1895	***	1849/1921
$D_{13}(2120)$	2080-2210	**	many res.
$D_{15}(1675)$	1670-1685	****	1678
$D_{15}(2060)$	2045-2075	***	1922/2017
$F_{15}(1680)$	1675-1690	****	1734
$F_{15}(1860)$	1820-1960	**	1933
$F_{15}(2000)$	1816-2175	**	1978/2062
$F_{17}(1990)$	1855-2155	**	1997
$G_{17}(2190)$	2100-2200	****	1980
$G_{19}(2250)$	2170-2310	****	2169
$H_{19}(2220)$	2180-2310	****	2159
$I_{1,11}(2600)$	2550-2750	***	2342
$K_{1,13}(2700)$	2567-3100	**	2510

upwards by approximately 50 MeV, the description of all known excited states is of a similar quality as that of model $\mathcal{A}$. In particular the position of the lowest $J^\pi = \frac{7}{2}^-$-resonance is still underestimated by more than 100 MeV.

In the following, we compare the predictions obtained in model $\mathcal{C}$ for nucleon resonances with $J \leq \frac{5}{2}$ and masses larger than 1.8 GeV with new results obtained in the Bonn-Gatchina analyses as reported in [15–17] and included in the new PDG [8], see also Tab. (4.6). The ratings of the new results are also from the PDG [8]: In particular in [8, 16, 17] a fourth $J^\pi = \frac{1}{2}^+$-state was found, called $N_{1/2^+}(1880)$ which could correspond

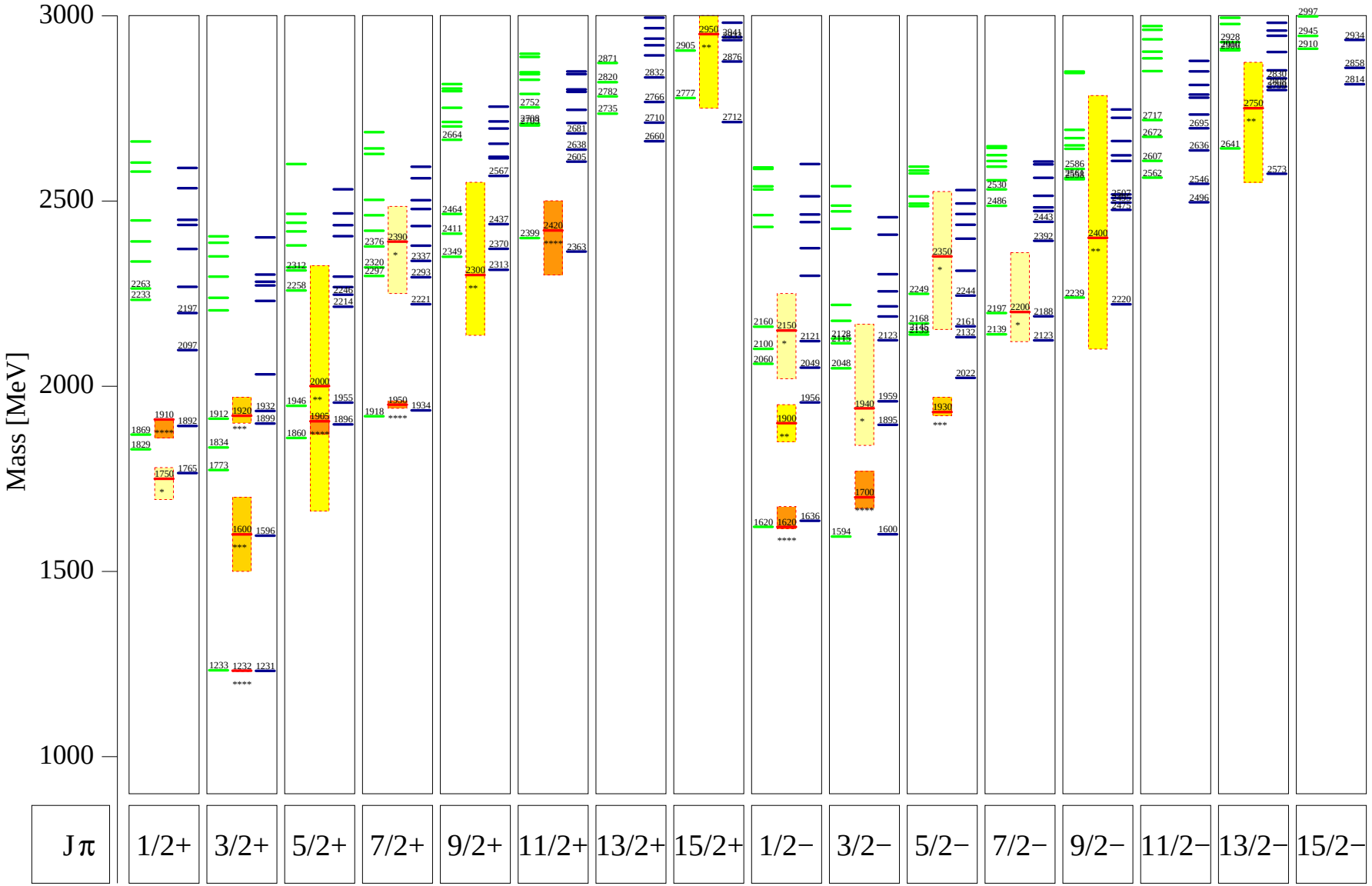

Fig. 4.3: Comparison of the Δ-Spectrum calculated within the present model $\mathcal{C}$ (right side of each column) with experimental data from the Particle Data Group [8] (central in each column) and with the results from model $\mathcal{A}$ of [5] (left side in each column), note the caption to Fig. 3.2; Lines indicate the resonance position (mass) with the mass uncertainty represented by a shaded box and the rating of [8] indicated by stars. The small numbers give the mass in MeV. J and π denote total angular momentum and parity, respectively.

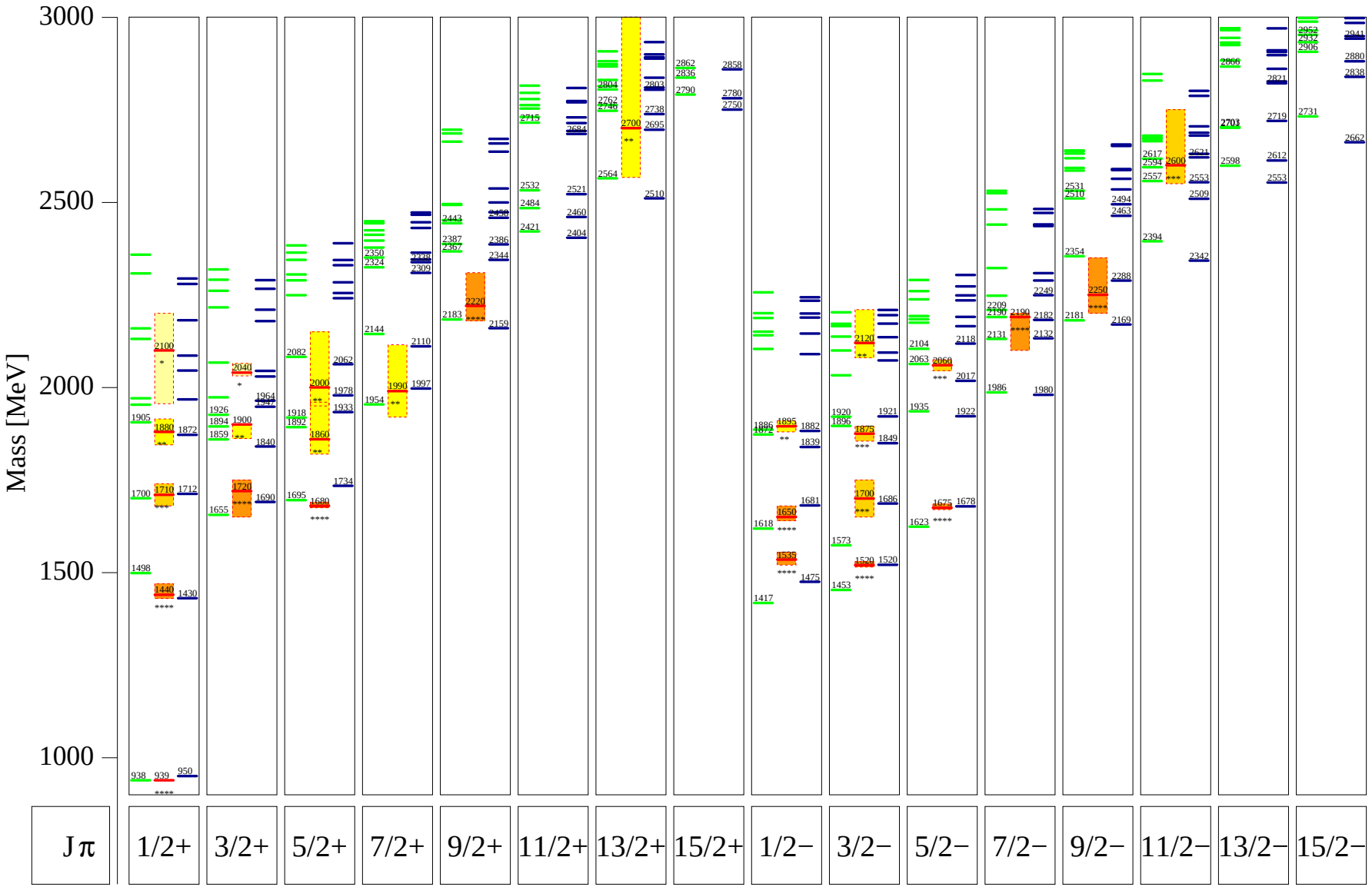

Fig. 4.4: Comparison of the N-Spectrum calculated within the present model $\mathcal{C}$ (right side of each column) with experimental data from the Particle Data Group [8] (central in each column) and with the results from model $\mathcal{A}$ of [5] (left side in each column). See also caption to Fig. 4.3.

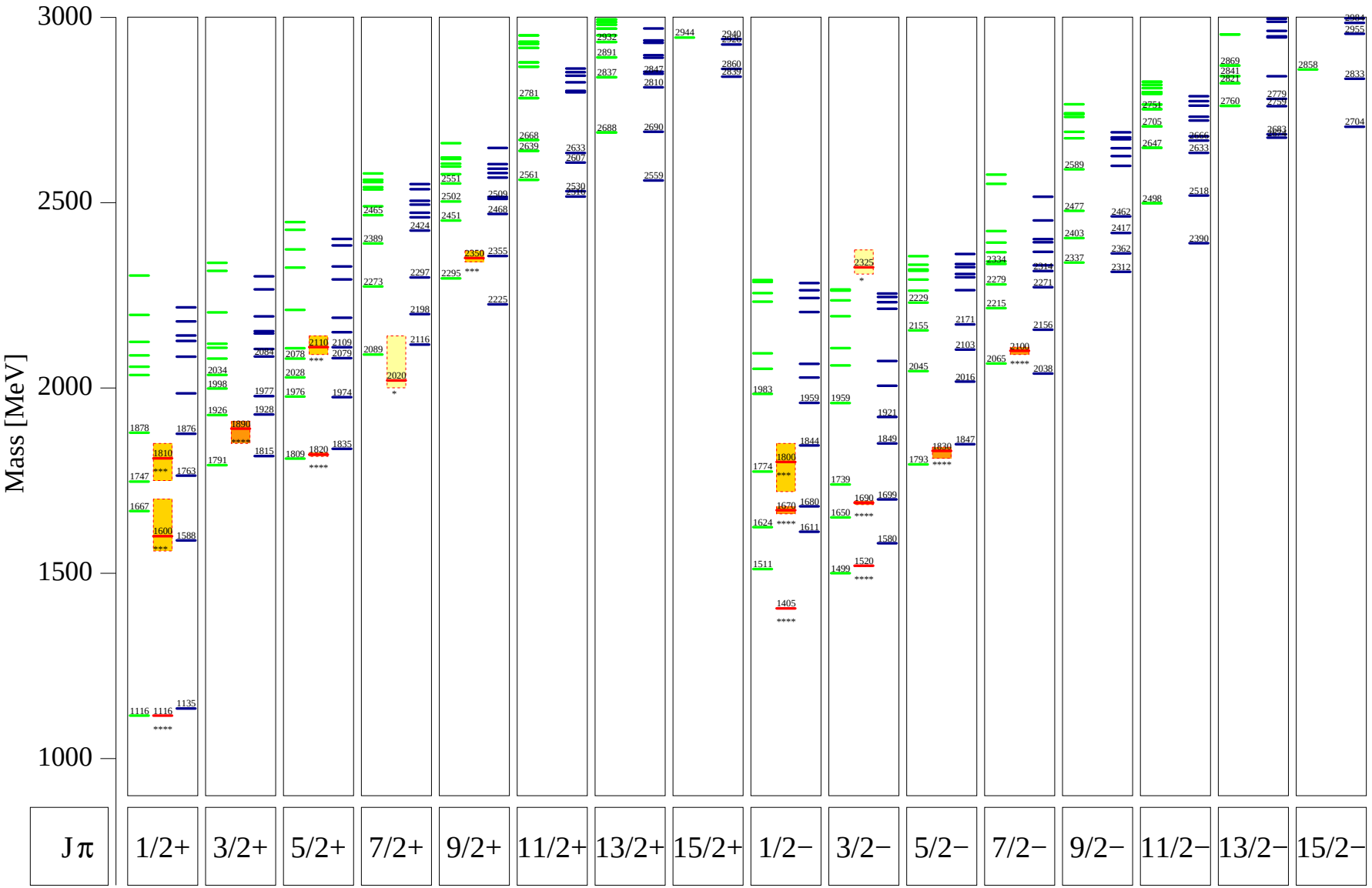

Fig. 4.5: Comparison of the Λ-Spectrum calculated within the present model $\mathcal{C}$ (right side of each column) with experimental data from the Particle Data Group [8] (central in each column) and with the results from model $\mathcal{A}$ of [5] (left side in each column), see also caption to Fig. 4.3.

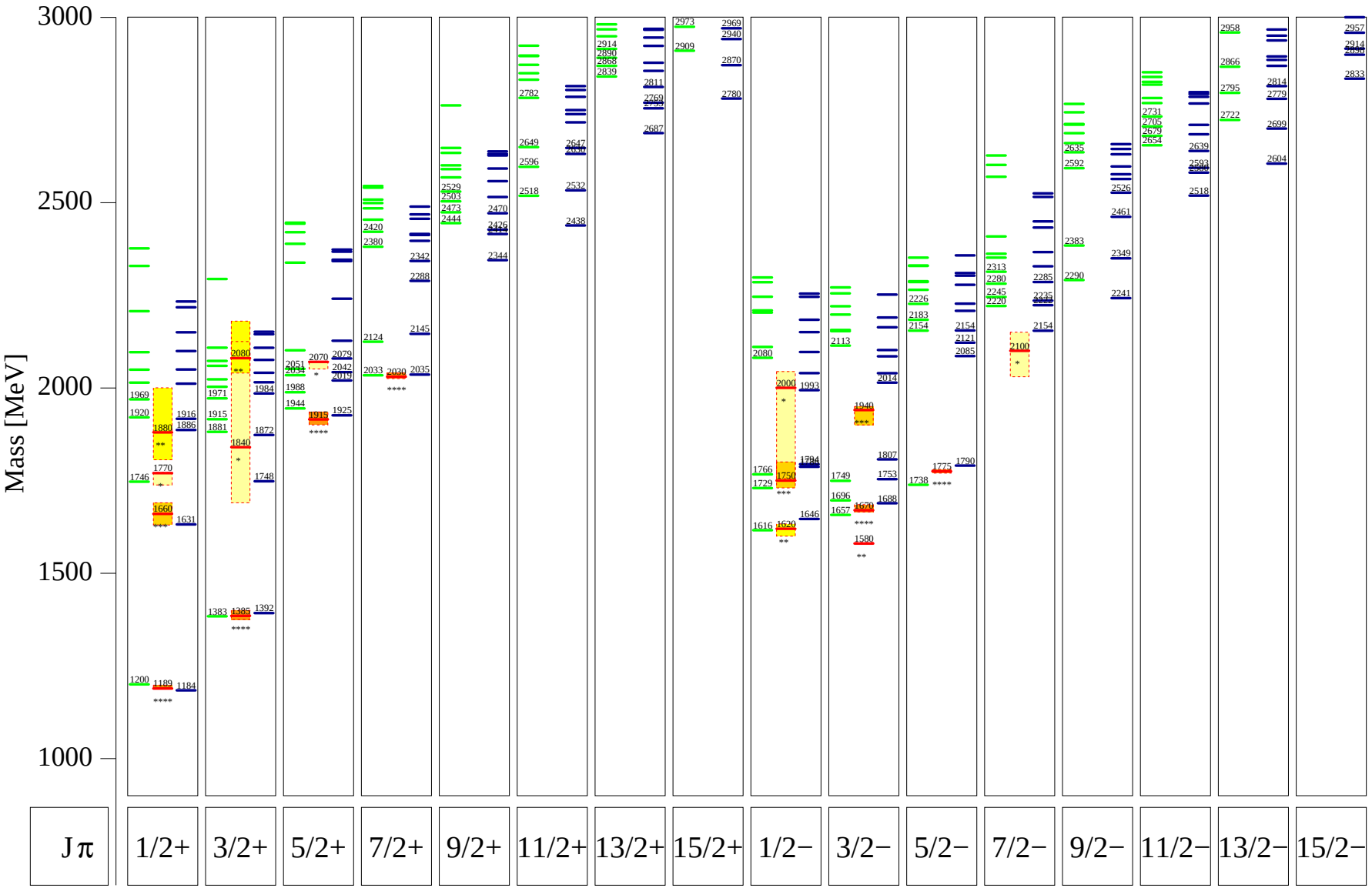

Fig. 4.6: Comparison of the Σ-Spectrum calculated within the present model $\mathcal{C}$ (right side of each column) with experimental data from the Particle Data Group [8] (central in each column) and with the results from model $\mathcal{A}$ of [5] (left side in each column), see also caption to Fig. 4.3.

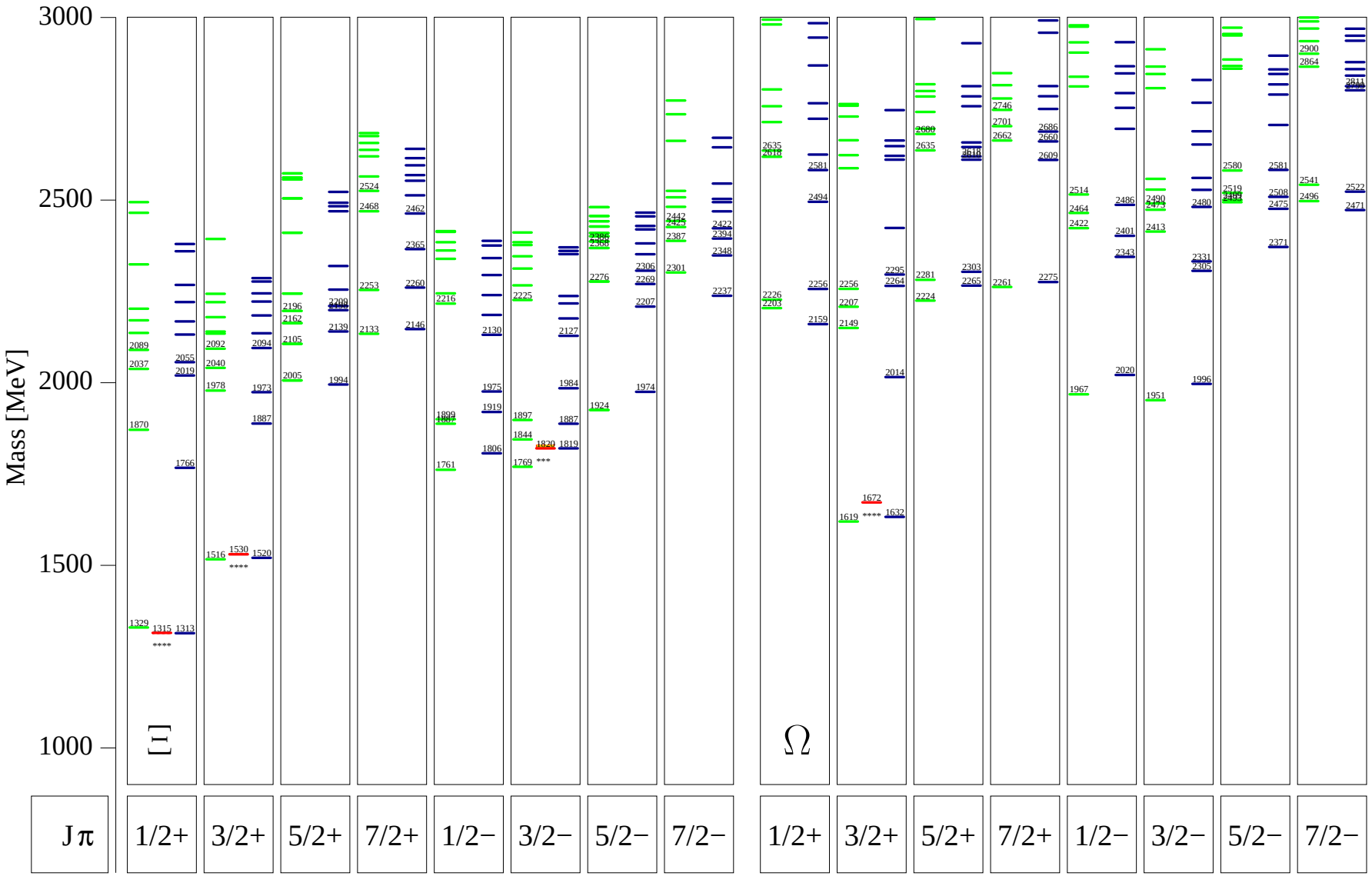

Fig. 4.7: Comparison of the Ξ-Spectrum (first eight columns) and the Ω-Spectrum (rightmost eight columns) calculated within the present model $\mathcal{C}$ (right side of each column) with the experimental data from the Particle Data Group [8] (central in each column) and with the results from model $\mathcal{A}$ of [5] (left side in each column), see also caption to Fig. 4.3.

to our calculated state at 1872 MeV. Furthermore the analysis in [15] contains two $J^\pi = \frac{3}{2}^+$-states, called $N(1900)P_{13}$ and $N_{3/2^+}(1975)$[1], which might be identified with the model $\mathcal{C}$ states calculated at 1840 MeV and 1947 MeV (or 1964 MeV), respectively. Concerning the negative parity states, in [8, 16, 17] a new $J^\pi = \frac{1}{2}^-$-state was found ($N_{1/2^-}(1895)$), which could be identified with the calculated state at 1839 MeV (or with that at 1882 MeV). In addition, two $J^\pi = \frac{3}{2}^-$ states were found: $N_{3/2^-}(1875)$ could correspond to the calculated states at 1849 MeV (or at 1921 MeV) and $N_{3/2^-}(2120)$ with one of the three states with calculated masses 2073 MeV, 2094 MeV and 2136 MeV. Furthermore a $J = \frac{5}{2}^+$-state has been found $N_{5/2^+}(1860)$ in [8, 17], which could correspond to predicted state at 1933 MeV. The new $N_{5/2^-}(2060)$-state reported in [8, 16, 17] is closest to the states calculated at 1922 MeV and at 2017 MeV. Finally, for $J^\pi = \frac{5}{2}^+$ the analysis is ambiguous: Although a solution with a single pole around 2.1 GeV is not excluded, solutions with 2 poles, either an ill-defined pole in the 1800-1950 MeV mass region and one at nearly 2.2 GeV or two close poles at approximately 2.0 GeV were found and could correspond to the model $\mathcal{C}$ states calculated at 1933 MeV and 1978 MeV. Note, that these new resonances were not included in the parameter fit (see Tab. 4.2). An overview of the identification of nucleon resonances is given in Tab. 4.6.

4.2.4 Hyperon-spectra

The resulting spectra for hyperon resonances, *viz.* the Λ-, Σ- and Ξ-states are depicted in Figs. 4.5, 4.6 and 4.7, respectively. Again we indeed find an improved description of the "Roper-like" resonances $\Lambda_{1/2^+}(1600)$ and $\Sigma_{3/2^+}(1660)$. Note, however, that both were used to determine the model parameters. Concerning the negative parity resonances, although we do find an acceptable description of the Λ-resonances with $J^\pi = \frac{3}{2}^-, \frac{5}{2}^-$ and $\frac{7}{2}^-$, also the new calculation cannot account for the low position of the $\Lambda_{1/2^-}(1405)$-resonance, which now is 200 MeV below the calculated position. In our opinion this underlines the conclusion, that this state cannot indeed be accounted for in terms of a q^3 excitation alone and that its position is determined by a strong coupling of a "bare" q^3-state to meson-baryon decay channels due to the proximity of the $\bar{K}N$-threshold, see also ref. [57–59] for a description of this state in a chiral unitary approach.

Concerning the Ξ-resonances, with respect to model $\mathcal{A}$ of [6] mainly the prediction for the excited state $\Xi_{1/2^+}$ at 1766 MeV is 100 MeV lower in model $\mathcal{C}$. To a lesser extend this also holds for the excited $\Xi_{3/2^+}$, which is now predicted at 1887 MeV. The PDG [8] lists many baryon resonances in the hyperon sector for which no quantum numbers are quoted. With the predictions of model $\mathcal{C}$ we are able to suggest a classification for some of these resonances based on their masses. It is plausible, that the $\Xi(1690)$ corresponds to the Roper-like excitation at 1766 MeV of the $J^\pi = \frac{1}{2}^+$ *e.g.* within the framework of model $\mathcal{C}$, mainly, because there is no other low lying resonance within the Ξ-spectrum of model $\mathcal{C}$, the $\Xi_{3/2^+}(1530)$-resonance being already assigned. Here, also the interpretation as a $J^\pi = \frac{1}{2}^-$ groundstate could be possible, which lies slightly above the Roper-like resonance at 1806 MeV. In addition to the $\Xi(1690)$-resonance, the PDG lists also a resonance $\Xi(1620)$, but with a low one-star rating, which could also be interpreted as the Roper-like excitation as mentioned above. Another candidate is the $\Omega(2250)$-resonance. In the Ω-spectrum model $\mathcal{C}$ predicts a clearly separated band of states. For positive parity this band lies around ≈ 2250 MeV and for negative parity at approximately ≈ 2330 MeV. Thus, believing in the predictions of model $\mathcal{C}$, the $\Omega(2250)$-resonance could have a positive parity.

4.2.5 Electroweak form factors of the nucleon

In Fig. 4.8 and 4.9 we display the electric proton and neutron elastic form factor, respectively, up to a momentum transfer of $Q^2 = 6.0\,\mathrm{GeV}^2$. The black solid curve is the result of the present model $\mathcal{C}$, the black dashed curve is the result obtained with the parameters of model $\mathcal{A}$, as in [9], albeit with a better numerical precision as mentioned in section 3.5 in the previous chapter.

Although the electric form factor of the proton, see Fig. 4.8, as calculated with model $\mathcal{A}$ in [9] fell too steeply in comparison to experimental data, with the present interaction we find a much improved shape, which yields a satisfactory description even up to momentum transfers of $6.0\,\mathrm{GeV}^2$. Indeed, in contrast

[1] The $N_{3/2^+}(1975)$-resonance is not shown in Fig. 4.4, displaying PDG-data [8] only.

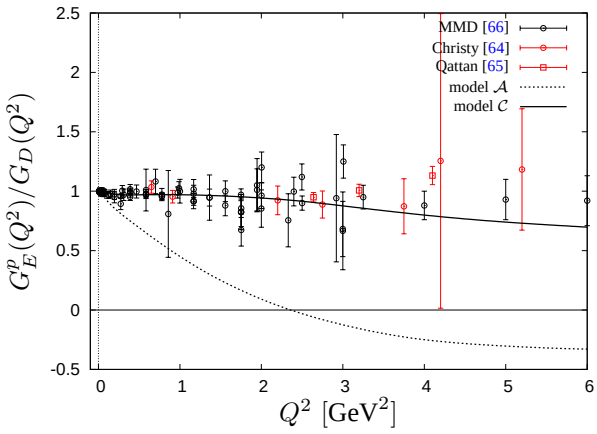

Fig. 4.8: The electric form factor of the proton divided by the dipole form $G_D(Q^2)$, Eq. (4.7). MMD-Data are taken from Mergell *et al.* [66], supplemented by data from Christy *et al.* [64] and Qattan *et al.* [65] . The solid black line represents the results from the present model $\mathcal{C}$; the dashed black line those from model $\mathcal{A}$ of [9], albeit recalculated with higher numerical precision. Red data points are taken from polarisation experiments and black ones are obtained by Rosenbluth separation.

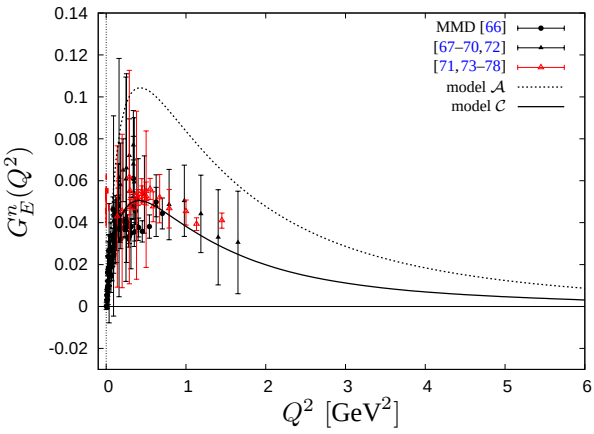

Fig. 4.9: The electric form factor of the neutron. MMD-Data are taken from the compilation of Mergell *et al.* [66]. The solid black line represents the results from the present model $\mathcal{C}$; the dashed black line in the result from model $\mathcal{A}$ of [9], albeit recalculated with higher numerical precision. Red data points are taken from polarisation experiments and black ones are obtained by Rosenbluth separation.

to model $\mathcal{A}$, which mainly failed with respect to the isovector part of the form factor, in the present model $\mathcal{C}$, this form factor shows an almost perfect dipole shape with the parametrisation

$$G_D(Q^2) = \frac{1}{(1+Q^2/M_V^2)^2}\,, \tag{4.8}$$

taken from [66, 79] with $M_V^2 = 0.71\,\mathrm{GeV}^2$.

The resulting electric neutron form factor, see Fig. 4.9, has a maximum at approximately the experimental value of $Q^2 \approx 0.4\,\mathrm{GeV}^2$ with an excellent description of the experimental data. The earlier calculation overestimated the data. However, the prediction of model $\mathcal{C}$ is very similar to the predictions of the Graz group [30] and [28] for the Goldstone-Boson exchange quark models. The corresponding charge radii are given in Tab. 4.7 and can be extracted via

$$\langle r^2\rangle := -\frac{6}{G(0)}\frac{\mathrm{d}G(Q^2)}{\mathrm{d}Q^2}\bigg|_{Q^2=0}, \tag{4.9a}$$

$$\langle r^2\rangle_E^n := -6\frac{\mathrm{d}G_E^n(Q^2)}{\mathrm{d}Q^2}\bigg|_{Q^2=0}, \tag{4.9b}$$

Table 4.7: Static properties of the nucleon. The values in parentheses are as reported in [9], the values on top of these are obtained within the same model $\mathcal{A}$, but with higher numerical accuracy. The static values are extrapolated from a dipole-shape-like fit.

	model $\mathcal{A}$	model $\mathcal{C}$	exp.	ref.
$\mu_p[\mu_N]$	2.76 [2.74]	2.62	2.793	[8]
$\mu_n[\mu_N]$	-1.71 [-1.70]	-1.63	-1.913	[8]
$\sqrt{\langle r^2\rangle_E^p}$[fm]	0.91 [0.82]	0.84	0.847	[66]
$\langle r^2\rangle_E^n$[fm]^2	-0.20 [-0.11]	-0.10	-0.123 $\pm$0.004	[66]
$\sqrt{\langle r^2\rangle_M^p}$[fm]	0.90 [0.91]	0.88	0.836	[66]
$\sqrt{\langle r^2\rangle_M^n}$[fm]	0.84 [0.86]	0.75	0.85	[66]
g_A	1.22 [1.21]	1.13	1.267 $\pm$0.0035	[8, 79]
$\sqrt{\langle r^2\rangle_A}$[fm]	0.68 [0.62]	0.65	0.67 $\pm$0.01	[80]

where the form factors were approximated with functions of the type

$$f(Q^2) = \frac{a}{(1+bQ^2)^c}\,, \tag{4.10a}$$

$$f_E^n(Q^2) = \frac{aQ^2}{(1+bQ^2)^c} + d\,, \tag{4.10b}$$

by fitting their parameters a, b, c, d to the calculated values in the vicinity of the photon point. As for the form factor the resulting squared charge radius of the neutron is calculated close to the experiment value. The r.m.s. proton radius is slightly smaller than the experimental value.

Table 4.8: Octet hyperon magnetic moments μ for model $\mathcal{A}$ and $\mathcal{C}$ calculated as in [13, 14]. The values are given in units of μ_N.

hyp.	model $\mathcal{A}$	model $\mathcal{C}$	PDG [8]
Λ	-0.606	-0.578	-0.613 $\pm$0.004
Σ^+	2.499	2.360	2.458 $\pm$0.010
Σ^0	0.743	0.712	-
Σ^-	-1.013	-0.937	-1.160 $\pm$0.025
Ξ^0	-1.325	-1.240	-1.250 $\pm$0.014
Ξ^-	-0.533	-0.532	-0.651$\pm$0.0025

Table 4.9: Decuplet hyperon magnetic moments μ for model $\mathcal{A}$ and $\mathcal{C}$ calculated as in [13, 14]. The values are given in units of μ_N.

hyp.	model $\mathcal{A}$	model $\mathcal{C}$	PDG [8]
Δ^{++}	7.906	6.846	3.7 to 7.5
Δ^+	3.953	3.423	$2.7^{+1.0}_{-1.3} \pm 1.5 \pm 3$
Δ^0	0.0	0.0	
Δ^-	-3.953	-3.423	
Σ^{*+}	4.830	2.431	
Σ^{*0}	0.702	0.215	
Σ^{*-}	-3.426	-1.981	
Ξ^{*0}	1.720	0.464	
Ξ^{*-}	-2.949	-1.823	
Ω^-	-1.698	-1.654	-2.02 ± 0.05

In Figs. 4.10 and 4.11 we display the magnetic proton- and neutron form factor up to a momentum transfer of $Q^2 = 6.0\,\mathrm{GeV}^2$, respectively. Again, the black solid curve is the result of the present model $\mathcal{C}$, the black dashed curve is the result obtained with the parameters of model $\mathcal{A}$, as in [9], albeit with a better numerical precision as mentioned in section 3.5 in the previous chapter.

Whereas in the original calculation (model $\mathcal{A}$ of [9]) the absolute value of these form factors dropped slightly too fast as a function of the momentum transfer, in the present calculation we now find a very good description even at the highest momentum transfers. Only at low momentum transfer the values are too small as is reflected by the rather small values for the various magnetic radii, see Tab. 4.7 and the too small values of the calculated magnetic moments. Note, however, that the ratio $\frac{\mu_p}{\mu_n} \approx 1.597$ for model $\mathcal{C}$ slightly changes (previously $\frac{\mu_p}{\mu_n} \approx 1.605$ for model $\mathcal{A}$) and is slightly larger than the experimental value $\frac{\mu_p}{\mu_n} \approx 1.46$; all values are remarkably close to the non-relativistic constituent quark model value $\frac{\mu_p}{\mu_n} = \frac{3}{2}$. The magnetic moments of flavour octet and decuplet baryons has been calculated according to the method outlined in [13, 14]. The results are compared to experimental values in Tab. 4.8 and 4.9, respectively. As a consequence of the better description of the momentum transfer dependencies in the individual form factors, we now also find an improved description of the momentum transfer dependence of the form factor ratio $\frac{\mu_p G_E^p}{G_M^p}(Q^2)$, which has been the focus on the discussion whether two-photon amplitudes are relevant for the discrepancy [84] found between recent measurements based on polarisation data (red data points of Fig. 4.12) [85–87, 89–95] versus the traditional Rosenbluth separation (black data points of Fig. 4.12), see *e.g.* [96–100]. Whereas in the original model $\mathcal{A}$ this

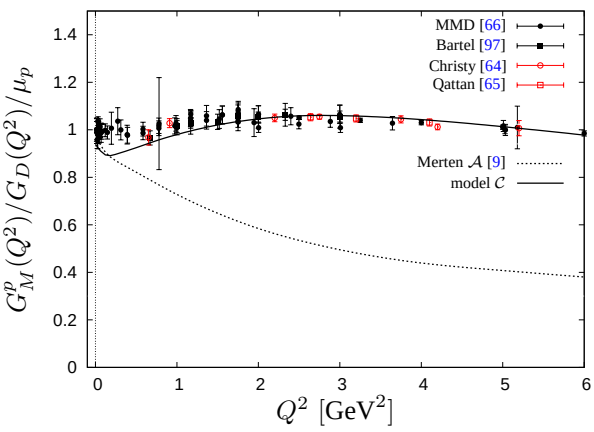

Fig. 4.10: The magnetic form factor of the proton divided by the dipole form $G_D(Q^2)$, Eq. (4.7) and the magnetic moment of the proton $\mu_p = 2.793\,\mu_N$. MMD-Data are taken from the compilation of Mergell *et al.* [66]. Additionally, polarisation experiments are marked in red. The black marked data points are obtained by Rosenbluth separation.

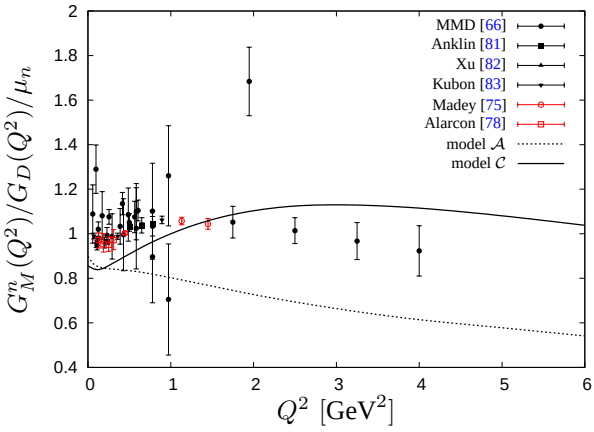

Fig. 4.11: The magnetic form factor of the neutron divided by the dipole form $G_D(Q^2)$, Eq. (4.7) and the magnetic moment of the neutron $\mu_n = -1.913\,\mu_N$. MMD-Data are taken from the compilation by Mergell *et al.* [66] and from more recent results from MAMI [81, 83]. Additionally, polarisation experiments are marked in red data points. The black marked ones are obtained by Rosenbluth separation.

ratio fell much too steep, we now find in model $\mathcal{C}$ a much better description of this quantity, see Fig. 4.12 for a comparison with various data. Up to $Q^2 \approx 3\,\text{GeV}^2$ we indeed find the observed linear dependence.

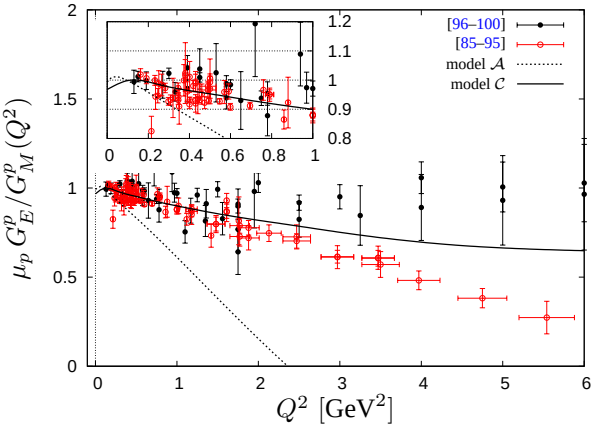

Fig. 4.12: The ratio $\frac{\mu_p\,G_E^p}{G_M^p}$ compared to recent JLAB data (see legend). In the insert the low momentum transfer region is enlarged. The solid black line is the result of model $\mathcal{C}$, the dashed black line the result in model $\mathcal{A}$. Red data points are taken from polarisation experiments and the black ones are obtained from Rosenbluth separation.

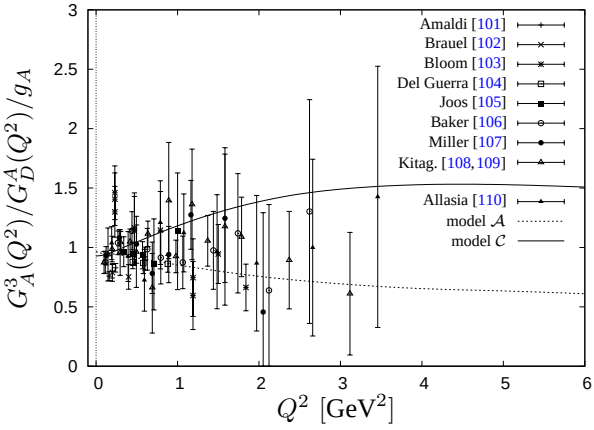

Fig. 4.13: The axial form factor of the nucleon divided by the axial dipole form in Eq. (4.11) and the axial coupling $g_A = 1.267$. The black solid line is the result of model $\mathcal{C}$, the blue dashed line the result in model $\mathcal{A}$. Experimental data are taken from the compilation by Bernard *et al.* [80].

Finally, the axial form factor, see Fig. 4.13, was already very well described in model $\mathcal{A}$ of [9]. Although falling slightly less steeply, the present calculation still gives a very satisfactory description of the data also at higher momentum transfers in the same manner as in Glozman and Wagenbrunn *et al.* [111–113] also the value of the axial coupling constant is too small, but of course much better than the non-relativistic constituent quark

model result $g_A = \frac{5}{3}$. The axial form factor, presented in Fig. 4.13, is divided by the axial dipole form

$$G_D^A(Q^2) = \frac{g_A}{(1 + Q^2/M_A^2)^2}\,, \tag{4.11}$$

with the parameters $M_A = 1.014 \pm 0.014\,\text{GeV}$ and $g_A = 1.267$ taken from Bodek *et al.* [79].

In summary we find, that the new model $\mathcal{C}$, apart from some improvements in the description of the excitation spectra at the expense of additional parameters of a phenomenologically introduced spin-flavour dependent interaction does allow for a parameter-free description of electromagnetic groundstate properties of a similar overall quality as has been obtained before, with some distinctive improvements on the momentum transfer dependence of various form factors.

4.2.6 Helicity amplitudes

In the last decade new experiments were performed at the Jefferson-Laboratory in order to study helicity amplitudes up to $6.0\,\text{GeV}^2$. These new experiments were designed to determine the helicity amplitudes for the electro-excitation of the $P_{11}(1440)$-, $S_{11}(1535)$- and $D_{13}(1520)$-resonances. The results can be found in Aznauryan *et al.* [18–20] and the MAID-analysis [114, 125]. In addition novel data for the longitudinal $S_{1/2}^N$-amplitudes were obtained.

We calculated the corresponding helicity amplitudes of these and other states on the basis of the Salpeter amplitudes obtained in the novel model $\mathcal{C}$ [31, 32]. As mentioned in section 3.6, the eigenvalue problem is solved with higher numerical accuracy by an expansion into a larger basis, which presently includes all three-particle harmonic oscillator states up to an excitation quantum number $N_{\text{max}} = 18$, whereas previously [5, 6, 9] the results for baryon masses and amplitudes in model $\mathcal{A}$ were obtained with $N_{\text{max}} = 12$. For comparison and to study the effects of the newly introduced phenomenological spin-flavour dependent interaction of model $\mathcal{C}$ we thus also recalculated the spectrum and the amplitudes for model $\mathcal{A}$ within the same larger model space.

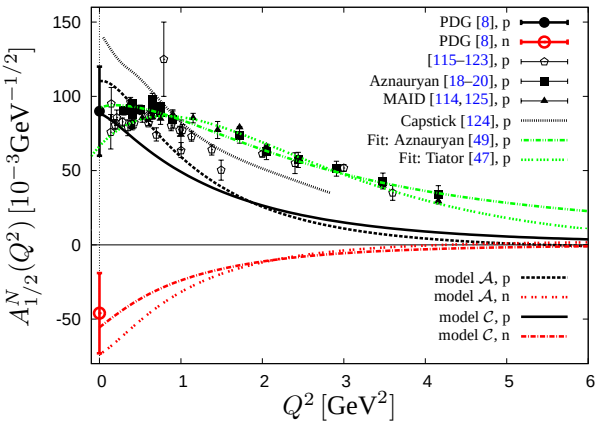

Fig. 4.14: Comparison of the $S_{11}(1535)$ transverse helicity amplitude $A_{1/2}^N$ for the proton and the neutron calculated in the model $\mathcal{C}$ (solid and dashed-dotted line) and model $\mathcal{A}$ (dashed lines) to experimental data [8, 18–20, 114–123, 125]. The dotted line is the result obtained by Keister and Capstick [124]. Additionally recent fits obtained by Tiator *et al.* [47] and by Aznauryan *et al.* [49] are displayed as green dotted and dashed-dotted lines, respectively. Note, that the results for model $\mathcal{A}$ were recalculated with higher numerical accuracy and thus deviate from the results published previously in [9].

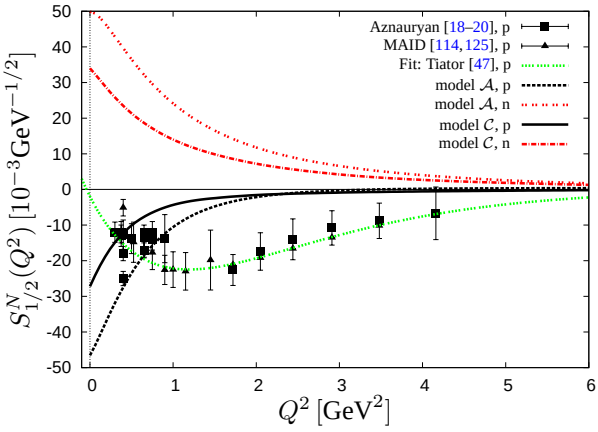

Fig. 4.15: Comparison of the $S_{11}(1535)$ longitudinal helicity amplitude $S_{1/2}^N$ of proton and neutron calculated in model $\mathcal{C}$ (solid and dashed-dotted line) and model $\mathcal{A}$ (dashed lines) with experimental data [18–20, 114, 125]. Note, that for the data points of the MAID-analysis by Tiator *et al.* [125] no errors are quoted. See also caption to Fig. 4.14.

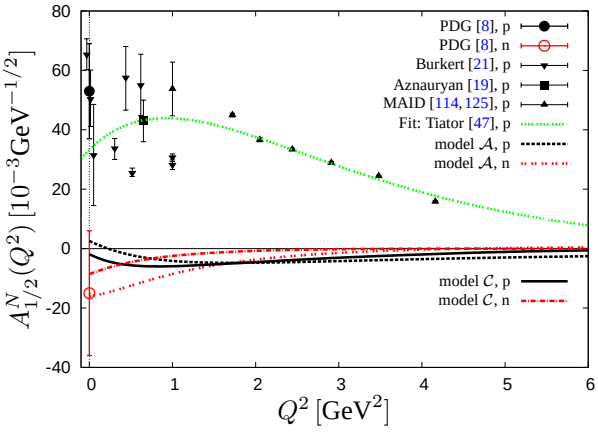

Fig. 4.16: Comparison of the $S_{11}(1650)$ transverse helicity amplitude $A^N_{1/2}$ of proton and neutron calculated in model $\mathcal{C}$ (solid and dashed-dotted line) and model $\mathcal{A}$ (dashed lines) to experimental data from [8, 19, 21, 114, 125]. See also caption to Fig. 4.14.

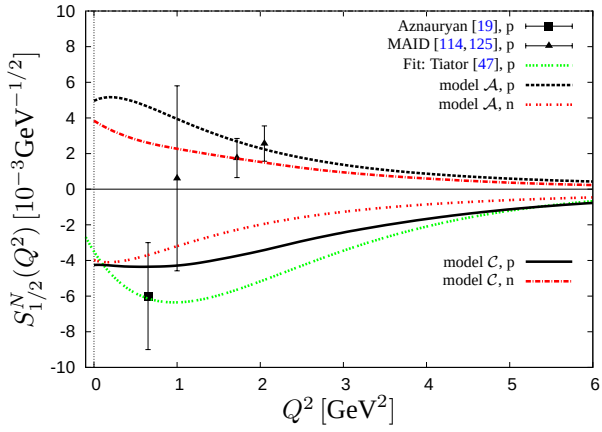

Fig. 4.17: Comparison of the $S_{11}(1650)$ longitudinal helicity amplitude $S^N_{1/2}$ of proton and neutron calculated in model $\mathcal{C}$ (solid and dashed-dotted line) and model $\mathcal{A}$ (dashed lines). See also caption to Fig. 4.14.

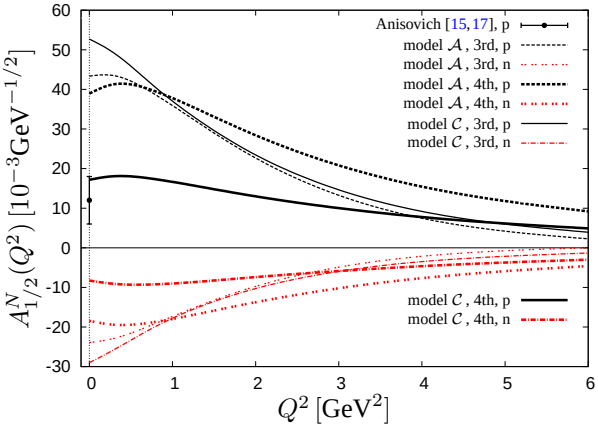

Fig. 4.18: Comparison of the $S_{11}(1895)$ transverse helicity amplitude $A^N_{1/2}$ for proton and neutron calculated in model $\mathcal{C}$ (solid and dashed-dotted line) and model $\mathcal{A}$ (dashed lines) with the single photon point value from Anisovich *et al.* [15]. See also caption to Fig. 4.14.

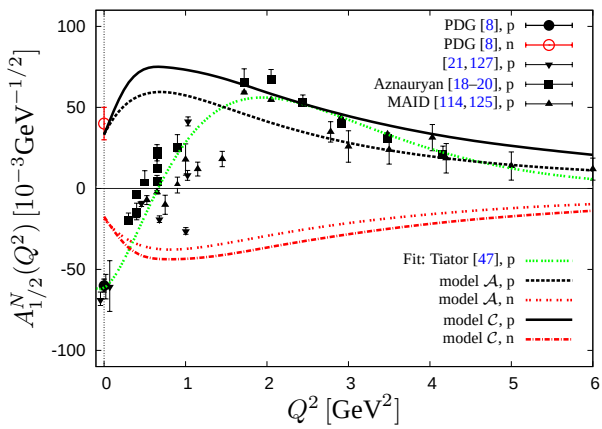

Fig. 4.19: Comparison of the $P_{11}(1440)$ transverse helicity amplitude $A^N_{1/2}$ for proton and neutron calculated in model $\mathcal{C}$ (solid and dashed-dotted line) and model $\mathcal{A}$ (dashed lines). See also caption to Fig. 4.14 .

Helicity amplitudes for nucleons

We now turn to the discussion of $N^* \leftrightarrow N$ helicity amplitudes for each angular momentum J and parity π.

The J $= \frac{1}{2}$ resonances: A comparison of calculated transverse and longitudinal helicity amplitudes with experimental data for the electro-excitation of the $S_{11}(1535)$-resonance is given in Figs. 4.14 and 4.15, respectively. Whereas the value of the transverse amplitudes at the photon point ($Q^2 = 0$), both for the proton and the neutron, are accurately reproduced in particular by the new model $\mathcal{C}$, in general the calculated transverse amplitudes are too small by a factor of two; in comparison to the results from model $\mathcal{A}$ the amplitudes of model $\mathcal{C}$ decrease more slowly with increasing momentum transfer, in better agreement with the experimental data. But, in particular the near constancy of the proton data for $0 < Q^2 < 1$ GeV^2 is not reflected by any of the calculated results. For comparison we also plotted the results from the quark model calculation of the transverse $A^p_{1/2}$-amplitude by Keister and Capstick [124] for $Q^2 \lesssim 3\,\mathrm{GeV}^2$ and the fit obtained by Aznauryan *et al.* [49]

and Tiator *et al.* [47]. Contrary to this, the momentum transfer dependence of the calculated longitudinal helicity amplitudes hardly bear any resemblance to what has been determined experimentally, in particular the minimum found for the proton at $Q^2 \approx 1.5\,\mathrm{GeV}^2$ is not reproduced. Only the non-relativistic calculation of Capstick and Keister [126] shows a pronounced minimum for the longitudinal $S_{11}(1535)$-amplitude, however this minimum is predicted at the wrong position.

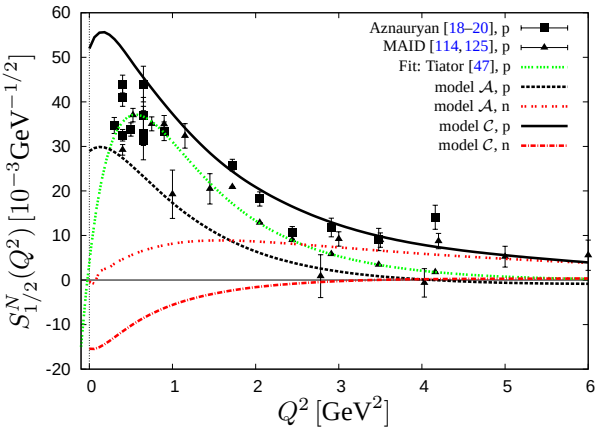

Fig. 4.20: Comparison of the $P_{11}(1440)$ longitudinal helicity amplitude $S^N_{1/2}$ for proton and neutron calculated in model $\mathcal{C}$ (solid and dashed-dotted line) and model $\mathcal{A}$ (dashed lines). Note, that for the data points of the MAID-analysis by Tiator *et al.* [125] no errors are quoted. See also caption to Fig. 4.14.

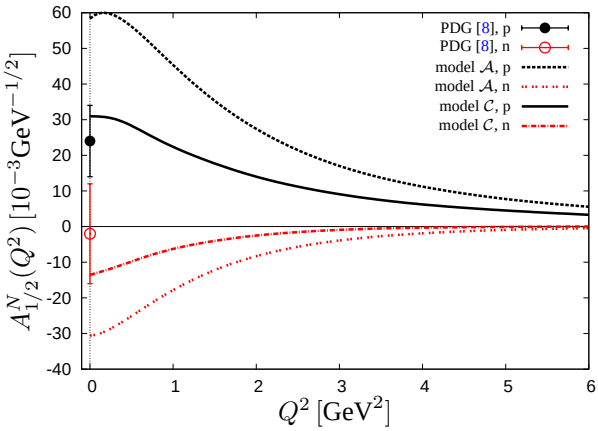

Fig. 4.21: Comparison of the $P_{11}(1710)$ transverse helicity amplitude $A^N_{1/2}$ for proton and neutron calculated in model $\mathcal{C}$ (solid and dashed-dotted line) and model $\mathcal{A}$ (dashed lines). See also caption to Fig. 4.14.

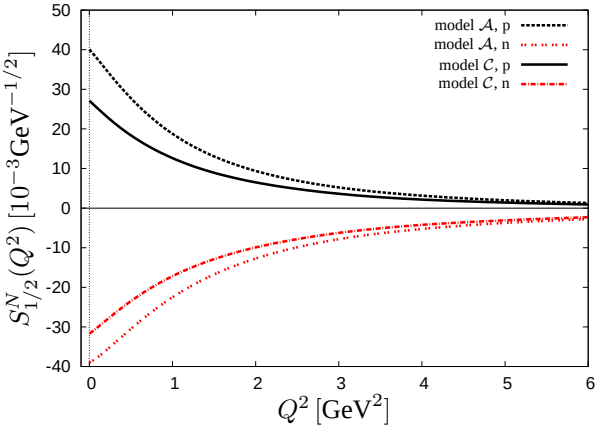

Fig. 4.22: Prediction of the $P_{11}(1710)$ longitudinal helicity amplitude $S^N_{1/2}$ for proton and neutron calculated in model $\mathcal{C}$ (solid and dashed-dotted line) and model $\mathcal{A}$ (dashed lines). See also caption to Fig. 4.14.

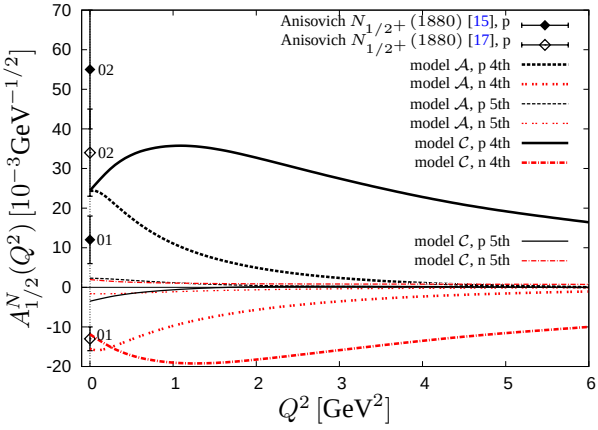

Fig. 4.23: Prediction of the P_{11} transverse helicity amplitudes $A^N_{1/2}$ for the third and fourth excitation of the proton and the neutron calculated within model $\mathcal{C}$ (solid and dashed-dotted line) and model $\mathcal{A}$ (dashed lines). The data at the photon point marked $''01''$ and $''02''$ were reported in [15, 17] as alternatives for the $N^+_{1/2}(1880)$-resonance. See also caption to Fig. 4.14.

Also the calculated transverse proton helicity amplitude $A^p_{1/2}$ for the next $S_{11}(1650)$-resonance shows a large disagreement with experimental data as shown in Fig. 4.16. This discrepancy was already found in the previous calculation of Merten *et al.* [9] and obviously is not resolved within model $\mathcal{C}$. Note, however, that the neutron amplitude $A^n_{1/2}$ calculated at the photon point does correspond to the data from PDG [8], as illustrated in Fig 4.16. The rather small longitudinal $S_{11}(1650)$-amplitude $S^N_{1/2}$ seems to agree with the scarce medium

Q^2-data from the MAID-analysis of [114, 125], however for lower Q^2 the single data point of Aznauryan *et al.* [19] seems to indicate a zero crossing of this amplitude not reproduced by either of the model calculations of the $S^p_{1/2}$-amplitude for the $S_{11}(1650)$-resonance (see Fig. 4.17).

The third and fourth $J^\pi = \frac{1}{2}^-$-nucleon resonances are predicted in model $\mathcal{A}$ at 1872 MeV and 1886 MeV and in model $\mathcal{C}$ at 1839 MeV and 1882 MeV, respectively. Indeed within the Bonn-Gatchina Analysis of the CB-ELSA collaboration data [15, 17] evidence for a $J^\pi = \frac{1}{2}^-$-nucleon resonance at 1895 MeV was found. As can be seen from Fig. 4.18 the predicted transverse amplitudes for the third resonance are rather large in both models and the calculated value at the photon point ($Q^2 = 0$) is much larger than the experimental value quoted in [15, 17], but the value of the fourth resonance matches the PDG photon decay amplitude.

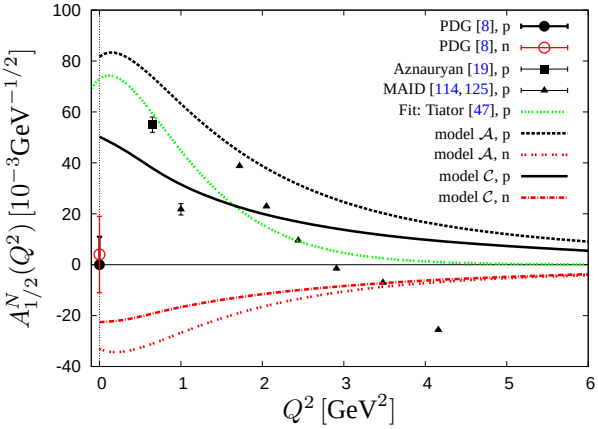

Fig. 4.24: Comparison of the $P_{13}(1720)$ transverse helicity amplitude $A^N_{1/2}$ of proton and neutron calculated in model $\mathcal{C}$ (solid and dashed-dotted line) and model $\mathcal{A}$ (dashed lines). Note, that for the data points of the MAID-analysis by Tiator *et al.* [125] no errors are quoted. See also caption to Fig. 4.14.

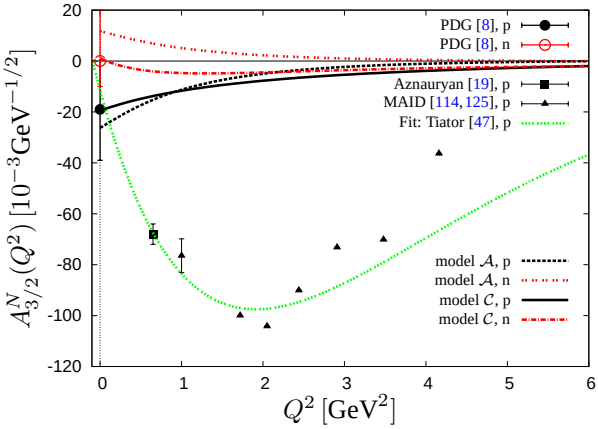

Fig. 4.25: Comparison of the $P_{13}(1720)$ transverse helicity amplitude $A^N_{3/2}$ of proton and neutron calculated in model $\mathcal{C}$ (solid and dashed-dotted line) and model $\mathcal{A}$ (dashed lines). Note, that for the data points of the MAID-analysis by Tiator *et al.* [125] no errors are quoted. See also caption to Fig. 4.14.

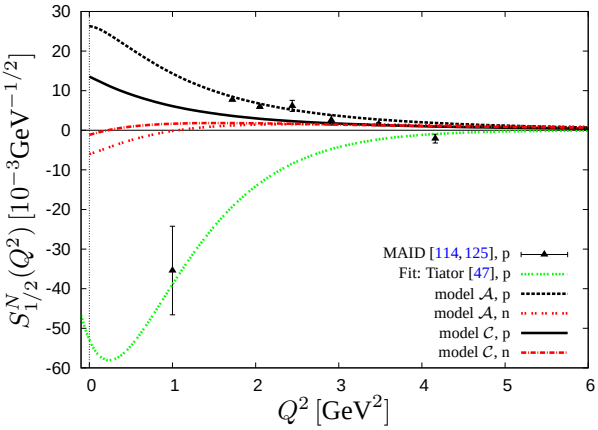

Fig. 4.26: Comparison of the $P_{13}(1720)$ longitudinal helicity amplitude $S^N_{1/2}$ of proton and neutron calculated in model $\mathcal{C}$ (solid and dashed-dotted line) and model $\mathcal{A}$ (dashed lines). Note, that for the data points of the MAID-analysis by Tiator *et al.* [125] no errors are quoted. See also caption to Fig. 4.14.

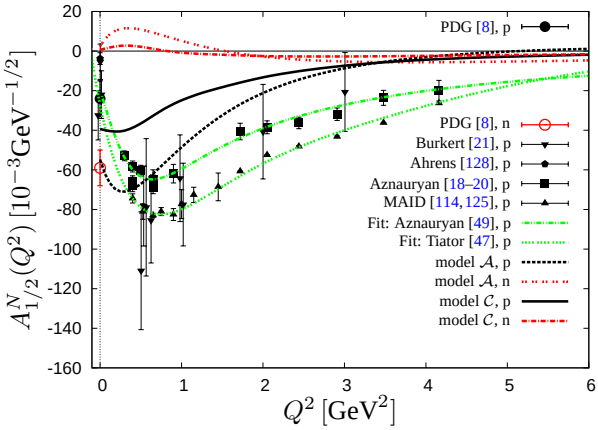

Fig. 4.27: Comparison of the $D_{13}(1520)$ transverse helicity amplitude $A^N_{1/2}$ of proton and neutron calculated in model $\mathcal{C}$ (solid and dashed-dotted line) and model $\mathcal{A}$ (dashed lines). See also caption to Fig. 4.14.

The transverse and longitudinal helicity amplitudes of the Roper-resonance $P_{11}(1440)$ are displayed in Figs. 4.19 and 4.20, respectively. It is obvious, that the zero crossing found in the data at $Q^2 \approx 0.5\,\mathrm{GeV}^2$, see Fig. 4.19, is not reproduced in the calculated curves, although the Q^2-dependence of the positive values at higher

momentum transfers can be accounted for in both models after changing the sign of the old prediction [9]. On the other hand we do find a satisfactory description of the longitudinal $S^p_{1/2}$-amplitude displayed in Fig. 4.20 in particular in the new model $\mathcal{C}$.

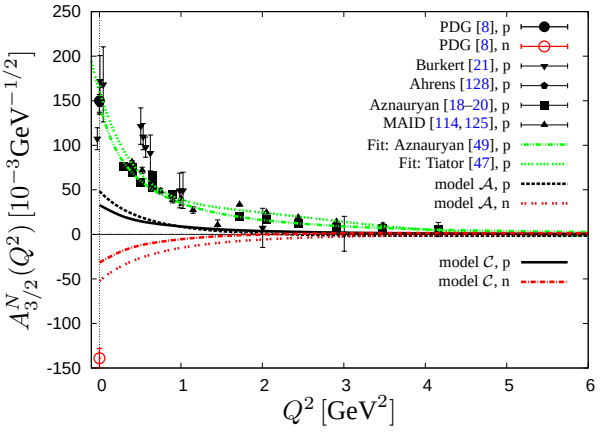

Fig. 4.28: Comparison of the $D_{13}(1520)$ transverse helicity amplitude $A^N_{3/2}$ for proton and neutron calculated in model $\mathcal{C}$ (solid and dashed-dotted line) and model $\mathcal{A}$ (dashed lines). See also caption to Fig. 4.14.

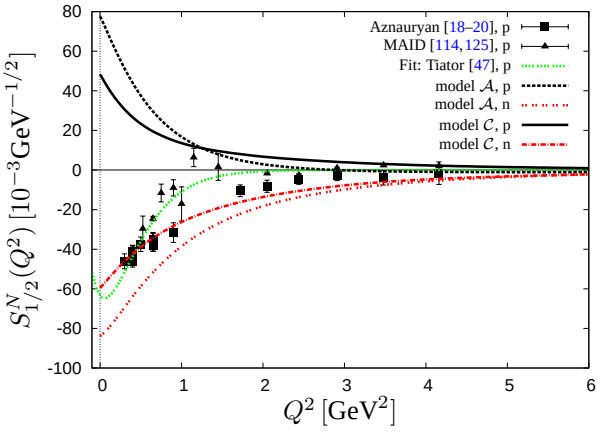

Fig. 4.29: Comparison of the $D_{13}(1520)$ longitudinal helicity amplitude $S^N_{1/2}$ for proton and neutron calculated in model $\mathcal{C}$ (solid and dashed-dotted line) and model $\mathcal{A}$ (dashed lines). See also caption to Fig. 4.14.

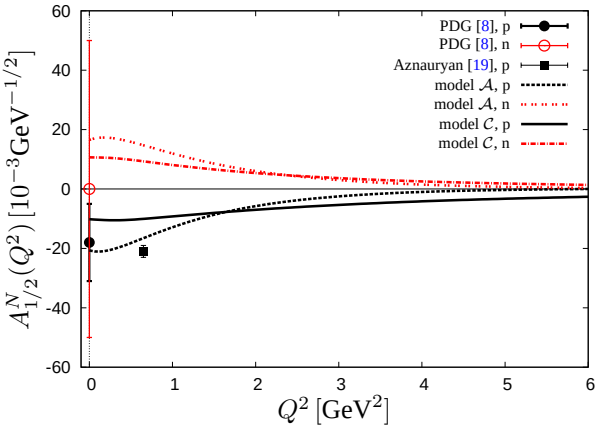

Fig. 4.30: Comparison of the $D_{13}(1700)$ transverse helicity amplitude $A^N_{1/2}$ for proton and neutron calculated in model $\mathcal{C}$ (solid and dashed-dotted line) and model $\mathcal{A}$ (dashed lines). See also caption to Fig. 4.14.

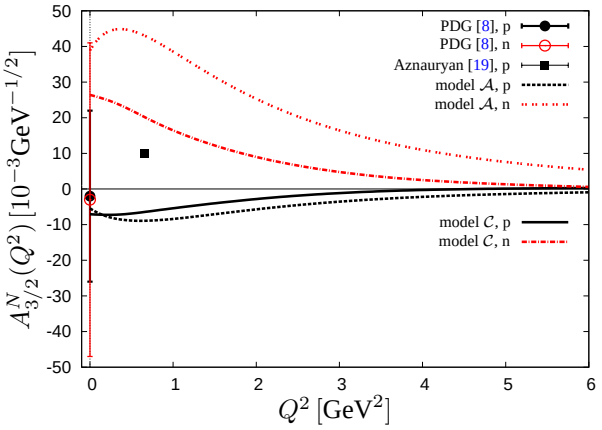

Fig. 4.31: Comparison of the $D_{13}(1700)$ transverse helicity amplitude $A^N_{3/2}$ for proton and neutron calculated in model $\mathcal{C}$ (solid and dashed-dotted line) and model $\mathcal{A}$ (dashed lines). See also caption to Fig. 4.14.

Helicity amplitudes of higher lying resonances in the P_{11}-channel are only poorly studied in experiments. Nevertheless, we shall discuss briefly the $P_{11}(1710)$-helicity amplitude before treating the higher excitations $P_{11}(1880)$ and $P_{11}(2100)$. For the $P_{11}(1710)$-resonance only the photon decay amplitude is reported [8]. In Figs. 4.21 and 4.22 we display our predictions for these amplitudes. The transverse $A^N_{1/2}$-amplitude of model $\mathcal{C}$ matches the PDG-data at the photon point in contrast to model $\mathcal{A}$, which overestimates the proton- and neutron amplitudes by a factor of two. On the other hand this would be in accordance with the larger value obtained by Anisovich *et al.* [17], $A^p_{1/2} = (52 \pm 15) \times 10^{-3}$ GeV^2. The prediction of the longitudinal $S^N_{1/2}$-amplitudes is given in Fig. 4.22.

Finally we present the results for the fourth and fifth $J^\pi = \frac{1}{2}^+$-nucleon state in Fig. 4.23, where we show the transverse helicity amplitudes only. The corresponding masses predicted by model $\mathcal{A}$ are 1905 MeV for the fourth and 1953 MeV for the fifth state; for model $\mathcal{C}$ the predicted masses are 1872 MeV and 1968 MeV, respec-

tively. The two data at the photon point marked ″01″ and ″02″ were obtained by the CB-ELSA collaboration within the Bonn-Gatchina Analysis as reported in [15, 17] for the $N_{1/2^+}(1880)$-resonance. They correspond to two different partial wave solutions in order to extract the corresponding baryon mass and helicity amplitudes. The prediction for the fourth state lies between these values, the values found for the fifth state are much smaller. This also applies for higher $J^\pi = \frac{1}{2}^+$-excitations not displayed here.

The J $= \frac{3}{2}$ resonances: In Figs. 4.24 and 4.25 the transverse helicity amplitudes of the $P_{13}(1720)$-resonance are displayed. Although a reasonable agreement with the data of Aznauryan *et al.* [19] and with the photon decay amplitude is found for both models, the data from the MAID-analysis [114, 125] indicate a sign change for the $A^p_{1/2}$-amplitude at $Q^2 \approx 3\,\mathrm{GeV}^2$ not reproduced by either model. In spite of not being able to account at all for the large $A^p_{3/2}$-amplitude found experimentally, the longitudinal helicity amplitude as reported in the MAID-analysis with exception of the value at $Q^2 \approx 1\,\mathrm{GeV}^2$ is reproduced by both models rather well, as shown in Fig. 4.26.

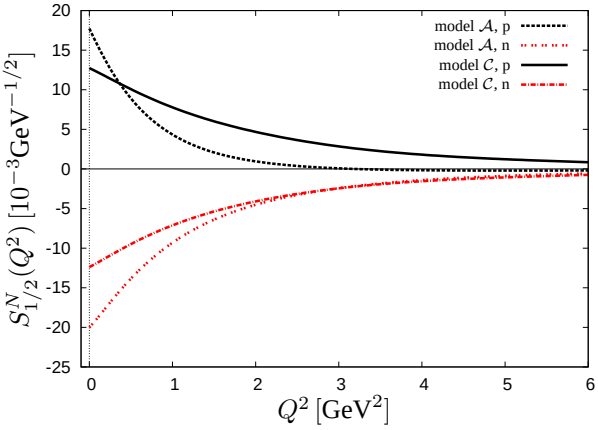

Fig. 4.32: Prediction of the $D_{13}(1700)$ longitudinal helicity amplitude $S^N_{1/2}$ for proton and neutron calculated in model $\mathcal{C}$ (solid and dashed-dotted line) and model $\mathcal{A}$ (dashed lines). See also caption to Fig. 4.14.

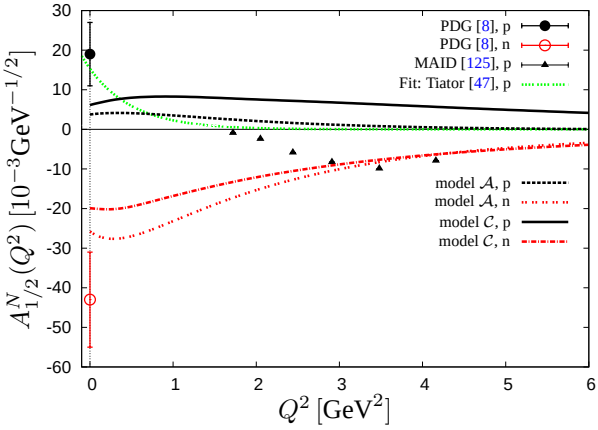

Fig. 4.33: Comparison of the $D_{15}(1675)$ transverse helicity amplitude $A^N_{1/2}$ for proton and neutron calculated in model $\mathcal{C}$ (solid and dashed-dotted line) and model $\mathcal{A}$ (dashed lines). See also caption to Fig. 4.14.

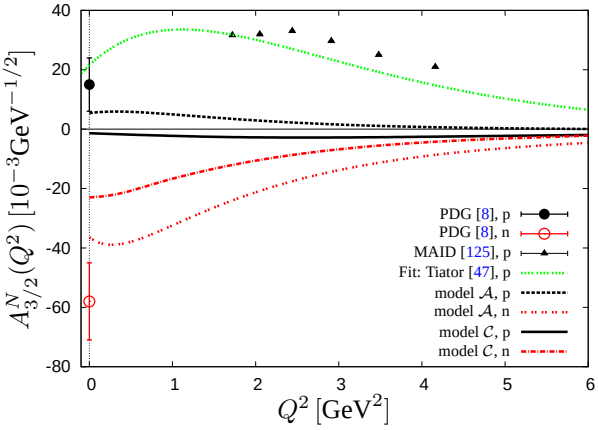

Fig. 4.34: Comparison of the $D_{15}(1675)$ transverse helicity amplitude $A^N_{3/2}$ for proton and neutron calculated in model $\mathcal{C}$ (solid and dashed-dotted line) and model $\mathcal{A}$ (dashed lines). See also caption to Fig. 4.14.

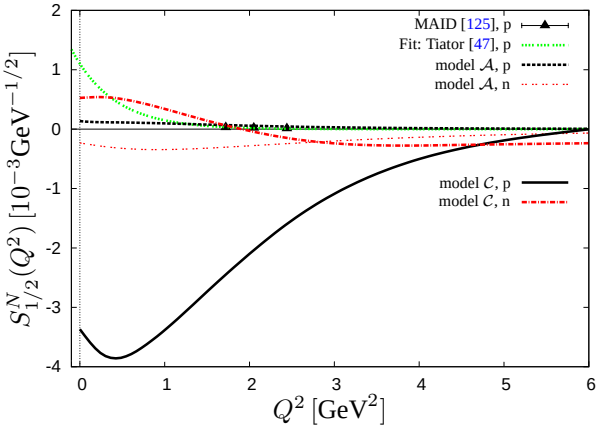

Fig. 4.35: Comparison of the $D_{15}(1675)$ longitudinal helicity amplitude $S^N_{1/2}$ for proton and neutron calculated in model $\mathcal{C}$ (solid and dashed-dotted line) and model $\mathcal{A}$ (dashed lines). See also caption to Fig. 4.14.

For the transverse helicity amplitude $A^p_{1/2}$ (see Fig. 4.27) of the $D_{13}(1520)$-resonance we find a reasonable

quantitative agreement with experimental data for low momentum transfers, while apart from the fact, that in model $\mathcal{C}$ the amplitude is too small by about a factor of two, the Q^2-dependence is reproduced up to $Q^2 \approx 6\,\mathrm{GeV}^2$. The minimum at $Q^2 \approx 1\,\mathrm{GeV}^2$ is clearly visible for model $\mathcal{A}$, whereas this feature is not so pronounced in model $\mathcal{C}$. The $A^p_{3/2}$-amplitudes are displayed in Fig. 4.28; here both models underestimate the data by more than a factor of three. Likewise the calculated neutron $A^n_{1/2}$- and $A^n_{3/2}$-amplitudes at the photon point are too small. In particular for the $A^n_{1/2}$-amplitude the predicted value close to zero is in contradiction to the experimental value $-59 \pm 9 \times 10^{-3}\mathrm{GeV}^{-1/2}$ from PDG [8]. Unfortunately, although the Q^2-dependence of the magnitude of the longitudinal amplitude $S^p_{1/2}$, see Fig. 4.29, would describe the experimental data of Aznauryan *et al.* [18–20] and MAID [114] very well, the amplitude has the wrong sign. Note, that although, as mentioned in section 2.7, the common phase ζ in the definition of the helicity amplitudes is not determined in our framework, relative signs between the three helicity amplitudes are fixed.

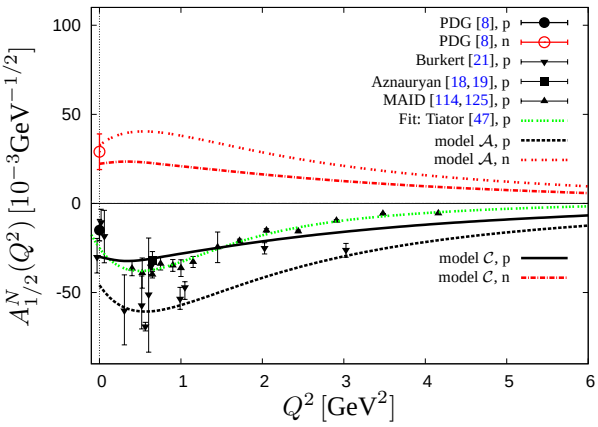

Fig. 4.36: Comparison of the $F_{15}(1680)$ transverse helicity amplitude $A^N_{1/2}$ for proton and neutron calculated in model $\mathcal{C}$ (solid and dashed-dotted line) and model $\mathcal{A}$ (dashed lines). See also caption to Fig. 4.14.

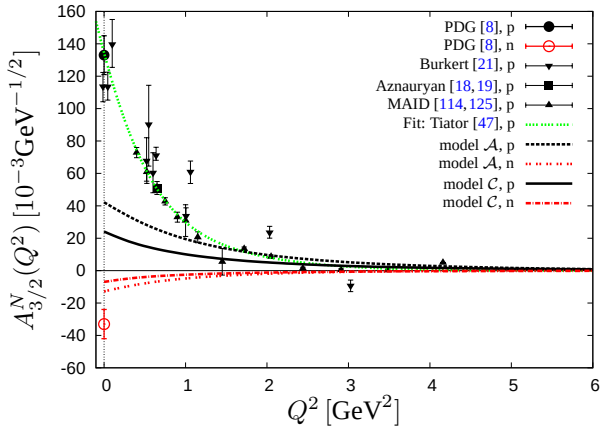

Fig. 4.37: Comparison of the $F_{15}(1680)$ transverse helicity amplitude $A^N_{3/2}$ for proton and neutron calculated in model $\mathcal{C}$ (solid line) and model $\mathcal{A}$ (dashed line). See also caption to Fig. 4.14.

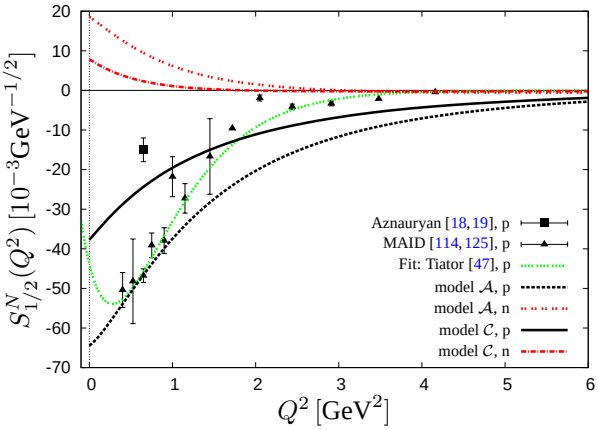

Fig. 4.38: Comparison of the $F_{15}(1680)$ longitudinal helicity amplitude $S^N_{1/2}$ for proton and neutron calculated in model $\mathcal{C}$ (solid and dashed-dotted line) and model $\mathcal{A}$ (dashed lines). See also caption to Fig. 4.14.

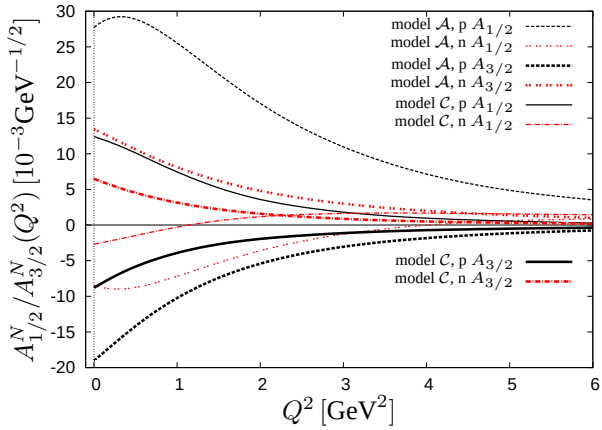

Fig. 4.39: Prediction of the $G_{17}(2190)$ transverse helicity amplitudes $A^N_{1/2}$ and $A^N_{3/2}$ for proton and neutron calculated in model $\mathcal{C}$ (solid and dashed-dotted line) and model $\mathcal{A}$ (dashed lines). See also caption to Fig. 4.14.

The transverse amplitudes for the next $J^\pi = \frac{3}{2}^-$-nucleon resonance, *i.e.* $D_{13}(1700)$, are displayed in Figs. 4.30 and 4.31. In contrast to the situation for the $D_{13}(1520)$-resonance described above, here both models are in accordance with the PDG-data [8] as well as with the data from Aznauryan *et al.* [19] for the

$A_{1/2}$-amplitude, whereas the $A_{3/2}$-amplitude only reproduces the PDG-data [8] and not the data point from Aznauryan *et al.* [19] at finite momentum transfer. The prediction for the longitudinal $D_{13}(1700)$-amplitudes is given in Fig. 4.32. The calculated amplitudes turn out to be rather small.

The J $= \frac{5}{2}$ resonances: Although the transverse $D_{15}(1675)$-helicity amplitudes at the photon point reproduce the experimental data from MAID [114, 125] and the PDG [8] rather well, as displayed in Figs. 4.33 and 4.34, both calculations cannot account for the apparent zero of the experimental $A^p_{1/2}$-amplitude at $Q^2 \approx 1.5\,\mathrm{GeV}^2$. Furthermore, the $A^p_{3/2}$-amplitude, displayed in Fig. 4.34 is severely underestimated in magnitude by both models and model $\mathcal{C}$ even yields the wrong sign. The transverse amplitudes for the neutron are predicted to be negative, here the calculated value at the photon point for model $\mathcal{A}$ is closer to the experimental value

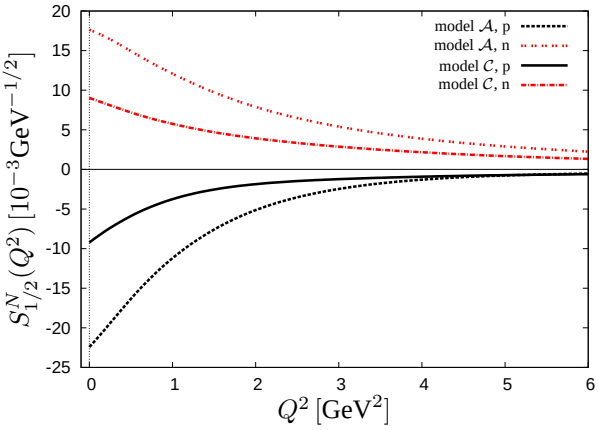

Fig. 4.40: Prediction of the $G_{17}(2190)$ longitudinal helicity amplitude $S^N_{1/2}$ for proton and neutron calculated in model $\mathcal{C}$ (solid and dashed-dotted line) and model $\mathcal{A}$ (dashed lines). See also caption to Fig. 4.14.

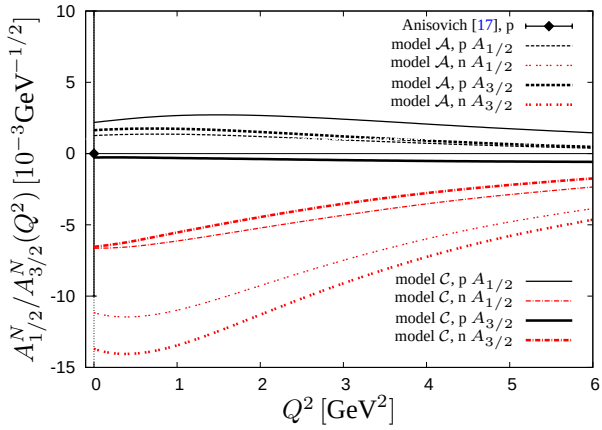

Fig. 4.41: Comparison of the $G_{19}(2250)$ transverse helicity amplitudes $A^N_{1/2}$ and $A^N_{3/2}$ for proton and neutron calculated in model $\mathcal{C}$ (solid and dashed-dotted line) and model $\mathcal{A}$ (dashed lines). The bar at the photon point corresponds to an estimate by Anisovich *et al.* [17] for $A^N_{1/2}$ and $A^N_{3/2}$ within $|A^p| < 10 \times 10^{-3}\mathrm{GeV}^{-1/2}$. See also caption to Fig. 4.14.

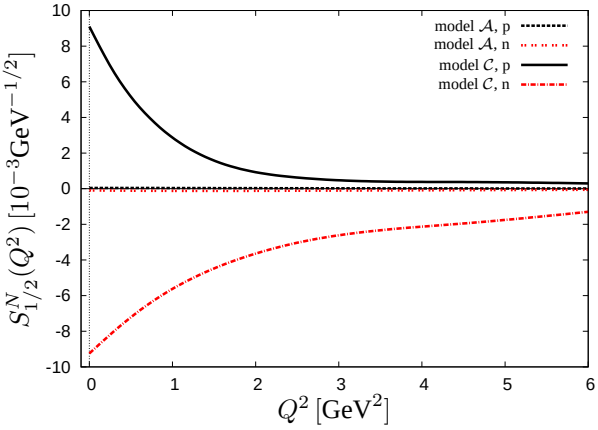

Fig. 4.42: Prediction of the $G_{19}(2250)$ longitudinal helicity amplitude $S^N_{1/2}$ for proton and neutron calculated in model $\mathcal{C}$ (solid and dashed-dotted line) and model $\mathcal{A}$ (dashed lines). See also caption to Fig. 4.14.

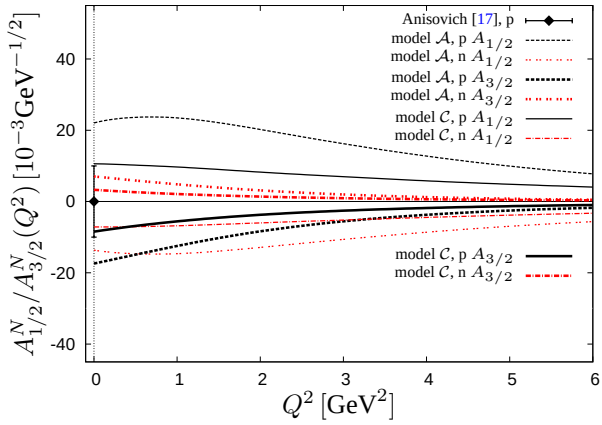

Fig. 4.43: Comparison of the $H_{19}(2220)$ transverse helicity amplitudes $A^N_{1/2}$ and $A^N_{3/2}$ for proton and neutron calculated in model $\mathcal{C}$ (solid and dashed-dotted line) and model $\mathcal{A}$ (dashed lines). The bar at the photon point corresponds to an estimate by Anisovich *et al.* [17] for $A^N_{1/2}$ and $A^N_{3/2}$ within $|A^p| < 10 \times 10^{-3}\mathrm{GeV}^{-1/2}$. See also caption to Fig. 4.14.

than for model $\mathcal{C}$. The longitudinal amplitudes are calculated to be very small for both models. There exists only experimental data from the MAID-analysis [125], indicating that the experimental values are consistent with zero (see Fig. 4.38).

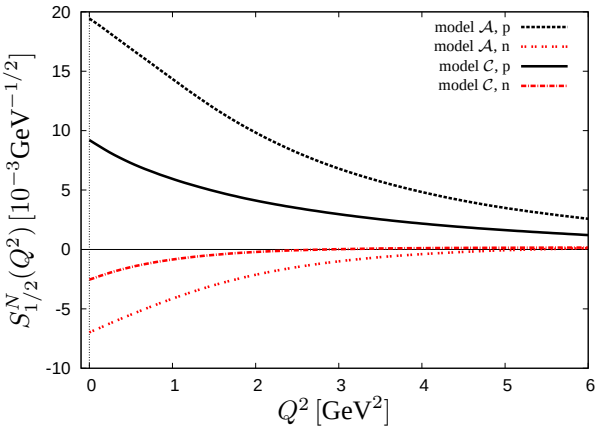

Fig. 4.44: Prediction of the $H_{19}(2220)$ longitudinal helicity amplitude $S^N_{1/2}$ for proton and neutron calculated in model $\mathcal{C}$ (solid and dashed-dotted line) and model $\mathcal{A}$ (dashed lines). See also caption to Fig. 4.14.

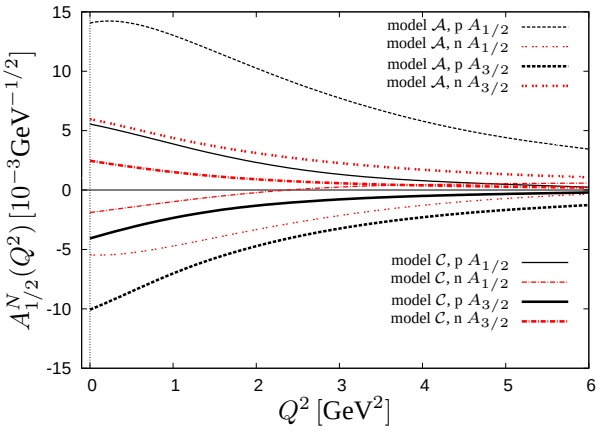

Fig. 4.45: Prediction of the $I_{1\,11}(2600)$ transverse helicity amplitudes $A^N_{1/2}$ and $A^N_{3/2}$ for proton and neutron calculated in model $\mathcal{C}$ (solid and dashed-dotted line) and model $\mathcal{A}$ (dashed lines). See also caption to Fig. 4.14.

There also exist data for the helicity amplitudes of the $F_{15}(1680)$-resonance. The comparison with the calculated values is given in Figs. 4.36 and 4.37. In particular in model $\mathcal{C}$ a reasonable description of the $A^p_{1/2}$-amplitudes is found for the newer data from Aznauryan *et al.* [18, 19] and MAID [114, 125] both at the photon point and for the values at higher momentum transfers. The calculated values in model $\mathcal{A}$ are in better accordance with the the older data from Burkert *et al.* [21], which are larger in magnitude. In contrast to this, the $A^p_{3/2}$-amplitudes are again severely underestimated in magnitude, see Fig. 4.37. However, for the longitudinal $S^p_{1/2}$-amplitude we observe a rather good agreement with the data as displayed in Fig. 4.38, the values obtained in model $\mathcal{C}$ being too small at lower momentum transfers.

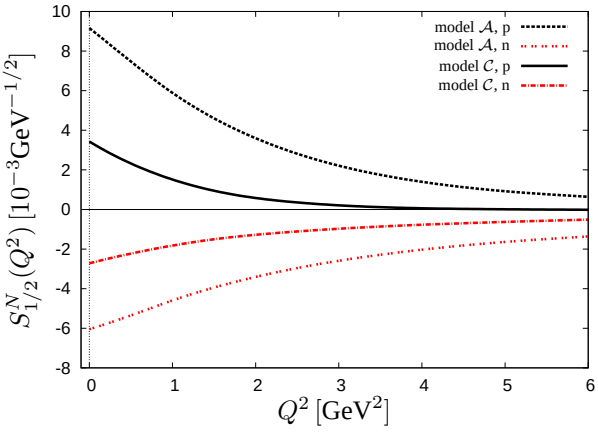

Fig. 4.46: Prediction of the $I_{1\,11}(2600)$ longitudinal helicity amplitude $S^N_{1/2}$ for proton and neutron calculated in model $\mathcal{C}$ (solid and dashed-dotted line) and model $\mathcal{A}$ (dashed lines). See also caption to Fig. 4.14.

The J $= \frac{7}{2}$ resonances: For positive parity PDG [8] lists the $F_{17}(1990)$-resonance rated with two stars. Both in model $\mathcal{A}$ and in model $\mathcal{C}$ we can relate this to states with a calculated mass of 1954 MeV and 1997 MeV, respectively. The corresponding photon amplitudes are very small, see Tab. 4.10. Otherwise, concerning the $J = \frac{7}{2}$ resonances there exists only one negative parity resonance with more than at least a three star rating, the $G_{17}(2190)$. The corresponding predictions for transverse and longitudinal helicity amplitudes are shown in Figs. 4.39 and 4.40.

The J $= \frac{9}{2}$ resonances: The transverse and longitudinal helicity amplitudes of the $J^\pi = \frac{9}{2}^+$-resonance $G_{19}(2250)$ are predicted to be very small as shown in Figs. 4.41 and 4.42 and coincide with the estimate by Anisovich *et al.* [17] for the transverse amplitudes. Obviously, the $A^p_{3/2}$-amplitude of model $\mathcal{C}$ and the longitudinal amplitudes of model $\mathcal{A}$ are effectively zero. Although the resonance with $J^\pi = \frac{9}{2}^-$, $H_{19}(2220)$ has a

four star rating by the PDG, only the proton photon decay amplitude has been estimated in [17]. The calculated values are displayed in Fig. 4.43 and Fig. 4.44; the amplitudes turn out to be smaller in model $\mathcal{C}$ than in model $\mathcal{A}$ in better agreement with the estimate of [17].

The J $= \frac{11}{2}$ resonances: Figs. 4.45 and 4.46 shows predictions of the transverse and longitudinal helicity amplitudes for the $J^\pi = \frac{1}{2}^-$ $I_{1\,11}(2600)$-resonances. So far no data available.

$\Delta \leftrightarrow N$ helicity amplitudes

We now turn to a discussion of the results for $\Delta \leftrightarrow N$ electro-excitation.

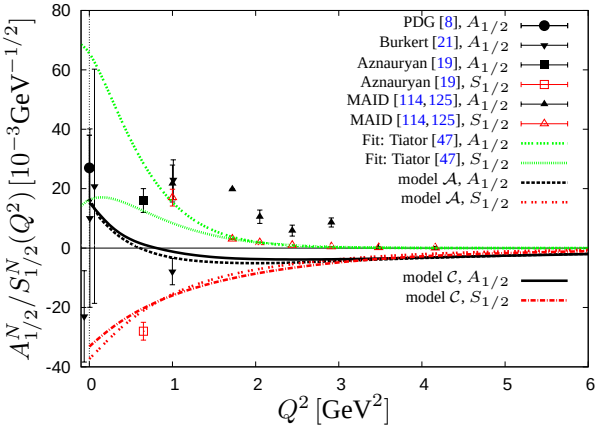

Fig. 4.47: Comparison of the $S_{31}(1620)$ transverse and the longitudinal helicity amplitudes $A^N_{1/2}$ and $S^N_{1/2}$ calculated in model $\mathcal{C}$ (solid and dashed-dotted line) and model $\mathcal{A}$ (dashed lines) with experimental data from [8, 19, 21, 114, 125]. Note, that for the data points of the MAID-analysis by Tiator *et al.* [125] no errors are quoted. See also caption to Fig. 4.14.

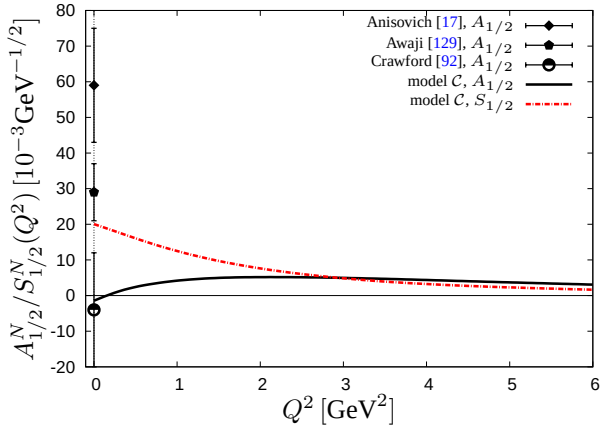

Fig. 4.48: Comparison of the $S_{31}(1900)$ transverse $A^N_{1/2}$ (black line) and longitudinal helicity amplitude $S^N_{1/2}$ (red line) in model $\mathcal{C}$. See also caption to Fig. 4.14.

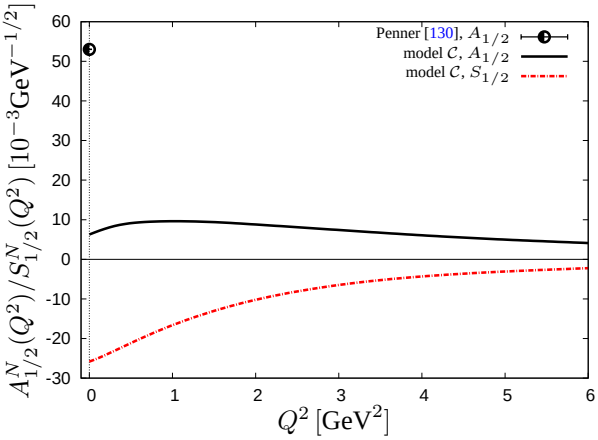

Fig. 4.49: Comparison of the $P_{31}(1750)$ transverse helicity amplitude $A^N_{1/2}$ calculated in model $\mathcal{C}$ (solid line) and the data from Penner *et al.* [130]. See also caption to Fig. 4.14.

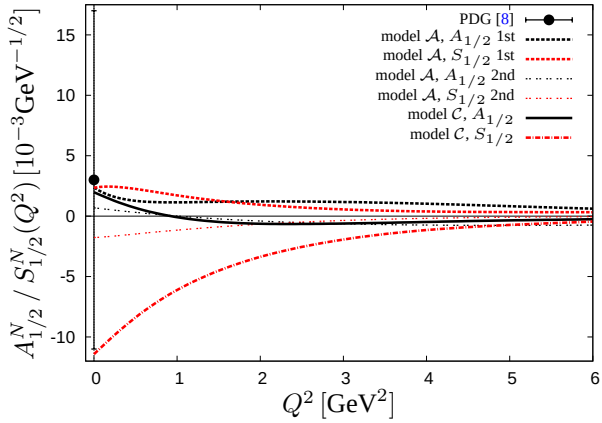

Fig. 4.50: Comparison of the $P_{31}(1910)$ transverse $A^N_{1/2}$ and longitudinal $S^N_{1/2}$-helicity amplitude calculated in model $\mathcal{C}$ (solid and dashed-dotted line) and model $\mathcal{A}$ (dashed lines). See also caption to Fig. 4.14.

The $\mathbf{J = \frac{1}{2}}$ resonances: We start the discussion with the positive parity $S_{31}(1620)$-resonance. For the $S_{31}(1620)$ transverse and longitudinal helicity amplitudes, depicted in Fig. 4.47, a wide variety of experimental data at and near the photon point exists. The calculated values lie well within the region of experimental data obtained due to the spread in partially contradictory experimental data, but an assessment of the quality is hardly possible. The positive longitudinal amplitude $S^N_{1/2}$ in Fig. 4.47 as determined in [114, 125] together with the single data point from [19] suggest a sign change in the region $Q^2 \approx 0.7 - 1.0\,\mathrm{GeV}^2$ not reproduced by both calculations, this clearly needs more experimental clarification.

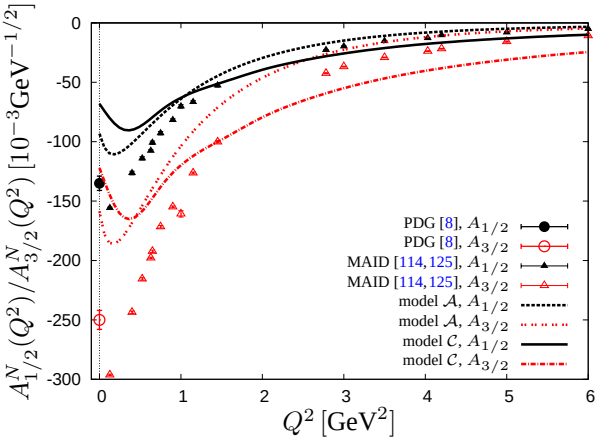

Fig. 4.51: Comparison of the $P_{33}(1232)$ transverse helicity amplitudes $A^N_{1/2}$ and $A^N_{3/2}$ as calculated in model $\mathcal{C}$ (solid and dashed-dotted line) and model $\mathcal{A}$ (dashed lines). See also caption to Fig. 4.14 and the magnetic and electric transition form factor in Fig. 4.64.

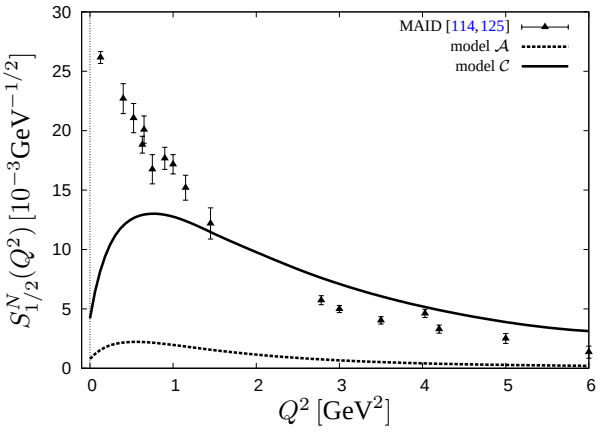

Fig. 4.52: Comparison of the $P_{33}(1232)$ longitudinal helicity amplitude $S^N_{1/2}$ calculated in model $\mathcal{C}$ (solid line) and model $\mathcal{A}$ (dashed line) to experimental data from [8, 114, 125]. See also caption to Fig. 4.14 and the Coulomb transition form factor in Fig. 4.66.

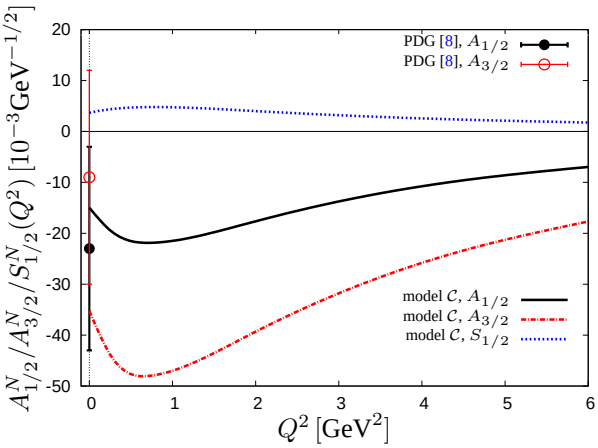

Fig. 4.53: Comparison of the $P_{33}(1600)$ transverse and longitudinal helicity amplitudes $A^N_{1/2}$, $A^N_{3/2}$ and $S^N_{1/2}$ calculated in model $\mathcal{C}$ with the PDG-data [8] and [17]. See also caption to Fig. 4.14.

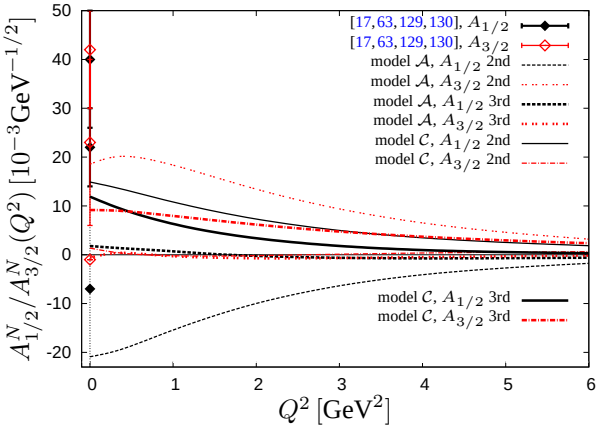

Fig. 4.54: Comparison of the $P_{33}(1920)$ transverse helicity amplitudes $A^N_{1/2}$ and $A^N_{3/2}$ as calculated in model $\mathcal{C}$ (solid and dashed-dotted line) and model $\mathcal{A}$ (dashed lines) with the data from [63, 129, 130]. Note, that the values at $Q^2 = 0$ of Anisovich *et al.* [17], $A^p_{1/2} = 130^{+30}_{-60} \times 10^{-3}\mathrm{GeV}^{-1/2}$ and $A^p_{3/2} = -150^{+25}_{-50} \times 10^{-3}\mathrm{GeV}^{-1/2}$, are beyond the range displayed. See also caption to Fig. 4.14.

The next excitation in this channel is the $S_{31}(1900)$-resonance; the corresponding transverse and longitudi-

nal helicity amplitudes are displayed in Fig. 4.48. Here, we only give the results for model $\mathcal{C}$, since the original model $\mathcal{A}$ does not describe a resonance in this region. The values at the photon point seems to be in better agreement with the data from Crawford *et al.* [92] than with the data from Awaji *et al.* [129] and Anisovich *et al.* [17]. Note, that for both S_{31}-resonances we judiciously fixed the phase ζ in order to reproduce the sign of the PDG value at the photon point, as has been mentioned above. Reversing the sign of ζ would in case of the $S_{31}(1620)$-resonance in fact better reproduce the data at larger momentum transfers.

Also the lowest positive parity Δ-resonance $P_{31}(1750)$ is only reproduced in model $\mathcal{C}$ as shown in [31]. The calculation does not account for the large value found by Penner *et al.* [130] at the photon point, see Fig. 4.49. The longitudinal amplitude is predicted to be negative for this resonance.

The helicity amplitudes for the next excited state, $P_{31}(1910)$ are shown in Fig. 4.50. Note, that model $\mathcal{A}$ does produce two nearby resonances at the position of the $P_{31}(1910)$-resonance, see [5, 31]. The calculated amplitudes for both resonances as well as the calculated amplitude in model $\mathcal{C}$ are very small and in rough agreement with the experimental value found at the photon point which has a large error. Again the assessment cannot be conclusive. Also shown are the predictions for the rather small longitudinal amplitudes.

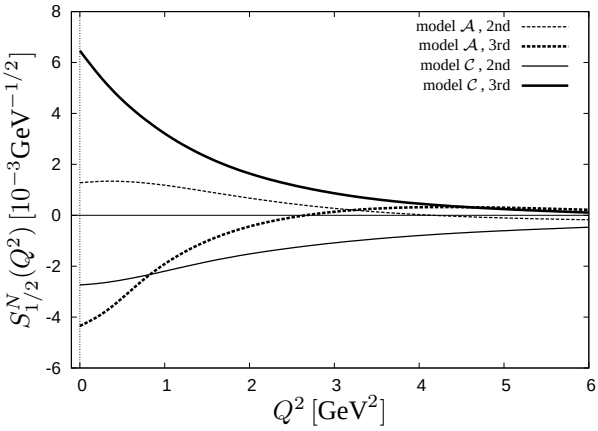

Fig. 4.55: Prediction of the $P_{33}(1920)$ longitudinal helicity amplitude $S^N_{1/2}$ calculated in model $\mathcal{C}$ (solid and dashed-dotted line) and model $\mathcal{A}$ (dashed lines). See also caption to Fig. 4.14.

The J $= \frac{3}{2}$ resonances: We shall discuss the electro-excitation of the ground-state Δ-resonance, $P_{33}(1232)$ in some more detail below; the transverse amplitudes are shown in Fig. 4.51, while Fig. 4.52 displays the results for the longitudinal amplitude. With the exception of the low momentum transfer region $Q^2 < 0.5\,\mathrm{GeV}^2$ we

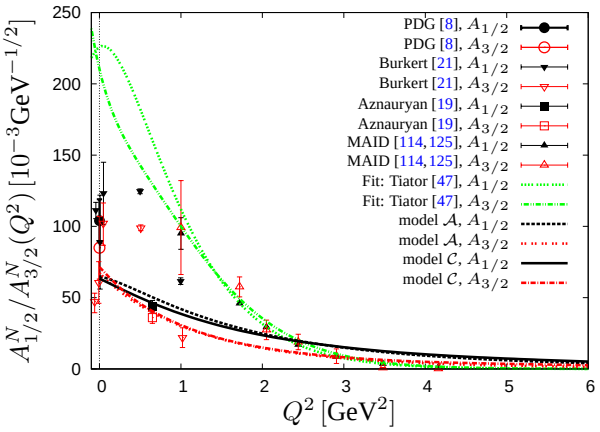

Fig. 4.56: Comparison of the $D_{33}(1700)$ transverse helicity amplitudes $A^N_{1/2}$ respectively $A^N_{3/2}$ calculated in model $\mathcal{C}$ (solid and dashed-dotted line) and model $\mathcal{A}$ (dashed lines). See also caption to Fig. 4.14.

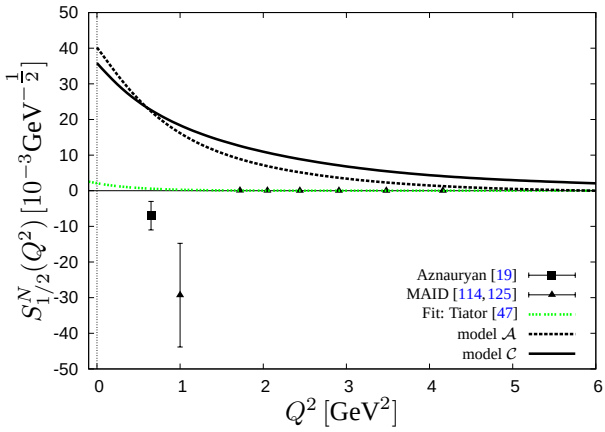

Fig. 4.57: Comparison of the $D_{33}(1700)$ longitudinal helicity amplitude $S^N_{1/2}$ of the nucleon calculated in model $\mathcal{C}$ (solid line) and model $\mathcal{A}$ (dashed line). Note, that for the data points of the MAID-analysis by Tiator *et al.* [125] no errors are quoted. See also caption to Fig. 4.14.

observe a fair agreement with experimental data for the transverse amplitude $A^N_{1/2}$ for both models, which, however, both show a minimum in the amplitudes for $Q^2 \lesssim 0.5\,\mathrm{GeV}^2$ (which, in contradiction to data, also persists in the magnetic transition form factor, see Fig. 4.64), whereas the data show a minimum of some kinematical origin at much smaller momentum transfers $Q^2 \lesssim 0.1\,\mathrm{GeV}^2$.

Also the experimental data for the $S^N_{1/2}$-helicity amplitude can be accounted for by the calculated curve for model $\mathcal{C}$ at the highest momentum transfers only, while the amplitude calculated in $\mathcal{A}$ is much smaller. Note, that more data is available for the magnetic transition form factor, which is a linear combination of the $A^N_{1/2}$- and $A^N_{3/2}$-amplitudes, see section 4.2.8.

The Roper-like excitation of the groundstate Δ-resonance, $P_{33}(1600)$, is only described adequately in model $\mathcal{C}$. The corresponding helicity amplitudes $A^N_{1/2}$, $A^N_{3/2}$ and $S^N_{1/2}$ are displayed in Fig. 4.53. The $A^N_{1/2}$-amplitude is calculated to be smaller than the decay amplitude quoted by the PDG [8] and [17]. Contrary to this we find a rather large $A^N_{3/2}$-amplitude with a pronounced minimum around $Q^2 \approx 0.75\,\mathrm{GeV}^2$. However, in this case, the value at the photon point is overestimated.

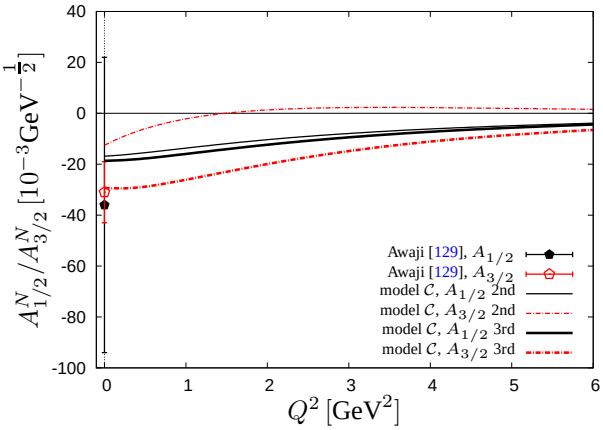

Fig. 4.58: Comparison of the $D_{33}(1940)$ transverse helicity amplitudes $A^N_{1/2}$ (solid and dashed-dotted line) and $A^N_{3/2}$ (dashed lines) calculated in model $\mathcal{C}$ with the data from Awaji *et al.* [129]. Due to the fact that model $\mathcal{C}$ offers two alternatives for the $D_{33}(1940)$-resonance, as shown in [31], both amplitudes, labelled with "second" and "third" are displayed. Note, that the values at $Q^2 = 0$ of Horn *et al.* [63], $A^p_{1/2} = (160 \pm 40) \times 10^{-3}\mathrm{GeV}^{-1/2}$ and $A^p_{3/2} = (130 \pm 30) \times 10^{-3}\mathrm{GeV}^{-1/2}$, are beyond the range displayed. See also caption to Fig. 4.14.

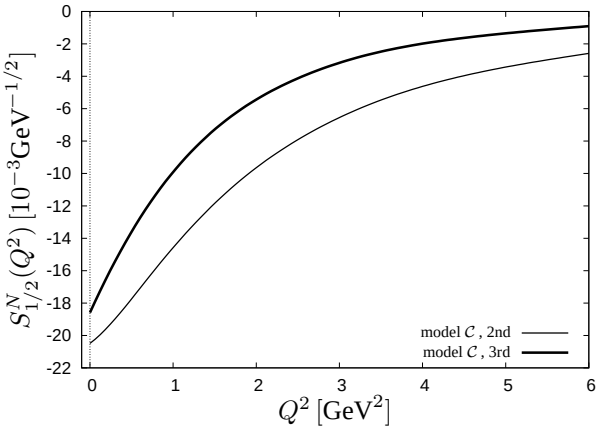

Fig. 4.59: Prediction of the $D_{33}(1940)$ longitudinal helicity amplitudes $S^N_{1/2}$ (solid and dashed-dotted line) of the nucleon calculated in model $\mathcal{C}$. Due to the fact that model $\mathcal{C}$ offers two alternatives for the $D_{33}(1940)$-resonance, as shown in [31], both amplitudes, labelled with "first" and "second" are displayed. See also caption to Fig. 4.14.

For the $P_{33}(1920)$-state with positive parity the helicity amplitudes are displayed in Figs. 4.54 and 4.55. In [31] it is shown, that there exist several states around 1920 MeV, which correspond to the second and third excited $\Delta_{3/2^+}$-state and which are predicted at 1834 MeV and at 1912 MeV for model $\mathcal{A}$ and at 1899 MeV and at 1932 MeV for model $\mathcal{C}$, respectively. The transverse amplitudes are in general very small and match the photon decay data of [63, 129, 130], whereas the data of Anisovich *et al.* [17] cannot be reproduced. The predictions for the longitudinal amplitude as well as the $A^N_{3/2}$-amplitude for the third excitation are effectively zero.

We now turn to negative parity excited Δ-resonances. For the $D_{33}(1700)$ transition amplitudes we find, that the predictions of both models are rather close, as displayed in Figs. 4.56 and 4.57. Note, that the calculated masses of the $D_{33}(1700)$-resonance, *viz.* $M = 1594\,\mathrm{MeV}$ for model $\mathcal{A}$ and $M = 1600\,\mathrm{MeV}$ for model $\mathcal{C}$, are about $100\,\mathrm{MeV}$ lower than the experimental mass at approximately $1700\,\mathrm{MeV}$. This of course affects the prefactors in Eqs. (2.125a) and (2.125b) leading to the conclusion that the current-matrix elements are calculated to be too small. For the transverse amplitude $A^N_{1/2}$ only the single data point from Aznauryan *et al.* [19] is close to the calculated curves. At the photon point the calculated values also agree with the PDG-data [8]. In contrast, the data from MAID [114, 125] and Burkert *et al.* [21] cannot be accounted for. Similar observations are made for the $A^N_{3/2}$-amplitude. The longitudinal $S^N_{1/2}$-amplitude has a sign opposite to the rare data from Aznauryan

et al. [19] and MAID [114, 125] as shown in Fig. 4.57. Note, however, that the MAID-analysis of Tiator *et al.* [125] yields a vanishing $S^N_{1/2}$-amplitude in contrast to the appreciable amplitudes found in the calculations.

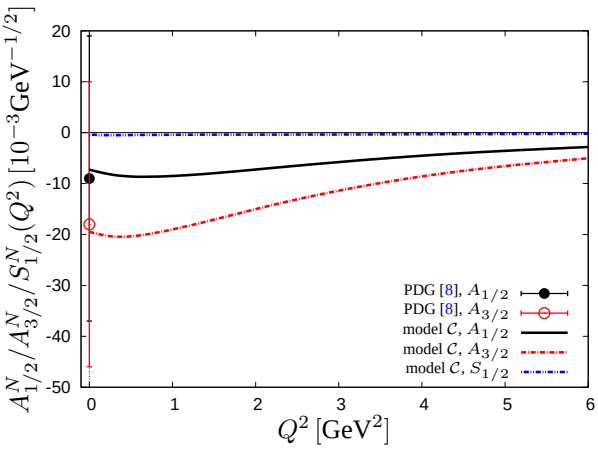

Fig. 4.60: Comparison of the $D_{35}(1930)$-helicity amplitudes $A^N_{1/2}$ (black line), $A^N_{3/2}$ (red line) and $S^N_{1/2}$ (blue line) calculated in model $\mathcal{C}$ with the PDG-data [8]. See also caption to Fig. 4.14.

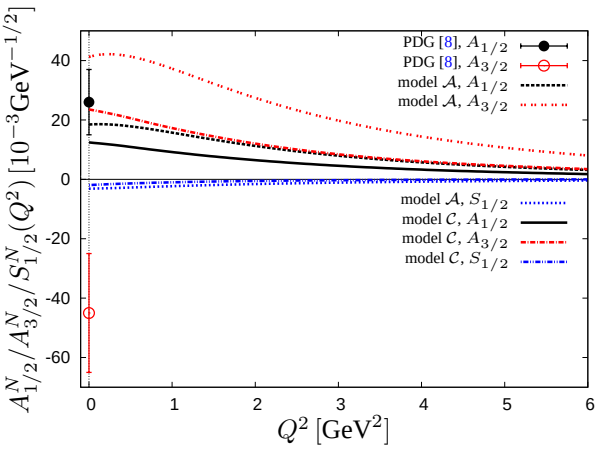

Fig. 4.61: Comparison of the $F_{35}(1905)$ transverse and longitudinal helicity amplitudes $A^N_{1/2}$, $A^N_{3/2}$ and $S^N_{1/2}$ calculated in model $\mathcal{C}$ (solid and dashed-dotted line) and model $\mathcal{A}$ (dashed lines). See also caption to Fig. 4.14.

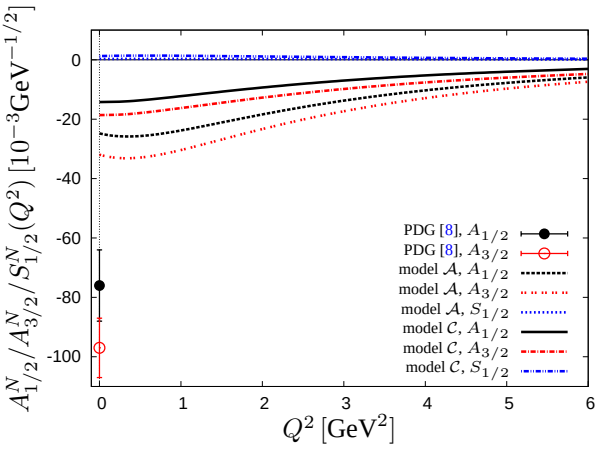

Fig. 4.62: Comparison of the $F_{37}(1950)$ transverse and longitudinal helicity amplitudes $A^N_{1/2}$, $A^N_{3/2}$ and $S^N_{1/2}$ calculated in model $\mathcal{C}$ (solid and dashed-dotted line) and model $\mathcal{A}$ (dashed lines). See also caption to Fig. 4.14.

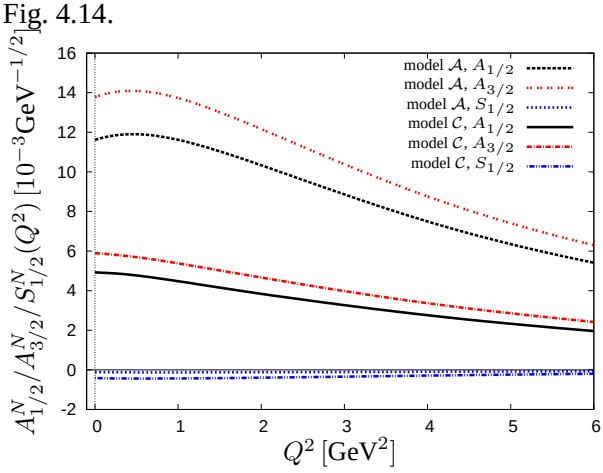

Fig. 4.63: Prediction of the $H_{3\,11}(2420)$ transverse and longitudinal helicity amplitudes $A^N_{1/2}$, $A^N_{3/2}$ and $S^N_{1/2}$ calculated in model $\mathcal{C}$ (solid and dashed-dotted line) and model $\mathcal{A}$ (dashed lines). See also caption to Fig. 4.14.

Figs. 4.58 and 4.59 contain the prediction for the transverse and longitudinal helicity amplitudes of the $D_{33}(1940)$ resonance in model $\mathcal{C}$. Note, that in this model two resonances with masses $M = 1895\,\mathrm{MeV}$ and $M = 1959\,\mathrm{MeV}$ are predicted in this energy range, as shown in [31]. Accordingly, we have displayed two alternative predictions for the helicity amplitudes. The results for the transverse amplitudes, see Fig. 4.58, for both resonances are rather similar; the photon decay amplitudes measured by Horn *et al.* [63] and Awaji *et al.* [129] are in conflict, the calculated values favour a small negative value at the photon point, which agrees with the data from Awaji *et al.* [129]. In Fig. 4.59 we also show the corresponding longitudinal amplitudes.

The J $= \frac{5}{2}$ resonances: In Fig. 4.60, we show the $A^N_{1/2}$, $A^N_{3/2}$ and $S^N_{1/2}$ helicity amplitudes calculated in model $\mathcal{C}$ [31] for the $D_{35}(1930)$-resonance. Also displayed is the PDG-data at the photon point [8], where we find that the transverse amplitudes agree well with the experimental values. The longitudinal amplitude is

found to be almost vanishing. Since model $\mathcal{A}$ cannot account for a resonance in this energy region no results are given in this case.

Both models are able to reproduce the lowest $J^\pi = \frac{5}{2}^+$ Δ-resonance with positive parity. The prediction of the helicity amplitudes of the $F_{35}(1905)$-resonance can be found in Fig. 4.61. Both models can account very well for the PDG-data at the photon point for the $A_{1/2}$ transverse amplitudes, but the $A_{3/2}$-amplitude is found with a sign opposite to that of the data. As for the previously discussed resonance the results for the longitudinal amplitudes turn out to be very small.

The J $= \frac{7}{2}$ resonances: For $J = \frac{7}{2}$ there exists only one four star resonance, the $F_{37}(1950)$. The predictions of the corresponding transverse and longitudinal helicity amplitudes are shown in Fig. 4.62. Here, the predictions of the transverse amplitudes are much too small in order to explain the experimental photon coupling.

The J $= \frac{11}{2}$ resonances: Fig. 4.63 shows the prediction of the transverse and longitudinal helicity amplitudes of the $\Delta_{11/2^+}(2420)$-resonance. The amplitudes found in model $\mathcal{C}$ are slightly smaller than those in model $\mathcal{A}$. In both cases the longitudinal amplitude virtually vanishes.

4.2.7 Photon couplings

In Tabs. 4.10 and 4.11 we have summarised the results for the photon decay amplitudes as partially already discussed in subsections 4.2.6 and 4.2.6 for the helicity amplitudes. This tables also lists the available experimental data. Most of the decay amplitudes can be accounted for quite satisfactory. In general no large differences between both models are found. For some amplitudes of resonances with higher angular momentum no experimental data are available to our knowledge.

Table 4.10: Transverse photon couplings calculated for $N \to \Delta$ transitions in model $\mathcal{A}$ and $\mathcal{C}$ in comparison to experimental data. All calculated photon couplings were determined by calculating the helicity amplitudes at $Q^2 = 10^{-4}\,\mathrm{GeV}^2$ close to the photon point. A hyphen indicates, that data do not exist. All amplitudes are in units of $10^{-3}\mathrm{GeV}^{-1/2}$, all masses are given in MeV. Reference [130] does not quote errors.

State	Rat.	Mass model $\mathcal{A}$	Mass model $\mathcal{C}$	Ampl.	Model $\mathcal{A}$	Model $\mathcal{C}$	Exp.	Ref.
$S_{31}(1620)$	****	1620	1636	$A_{1/2}$	16.63	15.33	27±11	[8]
$S_{31}(1900)$	**	–	1956	$A_{1/2}$	–	-1.43	59±16/29±8/-4±16	[17]/ [129]/ [92]
$P_{31}(1750)$	*	–	1765	$A_{1/2}$	–	6.27	53	[130]
$P_{31}(1910)$	****	1829/1869	1892	$A_{1/2}$	2.38/0.69	1.98	3±14	[8]
$P_{33}(1232)$	****	1233	1231	$A_{1/2}$	-93.23	-68.08	-135±6	[8]
				$A_{3/2}$	-158.61	-122.08	-250±8	[8]
$P_{33}(1600)$	***	–	1596	$A_{1/2}$	–	-14.98	-23±20	[8]
				$A_{3/2}$	–	-35.24	-9±21	[8]
$P_{33}(1920)$	***	1834/1912	1899/1932	$A_{1/2}$	20.89/1.79	14.89/11.90	130^{+30}_{-60}/40±14/ 22±8/-7	[17]/ [129]/ [63]/ [130]
				$A_{3/2}$	-18.56/-0.58	1.36/9.16	-115^{+25}_{-50}/23±17/ 42±12/-1	[17]/ [129]/ [63]/ [130]
$D_{33}(1700)$	****	1594	1600	$A_{1/2}$	64.99	63.39	104±15	[8]
				$A_{3/2}$	67.25	71.47	85±22	[8]
$D_{33}(1940)$	**	–	1895/1959	$A_{1/2}$	–	-16.86/-14.98	-36±58/160±40	[129]/ [63]
				$A_{3/2}$	–	-12.56/-27.19	-31±12/110±30	[129]/ [63]
$D_{35}(1930)$	***	–	2022	$A_{1/2}$	–	-7.27	-9±28	[8]
				$A_{3/2}$	–	-19.49	-18±28	[8]
$F_{35}(1905)$	****	1860	1896	$A_{1/2}$	18.46	12.42	26±11	[8]
				$A_{3/2}$	41.22	23.54	-45±20	[8]
$F_{37}(1950)$	****	1918	1934	$A_{1/2}$	-24.80	-14.22	-76±12	[8]
				$A_{3/2}$	-31.94	-18.62	-97±10	[8]
$H_{39}(2420)$	****	2399	2363	$A_{1/2}$	11.62	4.92	–	–
				$A_{3/2}$	13.78	5.90	–	–

Table 4.11: Transverse photon couplings calculated for $N \leftrightarrow N^*$ transitions in model $\mathcal{A}$ and $\mathcal{C}$ in comparison to experimental data. All calculated photon couplings were determined by calculating the helicity amplitudes at $Q^2 = 10^{-4}\,\mathrm{GeV}^2$ close to the photon point. A hyphen indicates, that data do not exist. All amplitudes are in units of $10^{-3}\mathrm{GeV}^{-1/2}$, all masses are given in MeV. The references [130, 131] do not quote errors.

State	Rat.	Mass model $\mathcal{A}$	Mass model $\mathcal{C}$	Ampl.	Model $\mathcal{A}$ p	Model $\mathcal{A}$ n	Model $\mathcal{C}$ p	Model $\mathcal{C}$ n	Exp. p	Exp. n	Ref.
$S_{11}(1535)$	****	1417	1475	$A_{1/2}$	111.68	-74.75	85.93	-54.96	90±30	-46±27	[8]
$S_{11}(1650)$	****	1618	1681	$A_{1/2}$	2.55	-16.03	-4.56	-6.86	53±16	-15±21	[8]
$S_{11}(1895)$	**	1872 1886	1839 1882	$A_{1/2}$	43.36 38.95	-23.93 -18.44	52.71 17.18	-29.01 -8.27	12±6	–	[17]
$P_{11}(1440)$	****	1498	1430	$A_{1/2}$	33.51	-18.68	33.10	-17.43	-60±4	40±10	[8]
$P_{11}(1710)$	***	1700	1712	$A_{1/2}$	58.36	-30.59	30.95	-13.57	24±10	-2±14	[8]
$P_{11}(1880)$	**	1905	1872	$A_{1/2}$	24.35	-15.55	24.44	-11.87	14±3	–	[17]
$P_{13}(1720)$	****	1655	1690	$A_{1/2}$	81.69	-33.06	50.28	-22.56	18±30	1±15	[8]
				$A_{3/2}$	-26.24	11.76	-17.10	2.69	-19±20	-29±61	[8]
$P_{13}(1900)$	***	1859 1894	1840	$A_{1/2}$	5.06 12.58	3.17 -14.53	2.31	5.17	26±15/-17	–/-16	[17]/ [130]
				$A_{3/2}$	2.29 6.49	18.15 -14.90	4.03	13.79	-65±30/31	–/-2	[17]/ [130]
$D_{13}(1520)$	****	1453	1520	$A_{1/2}$	-54.80	2.47	-39.39	0.65	-24±9	-59±9	[8]
				$A_{3/2}$	48.45	-52.27	32.80	-31.64	150±15	-139±11	[8]
$D_{13}(1700)$	***	1573	1686	$A_{1/2}$	-20.69	16.52	-10.16	10.65	-18±13	0±50	[8]
				$A_{3/2}$	-5.45	38.89	-7.08	26.42	-2±24	-3±44	[8]
$D_{13}(1875)$	***	1896 1920	1849 1921	$A_{1/2}$	49.87 1.62	-19.04 -6.73	42.29 -3.72	-13.71 -6.76	18±10/-20±8 12/26±52	7±13	[17]/ [129]/ [8]/ [130]/ [132]
				$A_{3/2}$	-20.86 -5.78	13.11 -2.38	-21.46 0.64	10.17 -4.27	-9±5/17±11 -10/128±57	-53±34	[17]/ [129]/ [8]/ [130]/ [132]
$D_{15}(1675)$	****	1623	1678	$A_{1/2}$	3.74	-25.80	6.16	-19.91	19±8	-43±12	[8]
				$A_{3/2}$	5.39	-36.41	-1.36	-22.98	15±9	-58±13	[8]
$D_{15}(2060)$	**	1935 2063	1922 2017	$A_{1/2}$	50.63 0.83	-28.09 -14.53	26.71 2.74	-16.48 -12.84	65±12	–	[17]
				$A_{3/2}$	-17.97 1.35	10.01 -20.16	-8.99 -2.92	2.06 -17.67	55^{+15}_{-35}	–	[17]
$F_{15}(1680)$	****	1695	1734	$A_{1/2}$	-45.91	32.65	-29.98	22.25	-15±6	29±10	[8]
				$A_{3/2}$	42.16	-12.85	24.10	-6.95	133±12	-33±9	[8]
$F_{15}(1860)$	**	1892 1918	1933 1978	$A_{1/2}$	-9.86 -5.33	-11.41 17.12	1.22 -5.41	-13.86 4.31	20±12	–	[17]
				$A_{3/2}$	-0.41 -5.34	-23.28 6.48	-0.60 -2.21	-11.28 -2.67	50±20	–	[17]
$F_{15}(2000)$	**	2082	1978 2062	$A_{1/2}$	-0.05	0.59	-5.41 32.96	4.31 -21.35	35±15	–	[17]
				$A_{3/2}$	-0.02	0.61	-2.21 -16.72	-2.70 6.06	50±14	–	[17]
$F_{17}(1990)$	**	1954	1997	$A_{1/2}$	-2.98	-9.19	-3.94	-3.22	42±14/30±29 40	–/-1 -69	[17]/ [129] [131]
				$A_{3/2}$	-3.96	-11.81	0.39	-5.88	58±12/86±60 4	–/-178 -72	[17]/ [129] [131]
$G_{17}(2190)$	****	1986	1980	$A_{1/2}$	-27.72	8.47	-12.42	2.69	-65±8	–	[17]
				$A_{3/2}$	19.04	-13.45	8.80	-6.48	35±17	–	[17]
$G_{19}(2250)$	****	2181	2169	$A_{1/2}$	1.26	-11.16	2.18	-6.65	$\lvert A^p_{\frac{1}{2}}\rvert < 10$	–	[17]
				$A_{3/2}$	1.64	-13.70	-0.27	-6.54	$\lvert A^p_{\frac{1}{2}}\rvert < 10$	–	[17]
$H_{19}(2220)$	****	2183	2159	$A_{1/2}$	22.06	-13.65	10.63	-6.93	$\lvert A^p_{\frac{1}{2}}\rvert < 10$	–	[17]
				$A_{3/2}$	-17.40	7.04	-7.78	3.05	$\lvert A^p_{\frac{1}{2}}\rvert < 10$	–	[17]
$I_{1,11}(2600)$	***	2394	2342	$A_{1/2}$	14.06	-5.45	-5.56	-1.89	–	–	–
				$A_{3/2}$	-10.07	5.97	-4.07	2.46	–	–	–

4.2.8 $\Delta(1232) \leftrightarrow N$ transition form factors

The $\Delta \leftrightarrow N$ electric and magnetic transition form factors between the ground-state nucleon and the $P_{33}(1232)$-state are related to the helicity amplitudes according to Eqs. (2.127a), (2.127b) and (2.130). In Fig. 4.64

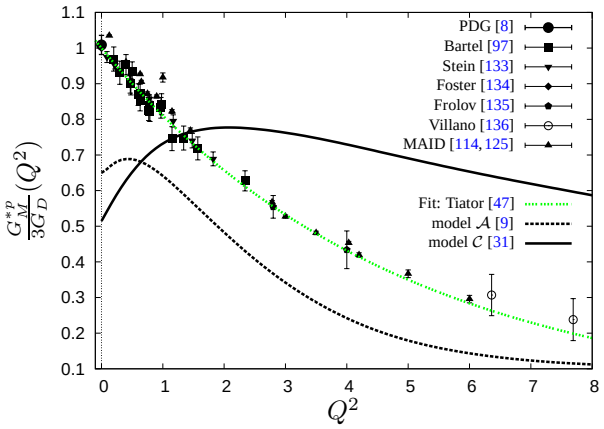

Fig. 4.64: Comparison of $\Delta(1232)$ magnetic transition form factor G_M^{*p} calculated within model $\mathcal{C}$ (solid line) and model $\mathcal{A}$ (dashed line). See also caption to Fig. 4.14.

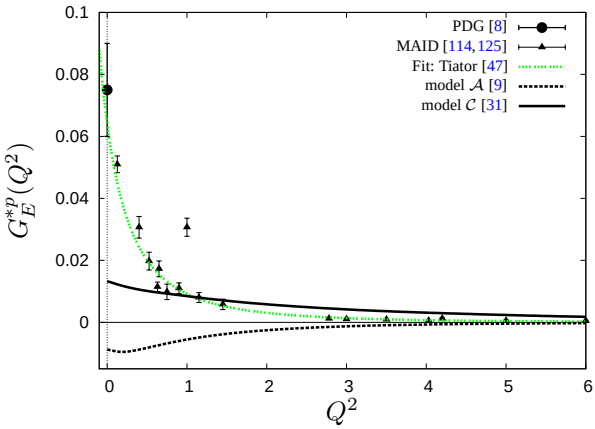

Fig. 4.65: Comparison of $\Delta(1232)$ electric transition form factor G_E^{*p} calculated within model $\mathcal{C}$ (solid line) and model $\mathcal{A}$ (dashed line). See also caption to Fig. 4.14.

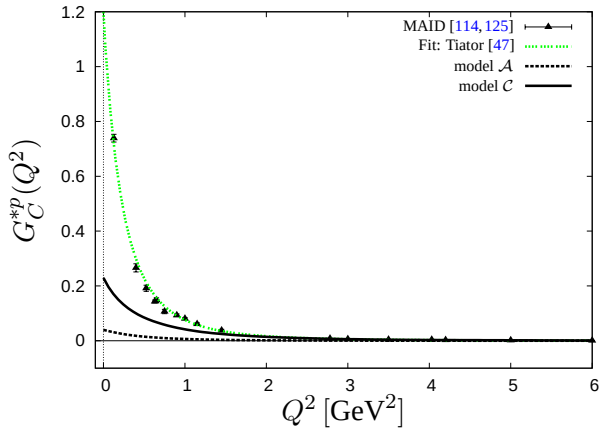

Fig. 4.66: Comparison of $\Delta(1232)$ Coulomb transition form factor G_E^{*p} calculated within model $\mathcal{C}$ (solid line) and model $\mathcal{A}$ (dashed line). See also caption to Fig. 4.14.

the calculated magnetic transition form factor divided by thrice the standard dipole form factor is compared to experimental data and analyses. This representation enhances the discrepancies between the calculated and experimental results: Although model $\mathcal{A}$ still gives a fair description at larger momentum transfers, albeit in general too small, model $\mathcal{C}$ yields too large values in this regime. In both models the values at low momenta are too small, a discrepancy which this calculation shares with virtually all calculations within a constituent quark model. Usually this is regarded to be an indication of effects due to the coupling to pions. In Fig. 4.65 we also present to corresponding electric transition form factor. Only model $\mathcal{C}$ agrees with the PDG-data [8] of the MAID-analysis [114, 125], whereas model $\mathcal{A}$ even has the wrong sign. In model $\mathcal{A}$ we recalculated the form factor with a higher numerical accuracy than was done by Merten *et al.* in [9]. The Coulomb transition form factor is displayed in Fig. 4.66. Although the calculated result in model $\mathcal{C}$ is significantly larger than in model $\mathcal{A}$, both are too small to account for the data from the MAID-analysis [47, 114, 125].

4.3 A modified quark-quark confinement potential

A possible modification of the description of confinement can be achieved by another choice of its Dirac-structure. On the basis of the Dirac-structure of the one-gluon exchange as used by Löring *et al.* [7] and Murota [55], see also Eq. (3.8), we found the following confinement potential to yield satisfactory results. Moreover, we introduce the confinement potential as a two-body interaction given by

$$\mathcal{V}^{(2)}(x_1, x_2; x_1', x_2') := V_{conf}(\mathbf{x})\delta(x^0)\delta^{(4)}(x_1 - x_1')\delta^{(4)}(x_2 - x_2')\,, \tag{4.12}$$

with $x := x_1 - x_2$ and

$$V_{conf}(\mathbf{x}) = ar\left(\gamma^0 \otimes \gamma^0 - \tfrac{1}{3}(\boldsymbol{\gamma}\cdot\otimes\boldsymbol{\gamma}) - \tfrac{1}{2}S_{12}(\hat{\mathbf{x}})\right)\,. \tag{4.13}$$

Here, $S_{12}(\hat{\mathbf{x}})$ represents a tensor of rank 2 and is defined as $S_{12}(\hat{\mathbf{x}}) := \frac{1}{3}[\boldsymbol{\gamma}\cdot\otimes\boldsymbol{\gamma}] - [(\boldsymbol{\gamma}\cdot\hat{\mathbf{x}})\otimes(\boldsymbol{\gamma}\cdot\hat{\mathbf{x}})]$. Moreover, we have defined $r := |\mathbf{x}|$ and $\hat{\mathbf{x}} := \frac{\mathbf{x}}{r}$.

4.3.1 Model parameters

The prescription of the modified confinement does not introduce new model parameters, because the Dirac-structure of the linear potential is fixed by Eq. (4.13) and thus needs no further parameters. Additionally, to the slope we have to choose the offset Dirac-structure and the complete confinement involves finally two parameters, where the offset Dirac-structure can be chosen judiciously as before in model $\mathcal{A}$ or $\mathcal{C}$. The new model will be called model $\mathcal{D}$ and includes a confinement potential according to Eq. (4.13). Furthermore, it is possible to include additionally the new spin-flavour dependent interaction from the previous section, *i.e.* combining both approaches, this is called model $\mathcal{E}$. For the determination of the model parameters the same compilation of resonances as for model $\mathcal{A}$ and $\mathcal{C}$ have been used, these are summarised in Tab. 4.2. The parameter values are listed in Tab. 4.12, where the value of the slope parameter of the confinement have the same magnitude for the models $\mathcal{C}$, $\mathcal{D}$ and $\mathcal{E}$. Here, the offset confinement Dirac-structure is chosen as $\Gamma_0 = \mathbb{1}\otimes\mathbb{1}\otimes\mathbb{1}$ for both models.

Table 4.12: Model parameters for the new models $\mathcal{D}$ and $\mathcal{E}$ within the modified confinement potential. See also text and Tab. 3.3.

parameter		model $\mathcal{D}$	model $\mathcal{E}$
masses	m_n [MeV]	300.0	450.0
	m_s [MeV]	680.0	675.0
confinement	a [MeV]	-536.2	-376.6
	b [MeV/fm]	220.8	190.0
instanton-induced interaction	g_{nn} [MeVfm^3]	224.9	351.4
	g_{ns} [MeVfm^3]	148.1	284.2
	λ [fm]	0.4	0.4
octet exchange	$\frac{g_8^2}{4\pi}$ [MeVfm^3]	–	0.0
singlet exchange	$\frac{g_0^2}{4\pi}$ [MeVfm^3]	–	2098.5
	λ_0 [fm]	–	0.25

Table 4.13: Optimal values of the length scale β for various baryons in the models $\mathcal{D}$ and $\mathcal{E}$.

baryon	$2J+1$	β [fm] model $\mathcal{D}$	β [fm] model $\mathcal{E}$
Δ	2	0.60	0.45
	4	0.80	0.45
	6, 8	0.80	0.55
	$\geq$10	0.80	0.60
N	2	0.60	0.45
	$\geq$4	0.80	0.50
Λ	2	0.55	0.45
	$\geq$4	0.60	0.50
Σ, Ξ	2, 4	0.50	0.40
	$\geq$6	0.50	0.45
Ω	$\geq$2	0.80	0.40

Note, that the optimal octet-coupling for model $\mathcal{E}$ turns out to be vanishing. Then, the singlet exchange contribution can also be considered as a part of the confinement potential. Accordingly, model $\mathcal{D}$ and $\mathcal{E}$ only differ by an additional spin-dependent short-range contribution to the confinement potential. In this interpretation, the confinement in model $\mathcal{E}$ includes a repulsive short-range part (additionally to its linear and constant part), which has the Dirac-structure $\gamma^5\otimes\gamma^5$. For completeness, the scale dependence is shown in Fig. 4.67 for the

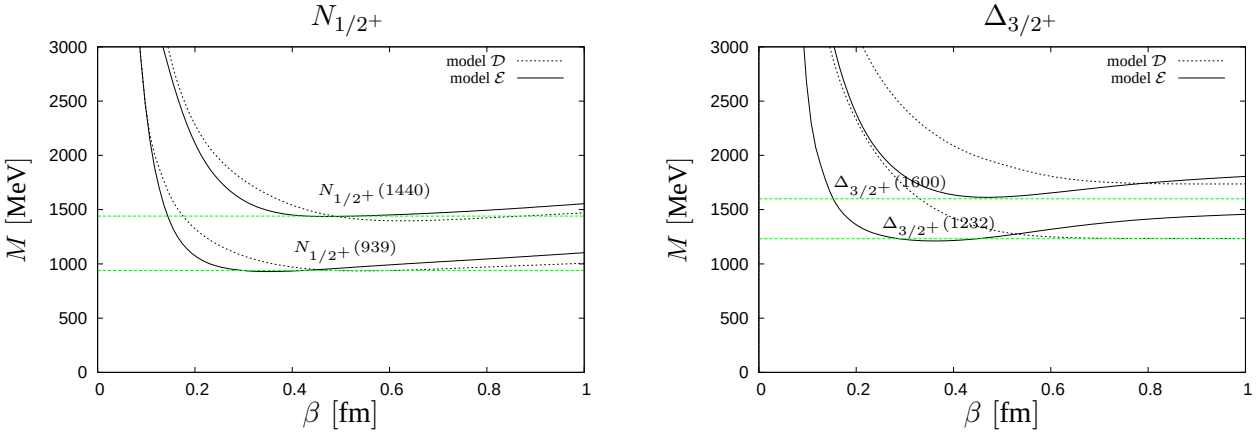

Fig. 4.67: Scale dependence of the ground- and its first excited states shown for model $\mathcal{D}$ and $\mathcal{E}$, respectively. On the left side we have displayed the $N_{1/2}$ nucleon resonances and on the right side the $\Delta_{3/2}$-resonances. The optimal β is chosen close to the average of the positions of the minima of the ground- and first excited states. For $N_{1/2}$-states, β has been chosen at $\beta = 0.60\,\text{fm}$ for model $\mathcal{D}$ and $\beta = 0.45\,\text{fm}$ for model $\mathcal{E}$, respectively. On the right side, for the $\Delta_{3/2}$-states, β has been chosen in the same way as for the nucleon $N_{1/2}$. All other baryon states has been checked in the same way. Their results are summarised in Tab. 4.13. The curves are calculated at $N_{\text{max}} = 20$ for the nucleon $N_{1/2}$ and $N_{\text{max}} = 18$ for all other baryons.

$N_{1/2}$- and $\Delta_{3/2}$-states. The plots are calculated with $N_{\text{max}} = 18$ and $N_{\text{max}} = 20$ oscillator shells, respectively. Tab. 4.13 summarises the optimal length scales used in the calculations of Δ-, nucleon- and hyperon-spectra.

4.3.2 Δ- and Ω-spectrum

As in the discussion of model $\mathcal{A}$ and $\mathcal{C}$, we start with the discussion of the Δ-spectra for model $\mathcal{D}$ and $\mathcal{E}$. They are displayed in Fig. 4.68. On the left side of each column it can be verified, that, compared with the Δ-spectra shown in Fig. 3.2, model $\mathcal{D}$ describes the states in similar fashion as model $\mathcal{A}$ from Löring *et al.* [5–7], also compare Tabs. 4.5 and 4.14. This property is surprising, because model $\mathcal{A}$ and $\mathcal{D}$ have different confinement Dirac-structures and consequently have different values for the parameters as is evident from a comparison of Tabs. 4.3 and 4.15. In model $\mathcal{D}$, the $\Delta_{3/2^+}(1600)$-state as well as the three excited negative parity Δ^*-states, $\Delta_{1/2^-}(1900)$, $\Delta_{3/2^-}(1940)$ and $\Delta_{5/2^-}(1930)$, are not reproduced and the predictions of model $\mathcal{D}$ are close to those of model $\mathcal{A}$. Furthermore, the mass-splitting of the $\Delta_{5/2^+}$-states close to 1900 MeV is slightly smaller compared to that of model $\mathcal{A}$. Additionally, both states are shifted slightly downwards. In comparison to model $\mathcal{A}$ and $\mathcal{D}$, model $\mathcal{E}$ reproduces the spectra much better, as did the previously discussed model $\mathcal{C}$. Most of the Δ-states can be reproduced by model $\mathcal{E}$: As in model $\mathcal{C}$ and we can thus account for the $\Delta_{1/2^-}(1900)$-, $\Delta_{3/2^-}(1940)$-, $\Delta_{5/2^-}(1930)$- and $\Delta_{3/2^+}(1600)$-states as well. Partially, model $\mathcal{E}$ even improves the prediction of these states, *e.g.* the $D_{33}(1700)$-groundstate, which was predicted too low in model $\mathcal{C}$ and is now shifted slightly upwards in the direction of the experimental mass.

In the Ω-spectrum, displayed on the right side in Fig. 4.72, we find also a very good agreement with the single Ω-resonance for both models. In the next subsection we will analyse the N-spectrum for model $\mathcal{D}$ and $\mathcal{E}$.

4.3.3 N-spectrum

The N-spectrum is indeed also well described by both models as shown in Fig. 4.69. The results for model $\mathcal{D}$ are again very close to those of model $\mathcal{A}$. Some states are slightly shifted, *e.g.* the mass of the Roper-resonance $N_{1/2^+}(1440)$ is now calculated too low, whereas in model $\mathcal{A}$ it was calculated to high by nearly the same amount. The next $J = \frac{1}{2}^+$-excitation, the $N_{1/2^+}(1710)$, is predicted too low at 1638 MeV. However, model $\mathcal{D}$ predicts most of the negative parity states too low, *e.g.* the $N_{1/2^-}(1535)$, is predicted at 1375 MeV. This also holds for the $J^\pi = \frac{3}{2}^-$ negative parity states, *e.g.* $N_{3/2^-}(1520)$ and $N_{3/2^-}(1700)$, which lie too low

Table 4.14: Comparison of experimental [8] and calculated masses in MeV of Δ-resonances for model $\mathcal{D}$ and $\mathcal{E}$. The corresponding spectra are shown in Fig. 4.68.

exp.	error	rating	model $\mathcal{D}$	model $\mathcal{E}$
$S_{31}(1620)$	1615-1675	****	1568	1625
$S_{31}(1900)$	1850-1950	***	–	1958
$S_{31}(2150)$	2020-2250	*	many res.	2036/2124
$P_{31}(1750)$	1708-1780	*	–	1772
$P_{31}(1910)$	1870-1920	****	1820/1851	1889
$P_{33}(1232)$	1230-1234	****	1234	1232
$P_{33}(1600)$	1550-1700	***	–	1614
$P_{33}(1920)$	1900-1970	***	1810/1859	1906/1938
$D_{33}(1700)$	1670-1770	****	1556	1612
$D_{33}(1940)$	1840-2167	*	1985	1919/1965
$D_{35}(1930)$	1920-1970	***	–	2019
$F_{35}(1905)$	1870-1920	****	1858/1899	1912/1936
$F_{35}(2000)$	1720-2325	*	>2220	>2220
$F_{37}(1950)$	1940-1960	****	1925	1938
$F_{37}(2390)$	2250-2485	*	many res.	many res.
$G_{37}(2200)$	2120-2360	*	2134/2196	2125/2178
$G_{39}(2400)$	2100-2518	**	2258	2209/2462
$H_{39}(2300)$	2137-2550	**	2367/2419	2322/2349
$H_{3,11}(2420)$	2300-2500	****	2453	2363
$I_{3,13}(2750)$	2550-2874	**	2719	2564
$K_{3,15}(2950)$	2750-3090	**	2879	2718/2849

Table 4.15: Comparison of experimental [8] and calculated masses in MeV of N-resonances for model $\mathcal{D}$ and $\mathcal{E}$. The corresponding spectra are shown in Fig. 4.69.

exp.	error	rating	model $\mathcal{D}$	model $\mathcal{E}$
$S_{11}(1535)$	1520-1555	****	1375/1531	1482
$S_{11}(1650)$	1640-1680	****	1751	1658
$S_{11}(1895)$	1880-1910	**	1751/1831	1830/1897
$P_{11}(939)$	939-939	****	938	946
$P_{11}(1440)$	1430-1470	****	1397	1437
$P_{11}(1710)$	1680-1740	***	1638	1729
$P_{11}(1880)$	1915-1845	**	1822	1861
$P_{11}(2100)$	1855-2200	*	many res.	many res.
$P_{13}(1720)$	1650-1750	****	1649	1677
$P_{13}(1900)$	1862-1900	**	1830/1842	1851/1919
$P_{13}(2040)$	2031-2065	*	2000	1999/2021
$D_{13}(1520)$	1515-1530	****	1440	1513
$D_{13}(1700)$	1650-1750	***	1562	1704
$D_{13}(1875)$	1855-1895	***	1818/1881	1823/1927
$D_{13}(2120)$	2080-2210	**	many res.	many res.
$D_{15}(1675)$	1670-1685	****	1615	1690
$D_{15}(2060)$	2045-2075	***	1921/2033	1905/2009
$F_{15}(1680)$	1675-1690	****	1701	1708
$F_{15}(1860)$	1820-1960	**	1870/1899	1930
$F_{15}(2000)$	1816-2175	**	2036	1974/2036
$F_{17}(1990)$	1855-2155	**	1954	1990
$G_{17}(2190)$	2100-2200	****	1996/2137	1951/2135
$G_{19}(2250)$	2170-2310	****	2210	2167/2270
$H_{19}(2220)$	2180-2310	****	2217	2131
$I_{1,11}(2600)$	2550-2750	***	2440	2317/2515
$K_{1,13}(2700)$	2567-3100	**	2633	2490/2705

in model $\mathcal{D}$ at $1440\,\text{MeV}$ and at $1562\,\text{MeV}$, respectively. For model $\mathcal{E}$ most of the problems of model $\mathcal{D}$ are absent, as displayed in Fig. 4.69: The Roper- as well as the $N_{1/2^-}(1535)$-resonance are reproduced rather well by model $\mathcal{E}$ at $1437\,\text{MeV}$ and $1482\,\text{MeV}$. Likewise, the $J = \frac{1}{2}$-excitations, $N_{1/2^+}(1710)$ and $N_{1/2^-}(1650)$, are well reproduced, which leads to the conclusion, that model $\mathcal{E}$ even calculated the prediction of model $\mathcal{C}$, see *e.g.* the $N_{5/2^+}(1680)$-state, which is now predicted closer to experiment. Masses of higher resonances with $J \geq \frac{7}{2}$ are in general too low in model $\mathcal{E}$, analogous to model $\mathcal{C}$. Here, model $\mathcal{D}$ underestimates the mass of the negative parity $J^\pi = \frac{7}{2}^-$, $\frac{11}{2}^-$-states less than model $\mathcal{E}$. Additionally new states, which are reported in the Bonn-Gatchina analyses from the CB-ELSA collaboration [15–17] and now already included in the new PDG-data [8], are displayed in Fig. 4.69. Model $\mathcal{E}$ accounts for most of them quite well just as model $\mathcal{C}$, see *e.g.* the new $N_{1/2^+}(1880)$-resonance. In contrast, model $\mathcal{D}$ cannot account for most of the newer resonances. One example is again the $N_{1/2^+}(1880)$-resonance, which mass is predicted at 1822 MeV by model $\mathcal{D}$. In the next subsection we will briefly discuss the results on the hyperon-spectra.

4.3.4 Hyperon-spectra

The results of model $\mathcal{D}$ and $\mathcal{E}$ within the hyperon sector (Λ-, Σ- and Ξ-baryons) are displayed in Figs. 4.70, 4.71 and 4.72. Beginning with the Λ-spectrum, displayed in Fig. 4.70, model $\mathcal{D}$ and $\mathcal{E}$ reproduce the spectra as well

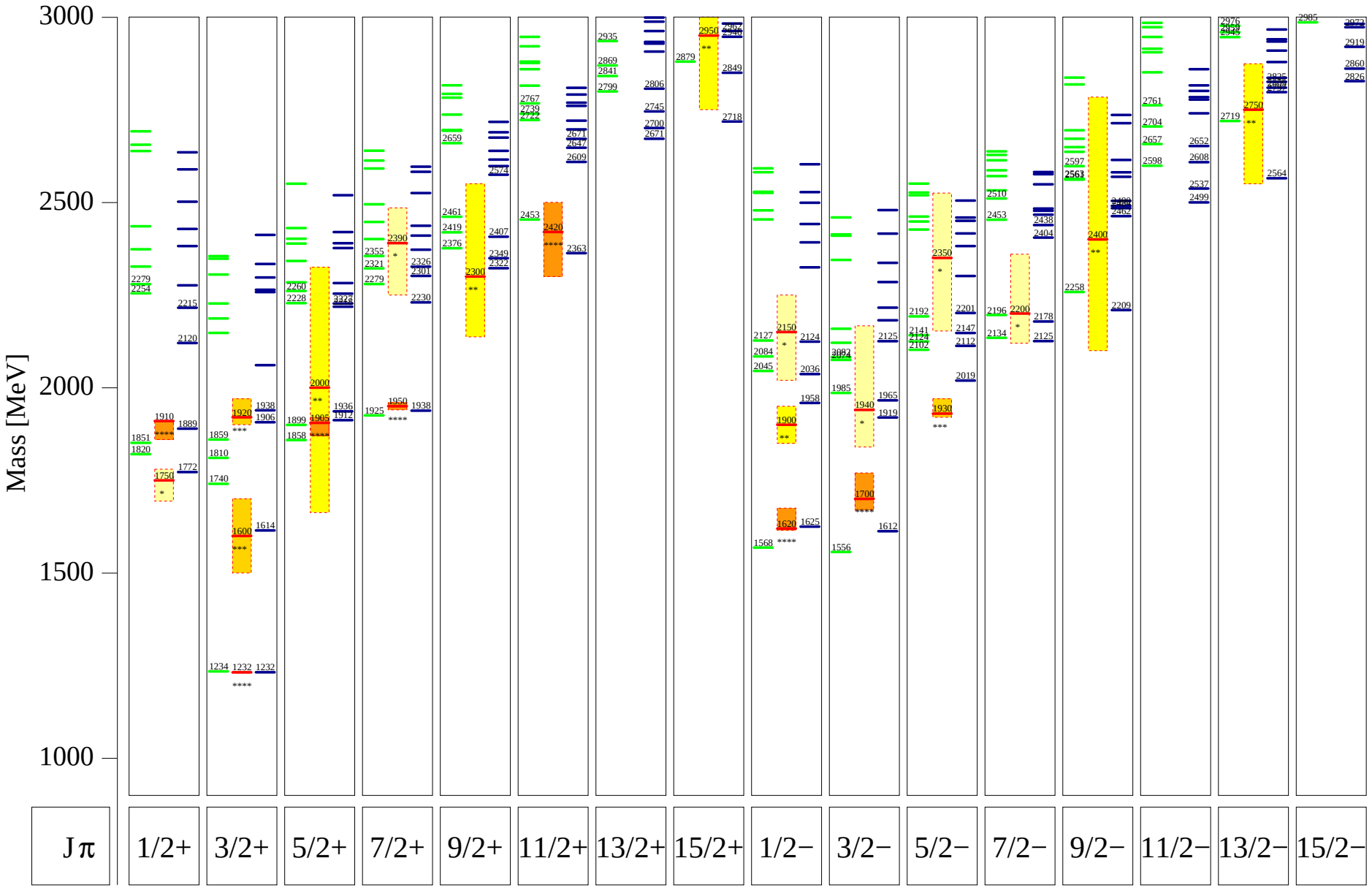

Fig. 4.68: Comparison of the Δ-spectrum calculated within the model $\mathcal{E}$ (right side of each column) with experimental data from the Particle Data Group [8] (central in each column) and with the results from model $\mathcal{D}$ (left side in each column). See also caption to Fig. 3.2.

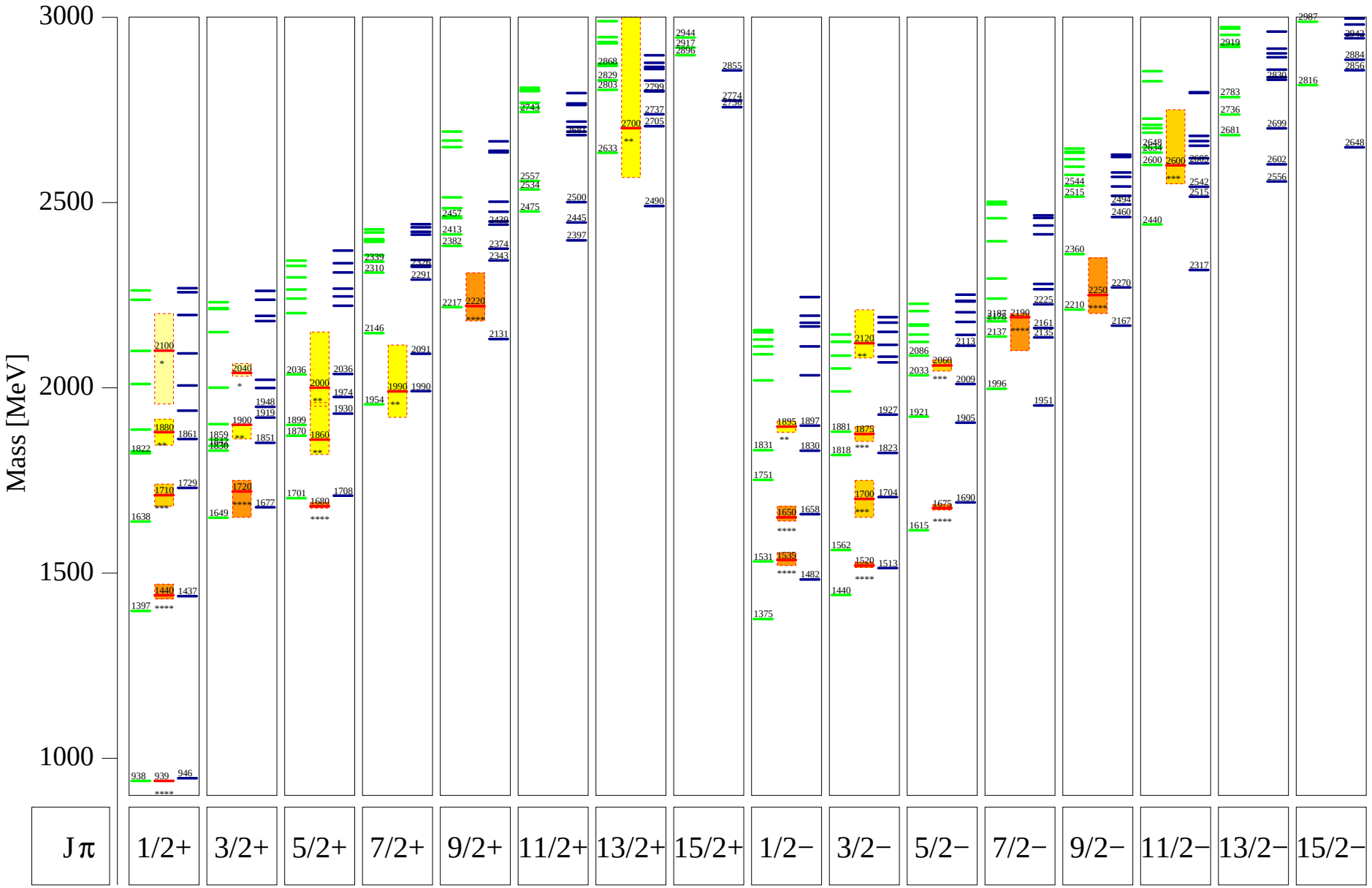

Fig. 4.69: Comparison of the N-spectrum calculated within the model $\mathcal{E}$ (right side of each column) with experimental data from the Particle Data Group [8] (central in each column) and with the results from model $\mathcal{D}$ (left side in each column). See also caption to Fig. 3.2.

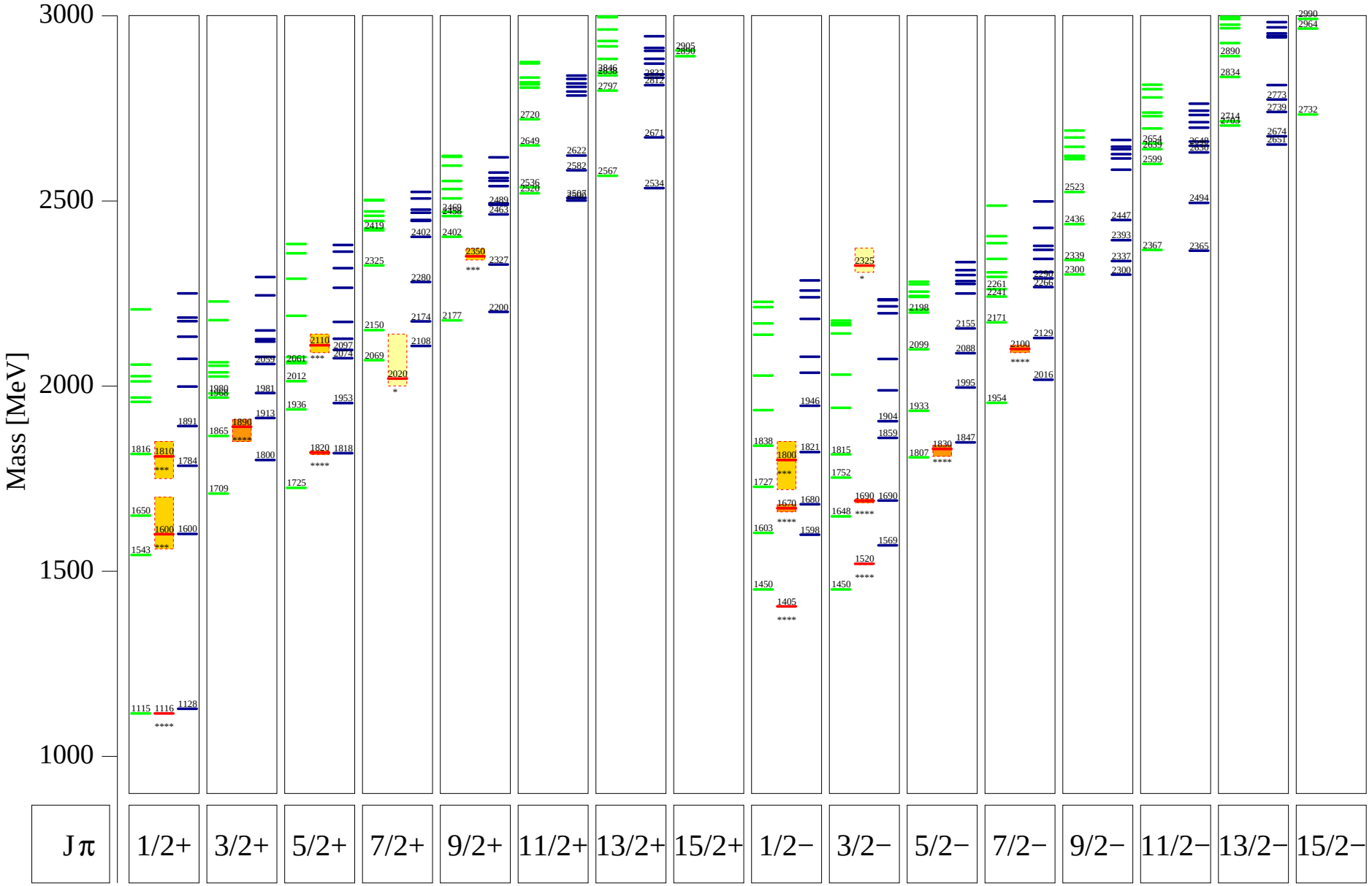

Fig. 4.70: Comparison of the Λ-spectrum calculated within the model $\mathcal{E}$ (right side of each column) with experimental data from the Particle Data Group [8] (central in each column) and with the results from model $\mathcal{D}$ (left side in each column). See also caption to Fig. 3.2.

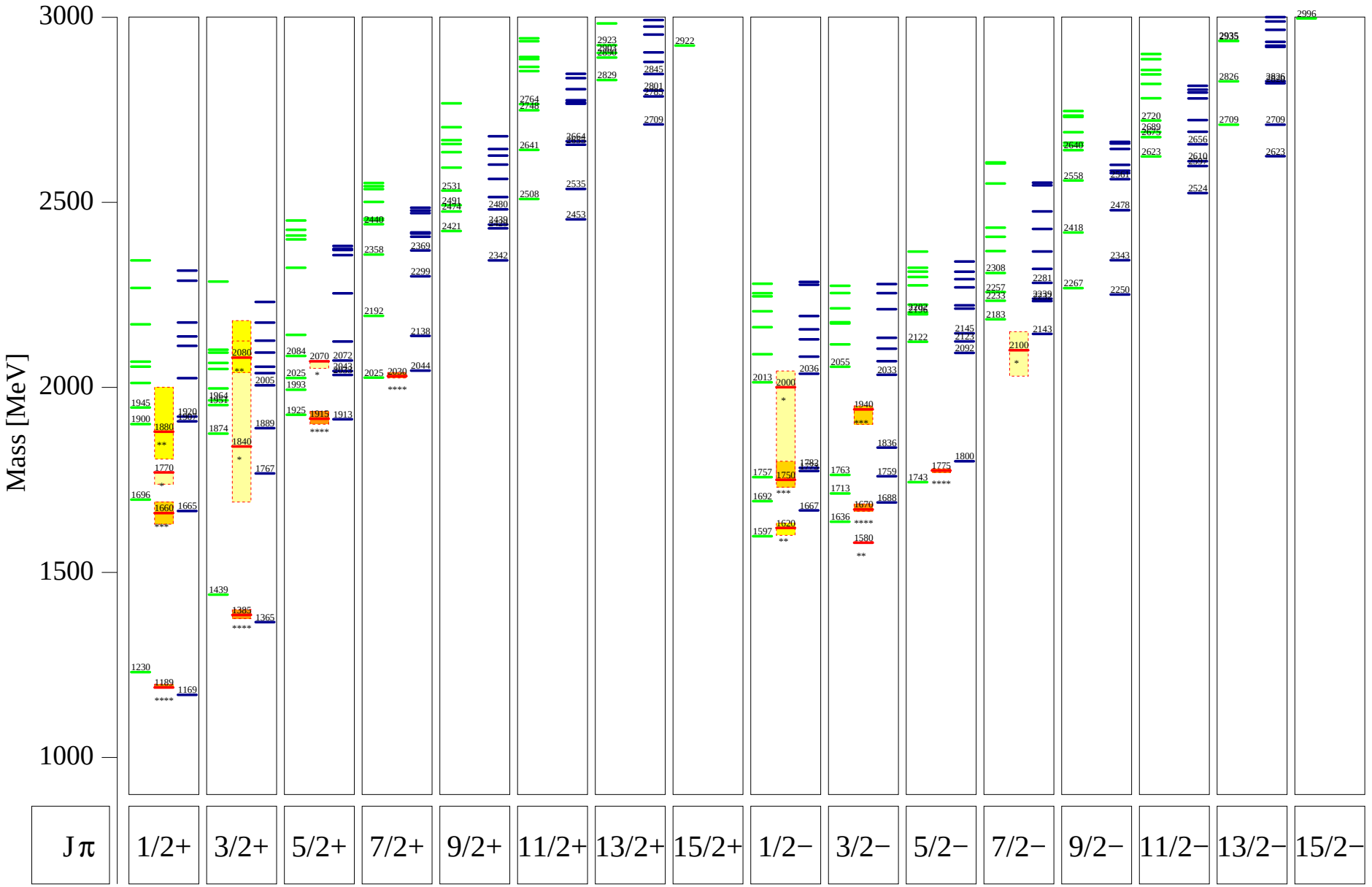

Fig. 4.71: Comparison of the Σ-Spectrum calculated within the model $\mathcal{E}$ (right side of each column) with experimental data from the Particle Data Group [8] (central in each column) and with the results from model $\mathcal{D}$ (left side in each column). See also caption to Fig. 3.2.

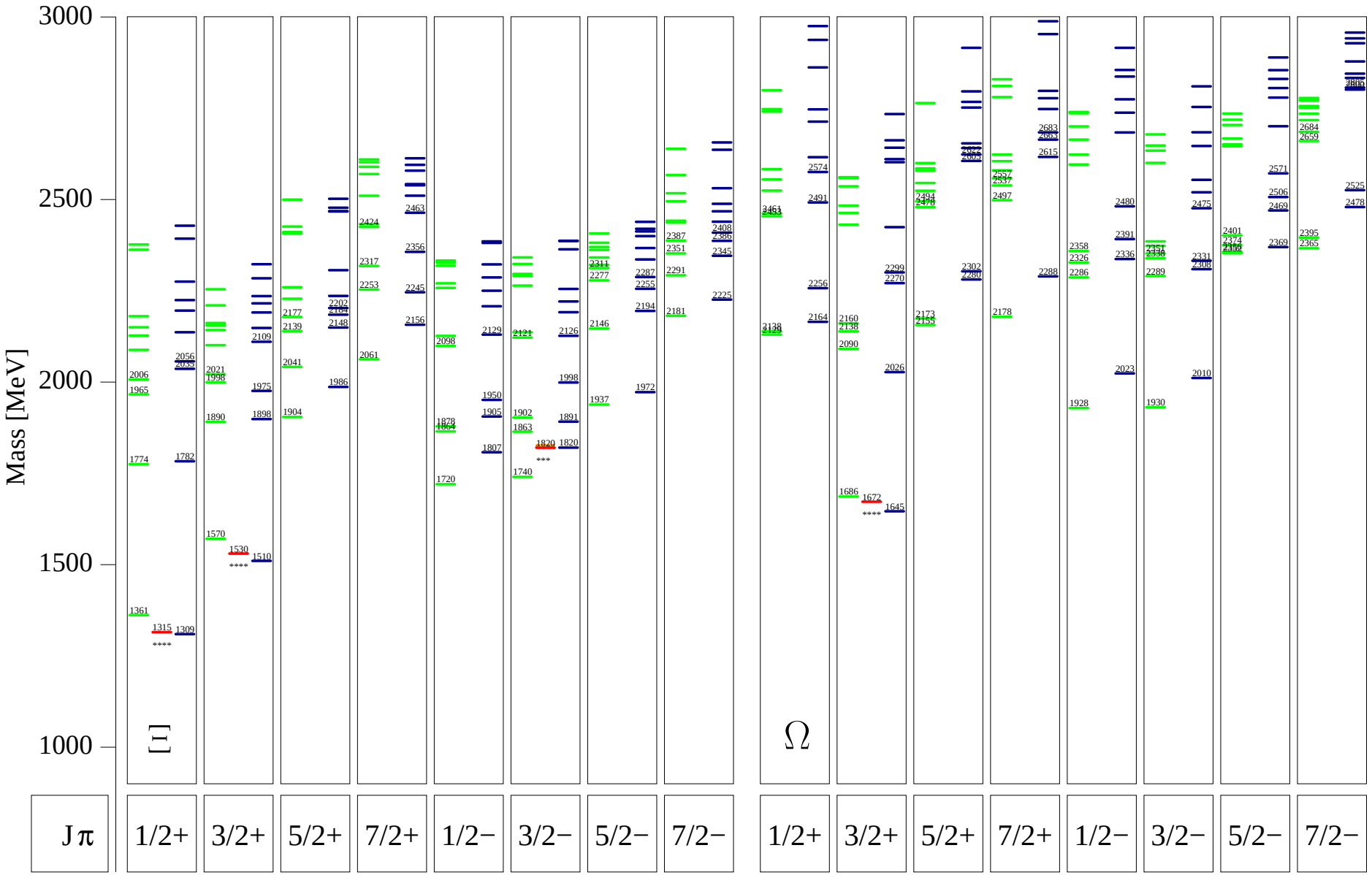

Fig. 4.72: Comparison of the Ξ-spectrum (first eight columns) and the Ω-Spectrum (rightmost eight columns) calculated within the present model $\mathcal{E}$ (right side of each column) with the experimental data from the Particle Data Group [8] (central in each column) and with the results from model $\mathcal{D}$ (left side in each column), see also caption to Fig. 3.2.

as model $\mathcal{A}$ and $\mathcal{C}$. Especially, model $\mathcal{E}$ describes the mass-splittings excellently compared to those of model $\mathcal{D}$, *e.g.* for the $J^\pi = \frac{1}{2}^+$ Roper-like resonances the first excitation $\Lambda_{1/2^+}(1600)$ is predicted at 1600 MeV.

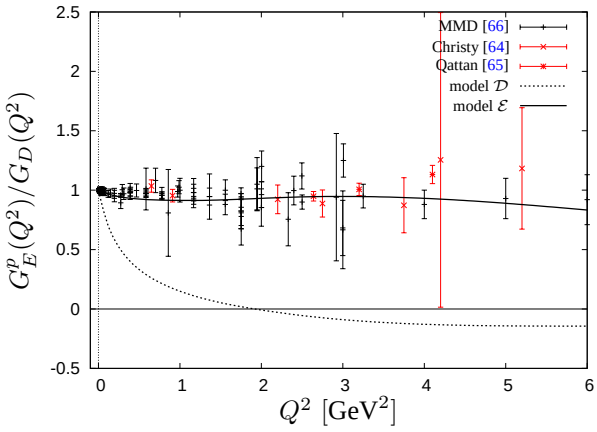

Fig. 4.73: The electric form factor of the proton divided by the dipole form $G_D(Q^2)$, Eq. (4.7). MMD-Data are taken from Mergell *et al.* [66], supplemented by data from Christy *et al.* [64] and Qattan *et al.* [65]. The solid black line represents the results from the model $\mathcal{E}$; the dashed black line those from model $\mathcal{D}$, albeit recalculated with higher numerical precision. Red data points are taken from polarisation experiments and black ones are obtained by Rosenbluth separation, see also caption to Fig. 4.8.

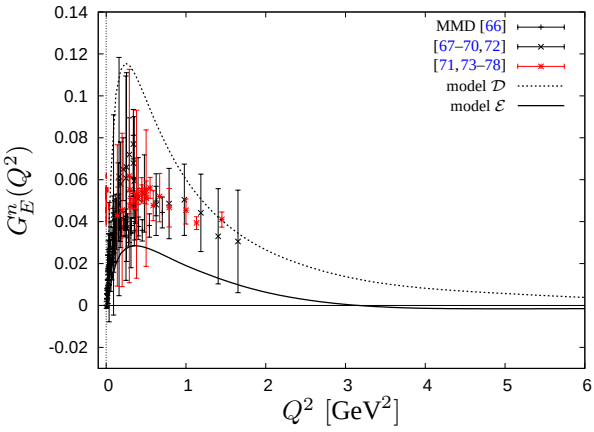

Fig. 4.74: The electric form factor of the neutron. MMD-Data are taken from the compilation of Mergell *et al.* [66]. The solid black line represents the results from the model $\mathcal{E}$; the dashed black line in the result from model $\mathcal{D}$, albeit recalculated with higher numerical precision. Red data points are taken from polarisation experiments and black ones are obtained by Rosenbluth separation, see also caption to Fig. 4.9.

But, both models cannot account for the low lying $\Lambda_{1/2^-}(1405)$-resonance, which again supports the interpretation as a meson-baryon bound-state close the $\bar{K}N$-threshold as already discussed in the previous subsection 4.2.4 for model $\mathcal{A}$ and $\mathcal{C}$. Further discussions on the nature of the $\Lambda_{1/2^-}(1405)$-resonance can be found in [57–59].

Concerning the Σ-spectrum, which is displayed in Fig. 4.71, again model $\mathcal{E}$ allows a better description of the resonances in particular for excited states. For the $J^\pi = \frac{1}{2}^+$-states, model $\mathcal{D}$ and $\mathcal{E}$ reproduces the first excitation, *i.e.* the one star rated $\Sigma_{1/2^+}(1660)$-state however, without reproducing the second excitation, the $\Sigma_{1/2^+}(1770)$-state. In opposite to that, the older model $\mathcal{A}$ predicts the $\Sigma_{1/2^+}(1770)$-resonance, but not the first excitation. The third excitation, $\Sigma_{1/2^+}(1880)$, is also reproduced by both models rather well. Furthermore, there is no satisfactory description of the $\Sigma_{3/2^-}(1580)$-resonance for both models. The scarce data of the Ξ-spectrum are satisfactorily reproduced by both models, as shown in Fig. 4.72 on the left side.

Table 4.16: Static properties of the nucleon for model $\mathcal{D}$ and $\mathcal{E}$. The static values are extrapolated from a dipole-shape-like fit due to Eqs. (4.8) and (4.11).

	model $\mathcal{D}$	model $\mathcal{E}$	exp.	ref.
$\mu_p[\mu_N]$	2.856	2.632	2.793	[8]
$\mu_n[\mu_N]$	-1.756	-1.688	-1.913	[8]
$\sqrt{\langle r^2\rangle_E^p}$[fm]	1.204	0.857	0.847	[66]
$\langle r^2\rangle_E^n$[fm]^2	-0.367	-0.100	-0.123±0.004	[66]
$\sqrt{\langle r^2\rangle_M^p}$[fm]	1.253	0.861	0.836	[66]
$\sqrt{\langle r^2\rangle_M^n}$[fm]	1.195	0.836	0.850	[66]
g_A	1.283	1.287	1.267±0.0035	[8, 79]
$\sqrt{\langle r^2\rangle_A}$[fm]	1.042	0.701	0.67±0.01	[80]

4.3.5 Electroweak form factors of the nucleon

The discussion of electroweak form factors for the models $\mathcal{D}$ and $\mathcal{E}$ starts again with the electric proton form factor, which is displayed in Fig. 4.73. The electric proton form factor is divided by its dipole-shape, see Eq. (4.7). Based on the fact that the baryon spectra, discussed in the previous subsections 4.3.2, 4.3.3, 4.3.4 for model $\mathcal{D}$ and $\mathcal{E}$, are very similar to that ones of model $\mathcal{A}$ and $\mathcal{C}$, respectively, one could expect that the corresponding form factors of the models $\mathcal{D}$ and $\mathcal{E}$ should also be similar. This is substantiated by comparing Fig. 4.73 with Fig. 4.8 of model $\mathcal{A}$ and $\mathcal{C}$, respectively. For the electric proton form factor we find an excellent description of model $\mathcal{E}$, whereas model $\mathcal{D}$ does not describe the experimental data similar to model $\mathcal{A}$. In particular, the electric proton form factor of model $\mathcal{D}$ has an unphysical node as does model $\mathcal{A}$. In contrast to model $\mathcal{D}$, model $\mathcal{E}$ is consistent with the data and gives a satisfactory description of the electric proton form factor up to $Q^2 = 6.0\,\mathrm{GeV}^2$.

The electric neutron form factor, displayed in Fig. 4.74, is also reproduced quite well by model $\mathcal{E}$ albeit that the data are slightly underestimated. The maximum agrees with the position of the maximum in the data, but the curve shows a node around $Q^2 = 3.0\,\mathrm{GeV}^2$ in contrast to the experiment. Model $\mathcal{D}$ overestimates the data by more than a factor 2 in the region $Q^2 \lesssim 1\,\mathrm{GeV}^2$ similar as model $\mathcal{A}$; the position of the maximum is also predicted too low. Figs. 4.75 and 4.76 show the predictions of the magnetic proton and neutron form

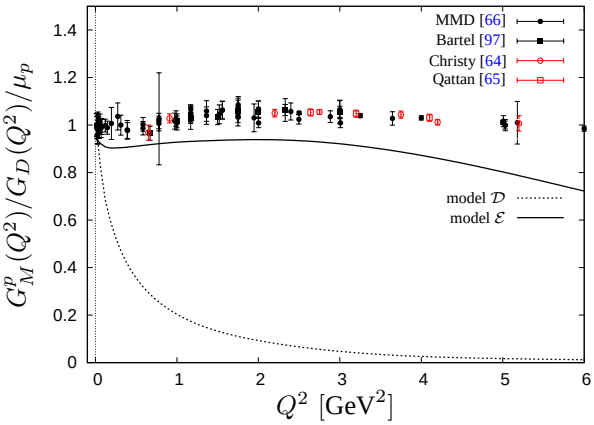

Fig. 4.75: The magnetic form factor of the proton divided by the dipole form $G_D(Q^2)$, Eq. (4.7) and the magnetic moment of the proton $\mu_p = 2.793\,\mu_N$. MMD-Data are taken from the compilation of Mergell *et al.* [66]. The solid black line represents the results from the model $\mathcal{E}$; the dashed black line in the result from model $\mathcal{D}$, albeit recalculated with higher numerical precision. Additionally, polarisation experiments are marked by red. The black marked data points are obtained by Rosenbluth separation, see also caption to Fig. 4.10.

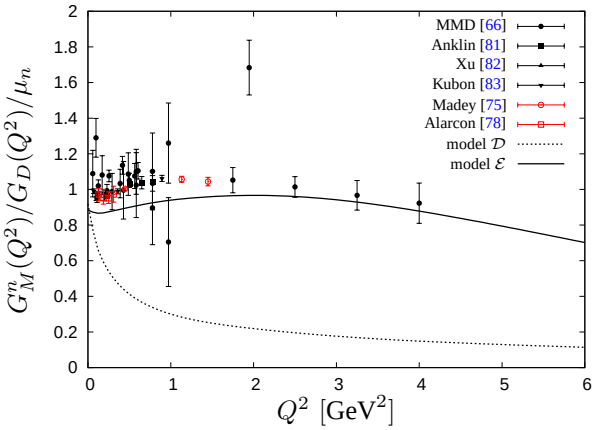

Fig. 4.76: The magnetic form factor of the neutron divided by the dipole form $G_D(Q^2)$, Eq. (4.7) and the magnetic moment of the neutron $\mu_n = -1.913\,\mu_N$. MMD-Data are taken from the compilation by Mergell *et al.* [66] and from more recent results from MAMI [81,83]. The solid black line represents the results from the model $\mathcal{E}$; the dashed black line in the result from model $\mathcal{D}$, albeit recalculated with higher numerical precision. Additionally, polarisation experiments are marked by red data points. The black marked ones are obtained by Rosenbluth separation, see also caption to Fig. 4.11.

factor divided by their dipole-shapes (see Eq. (4.7)), respectively. For the proton, both models underestimate the data. Only at the photon point, both models can reproduce the magnetic moments, see also Tab. 4.16 for numerical values. The curve for model $\mathcal{D}$ drops very fast, similar as model $\mathcal{A}$, which also decreases very fast away from the photon point as displayed in Fig. 4.11. Furthermore, model $\mathcal{E}$ cannot reproduce the magnetic form factor as well as model $\mathcal{C}$. In case of the corresponding magnetic neutron form factor, model $\mathcal{E}$ matches the data quite well in opposite to model $\mathcal{D}$, which drops to fast again. Note, that model $\mathcal{E}$ does not yield an improved description of the magnetic neutron form factor, when compared with the results of model $\mathcal{C}$, shown in Fig. 4.11.

Table 4.17: Octet hyperon magnetic moments μ for model $\mathcal{D}$ and $\mathcal{E}$ calculated as in [13, 14]. The values are given in units of μ_N.

hyp.	model $\mathcal{D}$	model $\mathcal{E}$	PDG [8]
Λ	-0.583	-0.618	-0.613 $\pm$0.004
Σ^+	2.673	2.360	2.458 $\pm$0.010
Σ^0	0.774	0.711	-
Σ^-	-1.126	-0.875	-1.160 $\pm$0.025
Ξ^0	-1.070	-0.914	-1.250 $\pm$0.014
Ξ^-	-0.371	-0.408	-0.651$\pm$0.0025

Table 4.18: Decuplet hyperon magnetic moments μ for model $\mathcal{D}$ and $\mathcal{E}$ calculated as in [13, 14]. The values are given in units of μ_N.

hyp.	model $\mathcal{D}$	model $\mathcal{E}$	PDG [8]
Δ^{++}	4.368	4.239	3.7 to 7.5
Δ^+	2.184	2.119	$2.7^{+1.0}_{-1.3} \pm 1.5 \pm 3$
Δ^0	0.0	0.0	
Δ^-	-2.184	-2.119	
Σ^{*+}	2.815	2.411	
Σ^{*0}	0.377	0.153	
Σ^{*-}	-2.062	-1.936	
Ξ^{*0}	0.802	0.262	
Ξ^{*-}	-1.730	-1.823	
Ω^-	-1.428	-1.294	-2.02 ± 0.05

Considering the ratio of $\frac{\mu_p G_E^p}{G_M^p}$, as displayed in Fig. 4.77, model $\mathcal{E}$ matches the data obtained from the Rosenbluth separation [96–100] better than the data taken from polarisation experiments. Here, model $\mathcal{E}$ leads to results intermediate between the Rosenbluth separated and polarisation data as shown in Fig. 4.12. This results for model $\mathcal{E}$ can be traced back to corresponding magnetic proton form factor, which underestimates the data. As expected from the magnetic and electric form factors (displayed in Figs. 4.73 and 4.75), model $\mathcal{D}$ underestimates the ratio of electric and magnetic proton form factors, again similar to the prediction of model $\mathcal{A}$. Thus, neither of the new models predicts the polarisation data [85–95] accurately.

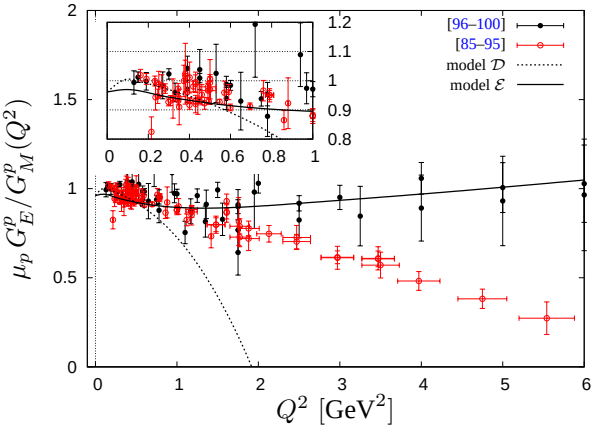

Fig. 4.77: The ratio $\frac{\mu_p G_E^p}{G_M^p}$ compared to recent JLAB data (see legend). In the insert the low momentum transfer region is enlarged. The solid black line is the result of model $\mathcal{E}$, the dashed black line the result in model $\mathcal{D}$. Red data points are taken from polarisation experiments and the black ones are obtained from Rosenbluth separation, see also caption to Fig. 4.12.

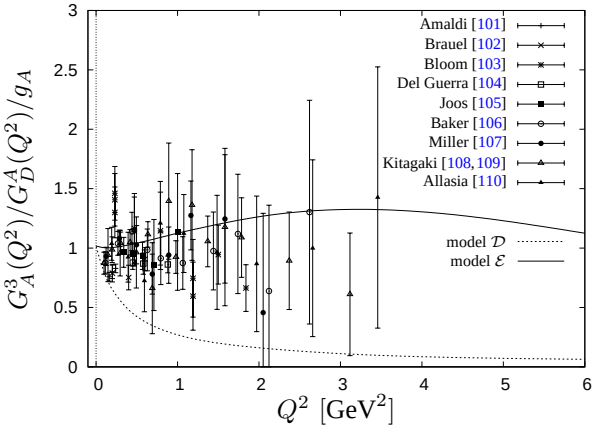

Fig. 4.78: The axial form factor of the nucleon divided by the axial dipole form in Eq. (4.8) and the axial coupling $g_A = 1.267$. The black solid line is the result of model $\mathcal{E}$, the blue dashed line the result in model $\mathcal{D}$. Experimental data are taken from the compilation by Bernard *et al.* [80]. See also caption to Fig. 4.13.

The axial form factor divided by its dipole-shape is shown in Fig. 4.78, where the dipole-shape is given by Eq. (4.11). As shown in Fig. 4.78, model $\mathcal{D}$ cannot reproduce the data, whereas model $\mathcal{E}$ matches the data in

particular for higher momenta. In the vicinity of $Q^2 = 0$, both models reproduces the experiment value, but model $\mathcal{D}$ drops again very fast now in contrast to the model $\mathcal{A}$, which does account for the axial form factor. The curves of model $\mathcal{C}$ and $\mathcal{E}$ runs very close to each other.

Tab. 4.16 summarises the static properties extracted from the electroweak form factors by fitting them according to Eqs. (4.8) and (4.11). It is obvious, that model $\mathcal{D}$ overestimates most of the quantities in particular the charge radii, which depend on the derivatives of the form factors, see Eqs. (4.9a) and (4.9b). Nevertheless, the magnetic moments and the axial coupling agree with the data reasonably. Model $\mathcal{E}$ reproduces all static quantities quite well and the magnetic moments being slightly too small in magnitude. The radii are reproduced also close to the experiment and the results are similar to these shown in Tab. 4.7 for model $\mathcal{C}$. The magnetic moments of the octet and decuplet hyperons are summarised in the Tabs. 4.17 and 4.18. Most of the values are close to the experiment [8], but there are still some mismatches, *e.g.* the values for the Ξ-resonances in the octet groundstate. Here, model $\mathcal{D}$ reproduces the data better than model $\mathcal{E}$, which is surprising in view of the other results obtained so far.

4.3.6 Some helicity amplitudes

The conclusions from the discussion of helicity amplitudes for model $\mathcal{D}$ and $\mathcal{E}$ are very similar to the discussion for model $\mathcal{A}$ and $\mathcal{C}$, respectively. We therefore restrict the discussion on only a few baryon resonances in the N- and Δ-sector.

$N^* \leftrightarrow N$ helicity amplitudes

We now turn to the discussion of $N^* \leftrightarrow N$ helicity amplitudes for each angular momentum J and parity π.

The J $= \frac{1}{2}$ resonances: In Figs. 4.79 and 4.80 we show the transverse and longitudinal helicity amplitudes of model $\mathcal{D}$ and $\mathcal{E}$ for the $N_{1/2^-}(1535)$ resonance. As expected, the helicity amplitudes of model $\mathcal{D}$ and $\mathcal{E}$

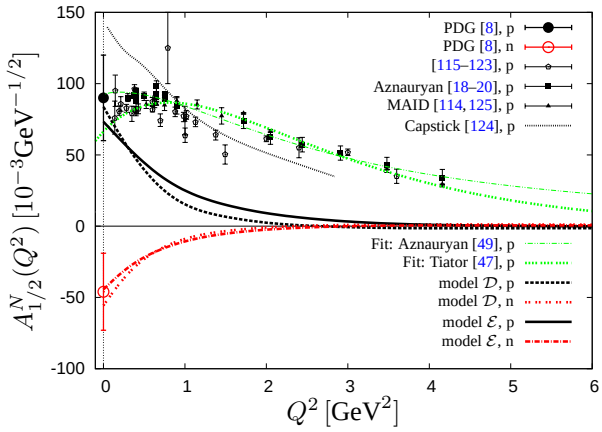

Fig. 4.79: Comparison of the $S_{11}(1535)$ transverse helicity amplitude $A^N_{1/2}$ for from the proton and the neutron calculated in the model $\mathcal{E}$ (solid and dashed-dotted line) and model $\mathcal{D}$ (dashed lines) to experimental data [8, 17–20, 114–123, 125]. The dotted line is the result obtained by Keister and Capstick [124]. Additionally, recent fits obtained by Tiator *et al.* [47] and by Aznauryan *et al.* [49] are displayed as green dotted and dashed-dotted lines, respectively. See also caption to Fig. 4.14.

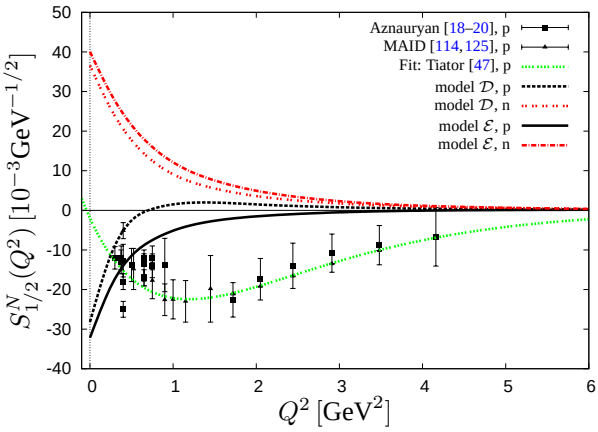

Fig. 4.80: Comparison of the $S_{11}(1535)$ longitudinal helicity amplitude $S^N_{1/2}$ of proton and neutron calculated in model $\mathcal{C}$ (solid and dashed-dotted line) and model $\mathcal{A}$ (dashed lines) with experimental data [18–20, 114, 125]. Note, that for the data points of the MAID-analysis by Tiator *et al.* [125] no errors are quoted. See also caption to Fig. 4.79.

are very similar to those of model $\mathcal{A}$ and $\mathcal{C}$, respectively, which were shown in Figs. 4.14 and 4.15. Here, the

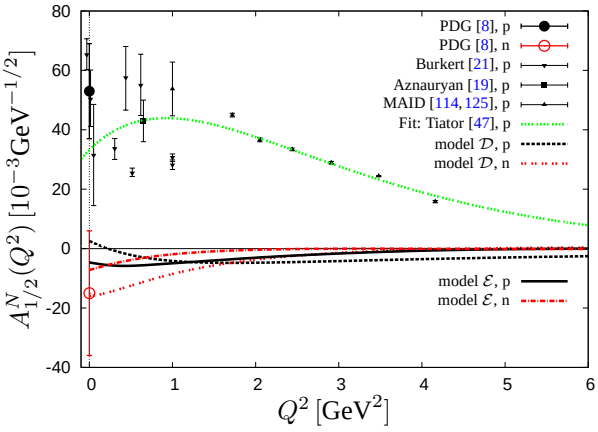

Fig. 4.81: Comparison of the $S_{11}(1650)$ transverse helicity amplitude $A^N_{1/2}$ of proton and neutron calculated in model $\mathcal{E}$ (solid and dashed-dotted line) and model $\mathcal{D}$ (dashed lines) to experimental data from [8, 19, 21, 114, 125]. See also caption to Fig. 4.79.

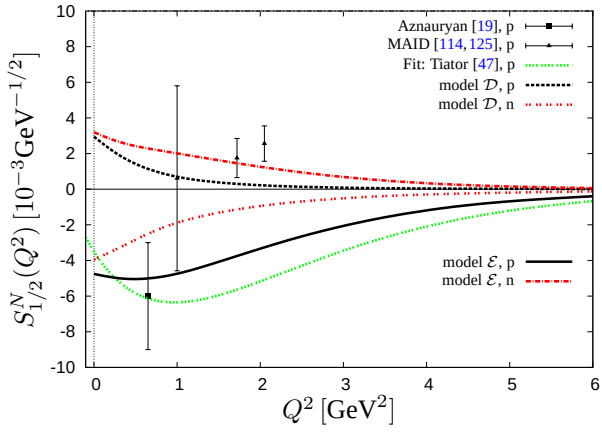

Fig. 4.82: Comparison of the $S_{11}(1650)$ longitudinal helicity amplitude $S^N_{1/2}$ of proton and neutron calculated in model $\mathcal{E}$ (solid and dashed-dotted line) and model $\mathcal{D}$ (dashed lines). See also caption to Fig. 4.79.

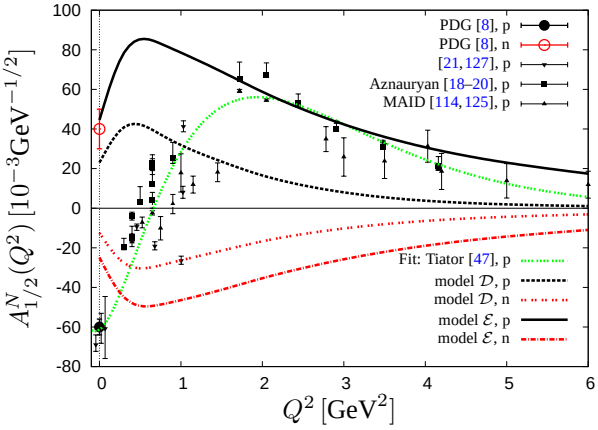

Fig. 4.83: Comparison of the $P_{11}(1440)$ transverse helicity amplitude $A^N_{1/2}$ for proton and neutron calculated in model $\mathcal{E}$ (solid and dashed-dotted line) and model $\mathcal{D}$ (dashed lines). See also caption to Fig. 4.79.

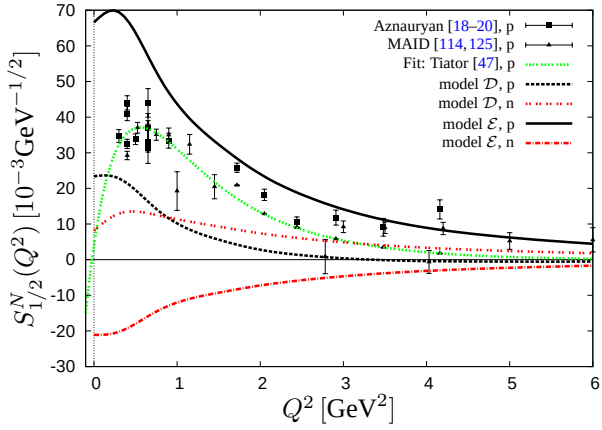

Fig. 4.84: Comparison of the $P_{11}(1440)$ longitudinal helicity amplitude $S^N_{1/2}$ for proton and neutron calculated in model $\mathcal{E}$ (solid and dashed-dotted line) and model $\mathcal{D}$ (dashed lines). Note, that for the data points of the MAID-analysis by Tiator *et al.* [125] no errors are quoted. See also caption to Fig. 4.79.

newer models yield curves, which are lower in magnitude than for model $\mathcal{A}$ and $\mathcal{C}$. Additionally, both curves have a node in the transverse proton and neutron amplitudes around $Q^2 \approx 3.0\,\mathrm{GeV}^2$, while the longitudinal amplitude only for model $\mathcal{D}$ shows a node at roughly $Q^2 \approx 0.75\,\mathrm{GeV}^2$. In particular, both models reproduce the transverse amplitudes at the photon point quite well, but are too low at higher transition momenta transfers, where model $\mathcal{D}$ drops even faster than model $\mathcal{E}$.

For comparison, we also displayed the transverse amplitude $A^p_{1/2}$ calculated with the quark model from Keister and Capstick [126] and a fit obtained from Aznauryan *et al.* [49] and Tiator *et al.* [47]. The longitudinal amplitudes are again far away from the experimental data as displayed in Fig. 4.80 similar to those of model $\mathcal{A}$ and $\mathcal{C}$. The expected minimum in the data and the fit from Tiator *et al.* [47] are not reflected by the calculations in both models.

For the $N_{1/2^-}(1650)$-resonance, analogous to the models $\mathcal{A}$ and $\mathcal{C}$ (see Figs. 4.81 and 4.82), the newer models $\mathcal{D}$ and $\mathcal{E}$ shows a large disagreement for the transverse helicity amplitude, while the neutron amplitude matches the prediction of the PDG at the photon point. The longitudinal amplitudes, as displayed in Fig. 4.82,

agrees with some values of the MAID-data [114, 125], but cannot reproduce the node expected from experimental data. Here, model $\mathcal{E}$ accounts for the single data point from Aznauryan *et al.* [19]. In opposite to model $\mathcal{A}$, model $\mathcal{D}$ does not have a maximum anymore and decreases rapidly.

Analogous to the previous results of model $\mathcal{A}$ and $\mathcal{C}$ for the transverse $P_{11}(1440)$-helicity amplitude the newer models $\mathcal{D}$ and $\mathcal{E}$ cannot account for the node in the amplitude, where model $\mathcal{D}$ underestimates the data more than model $\mathcal{A}$. Only model $\mathcal{E}$ accounts for the data for $Q^2 \gtrsim 1.5\,\mathrm{GeV}^2$. For the longitudinal amplitude, shown in Fig. 4.84, both models can account for the experimental data of Aznauryan *et al.* [18–20], where model $\mathcal{A}$ underestimates the data slightly and model $\mathcal{E}$ fits quite well. Finally, the expected maximum in the data is predicted too low in position by both models close to $Q^2 \approx 0.25\,\mathrm{GeV}^2$.

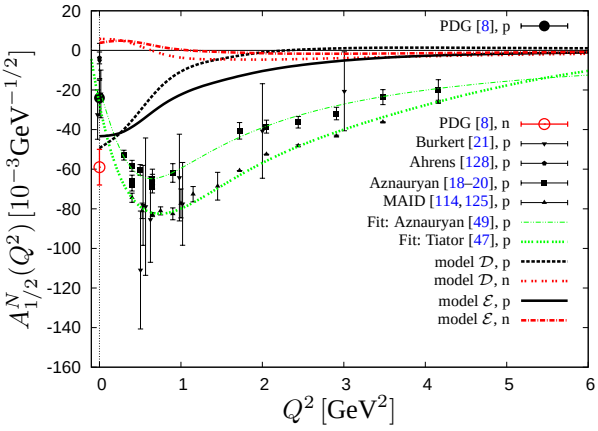

Fig. 4.85: Comparison of the $D_{13}(1520)$ transverse helicity amplitude $A^N_{1/2}$ of proton and neutron calculated in model $\mathcal{E}$ (solid and dashed-dotted line) and model $\mathcal{D}$ (dashed lines). See also caption to Fig. 4.79.

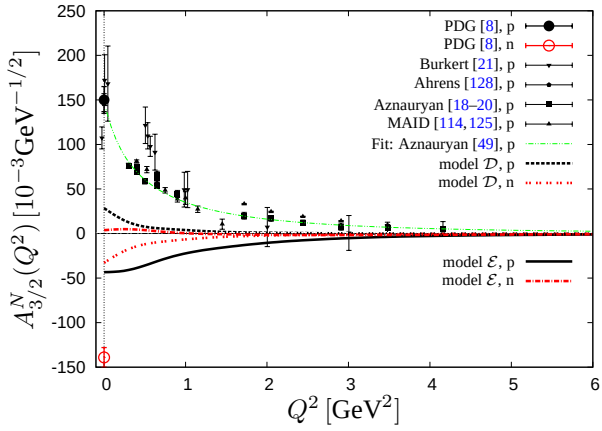

Fig. 4.86: Comparison of the $D_{13}(1520)$ transverse helicity amplitude $A^N_{3/2}$ for proton and neutron calculated in model $\mathcal{E}$ (solid and dashed-dotted line) and model $\mathcal{D}$ (dashed lines). See also caption to Fig. 4.79.

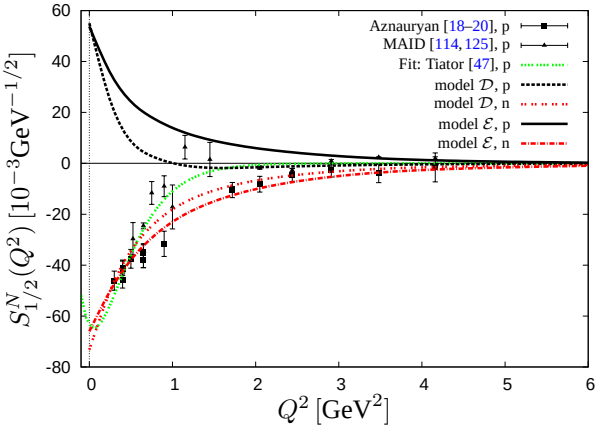

Fig. 4.87: Comparison of the $D_{13}(1520)$ longitudinal helicity amplitude $S^N_{1/2}$ for proton and neutron calculated in model $\mathcal{E}$ (solid and dashed-dotted line) and model $\mathcal{D}$ (dashed lines). See also caption to Fig. 4.79.

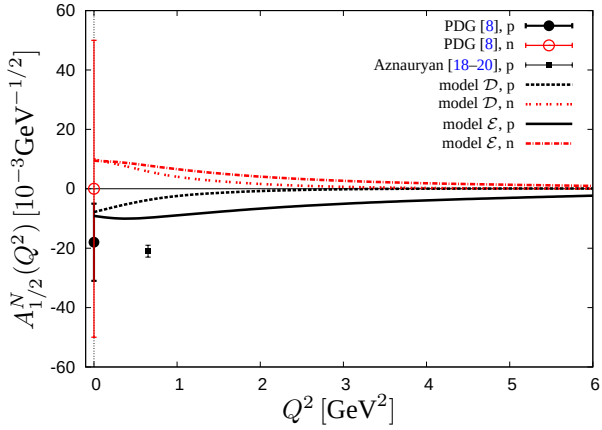

Fig. 4.88: Comparison of the $D_{13}(1700)$ transverse helicity amplitude $A^N_{1/2}$ of proton and neutron calculated in model $\mathcal{E}$ (solid and dashed-dotted line) and model $\mathcal{D}$ (dashed lines). See also caption to Fig. 4.79.

The $\mathbf{J = \frac{3}{2}}$ resonances: For the $J = \frac{3}{2}$-resonances we restrict to a discussion of the well measured $N_{3/2^-}(1520)$- and $N_{3/2^-}(1700)$-resonances. The transverse and longitudinal amplitudes of the $N_{3/2^-}(1520)$-resonances are displayed in Figs. 4.85, 4.86 and 4.87. The Q^2-dependence of the transverse $A^p_{1/2}$-amplitude is not as well reproduced as in the previous models $\mathcal{A}$ and $\mathcal{C}$ (see Figs 4.27 and 4.28). The calculations of

the $A^p_{1/2}$-amplitude are too low by roughly a factor of 2 in magnitude for both models, when compared to the experimental data. Also the $A^p_{3/2}$-amplitude is underestimated for low momenta $Q^2 \lesssim 1\,\mathrm{GeV}^2$. In contrast to the models $\mathcal{A}$, $\mathcal{C}$ and $\mathcal{D}$, model $\mathcal{E}$ yields the wrong sign and shows a smooth minimum close to $Q^2 = 0.2\,\mathrm{GeV}^2$. Furthermore, model $\mathcal{D}$ and $\mathcal{E}$ underestimate the experimental values by more than a factor 3 in magnitude. The PDG value of the transverse neutron amplitudes at the photon point cannot be accounted for by both models. The longitudinal amplitude is also not reproduced mainly, because the predictions of both models show the wrong sign. If the sign of the longitudinal amplitudes would be inverted, then both models would account for the data quite well, where model $\mathcal{E}$ would matches the data best.

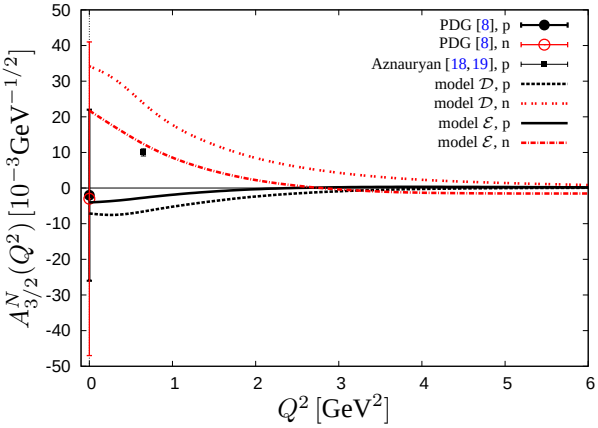

Fig. 4.89: Comparison of the $D_{13}(1700)$ transverse helicity amplitude $A^N_{3/2}$ for proton and neutron calculated in model $\mathcal{E}$ (solid and dashed-dotted line) and model $\mathcal{D}$ (dashed lines). See also caption to Fig. 4.79.

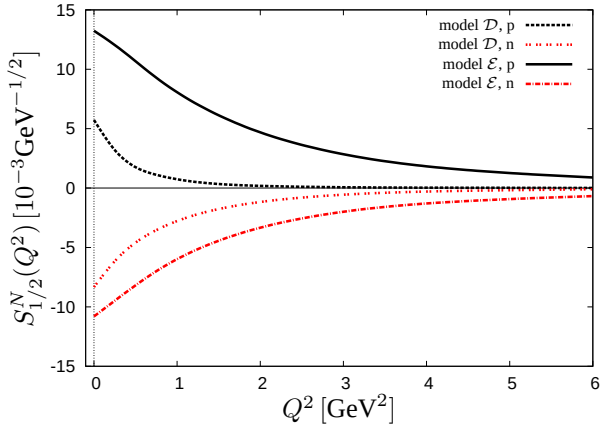

Fig. 4.90: Prediction of the $D_{13}(1700)$ longitudinal helicity amplitude $S^N_{1/2}$ for proton and neutron calculated in model $\mathcal{E}$ (solid and dashed-dotted line) and model $\mathcal{D}$ (dashed lines). See also caption to Fig. 4.79.

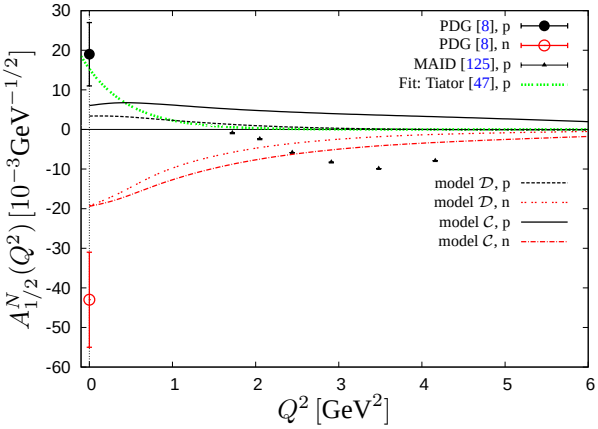

Fig. 4.91: Comparison of the $D_{15}(1675)$ transverse helicity amplitude $A^N_{1/2}$ for proton and neutron calculated in model $\mathcal{E}$ (solid and dashed-dotted line) and model $\mathcal{D}$ (dashed lines). See also caption to Fig. 4.79.

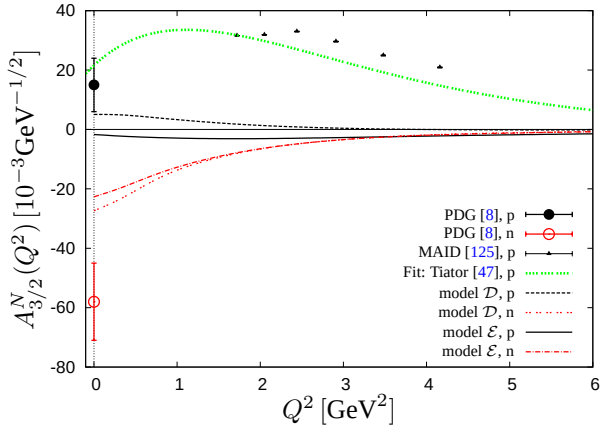

Fig. 4.92: Comparison of the $D_{15}(1675)$ transverse helicity amplitude $A^N_{3/2}$ for proton and neutron calculated in model $\mathcal{E}$ (solid and dashed-dotted line) and model $\mathcal{D}$ (dashed lines). See also caption to Fig. 4.79.

The helicity amplitudes of the next excitation, $D_{13}(1700)$, are shown in Figs. 4.88, 4.89 and 4.90, respectively. Here, the transverse amplitudes of both models match the PDG-data [8] at the photon point. The single data point of Aznauryan *et al.* [18, 19] for the $A_{1/2}$-amplitude is only approximately reproduced, whereas for the $A_{3/2}$-amplitude both models cannot account for the value of Aznauryan *et al.* [18, 19]. For the longitudinal amplitude no data are available.

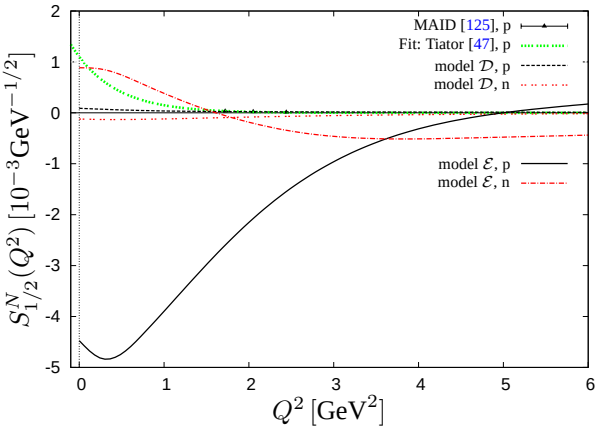

Fig. 4.93: Comparison of the $D_{15}(1675)$ longitudinal helicity amplitude $S^N_{1/2}$ for proton and neutron calculated in model $\mathcal{E}$ (solid and dashed-dotted line) and model $\mathcal{D}$ (dashed lines). See also caption to Fig. 4.79.

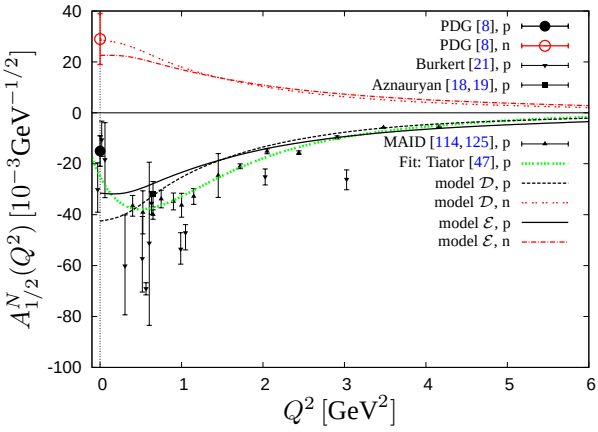

Fig. 4.94: Comparison of the $F_{15}(1680)$ transverse helicity amplitude $A^N_{1/2}$ for proton and neutron calculated in model $\mathcal{E}$ (solid and dashed-dotted line) and model $\mathcal{D}$ (dashed lines). See also caption to Fig. 4.79.

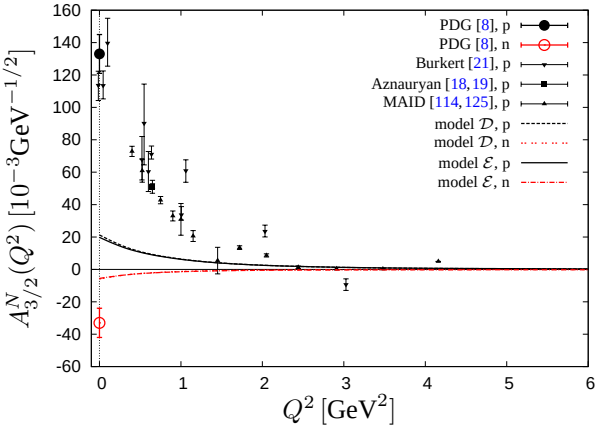

Fig. 4.95: Comparison of the $F_{15}(1680)$ transverse helicity amplitude $A^N_{3/2}$ for proton and neutron calculated in model $\mathcal{E}$ (solid line) and model $\mathcal{D}$ (dashed line). See also caption to Fig. 4.79.

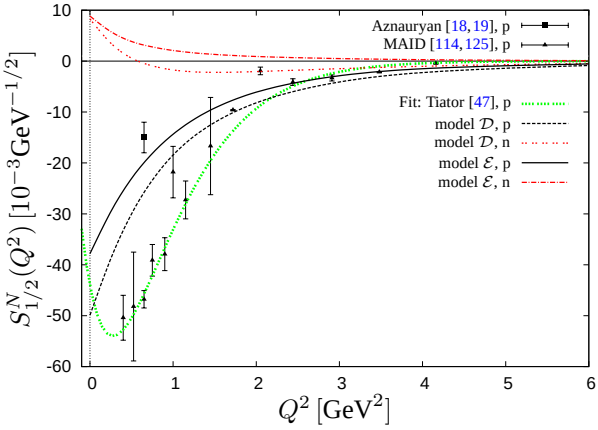

Fig. 4.96: Comparison of the $F_{15}(1680)$ longitudinal helicity amplitude $S^N_{1/2}$ for proton and neutron calculated in model $\mathcal{E}$ (solid and dashed-dotted line) and model $\mathcal{D}$ (dashed lines). See also caption to Fig. 4.79.

The J $= \frac{5}{2}$ resonances: The transverse helicity amplitudes of the $N_{5/2^-}(1675)$-resonance are shown in Figs. 4.91 and 4.92. As for models $\mathcal{A}$ and $\mathcal{C}$, the models $\mathcal{D}$ and $\mathcal{E}$ reproduce the data of the $A^N_{1/2}$-amplitude (see Fig. 4.91) quite well, however, without describing the expected node at roughly $Q^2 \approx 1.5\,\mathrm{GeV}^2$. Here, the photon decay amplitude from the PDG [8] is not reproduced satisfactorily by both models and is underestimated by nearly a factor of 2. This also applies to the PDG photon decay amplitude as well as MAID-data for the $A^N_{3/2}$-amplitude. Additionally, model $\mathcal{E}$ has a different sign, compared with model $\mathcal{D}$. Only model $\mathcal{D}$ matches the PDG-value roughly. The neutron decay amplitudes are also underestimated in magnitude by roughly a factor 2 by both models as displayed in Figs. 4.91 and 4.92.

The predictions of the $F_{15}(1680)$ transverse helicity amplitude $A^N_{1/2}$ are in fair agreement with the data, shown in the Fig. 4.94, whereas the $A^N_{3/2}$-amplitudes, see Fig. 4.95, are underestimated in both models by nearly a factor 3. Here, model $\mathcal{D}$ and $\mathcal{E}$ give very similar results. In case of the $A^N_{1/2}$-amplitude, both models match the proton and neutron PDG photon decay amplitude, while they describe the remaining data for $Q^2 > 0$ excellently. Only the older data from Burkert *et al.* [21] spreads around the curves with large errors. The

longitudinal amplitude also shows a reasonable agreement with the experimental data for both models, as displayed in Fig. 4.96. Here, model $\mathcal{E}$ stays closer to the single experimental value of Aznauryan *et al.* [18, 19] at $Q^2 = 0.65\,\mathrm{GeV}^2$, while model $\mathcal{D}$ prefers the older data from Burkert *et al.* [21]. For $Q^2 \geq 1.5\,\mathrm{GeV}^2$, both models agree fairly with the experimental data of the MAID-analysis. Finally, the minimum in the fit of Tiator *et al.* [47] is not reflected in the prediction of the models.

$\Delta \leftrightarrow N$ helicity amplitudes

We now turn to the discussion of $\Delta \leftrightarrow N$ helicity amplitudes for each angular momentum J and parity π.

The J $= \frac{1}{2}$ resonances: The discussion of $\Delta \leftrightarrow N$ helicity amplitudes starts again with the $S_{31}(1620)$-amplitudes for model $\mathcal{D}$ and $\mathcal{E}$. Here, the transverse and longitudinal amplitudes are shown in Fig. 4.97: the transverse amplitude is predicted too low compared to the MAID-data [114, 125] and the data from Aznauryan *et al.* [19]. Similar to the models $\mathcal{A}$ and $\mathcal{C}$, models $\mathcal{D}$ and $\mathcal{E}$ exhibit a node at roughly $Q^2 = 0.3\,\mathrm{GeV}^2$, which is not seen in the data, if one excludes the data from Burkert *et al.* [21]. The longitudinal amplitude of model $\mathcal{E}$ matches the single data point of Aznauryan *et al.* [19]. The data of the longitudinal amplitude then suggests a node around $Q^2 = 0.9\,\mathrm{GeV}^2$, which is not reproduced by the models. Model $\mathcal{D}$ underestimates this data point of Aznauryan *et al.* [19] by more than a factor of 4 in magnitude. Note, that the sign of the $S_{31}(1620)$-amplitudes has to be clarified experimentally as already mentioned within the discussion of the previous models $\mathcal{A}$ and $\mathcal{C}$ in section 4.2.6.

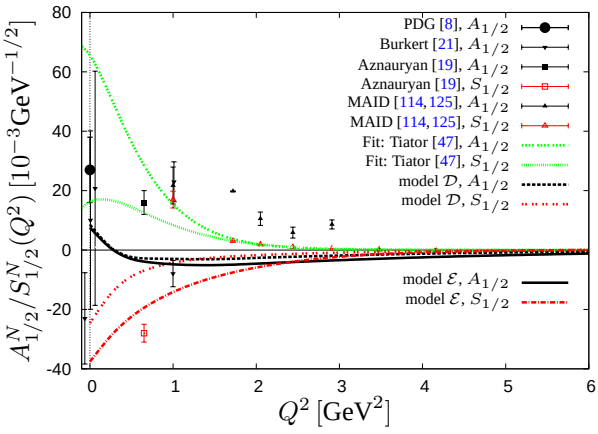

Fig. 4.97: Comparison of the $S_{31}(1620)$ transverse and the longitudinal helicity amplitudes $A^N_{1/2}$ and $S^N_{1/2}$ calculated in model $\mathcal{E}$ (solid and dashed-dotted line) and model $\mathcal{D}$ (dashed lines) with experimental data from [8, 19, 21, 114, 125]. Note, that for the data points of the MAID-analysis by Tiator *et al.* [125] no errors are quoted. See also caption to Fig. 4.79.

The J $= \frac{3}{2}$ resonances: Fig. 4.98 shows the prediction of the $P_{33}(1232)$ transverse amplitudes calculated in model $\mathcal{D}$ and $\mathcal{E}$. The $A^N_{1/2}$-amplitude of model $\mathcal{E}$ runs close to that of model $\mathcal{C}$ (see Fig. 4.51) and fits the data quite well, while the minimum is predicted close to the photon point at the expected position at $Q^2 \approx 0.4\,\mathrm{GeV}^2$. Here, the magnitude of the $A^N_{1/2}$-amplitude is predicted too low be nearly a factor 2, while model $\mathcal{D}$ underestimates the data by more than a factor 3. The position of the minimum for model $\mathcal{D}$ is found roughly at $Q^2 = 0$. The situation for the $A^N_{3/2}$-amplitude is similar to that of the $A^N_{1/2}$-amplitude, whereas the position of the minima of the transverse amplitudes coincides within both models. In subsection 4.3.8, the $P_{33}(1232)$ transverse helicity amplitudes will again be used for the calculation of the electric and magnetic $\Delta \leftrightarrow N$ transition form factor. In Fig. 4.99, we show the $P_{33}(1232)$ longitudinal amplitude in which only model $\mathcal{E}$ gives an acceptable prediction, while model $\mathcal{D}$ yields almost vanishing results. Analogous to the previous models $\mathcal{A}$ and $\mathcal{C}$, both models shows a maximum, which is not supported by the data.

Concerning the negative parity $J^\pi = \frac{3}{2}^-$-states, we only discuss the $D_{33}(1700)$ transverse and longitudinal helicity amplitudes, which are displayed in Figs. 4.100 and 4.101. The transverse amplitudes describe the data quite well. Both models can also account for the amplitudes at the photon point satisfactorily. Since the data of Burkert *et al.* [21] and the MAID-analysis [114, 125] spreads for $Q^2 \leq 1.0\,\mathrm{GeV}^2$, the newer models only match with the single data point of Aznauryan *et al.* [19]. Nevertheless, the PDG photon decay amplitudes can be accounted for by both models. At the photon point the data shows big fluctuations, which partially match the calculated values. In Fig. 4.101 we show the $D_{33}(1700)$ longitudinal helicity amplitude for model $\mathcal{D}$ and $\mathcal{E}$. The values of the MAID-data [125] are close to zero and include a non-vanishing value at $Q^2 = 1.0\,\mathrm{GeV}^2$. It is obvious, that both models then produce the wrong sign for the longitudinal amplitude. Model $\mathcal{D}$ accounts for

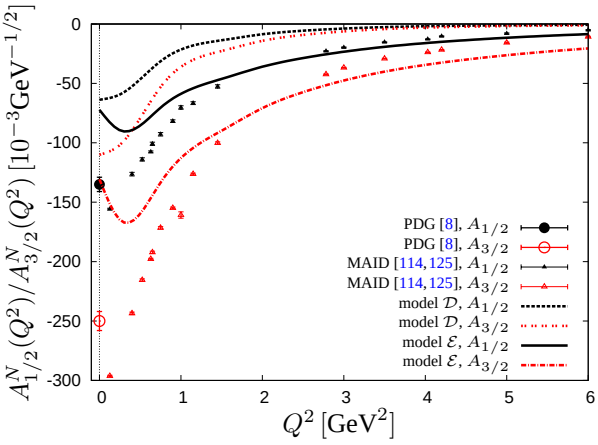

Fig. 4.98: Comparison of the $P_{33}(1232)$ transverse helicity amplitudes $A^N_{1/2}$ and $A^N_{3/2}$ as calculated in model $\mathcal{E}$ (solid and dashed-dotted line) and model $\mathcal{D}$ (dashed lines). See also caption to Fig. 4.79 and the magnetic transition form factor in Fig. 4.102.

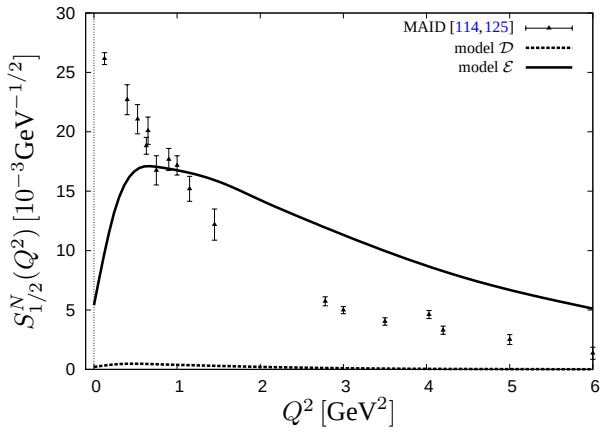

Fig. 4.99: Comparison of the $P_{33}(1232)$ longitudinal helicity amplitude $S^N_{1/2}$ calculated in model $\mathcal{E}$ (solid line) and model $\mathcal{D}$ (dashed line) to experimental data from [8, 114, 125]. See also caption to Fig. 4.79.

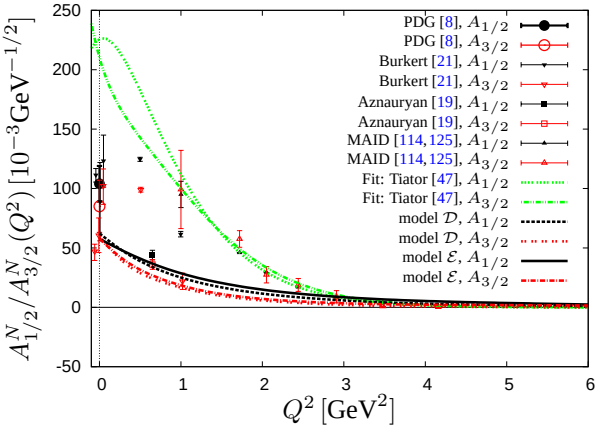

Fig. 4.100: Comparison of the $D_{33}(1700)$ transverse helicity amplitudes $A^N_{1/2}$ and $A^N_{3/2}$ calculated in model $\mathcal{E}$ (solid and dashed-dotted line) and model $\mathcal{D}$ (dashed lines). See also caption to Fig. 4.79.

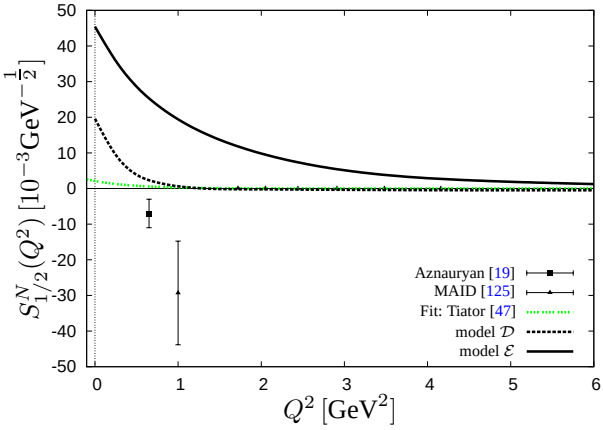

Fig. 4.101: Comparison of the $D_{33}(1700)$ longitudinal helicity amplitude $S^N_{1/2}$ of the nucleon calculated in model $\mathcal{E}$ (solid line) and model $\mathcal{D}$ (dashed line). Note, that for the data points of the MAID-analysis by Tiator *et al.* [125] no errors are quoted. See also caption to Fig. 4.79.

the MAID values close to zero. Note, that if the predicted amplitudes have opposite sign, they can reproduce the single data point of Aznauryan *et al.* [19] as well the value at $Q^2 = 1.0\,\mathrm{GeV}^2$ in the MAID-data at least in magnitude.

4.3.7 Photon couplings

Tables 4.19 and 4.20 summarise the calculations of the transverse photon decay amplitudes for model $\mathcal{D}$ and $\mathcal{E}$. The calculated values were determined at $Q^2 = 10^{-4}\,\mathrm{GeV}^2$, which gives a satisfactory approximation to the photon point. Similar to the tables for model $\mathcal{A}$ and $\mathcal{C}$ (see 4.10 and 4.11), the tables list the available experimental data, which have already been displayed in the discussion on helicity amplitudes in the previous subsection 4.3.6. In general no large difference between the models $\mathcal{A}$, $\mathcal{C}$, $\mathcal{D}$ and $\mathcal{E}$ has been found.

Table 4.19: Transverse photon couplings calculated for $\Delta \leftrightarrow N$ transitions in model $\mathcal{D}$ and $\mathcal{E}$ in comparison to experimental data. All calculated photon couplings were determined by calculating the helicity amplitudes at $Q^2 = 10^{-4}\,\mathrm{GeV}^2$ close to the photon point. A hyphen indicates that experimental data does not exist. All amplitudes are in units of $10^{-3}\mathrm{GeV}^{-1/2}$, all masses are given in MeV.

State	Rat.	Mass model $\mathcal{D}$	Mass model $\mathcal{E}$	Ampl.	Model $\mathcal{D}$	Model $\mathcal{E}$	Exp.	Ref.
$S_{31}(1620)$	****	1568	1625	$A_{1/2}$	-8.52	-7.57	27±11	[8]
$S_{31}(1900)$	**	–	1932	$A_{1/2}$	–	3.52	59±16/29±8/-4±16	[17]/ [129]/ [92]
$P_{31}(1750)$	*	–	1764	$A_{1/2}$	–	9.38	53	[130]
$P_{31}(1910)$	****	1820/1851	1879	$A_{1/2}$	7.09/11.49	0.56	3±14	[8]
$P_{33}(1232)$	****	1234	1232	$A_{1/2}$	-63.74	-72.27	-135±6	[8]
				$A_{3/2}$	-110.09	-130.69	-250±8	[8]
$P_{33}(1600)$	***	–	1609	$A_{1/2}$	–	-14.69	-23±20	[8]
				$A_{3/2}$	–	-34.20	-9±21	[8]
$P_{33}(1920)$	***	1810/1859	1896/1926	$A_{1/2}$	-0.23/-0.68	2.96/3.31	130^{+30}_{-60}/40±14/ 22±8/-7	[17]/ [129]/ [63]/ [130]
				$A_{3/2}$	2.32/1.36	7.23/7.25	-115^{+25}_{-50}/23±17/ 42±12/-1	[17]/ [129]/ [63]/ [130]
$D_{33}(1700)$	****	1556	1611	$A_{1/2}$	62.19	57.58	104±15	[8]
				$A_{3/2}$	59.74	57.64	85±22	[8]
$D_{33}(1940)$	**	–	1895/1947	$A_{1/2}$	29.00	-15.81/-15.74	-36±58/160±40	[129]/ [63]
				$A_{3/2}$	20.12	-4.77/-26.07	-31±12/110±30	[129]/ [63]
$D_{35}(1930)$	***	–	2009	$A_{1/2}$	–	-8.13	-9±28	[8]
				$A_{3/2}$	–	-16.89	-18±28	[8]
$F_{35}(1905)$	****	1858/1899	1915/1939	$A_{1/2}$	-13.45/4.72	-9.95/4.66	26±11	[8]
				$A_{3/2}$	-30.06/-8.52	-20.23/-5.94	-45±20	[8]
$F_{37}(1950)$	****	1925	1947	$A_{1/2}$	-17.20	-13.07	-76±12	[8]
				$A_{3/2}$	22.13	-17.29	-97±10	[8]
$H_{39}(2420)$	****	2453	2361	$A_{1/2}$	7.43	4.19	–	–
				$A_{3/2}$	8.79	4.80	–	–

Table 4.20: Transverse photon couplings calculated for $N^* \leftrightarrow N$ transitions in model $\mathcal{D}$ and $\mathcal{E}$ in comparison to experimental data. All calculated photon couplings were determined by calculating the helicity amplitudes at $Q^2 = 10^{-4}\,\mathrm{GeV}^2$ close to the photon point. A hyphen indicates that experimental data does not exist. All amplitudes are in units of $10^{-3}\mathrm{GeV}^{-1/2}$, all masses are given in MeV.

State	Rat.	Mass model $\mathcal{D}$	Mass model $\mathcal{E}$	Ampl.	Model $\mathcal{D}$ p	Model $\mathcal{D}$ n	Model $\mathcal{E}$ p	Model $\mathcal{E}$ n	Exp. p	Exp. n	Ref.
$S_{11}(1535)$	****	1375	1487	$A_{1/2}$	83.71	-55.64	73.26	-44.31	90±30	-46±27	[8]
$S_{11}(1650)$	****	1531	1658	$A_{1/2}$	-2.85	-10.90	-4.66	-7.19	53±16	-15±21	[8]
$S_{11}(1895)$	**	1751 1831	1825 1896	$A_{1/2}$	0.70 48.35	1.86 -25.57	0.02 6.96	-0.02 -3.93	12±6	–	[17]
$P_{11}(1440)$	****	1397	1439	$A_{1/2}$	23.05	-12.53	44.57	-24.86	-60±4	40±10	[8]
$P_{11}(1710)$	***	1638	1729	$A_{1/2}$	19.87	-12.91	11.96	-8.07	24±10	-2±14	[8]
$P_{11}(1880)$	**	1822	1859	$A_{1/2}$	3.93	-2.85	6.54	-4.07	14±3	–	[17]
$P_{13}(1720)$	****	1649	1682	$A_{1/2}$	61.84	-27.53	49.38	-23.37	18±30	1±15	[8]
				$A_{3/2}$	-13.91	5.62	-14.05	1.23	-19±20	-29±61	[8]
$P_{13}(1900)$	***	1830 1842 1859	1845	$A_{1/2}$	0.85 4.15 -2.16	6.19 -1.90 0.70	4.69	-8.89	26±15/-17	–/-16	[17]/ [130]
				$A_{3/2}$	-3.92 -0.06 1.12	0.02 -0.27 -0.22	-5.71	-12.92	-65±30/31	–/-2	[17]/ [130]
$D_{13}(1520)$	****	1440	1520	$A_{1/2}$	-49.30	5.81	-43.37	3.80	-24±9	-59±9	[8]
				$A_{3/2}$	28.48	-32.85	25.83	-22.10	150±15	-139±11	[8]
$D_{13}(1700)$	***	1562	1658	$A_{1/2}$	-7.84	9.91	-9.14	9.45	-18±13	0±50	[8]
				$A_{3/2}$	-7.13	34.18	-4.03	21.71	-2±24	-3±44	[8]
$D_{13}(1875)$	***	1818 1881	1820 1930	$A_{1/2}$	1.59 -1.12	0.12 0.28	1.61 -0.44	-0.32 0.15	18±10/-20±8 12/26±52	7±13	[17]/ [129]/ [8]/ [130]/ [132]
				$A_{3/2}$	0.82 0.49	-1.25 -0.94	0.34 0.32	-0.55 0.02	-9±5/17±11 -10/128±57	-53±34	[17]/ [129]/ [8]/ [130]/ [132]
$D_{15}(1675)$	****	1615	1690	$A_{1/2}$	3.39	-19.29	6.04	-19.41	19±8	-43±12	[8]
				$A_{3/2}$	5.05	-27.36	-1.69	-22.67	15±9	-58±13	[8]
$D_{15}(2060)$	**	1921 2033	1909 2002	$A_{1/2}$	35.36 -2.46	-19.07 1.28	22.12 1.40	-13.04 -0.61	67±15	–	[17]
				$A_{3/2}$	-8.55 0.24	5.26 -0.18	-6.22 -0.27	1.30 0.24	55±20	–	[17]
$F_{15}(1680)$	****	1701	1715	$A_{1/2}$	-42.54	28.61	-31.56	22.55	-15±6	29±10	[8]
				$A_{3/2}$	21.27	-5.89	19.77	-5.56	133±12	-33±9	[8]
$F_{15}(1860)$	* –	1870 1899	1930	$A_{1/2}$	-42.54 0.09	28.61 -0.45	-5.54	13.86	20±12	–	[17]
				$A_{3/2}$	-0.42 0.02	-13.81 -0.10	2.30	6.64	50±20	–	[17]
$F_{15}(2000)$	* –	2036	1977 2037	$A_{1/2}$	-2.74	1.83	-0.16 -1.42	-0.42 0.80	32±15	–	[17]
				$A_{3/2}$	0.45	-0.66	0.18 0.43	-0.68 -0.58	50±14	–	[17]
$F_{17}(1990)$	**	1954	1992	$A_{1/2}$	-2.40	-5.43	-3.80	-2.04	42±14/30±29 40	–/-1 -69	[17]/ [129] [131]
				$A_{3/2}$	-3.30	-6.92	0.39	-4.41	58±12/86±60 4	–/-178 -72	[17]/ [129] [131]
$G_{17}(2190)$	****	1996	1955	$A_{1/2}$	20.80	-6.05	10.53	-2.42	-65±8	–	[17]
				$A_{3/2}$	-8.63	6.86	-6.06	4.29	35±17	–	[17]
$G_{19}(2250)$	****	2210	2163	$A_{1/2}$	1.18	-7.35	1.95	-5.39	$\lvert A^p_{\frac{1}{2}}\rvert < 10$	–	–
				$A_{3/2}$	1.57	-9.07	-0.22	-5.20	$\lvert A^p_{\frac{1}{2}}\rvert < 10$	–	–
$H_{19}(2220)$	****	2217	2132	$A_{1/2}$	18.81	-11.70	8.99	-5.82	$\lvert A^p_{\frac{1}{2}}\rvert < 10$	–	[17]
				$A_{3/2}$	-8.70	3.23	-4.95	1.93	$\lvert A^p_{\frac{1}{2}}\rvert < 10$	–	[17]
$I_{1,11}(2600)$	***	2440	2315	$A_{1/2}$	10.84	-3.89	3.70	-1.14	–	–	–
				$A_{3/2}$	-4.66	3.05	-2.23	1.37	–	–	–

4.3.8 $\Delta(1232) \leftrightarrow N$ transition form factors

Since the $\Delta \leftrightarrow N$ electric and magnetic transition form factor of the $\Delta(1232)$ groundstate are related to the helicity amplitudes via Eqs. (2.127a, 2.127b) and (2.130) they can be extracted from the $P_{33}(1232)$-helicity amplitudes, which are displayed in Figs. 4.98 and 4.99 for model $\mathcal{D}$ and $\mathcal{E}$. In Fig. 4.102, we show the magnetic

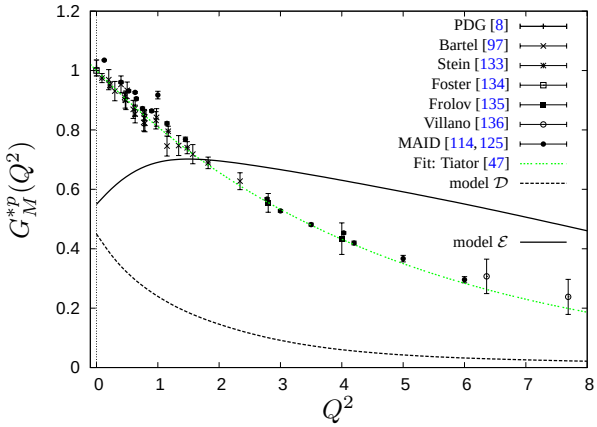

Fig. 4.102: Comparison of $\Delta(1232)$ magnetic transition form factor G_M^{*p} calculated within model $\mathcal{E}$ (solid line) and model $\mathcal{D}$ (dashed line). See also caption to Fig. 4.79.

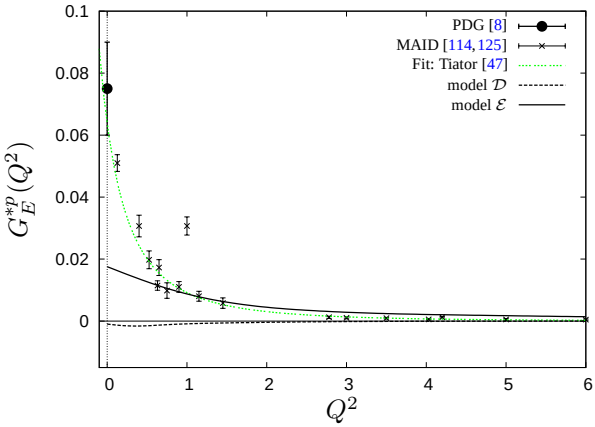

Fig. 4.103: Comparison of $\Delta(1232)$ electric transition form factor G_E^{*p} calculated within model $\mathcal{E}$ (solid line) and model $\mathcal{D}$ (dashed line). See also caption to Fig. 4.79.

transition form factor divided by thrice the standard dipole form factor in order to emphasise discrepancies between experimental and calculated values. The magnetic transition form factor of both models cannot account for the data as displayed in Fig. 4.102: the result of model $\mathcal{E}$ is similar to these of model $\mathcal{C}$, see also Fig. 4.64. Model $\mathcal{D}$ underestimates the data completely, here in contrast to the related model $\mathcal{A}$ (see also Fig. 4.64 for comparison). In Fig. 4.103 we display the electric transition form factor. For the electric transition form factor we find a similar situation, where model $\mathcal{E}$ reproduces the MAID-data [114, 125] quite well, if excluding the region in the vicinity of the photon point $Q^2 \lesssim 0.5\,\mathrm{GeV}^2$. Model $\mathcal{D}$ gives a small negative prediction for the electric transition form factor similar to the result of model $\mathcal{A}$. Here, the MAID-data have been calculated according to the Eqs. (2.127a) and (2.127b) from the transverse $P_{33}(1232)$-helicity amplitude data. Fig. 4.104 shows the Coulomb transition form factor calculated from the longitudinal $P_{33}(1232)$-amplitude. Only model $\mathcal{E}$ can roughly account for the momentum dependence of the Coulomb transition form factor, whereas model $\mathcal{D}$ is effectively zero.

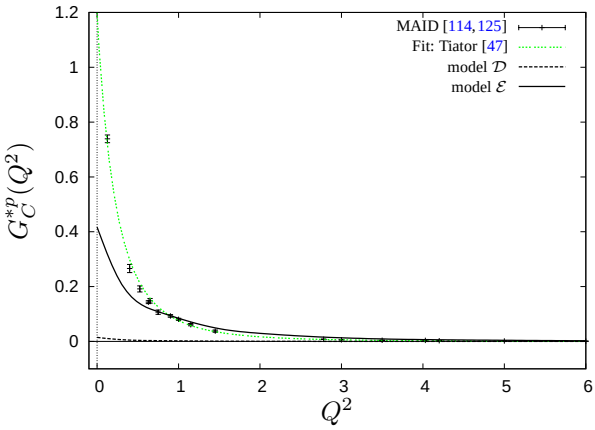

Fig. 4.104: Comparison of $\Delta(1232)$ Coulomb transition form factor G_C^{*p} calculated within model $\mathcal{E}$ (solid line) and model $\mathcal{D}$ (dashed line). See also caption to Fig. 4.79.

4.4 Summary

The major objective was the study of alternative interaction kernels additional to the linear confinement potential and the instanton-induced 't Hooft interaction within the framework of the Bethe-Baryon model. In this chapter we have discussed two different approaches for new interactions: A spin-flavour dependent interaction and a modified version of the linear confinement potential. Thus, this chapter contains the major results

of this thesis and summarises the publications of Ronniger *et al.* [31, 32] in its first part. Section 4.2 starts with the introduction of the novel spin-flavour dependent interaction by introducing interaction Lagrangians for pseudoscalar meson-exchange with pseudoscalar- and pseudovector coupling to fermions. From these Lagrangians we have extracted the second-order scattering matrix elements, which contains the corresponding meson-exchange potentials. In both cases expressions for the potentials have been given in momentum space. Subsequently, we have focused on the pseudoscalar coupled meson-exchange mainly, because it led to the best results. In coordinate space, the Yukawa potential has been substituted by a Gaussian short-range potential to improve the results. The model with this novel spin-flavour dependent interaction in combination with the confinement potential and the instanton-induced 't Hooft interaction is called model $\mathcal{C}$. In subsection 4.2.1 we discussed the model parameters for model $\mathcal{C}$ and an improved version of model $\mathcal{A}$, whereas the latter has been recalculated with increased numerical accuracy. Thus here, the model parameters of model $\mathcal{A}$ are slightly different compared to those of the previous chapter 3. Furthermore, the new model $\mathcal{C}$ uses a different confinement Dirac-structure than model $\mathcal{A}$: it is given by a two-body interaction for the linear part with a simpler Dirac-structure, $\gamma_0 \otimes \gamma_0$. Note, that model $\mathcal{C}$ introduces only three additional parameters compared to model $\mathcal{A}$: the octet- and singlet-coupling as well as the range of the Gaussian potential, which was chosen equal for the meson octet- and singlet interaction. The octet-coupling was found to be consistently smaller than the singlet-coupling; the latter can be interpreted as a short-range part of the confinement potential itself.

The first subsection of section 4.2 contains the discussion of the Δ-, N- and hyperon-spectra, where we have compared the results from the recalculated version of the older model $\mathcal{A}$ with the novel model $\mathcal{C}$. Concerning the Δ-spectrum, we indeed found in general a much better description by the novel model $\mathcal{C}$. In particular, model $\mathcal{C}$ can account for the $\Delta_{1/2^+}(1750)$-, the Roper-like $\Delta_{3/2^+}(1600)$- and the three excited negative parity Δ^*-resonances around 1900 MeV ($\Delta_{1/2^-}(1900)$, $\Delta_{3/2^-}(1940)$ and $\Delta_{5/2^-}(1930)$), whereas model $\mathcal{A}$ cannot describe these states, as already mentioned in the introduction 1 and chapter 3. Note, that model $\mathcal{C}$ predicts even two resonances for the $\Delta_{3/2^-}(1940)$-state close to the resonance position.

Also for the nucleon-spectrum we have found a satisfactory description by model $\mathcal{C}$, which improves again on the results by model $\mathcal{A}$. The novel model $\mathcal{C}$ reproduces the mass of the Roper-resonance in very good agreement with the data, whereas model $\mathcal{A}$ predicts the resonance too high by roughly 60 MeV. Furthermore, model $\mathcal{C}$ improves the predictions of the masses for the $N_{1/2^-}(1535)$- and $N_{1/2^-}(1650)$-resonances as well as for the $N_{3/2^-}(1520)$- and $N_{3/2^-}(1700)$-resonances. Here, model $\mathcal{A}$ predicts all of these resonances too low. Only for the $N_{5/2^+}(1680)$-resonance, the description in the new model $\mathcal{C}$ is slightly worse then in model $\mathcal{A}$. With this exception we conclude, that the novel model $\mathcal{C}$ indeed yields to an improved description of the nucleon-spectrum compared to the older model $\mathcal{A}$. Moreover, since 2012 there are more nucleon resonances available in the compilation of the PDG [8] to which we can compare. These resonances are in particular: $N_{1/2^+}(1880)$, $N_{1/2^-}(1895)$, $N_{3/2^+}(2040)$, $N_{3/2^-}(1875)$, $N_{5/2^+}(1860)$ and $N_{5/2^-}(2060)$. Here, both models can account for the new $N_{1/2^+}(1880)$-state as well as for the new negative parity $N_{1/2^-}(1895)$- and $N_{3/2^-}(1875)$-resonances.

Also the hyperon sector, *i.e.* the Λ-, Σ- and Ξ-baryons, is better described by model $\mathcal{C}$. In particular, model $\mathcal{C}$ can account for the Roper-like resonances, $\Lambda_{1/2^+}(1600)$ and $\Sigma_{1/2^+}(1660)$, whereas model $\mathcal{A}$ cannot describe the latter. However, both models cannot account for the low lying $\Lambda_{1/2^-}(1405)$-resonance. The prediction of model $\mathcal{A}$ is roughly 100 MeV too high, whereas for model $\mathcal{C}$ the prediction is about approximately 200 MeV to high and lies in the vicinity of the next $J^\pi = \frac{1}{2}^-$-excitation $\Lambda_{1/2^-}(1670)$. As already mentioned in subsection 3.5.5 of the previous chapter, this fortifies the interpretation of this state not as a q^3-state, but as a meson-baryon molecule close the $\bar{K}N$-threshold as claimed by Jido, Oset, Meißner and Hyodo *et al.* [57–59], which is supposed to be made out of at least five quarks and thus cannot be described in the three quark baryon model as used here. The rest of the Λ-resonances can be reproduced by both models. In the Σ-spectrum, model $\mathcal{C}$ cannot account for the one-star rated $\Sigma_{1/2^+}(1770)$-resonance and the four-star rated $\Sigma_{3/2^-}(1580)$-resonance only. However, the latter resonance can also not be reproduced by model $\mathcal{A}$. Moreover, we were able to suggest a classification for some resonances based on their masses. We relate the $\Xi(1690)$-resonance to the Roper-like excitation of the $J^\pi = \frac{1}{2}^+$-resonances, *e.g.* within the framework of model $\mathcal{C}$ mainly, which is not classified in the PDG [8] so far. Furthermore, the $\Omega(2250)$-resonance should have positive parity based on the predictions of model $\mathcal{C}$.

In subsection 4.2.5, we have discussed the calculation of the electroweak form factors, magnetic moments

and charge radii for model $\mathcal{A}$ and $\mathcal{C}$. Here, the electroweak quantities are calculated in the framework of the Bethe-Baryon model from the Salpeter amplitudes via the method from Merten and Kretzschmar *et al.* [9,10,12] without introducing additional parameters. We have found, that the electric proton- and neutron form factors are reproduced in excellent agreement with the data by model $\mathcal{C}$. For the electric neutron form factor, both models predicts the correct position of the maximum in the data. The magnetic proton and neutron form factors are also better reproduced by model $\mathcal{C}$, than by model $\mathcal{A}$, which predicts them too low in magnitude. This also effects the ratio of the electric and magnetic proton form factor. For the axial form factor both models are in agreement with the data. The extrapolation of the electroweak form factors to the photon point allows the extraction of the magnetic moments, charge radii and the axial coupling as well as the axial charge radius. According to Tab. 4.7, the magnetic moments and charge radii of the nucleon are in general in good agreement with experimental data. It was found, that model $\mathcal{A}$ overestimates the electric charge radius in magnitude, whereas model $\mathcal{C}$ reproduces it quite well. Also the magnetic moments of the hyperon octet and decuplet, calculated via the static method from Haupt *et al.* [13, 14], agree quite well with the experimental data.

The discussion on the helicity amplitudes can be found in subsection 4.2.6. It shows the transverse and longitudinal helicity amplitudes for most of the (at least three star-rated) resonances within the Δ and nucleon sector as well as for some other resonances. Note, that new data on helicity amplitudes is available since recent years from the CLAS-collaboration [18–20] and the MAID-analysis [114, 125]. We found reasonable descriptions for the transverse and longitudinal helicity amplitudes for the resonances: $S_{11}(1535)$, $P_{11}(1440)$, $D_{13}(1520)$, $F_{15}(1680)$, $P_{33}(1232)$ and the $D_{33}(1700)$. Our concluded values partially agree with the scarce experimental data of the remaining N- and Δ-helicity amplitudes. Also photon decay amplitudes were extracted from the calculated helicity amplitudes. The discussion on the results from the novel model $\mathcal{C}$ concludes with a discussion of the $\Delta(1232) \leftrightarrow N$ transition form factors. Here, we obtained reasonable results for the electric- and Coulomb transitions form factors, whereas the magnetic transition form factor cannot be accounted for in both models satisfactorily.

We also studied a modified version of the confinement potential with a spin-spin and tensor interaction, which can of course be combined with the novel spin-flavour dependent interaction as it has been done in section 4.3. This is supplemented by the confinement Dirac-structure for the offset chosen simply as the identity. Combined with the instanton-induced 't Hooft interaction we have called this model $\mathcal{D}$. It turns out, that model $\mathcal{D}$ produces results similar to the previous model $\mathcal{A}$ for the light-flavoured baryon spectra, which is amazing since both models have completely different Dirac-structures for the slope and offset. Additionally to the interactions of model $\mathcal{D}$, we have also introduced the new spin-flavour dependent interaction as discussed in the previous section 4.2 of this chapter. The corresponding new model has been called model $\mathcal{E}$ and was found to yield results similar to model $\mathcal{C}$. Thereby, the octet-coupling in model $\mathcal{E}$ vanishes and the remaining eta-singlet exchange could be interpreted as a short-range part of the confinement potential.

The discussion of the results for model $\mathcal{D}$ and $\mathcal{E}$ starts with subsection 4.3.1 in which we have discussed the model parameters in the same way as it has been done previously for model $\mathcal{A}$ and $\mathcal{C}$. Subsequent subsections then contain the discussion of the baryon spectra. The results of model $\mathcal{D}$ and $\mathcal{E}$ turned out to be very similar to these of model $\mathcal{A}$ and $\mathcal{C}$, respectively. Small differences are found mainly in the nucleon-spectrum and partially in the Λ- and Σ-spectra. Concerning the electroweak form factors discussed in subsection 4.3.5, we could not find a similar good description of the electric neutron form factor in model $\mathcal{E}$, in contrast to the excellent result found in model $\mathcal{C}$. This also applies to the axial form factor. In the discussion of helicity amplitudes in subsection 4.3.6, we compared results for a selection of resonances to these of models $\mathcal{A}$ and $\mathcal{C}$. In particular model $\mathcal{E}$ could not account for the $A^p_{3/2}$-helicity amplitude of the $D_{13}(1520)$-resonance, the calculated amplitude has a wrong overall sign. Furthermore, model $\mathcal{D}$ and $\mathcal{E}$ cannot account for the minimum in the $A^p_{1/2}$-helicity amplitude in contrast to model $\mathcal{A}$ and $\mathcal{C}$. In subsection 4.3.7 we have summarised the photon decay amplitudes for model $\mathcal{D}$ and $\mathcal{E}$ and concluded with the discussion of the $\Delta(1232) \leftrightarrow N$ transition form factors in subsection 4.3.8.

Chapter 5

Summary and Outlook

The major objective of this thesis was the search for and study of additional quark-quark interactions within the framework of a fully relativistic constituent quark model, which is based on the Bethe-Salpeter equation in order to reproduce some experimentally observed resonances, which cannot be accounted for so far. The quark model was originally formulated for mesons (see Münz and Resag *et al.* [36–45]) and then extended by Löring *et al.* [4–7] to describe baryons. In both approaches a phenomenologically motivated linear confinement potential and an instanton-induced 't Hooft interaction was used to describe the complete light-flavoured meson- and baryon mass spectra up to masses of 3 GeV (see PDG [8]). In this work, we focus on baryons and their properties. Although the quark model produced a very satisfactory overall description of the light-flavoured baryons, but it could not account for all of the light-flavoured baryon masses. In Löring *et al.* [4–7], two different models, called $\mathcal{A}$ and $\mathcal{B}$, were introduced, which differ only in their confinement Dirac-structure. It was found, that especially some specific excited states within the mass spectrum of the nucleon- and Δ-sector are not reproduced by these models. Within the hyperon-baryon sector also some disagreement with the experimental data was observed. This motivated the search for additional interactions to be introduced in the quark model of Löring *et al.* [4–7] in order to account for the above mentioned disagreements in the light-flavoured baryon spectra. Indeed, two new interactions were found, which are able to improve the description. The first *ansatz* is motivated by pseudoscalar flavour exchange between quarks. This leads to a spin-flavour dependent two-body interaction as discussed in chapter 4, see also in Ronniger *et al.* [31]. The second *ansatz* uses a modified confinement potential in which a different kind of Dirac-structure has been introduced by including spin-spin and tensor interactions. This was found to lead to additional terms for the Dirac-structure in the linear part of the confinement potential. For both approaches, many electroweak observables such as electromagnetic- and axial form factors as well as helicity amplitudes have been calculated (see Merten *et al.* [9, 10] and Ronniger *et al.* [32]). We want to emphasise that, no further parameters were introduced for the calculation of electroweak observables: These were calculated directly from the Salpeter amplitudes of the involved resonances, where the model parameters were fixed previously by the light-flavoured baryon spectra as shown by Löring and Ronniger *et al.* [4–7, 31].

Chapter 2 contains a brief recapitulation of the basics of the Bethe-Baryon model; it summarises the properties and extensions of the quark model by *e.g.* Löring, Merten, Kretzschmar and Haupt *et al.* [4–7, 9, 10, 12–14]. Here, on the basis of the relativistically covariant Bethe-Salpeter equation a constituent quark model is formulated, which is numerically tractable. The discussion starts with the formulation of a six-point Greens-function from which the Bethe-Salpeter equation can be deduced, which finally allows the calculation of bound-states within the framework of a quantum field theoretical approach. In instantaneous (*e.g.* unretarded) approximation, the Bethe-Salpeter equation reduces to the so-called Salpeter equation under the additional assumption, that the full quark-propagator can be approximated by a free form propagator with a constituent quark mass assumed to absorb some self-energy effects. Finally, the Salpeter equation can be formulated via a Hamilton-operator, which then allows the calculation of baryon bound-states and their Salpeter amplitudes by solving an eigenvalue problem. For completeness, we have also recapitulated some properties on the projective structure of the Salpeter equation in this chapter, which are of course important for the understanding of the baryon model. Based on this, it is possible to calculate electroweak properties in the model such as

the electromagnetic- and axial form factors, helicity amplitudes, photon decay amplitudes, magnetic moments and charge radii. The methods for the extraction of such properties within the framework of the Bethe-Baryon model have been summarised in the last sections of chapter 2 and follow the work of Merten, Kretzschmar and Haupt *et al.* [9, 10, 12–14]. Thereby, all electroweak properties are based on the calculation of current-matrix elements.

The existing results of the Bethe-Baryon model $\mathcal{A}$ and $\mathcal{B}$ as originally introduced by Löering *et al.* [4–7], on the baryon spectra are summarised in the subsequent chapter 3: Both models use a linear confinement potential, but differ in their Dirac-structures. Furthermore, both models use the instanton-induced 't Hooft interaction for the $\Delta - N$ mass-splitting. The models reproduce the light-flavoured baryon spectra satisfactorily, but some states could not be accounted for: Model $\mathcal{A}$ gives a better description of the spectra than model $\mathcal{B}$. Both models cannot reproduce all of the excited baryon states as mentioned already in the introduction. In particular the Roper $N_{1/2^+}(1440)$-resonance and Roper-like $\Delta_{3/2^+}(1600)$-, $\Lambda_{1/2^+}(1600)$-, $\Sigma_{1/2^+}(1660)$-resonances as well as the three excited negative parity states $\Delta_{1/2^-}(1900)$, $\Delta_{3/2^-}(1940)$ and $\Delta_{5/2^-}(1930)$ cannot be accounted for in both models. This motivated the introduction of new interactions within the Bethe-Baryon model in order to find a satisfactory description of these states.

In the first part of chapter 4 (section 4.2), we have introduced a novel spin-flavour dependent interaction motivated by pseudoscalar meson-exchange with pseudoscalar- and/or pseudovector coupling for the meson-octet and singlet and discussed the implementation of this new interaction within the framework of the Bethe-Baryon model. Subsequently, we focus on the pseudoscalar coupled meson-exchange only and substituted the radial dependence of the Yukawa-potential by a Gaussian short-range interaction, which eventually was found to lead to the best results. In combination with the linear confinement potential and the instanton-induced 't Hooft interaction thus a new model has been constructed, called model $\mathcal{C}$. It uses a different confinement Dirac-structure than that one of model $\mathcal{A}$. The major difference between these Dirac-structures is, that model $\mathcal{C}$ uses a simpler two-body interaction instead of a three-body interaction as used in model $\mathcal{A}$. Moreover, model $\mathcal{C}$ introduces three additional parameters: the range of the Gaussian potential and the octet- and singlet-coupling for the spin-flavour exchange interaction. Here it is important to mention, that the singlet-coupling dominates the octet-coupling by nearly a factor 18. This suggests the interpretation, of the flavour-independent singlet exchange as a part of the confinement potential. Furthermore, we have demonstrated, that by introducing this additional spin-flavour dependent interaction, parametrised with a Gaussian radial dependence with an universal range and two couplings for flavour-octet and flavour-singlet exchange, it is possible to improve the baryonic excitation spectra, electroweak form factors and helicity amplitudes simultaneously (see Ronniger *et al.* [31,32][1]). The results for model $\mathcal{C}$ are very similar to the predictions of the Graz group [22–30]. Although the overall agreement of calculated and experimental helicity data in both versions $\mathcal{A}$ and $\mathcal{C}$ of the relativistic quark models are of similar quality, the new model $\mathcal{C}$ apart from accounting better for the baryon mass spectrum also does improve on specific other observables, in particular on the groundstate form factors. The improvements can also be found in Ronniger *et al.* [31, 32] and include:

- A better description of the position of the excited negative parity states slightly below 2 GeV in the Δ-spectrum: The $\Delta_{1/2^-}(1900)$-, $\Delta_{3/2^-}(1940)$- and $\Delta_{5/2^-}(1930)$-resonances;
- A better description of the position of the first scalar, isoscalar excitation of the groundstate in all light-flavour sectors: The $\Delta_{1/2^+}(1750)$-, $\Delta_{3/2^+}(1600)$-, $N_{1/2^+}(1440)$-, $N_{1/2^-}(1535)$-, $\Lambda_{1/2^+}(1600)$- and $\Sigma_{1/2^+}(1660)$-resonances;
- An improved description of the momentum dependence of electromagnetic form factors of groundstates without the introduction of any additional parameters. Here, in particular the description of the electric neutron form factor has been improved in model $\mathcal{C}$. The result are in agreement with the predictions from Plessas *et al.* [30] for the Goldstone-Boson exchange model (GBE);

In case of the helicity amplitudes the calculated results have been compared to experimental data as far as available for resonances with a three or four star rating according to the PDG [8]. The experimental data

[1] Note, that the results within [31] are slightly different to the results discussed in chapter 4, since an improved parameter set has been found for model $\mathcal{C}$, as already mentioned in [32].

include the couplings at the photon point from PDG [8] and [17] as well as recent determinations of transverse and longitudinal amplitudes as reported by Aznauryan [18–20, 49] and in the MAID-analysis [114, 125], see also [47] . The results for the helicity amplitudes of nucleon resonances (see also Ronniger *et al.* [32]) can be summarised as follows:

- A satisfactory description of data for the $S_{11}(1535)$-, $P_{11}(1440)$-, $D_{13}(1520)$- and $F_{15}(1680)$-resonances was found. Exceptions are: A node in the transverse $P_{11}(1440)$-amplitude as found experimentally was not reproduced by the calculations; we also do not find the observed minimum in the longitudinal $S_{11}(1535)$-amplitude and the calculations underestimate the transverse $S_{11}(1650)$ as well as the longitudinal $F_{15}(1680)$-amplitude for low momentum transfers. Also the amplitudes of the $D_{13}(1520)$-resonances are slightly too small in model $\mathcal{C}$. Furthermore, predictions of helicity amplitudes are given for higher excited resonances for both models. Some of these were recently found by [15–17], *e.g.* for the $N_{1/2^+}(1880)$- and $N_{1/2^-}(1895)$-resonance;

- There exists agreement with the scarce data for the $S_{31}(1620)$-helicity amplitude if we disregard two data points for the longitudinal amplitude. There is an indication for a sign disagreement between the data of Aznauryan *et al.* [19] and that for the MAID-analysis [114, 125] or alternatively a node in the amplitude exists, which is not reproduced by both models in this case;

- The $P_{33}(1232)$-helicity amplitudes are generally too small in magnitude in both models, slightly more so in model $\mathcal{C}$. For the longitudinal amplitude in particular we find a maximum in the theoretical curves for which there exists no experimental evidence;

- Predictions of the negative parity excited $\Delta^*(1900, 1940, 1930)$-helicity amplitudes can be made in model $\mathcal{C}$. The position of these states could not be reproduced in the original model $\mathcal{A}$ and was the main motivation to supplement the dynamics of the model by an additional short-ranged spin-flavour dependent interaction. It is rewarding, that the calculated photon decay amplitudes agree reasonably well with the PDG-data [8] for these three resonances.

Some discrepancies remain, both in model $\mathcal{C}$ as well as in model $\mathcal{A}$:

- The description of the $N_{5/2^+}(1680)$- and $\Lambda_{3/2^-}(1520)$-resonance, which is predicted slightly too high by model $\mathcal{C}$ and thus cannot accounted for with the same accuracy as in model A. Furthermore, both models cannot account for the position of the $\Sigma_{3/2^-}(1580)$-resonance;

- The description of the $\Lambda_{1/2^-}(1405)$-resonance, where the mass value of the groundstate of model $\mathcal{C}$ agrees approximately with the $\Lambda_{1/2^-}(1670)$-resonance, which supports the statement, that the $\Lambda_{1/2^-}(1405)$-state cannot be described as a three-quark system. The same characteristics are less distinctive within model $\mathcal{A}$, which calculates the resonance approximately 100 MeV too high. In our opinion, this underlines the conclusion, that the $\Lambda_{1/2^-}(1405)$-resonance, which is close to the $\bar{K}N$-threshold, is largely dominated by meson-baryon molecule components as stipulated by *e.g.* Jido, Oset, Meißner and Hyodo *et al.* [57–59] in a chiral unitary approach;

- The low rated $\Sigma_{1/2^+}(1770)$-resonance cannot be reproduced within model $\mathcal{C}$, in contrast to model $\mathcal{A}$;

- Static properties are slightly better reproduced in model $\mathcal{A}$. This also applies to electroweak form factors in the vicinity of the photon point.

It must be conceded, that the additional spin-flavour dependent interaction was introduced in model $\mathcal{C}$ purely phenomenologically and required a drastic modification of the parametrisation of confinement and the other flavour dependent interaction of the original model $\mathcal{A}$, which had a form as inferred from instanton effects. In spite of this, with only 10 parameters in total we still consider the new model $\mathcal{C}$ to be an effective description of the multitude of resonances found for baryons made out of light flavoured quarks. Moreover, we have classified some resonance in the PDG [8] based on their masses in model $\mathcal{C}$, *e.g.* the $\Xi(1690)$-resonance as a $J^\pi = \frac{1}{2}^+$ Roper-like excitation. In case of the helicity amplitudes we presented predictions for helicity amplitudes of

some lower rated resonances, such as $P_{31}(1750)$- and $D_{33}(1940)$-resonance as well as predictions to some photon decay amplitudes analysed by the CB-ELSA collaboration *et al.* [17]. The corresponding photon decay amplitude data from the CB-ELSA collaboration are presently mostly included in the new PDG-data [8] and generally well described by models $\mathcal{A}$ and $\mathcal{C}$. For the magnetic form factor of the $\Delta(1232) \leftrightarrow N$ transition we have found that both models cannot accurately account for the data. Furthermore, for the electric transition form factor model $\mathcal{A}$ even produces a wrong sign compared to the MAID-data. The momentum dependence of the Coulomb transition form factor is well described by model $\mathcal{C}$, but not by model $\mathcal{A}$, which yields almost vanishing values in this case.

In the second part of chapter 4 (section 4.3) a new version for the Dirac-structure of the linear confinement potential with additional spin-spin and tensor contributions was introduced and discussed. This procedure introduces no additional parameters. The modified confinement structure enters as a two-body interaction and can be combined with the previous introduced spin-flavour dependent short-range interaction. The corresponding models are called model $\mathcal{D}$ and $\mathcal{E}$, where model $\mathcal{E}$ includes additionally the spin-flavour dependent short-range interaction. Here, in model $\mathcal{E}$ the strength of the octet-coupling practically vanishes, which means, that the flavour independent eta-singlet part can be interpreted as a part of the confinement potential. Thus, in model $\mathcal{E}$, there is no additional flavour dependent part. The predictions of model $\mathcal{D}$, which includes the confinement and the instanton-induced 't Hooft force, are very similar to those of model $\mathcal{A}$, although the latter uses a completely different confinement Dirac-structure. This feature is amazing, because the choice of the Dirac-structure in general has a very strong influence on the baryon spectra. In combination with the (spin-)flavour dependent short-range interaction, the description of the light-flavoured baryon spectra is slightly improved in model $\mathcal{E}$, if compared to model $\mathcal{C}$. It can be observed, that the models $\mathcal{D}$ and $\mathcal{E}$ are very similar in their predictions to models $\mathcal{A}$ and $\mathcal{C}$, respectively. Thus, most of the conclusions for model $\mathcal{A}$ and $\mathcal{C}$ also hold for model $\mathcal{D}$ and $\mathcal{E}$, respectively. Nevertheless, there are some exceptions:

- Model $\mathcal{E}$, compared with model $\mathcal{C}$, accounts slightly better for the $N_{1/2^-}(1535)$- and $N_{5/2^+}(1680)$-resonances;
- Model $\mathcal{D}$ cannot account for the $N_{1/2^-}(1535)$-resonance, which is predicted too low by roughly 160 MeV. Otherwise this induces a likewise very low lying $J^\pi = \frac{1}{2}^-$-resonance in the Λ-baryon sector close to $\Lambda_{1/2^-}(1405)$-resonance in opposite to the other models $\mathcal{A}$, $\mathcal{B}$, $\mathcal{C}$ and $\mathcal{E}$, which cannot reproduced the $\Lambda_{1/2^-}(1405)$-resonance;
- The electric neutron form factor is underestimated in model $\mathcal{E}$ by nearly a factor two, whereas model $\mathcal{C}$ can account for it accurately;
- The axial form factor of the nucleon for model $\mathcal{D}$ is much too small, in contrast to the prediction of model $\mathcal{A}$, which reproduces the axial form factor satisfactorily;
- In case of model $\mathcal{E}$, the $A^p_{3/2}$-helicity amplitude of the $D_{13}(1520)$-resonance has a wrong overall sign. For the $A^p_{1/2}$-amplitude, model $\mathcal{D}$ and $\mathcal{E}$ cannot account for the minima within the data.

Model $\mathcal{D}$ in general does not improve the predictions of model $\mathcal{A}$. Although, model $\mathcal{E}$ improves the baryon spectra slightly compared with the corresponding model $\mathcal{C}$, but it cannot reproduce the electroweak properties and helicity amplitudes with the same quality. In conclusion, we prefer model $\mathcal{C}$, which leads to the best results for the baryon spectra and electroweak observables. The results on the mass spectrum of model $\mathcal{C}$ could also be used to make some assignments of hyperon-resonances as mentioned in chapter 4. Here, *e.g.* we have classified $\Xi(1690)$-resonance as a $J^\pi = \frac{1}{2}^+$ Roper-like excitation based on its mass in model $\mathcal{C}$, not assigned in the PDG [8] so far. Moreover, the $\Omega(2250)$-resonance should have a positive parity.

Previous extensions of the Bethe-Baryon model (version $\mathcal{A}$), which have not been mentioned in this thesis so far, were calculations of charmed-flavoured baryons, semileptonic- and strong two-body decays. The results have been published by Migura *et al.* [33, 34, 137] and Metsch [138]. With respect to the novel models $\mathcal{C}$, $\mathcal{D}$ and $\mathcal{E}$, the calculation of these observables still remain to be done, but should in principle be feasible. Moreover, an extension to bottom-flavoured baryons should be also possible for the models $\mathcal{A}$, $\mathcal{C}$, $\mathcal{D}$ and $\mathcal{E}$

and it seems rewarding to repeat the calculation of heavy-flavoured baryons with these versions of the model. Since the dynamics of model $\mathcal{D}$ is very similar to that of model $\mathcal{A}$, the calculations for model $\mathcal{D}$ should be straightforward. However, in the case of model $\mathcal{C}$ and $\mathcal{E}$, it could be necessary to extend the spin-flavour dependent interaction to the heavy-flavoured baryon sector. This *ansatz* can be indeed motivated by a heavy-flavoured meson-exchange similar to the *ansatz* made for model $\mathcal{C}$ and $\mathcal{E}$ within the light-flavoured baryon sector. Possibly, this extension introduces additional parameters in the spin-flavour dependent interaction on the heavy-baryon sector. Without introducing any additional parameters and other interactions, it is possible to recalculate most of the semileptonic- and strong-two-body decays in the framework of the novel models $\mathcal{C}$, $\mathcal{D}$ and $\mathcal{E}$. These calculations still remain to be done.

Constituent quark models played a major role in the classification of the hadronic excitation spectrum. It is expected, that in the future lattice QCD will play a more important role in this respect. Compared with the underlying Bethe-Baryon model, which (although based on the relativistically covariant Bethe-Salpeter equation in view of its simplifying assumptions) still is a model, lattice QCD is a numerical simulation of QCD itself. In praxis lattice QCD is extremely expensive in computing power compared to quark models like the Bethe-Baryon model, which are very economical in their use of computational resources. The recent program of lattice QCD includes in particular a description of many states in the hadron spectrum, which are extracted from the numerical calculation of two-point correlation functions. The present model calculations give hints to states, which cannot be described as q^3-states. Such resonances are for instance the $\Lambda_{1/2^-}(1405)$- and $\Sigma_{3/2^-}(1580)$-resonances, which are not accounted for by the Bethe-Baryon model. Therefore, it could be very interesting to investigate, whether such states can be accounted for in lattice QCD. Note, *e.g.* that the nature of the $\Lambda_{1/2^-}(1405)$-resonance is an open field of research within lattice QCD, see *e.g.* Takahashi, Huey-Wen and Edwards *et al.* [2, 3, 139]. As it stands, the Bethe-Baryon model gives a very satisfactory description for light-flavoured baryon excitations and allows the identification of exotic states. As such it could support future investigations in lattice QCD.

Appendix A

The one-meson-exchange contribution to the interaction between two spin $\frac{1}{2}$-fermions

The one-meson-exchange can be derived by a standard application of the Feynman rules from the underlying Lagrangians given in section 4.2 by Eqs. (4.1) and (4.2). Following Caia *et al.* [60], the corresponding interaction Hamiltonians are given by

$$\mathcal{H}_I^{(ps)} = -\mathcal{L}_I^{(ps)}\,, \tag{A.1}$$

and

$$\mathcal{H}_I^{(pv)} = -\mathcal{L}_I^{(pv)} + \frac{1}{2}\sum_{a=0}^{8}\frac{g_a^2}{4m^2}(\lambda_a\lambda_a)(\bar{\psi}\gamma^5\gamma^0\psi)(\bar{\psi}\gamma^5\gamma^0\psi)\,, \tag{A.2}$$

via Legendre transformation for pseudoscalar- and pseudovector coupling, respectively. According to Fig. 4.1, the second-order scattering-matrix element $\mathcal{M}^{(2)}$ can be written in the CM-system for pseudoscalar and pseudovector coupled mesons as

$$\begin{aligned}
\mathrm{i}\mathcal{M}^{(2)}_{\text{(ps)}}(k_0,\mathbf{k}) &= \sum_{a,b} g_a^2\Big[\bar{\psi}(\mathbf{p}')(-\mathrm{i}\gamma^5)\lambda^a\,\psi(\mathbf{p})\,D^{ab}(k_0,\mathbf{k})\bar{\psi}(-\mathbf{p}')(-\mathrm{i}\gamma^5)\lambda^b\psi(-\mathbf{p})\Big] \\
&=: -\sum_{a,b} g_a^2 D^{ab}(k_0,\mathbf{k})\big[\lambda^a\,\gamma^5\big]\otimes\big[\lambda^b\,\gamma^5\big] \\
&=: \mathrm{i}[\bar{\psi}(-\mathbf{p}')\otimes\bar{\psi}(\mathbf{p}')]V_{(ps)}(k_0,\mathbf{k})[\psi(-\mathbf{p})\otimes\psi(\mathbf{p})]
\end{aligned} \tag{A.3}$$

and

$$\begin{aligned}
\mathrm{i}\,\mathcal{M}^{(2)}_{\text{(pv)}}(k_0,\mathbf{k}) &= \sum_{a,b}\frac{g_a^2}{4m^2}\Big[\bar{\psi}(\mathbf{p}')\gamma^5\gamma^\mu(-\mathrm{i}k_\mu)\lambda_a\psi(\mathbf{p})\,D^{ab}(k_0,\mathbf{k})\bar{\psi}(-\mathbf{p}')\gamma^5\gamma^\nu(-\mathrm{i}(-k_\nu))\lambda_b\psi(-\mathbf{p})\Big] \\
&\quad -\mathrm{i}\sum_{a}\frac{g_a^2}{4m^2}\Big[\bar{\psi}(\mathbf{p}')\gamma^5\gamma^0\lambda_a\psi(\mathbf{p})\,\bar{\psi}(-\mathbf{p}')\gamma^5\gamma^0\lambda_a\psi(-\mathbf{p})\Big] \\
&= \sum_{a,b}\frac{g_a^2}{4m^2}\Big[D^{ab}(k_0,\mathbf{k})\,k_\mu k_\nu\big[\lambda^a\gamma^5\gamma^\mu\big]\otimes\big[\lambda^b\gamma^5\gamma^\nu\big] - \tfrac{1}{2}\mathrm{i}\delta_{ab}\big[\lambda^a\gamma^5\gamma^0\big]\otimes\big[\lambda^b\gamma^5\gamma^0\big]\Big] \\
&:= \mathrm{i}\,[\bar{\psi}(-\mathbf{p}')\otimes\bar{\psi}(\mathbf{p}')]V_{(pv)}(k_0,\mathbf{k})[\psi(-\mathbf{p})\otimes\psi(\mathbf{p})]\,,
\end{aligned} \tag{A.4}$$

respectively. Here, calculating the corresponding interaction Hamiltonian (see Eq. (A.2) and Eq. (A6) in appendix A of Caia *et al.* [60], for further information), a contact term within the pseudovector coupled scattering-matrix element in Eq. (A.4) appears by applying the Legendre transformation. This is not the case for the pseudoscalar coupled interaction. The potentials are defined via the second-order matrix element $\mathcal{M}^{(2)}$ by isolating

the quark fields ψ and $\bar{\psi}$. Here, the meson propagator is given by

$$D^{ab}(k_0, \mathbf{k}) = \frac{\mathrm{i}\delta_{ab}}{k_0^2 - |\mathbf{k}|^2 - \mu_a^2}\,, \tag{A.5}$$

where $k_\mu := p'_\mu - p_\mu$ indicates the momentum transfer. Since the Salpeter equation deals only with instantaneous interactions, the meson propagator must be independent on k_0. This is achieved by putting $k_0 = 0$.

A.1 The instantaneous approximation

In instantaneous approximation the 0-th component of k is set to zero: $k_0 = 0$. From Eqs. (A.3) and (A.4) the corresponding potentials in momentum space can be extracted as

$$V^{(2)}_{(ps)}(\mathbf{k}) = \sum_a g_a^2 \left[\lambda^a \otimes \lambda^a\right] \frac{1}{|\mathbf{k}|^2 + \mu_a^2} \left[\gamma^5 \otimes \gamma^5\right] \tag{A.6}$$

for pseudoscalar coupling and as

$$\begin{aligned} V^{(2)}_{(pv)}(\mathbf{k}) &= \sum_a \frac{g_a^2}{4m^2} [\lambda^a \otimes \lambda^a] \left[\frac{-1}{|\mathbf{k}|^2 + \mu_a^2} \left[\left(\gamma^5 \boldsymbol{\gamma} \cdot \mathbf{k}\right) \otimes \left(\gamma^5 \boldsymbol{\gamma} \cdot \mathbf{k}\right) \right] - \frac{1}{2} \gamma^5\gamma^0 \otimes \gamma^5\gamma^0 \right] \\ &= \sum_a \frac{g_a^2}{4m^2} [\lambda^a \otimes \lambda^a] \left[\frac{-|\mathbf{k}|^2}{|\mathbf{k}|^2 + \mu_a^2} \left[\left(\gamma^5 \boldsymbol{\gamma} \cdot \widehat{\mathbf{k}}\right) \otimes \left(\gamma^5 \boldsymbol{\gamma} \cdot \widehat{\mathbf{k}}\right) \right] - \frac{1}{2} \gamma^5\gamma^0 \otimes \gamma^5\gamma^0 \right] \end{aligned} \tag{A.7}$$

for pseudovector coupling, respectively, where $\widehat{\mathbf{k}} := \frac{\mathbf{k}}{|\mathbf{k}|}$ is the direction of $\mathbf{k}$. In principle, both potentials can be Fourier transformed into coordinate space. This is not strictly necessary, since they can be calculated directly in momentum space in the Bethe-Baryon model. Models, based on Eqs. (A.6) or (A.7) have been tested, but were shown to be inadequate to explain the baryon spectra. We therefore pursued the following phenomenological approach: A Fourier transformation of the pseudoscalar coupled model leads to a Yukawa potential in coordinate space

$$V^{(2)}_{(ps)}(\mathbf{r}) = \sum_a g_a^2 \left[\lambda^a \otimes \lambda^a\right] \frac{\mathrm{e}^{-\mu_a |\mathbf{r}|}}{4\pi |\mathbf{r}|} \left[\gamma^5 \otimes \gamma^5\right]. \tag{A.8}$$

We *ad hoc* replace the radial dependence of the Yukawa potential by a Gaussian function and thus obtain for the spin-flavour dependent interaction the form

$$V^{(2)}_{(ps)}(\mathbf{r}) \overset{!}{\approx} V^{(2)}_{(\mathcal{C})}(\mathbf{r}) := \sum_a \tilde{g}_a^2 \left[\lambda^a \otimes \lambda^a\right] \frac{1}{\lambda_a^3 \pi^{\frac{3}{2}}} \mathrm{e}^{-\frac{|\mathbf{r}|^2}{\lambda_a^2}} \left[\gamma^5 \otimes \gamma^5\right]. \tag{A.9}$$

The model, with the additional interaction according to Eq. (A.9), will be called model $\mathcal{C}$ and is discussed in section 4.2. Furthermore, this spin-flavour dependent interaction has been also used in combination with a modified confinement potential (model $\mathcal{E}$) as discussed in section 4.3.

In case of pseudovector-coupling, potential (A.7) can be formulated in coordinate space as found in the publications of Lêvy and Brueckner *et al.* [61, 62]. Moreover, the Graz group [22–30] uses a similar pseudovector potential in the Goldstone-Boson exchange model, but neglect the spin-spin and tensor contributions. As already mentioned: In Bethe-Baryon model, we do not found a satisfactory description on the basis of potential (A.7) for the light-flavoured baryon spectra.

A.2 Flavour-matrix elements

The meson-exchange is a two-body interaction and the corresponding meson-exchange flavour-operators are $\sum_{a=1}^{3} \lambda^a(1) \otimes \lambda^a(2)$, $\lambda^8(1) \otimes \lambda^8(2)$ and $\sum_{a=4}^{7} \lambda^a(1) \otimes \lambda^a(2)$ representing a pion-, eta-octet- and kaon-like exchange. Here, λ^a, $a = 1, .., 8$ denote the generators of the $SU_F(3)$ flavour-group. The flavour-matrix

elements to the operators can be evaluated with the *Casimir* operators and the generators of the *Cartan algebra*. According to de Swart [140] they are defined by

$$C := \tfrac{1}{4}\sum_{a=1}^{8}\lambda_a^2 \qquad \text{and} \qquad I^2 := \tfrac{1}{4}\sum_{a=1}^{3}\lambda_a^2\,, \tag{A.10}$$

$$I_3 := \tfrac{1}{2}\lambda_3 \qquad \text{and} \qquad M := \tfrac{1}{2}\lambda_8\,, \tag{A.11}$$

which leads to corresponding flavour-operators of the meson-exchange

$$\text{Pion:} \quad \sum_{a=1}^{3}\lambda^a(1)\otimes\lambda^a(2) = 2\left(I^2(12) - I^2(1) - I^2(2)\right)\,, \tag{A.12a}$$

$$\text{Eta-octet:} \quad \lambda^8(1)\otimes\lambda^8(2) = 2\left(M^2(12) - M^2(1) - M^2(2)\right)\,, \tag{A.12b}$$

$$\text{Kaon:} \quad \sum_{a=4}^{7}\lambda^a(1)\otimes\lambda^a(2) = \sum_{a=1}^{8}\lambda^a(1)\otimes\lambda^a(2) - \lambda^8(1)\otimes\lambda^8(2) - \sum_{a=1}^{3}\lambda^a(1)\otimes\lambda^a(2)\,, \tag{A.12c}$$

$$\text{Eta-singlet:} \quad \lambda_0(1)\otimes\lambda_0(2) = \tfrac{2}{3}\mathbb{1}\otimes\mathbb{1}\,, \tag{A.12d}$$

with

$$\sum_{a=1}^{8}\lambda^a(1)\otimes\lambda^a(2) = 2\left(C(12)^2 - C(1)^2 - C(2)^2\right) \tag{A.13}$$

and the definitions

$$I(12) := I(1)\otimes\mathbb{1}(2) + \mathbb{1}(1)\otimes I(2)\,, \tag{A.14a}$$

$$M(12) := M(1)\otimes\mathbb{1}(2) + \mathbb{1}(1)\otimes M(2)\,, \tag{A.14b}$$

$$C(12) := C(1)\otimes\mathbb{1}(2) + \mathbb{1}(1)\otimes C(2)\,. \tag{A.14c}$$

Note, that λ_0 for the eta-singlet exchange is normalised to $\mathrm{tr}(\lambda_0\lambda_0) = 2$.

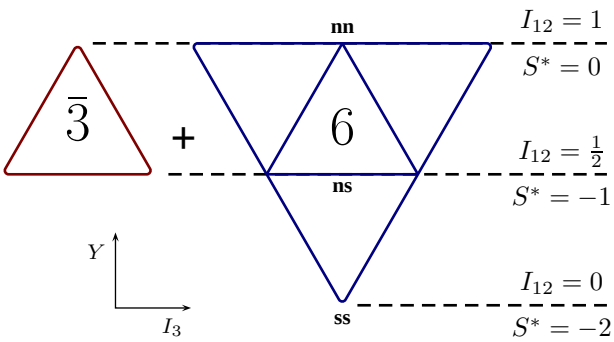

Fig. A.1: The schematic representation of the decomposition of $\mathbf{3}\otimes\mathbf{3}$ according to Eq. (A.16).

Fig. A.2: Summary of the flavour-matrix elements Eq. (A.15) for states in Fig. A.1 and .

exchange		**6**			$\bar{\mathbf{3}}$	
	I_{12}:	1	$\frac{1}{2}$	0	0	$\frac{1}{2}$
octet	π	1	0	0	-3	0
	η_8	$\frac{1}{3}$	$-\frac{2}{3}$	$\frac{4}{3}$	$\frac{1}{3}$	$-\frac{2}{3}$
	K	0	2	0	0	-2
singlet	η_1	$\frac{2}{3}$	$\frac{2}{3}$	$\frac{2}{3}$	$\frac{2}{3}$	$\frac{1}{6}$

Let $A(12)$ be a two-particle operator acting on the (12)-quark-pair of the three-quark state, which stands for one of the three meson-exchange flavour-operators, given by Eqs. (A.12a), (A.12b), (A.12c) and (A.12d). Then, the corresponding flavour-matrix elements are given by

$$\left\langle \left[f_1' f_2'\right]^{I_{12}', S_{12}^*} \middle| A(12) \middle| \left[f_1 f_2\right]^{I_{12}, S_{12}^*} \right\rangle\,. \tag{A.15}$$

Here, f_i, f_i' and $i = 1, 2, 3$ label the flavour content (u, d, s) of the coupled states with quantum numbers I_{12} and S_{12}^*.

The product of two fundamental triplet representations decomposes into a sextet and anti-triplet

$$\mathbf{3} \otimes \mathbf{3} = \mathbf{6} \oplus \bar{\mathbf{3}}\,, \tag{A.16}$$

see Fig. A.1. In [140], the $SU_F(3)$ irreducible representations are denoted by $D(p,q)$. For the simplest irreps we have $\mathbf{3} \triangleq D(1,0)$, $\bar{\mathbf{3}} \triangleq D(0,1)$ and $\mathbf{6} \triangleq D(2,0)$. The eigenvalue c for the Casimir operator C on a state of the representation $D(p,q)$ is then given by

$$c = \left(\tfrac{1}{3}\left(p^2 + pq + q^2\right) + p + q\right)\,. \tag{A.17}$$

If ϕ_h is the highest-weight state, the generators of the Cartan algebra have eigenvalues

$$I_3\phi_h = \tfrac{1}{2}(p+q)\phi_h \qquad \text{and} \qquad M\phi_h = \tfrac{1}{\sqrt{12}}\,(p-q)\,\phi_h\,. \tag{A.18a}$$

The flavour-matrix elements can be calculated for the sextet and anti-triplet representations separately starting from the highest-weight state of the corresponding representation via ladder-operators, which are defined in de Swart [140]. This leads to the flavour-matrix elements summarised in Tab. A.2.

Bibliography

[1] H. Leutwyler, Ann. Phys. **235**, 165 (1994).

[2] R. G. Edwards, J. J. Dudek, D. G. Richards, S.J. Wallace, JLAB-THY-1370, (2011) [arXiv:1104.5152v1].

[3] Huey-Wen Lin, NT@UW-11-09, (2011) [arXiv:1106.1608v1].

[4] U. Löring, K. Kretzschmar, B. C. Metsch, H. R. Petry, Eur. Phys. J. **A10**, 309 (2001) [arXiv:hep-ph/0103287].

[5] U. Löring, B. C. Metsch, H. R. Petry, Eur. Phys. J. **A10**, 395 (2001) [arXiv:hep-ph/0103289].

[6] U. Löring, B. C. Metsch, H. R. Petry, Eur. Phys. J. **A10**, 447 (2001) [arXiv:hep-ph/0103290].

[7] U. Löring, *'A Covariant Quark Model Baryons with Instanton-Induced forces'*, PhD thesis TK 01-02, (2001).

[8] J. Beringer *et al.* (Particle Data Group), Phys. Rev. D **86**, 010001 (2012).

[9] D. Merten, U. Löring, K. Kretzschmar, B. C. Metsch, H. R. Petry, Eur. Phys. J. **A14**, 477 (2002) [arXiv:hep-ph/0204024].

[10] D. Merten, *'Hadron Form factors and Decays'* PhD thesis TK 02-03, (2002).

[11] T. van Cauteren, D. Merten, T. Corthals, S. Janssen, B. C. Metsch, H. R. Petry, Eur. Phys. J. A **20**, 283 (2004) [arXiv:nucl-th/0310058].

[12] K. Kretzschmar, *'Electroweak Form Factors in a Covariant Quark Model of Baryons'* PhD thesis TK 01-01, (2001).

[13] C. Haupt, B. C. Metsch, H. R. Petry, Eur. Phys. J. A **28**, 213 (2006) [arXiv:hep-ph/0602151].

[14] C. Haupt, *'Electromagnetic Properties of Baryons'*, PhD thesis, (2006).

[15] A. V. Anisovich, E. Klempt, V. A. Nikonov, A. V. Sarantsev and U. Thoma, Eur. Phys. J. A **47**, 27 (2011).

[16] A. V. Anisovich, V. A. Nikonov, A. V. Sarantsev, U. Thoma and E. Klempt, Eur. Phys. J. A **47**, 27 (2011).

[17] A. V. Anisovich, R. Beck, E. Klempt, V. A. Nikonov, A. V. Sarantsev and U. Thoma, Eur. Phys. J. A **48**, 15 (2012).

[18] I. G. Aznauryan, V. D. Burkert, H. Egiyan, K. Joo, R. Minehart, and L. C. Smith, Phys. Rev. C **71**, 015201 (2005).

[19] I. G. Aznauryan, V. D. Burkert, G. V. Fedotov, B. S. Ishkhanov, and V. I. Mokeev, Phys. Rev. C **72**, 045201 (2005).

[20] I. G. Aznauryan and V. D. Burkert, Phys. Rev. C **80**, 055203 (2009).

[21] V. Burkert, *Reserach Program at CEBAF II*, edited by V. Burkert et al., CEBAF (USA), 161 (1986).

[22] L. Y. Glozman, D. O. Riska, Phys. Rep. **268**, 263 (1996).

[23] L. Ya. Glozman, Z. Papp, W. Plessas, K. Varga and R. F. Wagenbrunn, Nucl. Phys. A **623**, 90 (1997).

[24] L. Ya. Glozman, Z. Papp, W. Plessas, K. Varga and R. F. Wagenbrunn, Phys. Rev. C **57**, 3406 (1998).

[25] L. Ya. Glozman, W. Plessas, K. Varga and R. F. Wagenbrunn, Phys. Rev. D **58**, 094030 (1998).

[26] L. Theußl, R. F. Wagenbrunn, B. Desplanques and W. Plessas, Eur. Phys. J. A **12**, 91 (2001).

[27] K. Glantschnig, R. Kainhofer, W. Plessas , B. Sengl and R. F. Wagenbrunn, Eur. Phys. J. A **23**, 507 (2005).

[28] T. Melde, K. Berger, L. Canton, W. Plessas and R. F. Wagenbrunn Phys. Rev. D **76**, 074020 (2007).

[29] T. Melde, W. Plessas, and B. Sengl, Phys. Rev. D **77**, 114002 (2008).

[30] W. Plessas and T. Melde, AIP Conf. Proc. **1056**, 15 (2008).

[31] M. Ronniger, B. C. Metsch, Eur. Phys. J. A **47**, 162 (2011).

[32] M. Ronniger, B. C. Metsch, Eur. Phys. J. A **49**, 8 (2013).

[33] S. Migura, D. Merten, B. Metsch and H. R. Petry, Eur. Phys. J. A **28**, 55 (2006).

[34] S. Migura, *'Weak and Strong Baryon Decays in a Constituent Quark Model'*, PhD thesis TH 06-17, (2006).

[35] D. Lurie, *'Particles and Fields'*, Interscenic Publishers, New York (1968).

[36] C. R. Münz, J. Resag, B. C. Metsch, H. R. Petry, Nucl. Phys. A **578**, 418 (1994).

[37] J. Resag, C. R. Münz, B. C. Metsch, H. R. Petry, Nucl. Phys. A **578**, 397 (1994).

[38] E. Klempt, B. C. Metsch, C. R. Münz and H. R. Petry, Phys. Lett. B **361**, 160 (1995).

[39] C. R. Münz, J. Resag, B. C. Metsch and H. R. Petry, Phys. Rev. C **52**, 2110 (1995).

[40] C. R. Münz, Nucl. Phys. A **609**, 364 (1996).

[41] Ch. Ritter, B. C. Metsch, C. R. Münz and H. R. Petry, Phys. Lett. B **380**, 431 (1996).

[42] V. Keiner, Phys. Rev. C **54**, 3232 (1996).

[43] V. Keiner, Z. Phys. A **354**, 87 (1996).

[44] M. Koll, R. Ricken, D. Merten, B. C. Metsch, H. R. Petry, Eur. Phys. J. A **9**, 73 (2000).

[45] R. Ricken, M. Koll, D. Merten, B. C. Metsch, H. R. Petry, Eur. Phys. J. A **9**, 221 (2000).

[46] S. J. Wallace, V. B. Mandelzweig, Nucl. Phys. A **503**, 673 (1989).

[47] L. Tiator, D. Drechsel, S. S. Kamalov and M. Vanderhaeghen, Eur. Phys. J. Special Topics **198**, 141 (2011).

[48] M. Warns *et al.*, Z. Phys. C **45**, 627 (1990).

[49] I. G. Aznauryana and V. D. Burkert, Prog. Part. Nucl. Phys. 67, 1 (2012).

[50] W. W. Ash, K. Berkelman, C. A. Lichtenstein, A. Ramanaukas and R. H. Siemann Phys. Lett. B **24**, 165 (1967).

[51] J. Carlson, J. B. Kogut, V. R. Pandhariapande, Phys. Rev. D **27**, 233 (1983).

[52] J. Carlson, J. B. Kogut, V. R. Pandhariapande, Phys. Rev. D **28**, 2807 (1983).

[53] G. 't Hooft, Phys. Rev. D **14**, 3432 (1976), Erratum: ibid. D18, 2199 (1978).

[54] M. A. .Shifman, A. I. Vainshtein, V. I. Zakharov, Nucl. Phys. B **163**, 46 (1980).

[55] T. Murota, Progr. Theor. Phys. **69**, 181 (1994).

[56] K. Nakamura *et al.* (Particle Data Group), J. Phys. G **37**, 075021 (2010).

[57] D. Jido, J. A. Oller, E. Oset, A. Ramos, U. G. Meißner, Nucl. Phys. A **725**, 181 (2003).

[58] T. Hyodo, D. Jido and L. Roca, Phys. Rev. D **77**, 056010 (2008).

[59] T. Hyodo, D. Jido and A. Hosaka, Phys. Rev. C **78**, 025203 (2008).

[60] G. Caia, J. W. Durso, C. Elster, J. Haidenbauer, A. Sibirtsev and J. Speth, Phys. Rev. C **66**, 044006 (2002).

[61] M. M. Lêvy, Phys. Rev. **88**, 725 (1952).

[62] K. A. Brueckner and K. M. Watson, Phys. Rev. **92**, 1023 (1953).

[63] I. Horn *et al.*, Eur. Phys. J. A **38**, 173 (2008).

[64] M. E. Christy *et al.*, Phys. Rev. C **70**, 015206 (2004).

[65] I. A. Qattan *et al.*, Phys. Rev. Lett. **94**, 142301 (2005).

[66] P. Mergell, U. G. Meißner and D. Drechsel, Nucl. Phys. A **596**, 367 (1996).

[67] T. Eden *et al.*, Phys. Rev. C **50**, 1749 (1994).

[68] C. Herberg *et al.*, Eur. Phys. J. A **5**, 131 (1999).

[69] M. Ostrick *et al.*, Phys. Rev. Lett. **83**, 276 (1999).

[70] I. Passchier *et al.*, Phys. Rev. Lett. **82**, 4988 (1999).

[71] D. Rohe *et al.*, Phys. Rev. Lett. **83**, 21 (1999).

[72] R. Schiavilla *et al.*, Phys. Rev. C **64**, 041002 (2001).

[73] J. Golak *et al.*, Phys. Rev. C **63**, 034006 (2001).

[74] H. Zhu *et al.*, Phys. Rev. Lett. **87**, 081801 (2001).

[75] R. Madey *et al.*, Phys. Rev. Lett. **91**, 122002 (2003).

[76] G. Warren *et al.*, Phys. Rev. Lett. **92**, 042301 (2004).

[77] D. I. Glazier *et al.*, Eur. Phys. J. A **24**, 101 (2005).

[78] R. Alarcon *et al.*, Eur. Phys. J. A **31**, 588 (2007).

[79] A. Bodek, S. Avvakumov, R. Bradford, and H. Budd, J. Phys. Conf. Ser. **110**, 082004 (2008).

[80] V. Bernard, L. Elouadrhiri, and U. G. Meißner, J. Phys. G **28**, 1 (2002).

[81] H. Anklin *et al.*, Phys. Lett. B **428**, 248 (1998).

[82] W. Xu *et al.*, Phys. Rev. Lett. **85**, 2900 (2000).

[83] G. Kubon *et al.*, Phys. Lett. B **524**, 26 (2002).

[84] M. Vanderhaeghen, Nucl. Phys. A **755**, 269 (2005).

[85] B. D. Milbrath *et al.*, Phys. Rev. Lett. **80**, 452 (1998).

[86] M. K. Jones *et al.*, Phys. Rev. Lett. **84**, 1398 (2000).

[87] O. Gayou *et al.*, Phys. Rev. C **64**, 038202 (2001).

[88] T. Pospischil *et al.*, Eur. Phys. J. A **12**, 125 (2001).

[89] O. Gayou *et al.*, Phys. Rev. Lett. **88**, 092301 (2002).

[90] V. Punjabi *et al.*, Phys. Rev. C **71**, 055202 (2005).

[91] B. Hu *et al.*, Phys. Rev. C **73**, 064004 (2006).

[92] C. B. Crawford *et al.*, Phys. Rev. Lett. **98**, 052301 (2007).

[93] D. W. Higinbotham, AIP Conf. Proc. **1257**, 637 (2010).

[94] G. Ron *et al.*, arXiv:1103.5784v1 [nucl-ex] (2011).

[95] X. Zhan *et al.*, JLAB-PHY-11-1311, 5 (2011).

[96] L. E. Price *et al.*, Phys. Rev. D **4**, (1971).

[97] T. Bartel *et al.*, Nucl. Phys. B **58**, 469 (1973).

[98] C. Berger , V. Burkert , G. Knop , B. Langenbeck and K. Rith, Phys. Lett. B **35**, 1 (1971).

[99] R. C. Walker *et al.*, Phys. Rev. D **49**, (1994).

[100] L. Andivahis *et al.*, Phys. Rev. D **50**, (1994).

[101] E. Amaldi *et al.*, Phys. Lett. B **41**, 216 (1972).

[102] P. Brauel *et al.*, Phys. Lett. B **45**, 389 (1973).

[103] E. D. Bloom *et al.*, Phys. Rev. Lett. **30**, 1186 (1973).

[104] A. Del Guerra *et al.*, Nucl. Phys. B **99**, 253 (1975).

[105] P. Joos *et al.*, Phys. Lett. B **62**, 230 (1976).

[106] N. J. Baker *et al.*, Phys. Rev. D **23**, 2499 (1981).

[107] K. L. Miller *et al.*, Phys. Rev. D **26**, 537 (1982).

[108] T. Kitagaki *et al.*, Phys. Rev. D **28**, 436 (1983).

[109] T. Kitagaki *et al.*, Phys. Rev. D **42**, 1331 (1990).

[110] D. Allasia *et al.*, Nucl. Phys. B **343**, 285 (1990).

[111] L. Y. Glozman, M. Radici, R. F. Wagenbrunn, S. Boffi, W. Klink, W. Plessas, Phys. Lett. B **516**, 183 (2001).

[112] R. F. Wagenbrunn, S. Boffi, L. Y. Glozman, W. Klink, W. Plessas and M. Radici, AIP Conf. Proc. **603**, 319 (2001).

[113] R. F. Wagenbrunn, S. Boffi, L. Y. Glozman, W. Klink, W. Plessas, and M. Radici, Eur. Phys. J. A **18**, 155 (2003).

[114] D. Drechsel, S. S. Kamalov, and L. Tiator, Eur. Phys. J. A **34**, 69 (2007).

[115] P. Kummer *et al.*, Phys. Rev. Lett. **30**, 873 (1973).

[116] U. Beck *et al.*, Phys. Lett. B **51**, 103 (1974).

[117] J. Alder *et al.*, Nucl. Phys. B **91**, 386 (1975).

[118] H. Breuker *et al.*, Phys. Lett. B **74**, 409 (1978).

[119] F. W. Brasse *et al.*, Nucl. Phys. B **139**, 37 (1978).

[120] M. Benmerrouche *et al.*, Phys. Rev. Lett. **67**, 1070 (1991).

[121] B. Krusche *et al.*, Phys. Rev. Lett. **74**,3736 (1995) .

[122] C. S. Armstrong *et al.*, Phys. Rev. D **60**, 052004 (1999).

[123] R. Thompson *et al.*, Phys. Rev. Lett. **86**, 1702 (2001).

[124] B. D. Keister and S. Capstick, N* PHYSICS, edited by T.-S. H. Lee and W. Roberts, 341 World Scientific, Singapore (1997).

[125] L. Tiator, D. Drechsel, S. S. Kamalov, M. Vanderhaeghen, Chinese Phys. C **33**, 1069 (2009).

[126] S. Capstick and B. D. Keister, Phys. Rev. D **51**, 3598 (1995).

[127] C. Gerhardt, Z. Phys. C **4**, 311 (1980).

[128] J. Ahrens *et al.*, Phys. Rev. Lett. **88**, 232002 (2002).

[129] N. Awaji *et al.* DPNU-29-81, 11 (1981).

[130] G. Penner and U. Mosel, Phys. Rev. C **66**, 055212 (2002).

[131] I. M. Barbour, R. L. Crawford and N. H. Parsons, Nucl. Phys. B **141**, 253 (1978).

[132] R. C. E. Devenish D. H. Lyth and W. A. Rankin, Phys. Lett. B **52**, 227 (1974).

[133] S. Stein *et al.*, Phys. Rev. D **12**, 1884 (1975).

[134] F. Foster and G. Hughes, Rep. Prog. Phys. **46**, 1445 (1983).

[135] V. V. Frolov *et al.*, Phys. Rev. Lett. **82**, 45 (1999).

[136] A. N. Villano *et al.*, Phys. Rev. C **80**, 035203 (2009).

[137] S. Migura, D. Merten, B. Metsch and H. R. Petry, Eur. Phys. J. A **28**, 41 (2006).

[138] B. C. Metsch, Eur. Phys. J. A **35**, 275 (2008).

[139] T. T. Takahashi and M. Oka, Prog. Theor. Phys. Suppl. **186**, 172 (2010).

[140] J. J. de Swart, Rev. Mod. Phys. **35**, 916 (1963).

Danksagung

An erster Stelle möchte ich Herrn Priv. Doz. Dr. Bernard Chr. Metsch meinen Dank für die sehr intensive und freundliche Betreung während meiner gesamten Doktorarbeit aussprechen. Ohne die vielen und tiefgehenden Diskussionen mit Herrn Metsch wäre diese Arbeit nicht wie vorliegend zustande gekommen. Desweiteren möchte ich mich bei Ihm für das intensive Korrekturlesen und die zahllosen Verbesserungsvorschläge meines Manuskripts bedanken. Für die Übernahme des Koreferats danke ich sehr herzlich Carsten Urbach. Desweiteren danke ich auch den anderen Mitgliedern der Prüfungskommision für Ihre Zeit und Engagement.

Besonderen Dank gilt hier ebenfalls Simon Tölle für das intensive Korrekturlesen meiner Arbeit sowie für seine Hilfe bei der Optmierung des benutzten Bethe-Baryon Programms, durch die sich letztendlich die Arbeit erheblich vereinfachte und beschleunigte. Desweiteren danke ich auch Christoph Ditsche sowie Philipp Hagen für die vielen anregenden Diskussionen.

Ebenso möchte ich mich bei meinen Kolleginnen und Kollegen am Helmholtz-Institut für Strahlen- und Kernphysik für die freundschaftliche und familiäre Atmosphäre bedanken, die zu einer Vielzahl von wissenschaftlichen Diskussionen beitrug.

Schließlich möchte ich meiner ganzen Familie für Ihre immerwährende Unterstützung danken, die Sie mir gerade im Rahmen meiner Dissertation zukommen ließen. Darüber hinaus möchte ich Julia Snoei sehr herzlich danken, die mir als Freund immer zur Seite stand.